Università degli Studi di Padova

Dipartimento di Astronomia

SCUOLA DI DOTTORATO DI RICERCA IN ASTRONOMIA
XXIII ciclo
Sede amministrativa: Università degli Studi di Padova

The Herschel Space Observatory:
Pipeline development and early cosmological surveys results

Supervisore: Ch.mo Prof. Alberto Franceschini
Co-Supervisori: Dr. Pasquale Panuzzo
Dr. Mattia Vaccari
Direttore della Scuola: Ch.mo Prof. Giampaolo Piotto

DOTTORANDO:Gabriele Mainetti

January 21, 2011

A mio padre

...ricorda Signore questi servi disobbedienti
alle leggi del branco
non dimenticare il loro volto
che dopo tanto sbandare
è appena giusto che la fortuna li aiuti
come una svista
come un'anomalia
come una distrazione
come un dovere

F. De Andrè

Riassunto - *Abstract*

Questa Tesi tratta tutte le problematiche tecniche e scientifiche legate all'utilizzo delle lunghezze d'onda infrarosse e sub-millimetriche in astronomia. In particolare la Tesi si focalizza sull'Osservatorio Spaziale *Herschel* con particolare attenzione a uno degli strumenti a bordo, SPIRE del quale verranno descritti nel dettaglio il design e le componenti. Le problematiche legate alla riduzione dati vengono trattate in questa Tesi nei capitoli centrali nei quali si descriverà dettagliatamente il lavoro svolto in quest'ambito: verranno descritte tutte le fasi della pipeline di riduzione dati, cioè la trasformazione di dati grezzi di telemetria in dati "scientifici" usabili dalla comunità astronomica. La Tesi tratterà poi gli aspetti legati all'analisi di questi dati, con particolare riguardo agli strumenti sviluppati per analizzare facilmente i grandi datasets che compongono i "prodotti" finali delle osservazioni effettuate con *Herschel*. Il lato scientifico del problema verrà discusso nei capitoli finali con particolare attenzione per le cosiddette surveys cosmologiche. La Tesi si focalizzerà quindi sui primi risultati ottenuti nell'ambito di uno dei più grandi progetti pensati per *Herschel*, cioè HerMES e sulle applicazioni di una tecnica statistica nota come analisi della Probabilità delle Deflessioni - *P(D)* per ottenere informazioni accurate sull'andamento dei conteggi di sorgenti al di sotto del limite di confusione. Questa Tesi mette quindi in evidenza sia gli aspetti tecnici (con particolare attenzione a tutta l'infrastruttura software) di una missione importante come quella di *Herschel*, sia gli aspetti puramente scientifici (formazione ed evoluzione delle galassie, cosmologia osservative) legati alle osservazioni astronomiche nelle bande infrarosse e sub-millimetriche.

This thesis deals with all technical and scientific issues related to the use of infrared and sub-millimeter wavelengths in astronomy. In particular, the thesis focuses on the HerschelSpace Observatory with particular attention to one of the instruments on board, SPIRE of which the design and components will be described in detail. The problems related to data reduction are presented in this Thesis in the central chapters: all phases of the pipeline data reduction will be described, namely the transformation of raw telemetry data in "scientific" data usable by the astronomical community. The thesis will then deal with the aspects linked of analysis of these data, particularly with regard to the tools developed to analyze *easily the large datasets released to the astronomical community. The scientific side of the issue will be discussed in the final chapters with particular attention to the so-called cosmological surveys. The thesis will focus then on the first results obtained in one of the largest projects designed to Herschel, i.e. HerMES, and on the application of a technique known as statistical analysis of the probability of deflection - P(D) to improve our knowledge about the number counts below the confusion limit. This thesis emphasizes, therefore, both technical aspects (with particular attention to all the software infrastructure) of an important mission as the Herscheland the purely scientific aspects (formation and evolution of galaxies, observational cosmology) related to astronomical observations in the infrared and sub-millimetric bands.*

Contents

List of Figures

List of Tables

Acronyms

ADC	Analogue to Digital Converter
ADU	Analogue Data Unit
AO	Announcement of Opportunity
AOR	Astronomical Observation Request
AOT	Astronomical Observing Template
BSM	Beam Steering Mechanism
CCB	Data Processing Configuration Control Board
CVV	Cryostat Vacuum Vessel
CIRB	Cosmic InfraRed Background
COBE	Cosmic Background Explorer
CoP	Commissioning Phase
CVS	Concurrent Version System
DCU	Detector Control Unit
DP	Data Processing System
DPU	Digital Processing Unit
DRCU	Detector Readout and Control Unit
DTE	Detector Timeline Explorer
DTM	Detector Timeline Mosaic
FCU	FPU Control Unit

FIDEL	Spitzer Far-Infrared Deep Extra- galactic Legacy Survey
FPU	Focal Plane Unit
FSDL	Fast Science Data Link
FTS	Fourier Transform Spectrometer
GT	Guaranteed Time
GUI	Graphical User Interface
HCSS	Herschel Common Science System
HerMES	Herschel Multi-tiered Extragalactic Survey
HIFI	Heterodyne Instrument for the Far Infrared
HIPE	Herschel Integrated Processing Environment
HOTAC	Herschel Observing Time Allocation Committee
HSA	Herschel Science Archive
HSC	Herschel Science Centre
IA	Interactive Analysis
ICC	Instrument Control Center
IRAS	Infrared Astronomical Satellite
ISO	Infrared Space Observatory
IPAC	Infrared Processing and Analysis Center
KP	Key programmes
LSL	Low Speed Link
MOC	Mission Operations Centre
NHK	Nominal House Keeping Timeline (see product definition at `http://tinyurl.com/37dtmmp`)
OPD	Optical Path Difference
OT	Open Time

PACS	Photodetector Array Camera and Spectrometer
PCAL	Photometer CALibration source
PDT	Photometer Detector Timeline (see product definition at `http://tinyurl.com/2v62gu2`)
PI	Principal Investigator
PLW	Photometer Long (500 μm) Wavelength
PMW	Photometer Short (350 μm) Wavelength
POF	Photometer Observing Functions
PPT	Pointed Photometer Timeline (see product definition at `http://tinyurl.com/373pylt`)
PSF	Point-Spread Function
PSP	Photometer Scan Product (see product definition at `http://tinyurl.com/22o43rr`)
PSW	Photometer Short (250 μm) Wavelength
PVP	Performance verification phase
QCP	Quality Control Pipeline
QLA	Quick Look Analysis
RSP	Routine science phase
SAG	Science Advisory Groups
SCAL	Spectrometer CALibration source
SCUBA	Submillimetre Common-User Bolometer Array
SDI	Spectrometer Detector Interferogram (see product definition at `http://tinyurl.com/22sv6tn`)
SDP	Science Demonstration Phase
SDS	Spectrometer Detector Spectrum (see product definition at `http://tinyurl.com/2fk98hz`)

SDT	Spectrometer Detector Timeline (see product definition at `http://tinyurl.com/2fk98hz`)
SGS	Science Ground Segment
SLW	Spectrometer Long Wavelength
SMEC	Spectrometer Mirror Mechanism
SMP	Science Management Plan
SPG	Standard Product Generation
SSW	Spectrometer Short Wavelength
SPIRE	Spectral and Photometric Imaging REceiver
TSP	Timeline Simple Plot
ZPD	Zero Optical Path Difference

Introduction

Modern historians have reported that in the year 1800 Sir William Herschel discovered infrared (IR) light, and then Sir William presumably succeeded in measuring a spectral energy distribution by using a set of thermometers and a glass prism. After two century, this discovery has led to a better understanding of the universe that surrounds us, although several problems have limited the development of astronomy at these wavelengths, such as the barrier due to absorption caused by atmospheric water vapor and the technical difficulty in building detectors enough sensitive. But since the late 60's this branch of astronomy has had a continuous development and we can say that, in these years, it is in its heyday.

The astronomical use of these wavelengths allow us to research into the origin and composition of planets: the infrared observations can reveal the composition of objects within our solar system as well as detect the material that may be forming worlds around other stars. Likewise, in the infrared spectral range astronomers can study stars throughout their lives, from the earliest stages of formation in the hearts of dust clouds to their final years as they sputter and die. One of the outstanding challenges in modern cosmology is to explain the formation of structure in the universe. The assembly of matter into stars and galaxies and the subsequent evolution of such systems is accompanied by the release of radiant energy powered by gravitational and nuclear processes. Cosmic expansion and the absorption of short wavelength radiation by dust and re-emission at long wavelengths will shift a significant part of this radiant energy into infrared background radiation. A Cosmic InfraRed Background (CIRB) is therefore an expected relic of structure formation processes, and its measurement provides new insight into those processes.

For these reason looking the sky at these wavelength is not only important but also fundamental. In the last years, the already very satisfactory results of the first space missions such as IRAS, COBE and ISO or of the ground as SCUBA have been compounded by the extraordinary results obtained by Spitzer Space Telescope (Spitzer). All these results are only a prelude to what the *Herschel* Space Observatory is doing and will do in the coming years.

This thesis work will address in detail many of the scientific and technical problems that occur when the astronomers work at these wavelengths. Indeed, the focus of the thesis is *Herschel* and I will describe the issues related to the development of pipeline data reduction (in particular for the SPIRE instrument), the need to create and develop new and easy to use interactive analysis tools for exploring the huge datasets produced during the observations, the early scientific results obtained by one of the most important *Herschel* cosmological program (HerMES) and the problems faced by astronomers in the study of maps produced in these observations (namely the problem of confusion and identification of sources).

1

Infrared and Sub-Millimeter Astronomy

1.1 The Infrared Spectral Region

Infrared radiation (IR) lies between the visible and microwave portions of the electromagnetic spectrum, spans the wavelength range between 1 μm and 300 μm. Infrared is broken into three categories: near (NIR, 1-5 μm), mid (MIR, 5-30 μm) and far-infrared (FIR, 30-300μm). We refer to the regions beyond the FIR as the sub-millimeter (sub-mm, 300 μm-1 mm) and millimeter (mm) regions.

The IR radiation was discovered by Sir William Herschel in the 1800, but the astronomical use of this radiation had to wait more than 150 years. To study the astronomical phenomena in these wavelengths we need high sensitive detectors. Only after the second world war, in the 1950s, the scientists have begun to develop these detectors (Low et al. 2007) and only in the 60's the astronomers have begun to use them.

Another problem has stopped the development of IR and sub-mm astronomy: the observations from the ground are very limited by the large atmospheric absorption in these spectral regions. Figure 1.1 shows the transmission of Earth's atmosphere at NIR/MIR and Figure 1.3 at the sub-mm wavelengths: water vapor (concentrated in the lower portion of the atmosphere) and carbon dioxide are especially important absorbers throughout the IR, with water vapor making the atmosphere completely opaque over large wavelength ranges from almost all ground-based observing sites. In addition, the atmosphere itself radiates strongly in the infrared, often putting out more infrared light than the object in space being observed. For these reasons, the observation from ground is limited in some particular bands where these effects are negligible or limited. In general the good windows from ground are: 1-5 μm (where we have the standard filters J (1.25 μm), H (1.65 μm), K (2.2 μm), L (3.6 μm) and M (4.8 μm)), 8-14 μm (standard filter N) and 16-25 μm (standard filter Q). At FIR wavelengths the atmosphere is completely opaque because of water vapor, but is partially transparent at $\lambda > 300\ \mu m$, which marks the beginning of the sub-millimeter region.

1.2 The infrared astronomy

In the 1969 Neugebauer & Leighton (1969) made the first astronomical survey in IR, mapping the 30000 deg^2 of sky visible from California at a wavelength of 2.2 μm and cataloging 5600 sources. But, for the reasons explained before, becomes soon obvious that better results would be obtained if we eliminate the atmospheric barrier and during the 70's we have a lot of the experiments aboard rockets or balloons. The real beginning of this field of astronomy, however, it can coincide with the first space mission dedicated to this type of observations: Infrared Astronomical Satellite (IRAS). From this moment we will find numerous other missions and the results are always the most interesting.

But, what is the importance of astronomy in the IR and sub-mm? Why we are in a sense forced to observe at these wavelengths? What these wavelengths can tell us that we cannot obtain, for example, using the observations in the optical wavelengths? In fact, all the fields of astronomy can benefit from the observations in these wavelengths: one can discover the details of the origin and composition of the planets in our solar and other systems, one can study stellar evolution from its origins into clouds of dust until the final states, but in particular we can study the generation and assembly of stars in galaxies and all AGN phenomena that are often invisible in the optical because of the dust. Via IR and sub-mm observations remarkable progress has been made, particularly on galaxies bright in the rest-frame ultraviolet (UV) and visible. We have found that galaxies at high redshift often have different morphologies than the orderly Hubble sequence in the Local Universe. We have discovered different classes of object through surveys at different wavelengths and we have found evidence that major events of star formation in the universe happened at high redshifts, $z \sim 1$, and are likely responsible for the origin or assembly of the most massive galaxies today. Such events would be accompanied by major energy release, but, because of heavy dust extinction, would be detectable only through far-infrared observations. Submillimetric surveys indeed have identified sources that are extremely luminous at long wavelength, but almost undetectable in the optical (e.g. Chapman et al. 2005).

As said in the introduction, a Cosmic InfraRed Background (CIRB) is an expected relic of structure formation processes, due to the assembly of matter into stars and galaxies and the subsequent evolution of such systems. One of the first

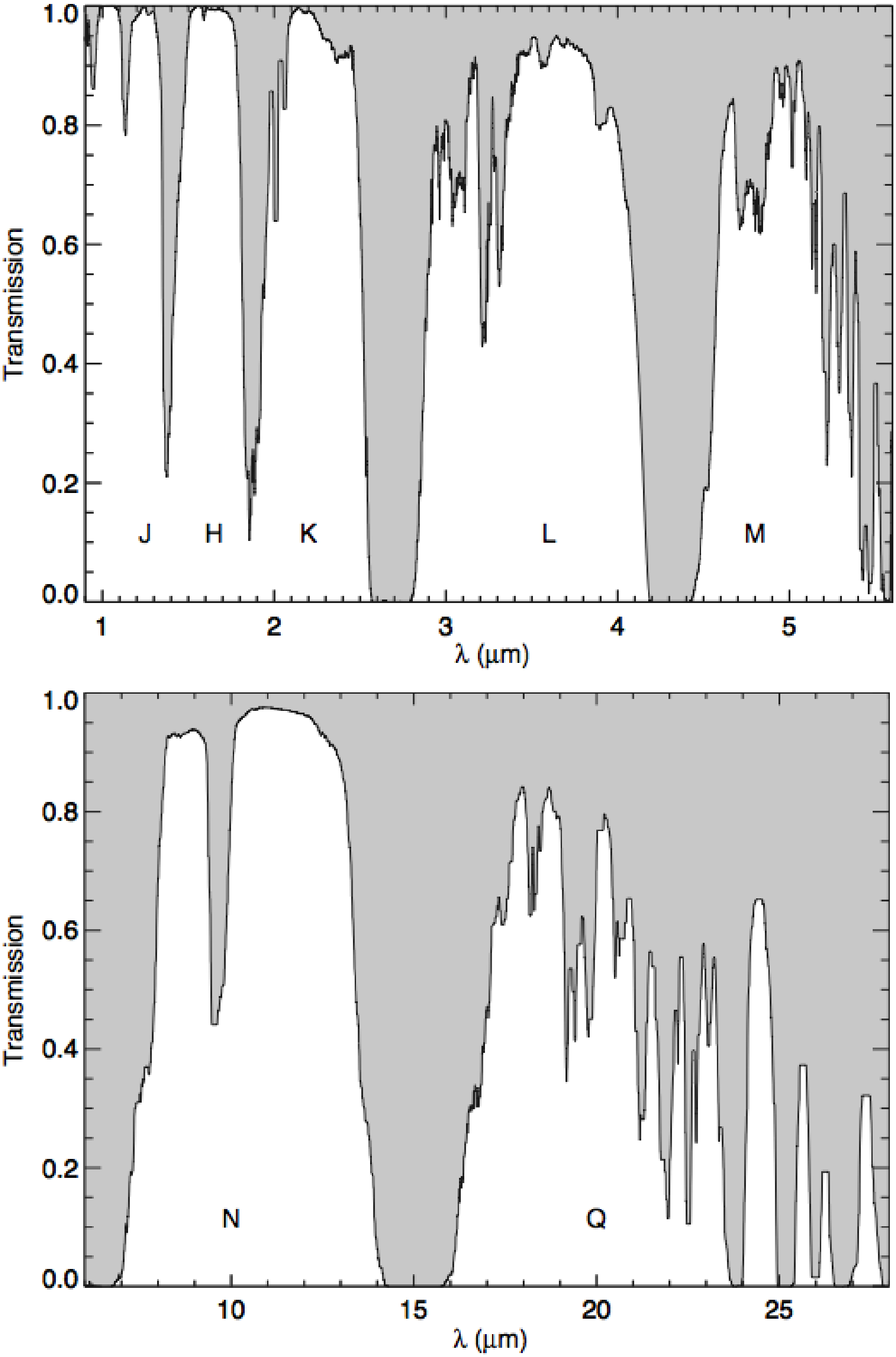

Figure 1.1: Atmospheric transmission in the near- and mid-infrared spectral region. Filter names in each spectral window are shown. From Vaccari (2004)

outcome for the infrared astronomy was the CIRB discovery realized by Cosmic Background Explorer (COBE). The COBE satellite was developed by NASA's Goddard Space Flight Center to measure the diffuse infrared and microwave radiation from the early universe to the limits set by our astrophysical environment. It was launched November 18, 1989 and carried three instruments, a Diffuse Infrared Background Experiment (DIRBE) to search for the cosmic infrared background radiation, a Differential Microwave Radiometer (DMR) to map the cosmic radiation sensitively, and a Far Infrared Absolute Spectrophotometer (FIRAS) to compare the spectrum of the cosmic microwave background radiation with a precise blackbody.

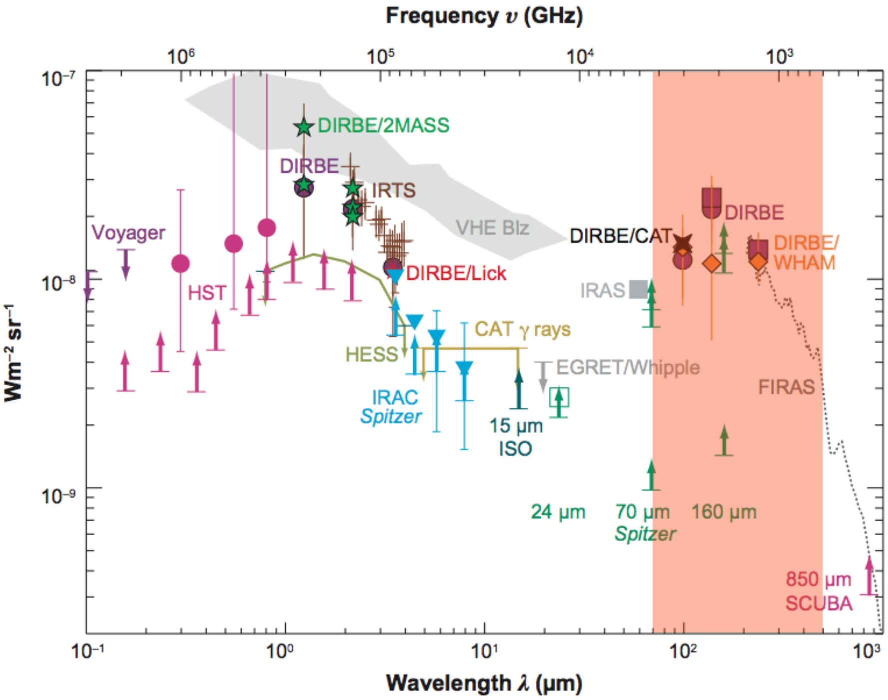

Figure 1.2: The extragalactic background light spectral energy distribution from 0.1 to 1000 μm as resolved by many missions. The overlapped orange band shows the wavelengths range for the SPIRE and PACS instruments on board *Herschel* Space Observatory. See Soifer et al. (2008) for a detailed explanation of the data sets and background estimates included in this figure.

The original detection of the CIRB was performed by Puget et al. (1996) and later confirmed with independent analyses by various other groups using FIRAS (Fixsen et al. 1998), as well as data from the DIRBE experiment in three broadband channels at λ =240, 140 and 100 μm (Hauser et al. 1998). The CIRB is the product of the light radiated by dust over a Hubble time and, from energetic consideration, it is primarily powered by star formation (the accretion around black-hole contribution is $< 20\%$). The integrated extragalactic background light in the far-infrared and sub-millimeter region of the spectrum is approximately equal to the integrated background light in the optical and UV part of the spectrum (see Figure 1.2 and Guiderdoni et al. 1997). To appreciate the relevance of this discovery consider that extragalactic backgrounds at other wavelengths contain only modest contributions by distant galaxies: the radio background is clearly dominated by radio- loud AGN; the microwave background includes photons generated at $z \sim 1500$; the X-ray and γ-ray backgrounds are dominated by distant quasars and AGN. On the other hand, the DIRBE experiment on board COBE has brought to the first detection of the integrated emission by distant galaxies in the form of an isotropic signal at far-IR and sub-mm wavelengths. Then the CIRB's intensity exceeding the optical background suggests that galaxies in the past should have been much more "active" in the far-IR than in the optical, and very luminous in an absolute sense. For this reason if we want develop a complete understanding of galaxy formation, this background light must be resolved into galaxies and their properties must be characterized: a powerful tools used by astronomers to resolve the CIRB in galaxies are the IR and sub-mm surveys. In the last years many long-wavelength surveys was performed using the main ground and space facilities and in particular the results obtained with Submillimetre Common-User Bolometer Array (SCUBA), Infrared Space Observatory (ISO) and Spitzer opened a new window on galaxies formation.

SCUBA Submillimetre Common-User Bolometer Array was designed and constructed at the Royal Observatory, Edinburgh in collaboration with Queen Mary, University of London. It was delivered to the James Clerk Maxwell Telescope (JCMT) in Hawaii in 1996 and was fully operational by 1997.

SCUBA had two arrays of bolometric detectors. The long-wave array has 37 detectors operating in the 750 and 850 μm atmospheric transmission windows, while the short-wave array has 91 detectors for observations at 350 and 450 μm (see Figure 1.3). The pixels are arranged in a close-packed hexagon arrangement. Both arrays have approximately the same field-of-view with a diameter of $2.3'$, and can be used simultaneously by means of a beam-splitter. There was also three pixels available for photometry in the transmission windows at 1.1, 1.35 and 2.0 mm, and these was located around the edge of the long-wave array. The detectors was cooled to approximately 100 mK to limit background noise from heat emitted by the instrument.

The results from SCUBA surveys showed that the previously theoretical model on galaxy formation based upon optically selected samples significantly underes-

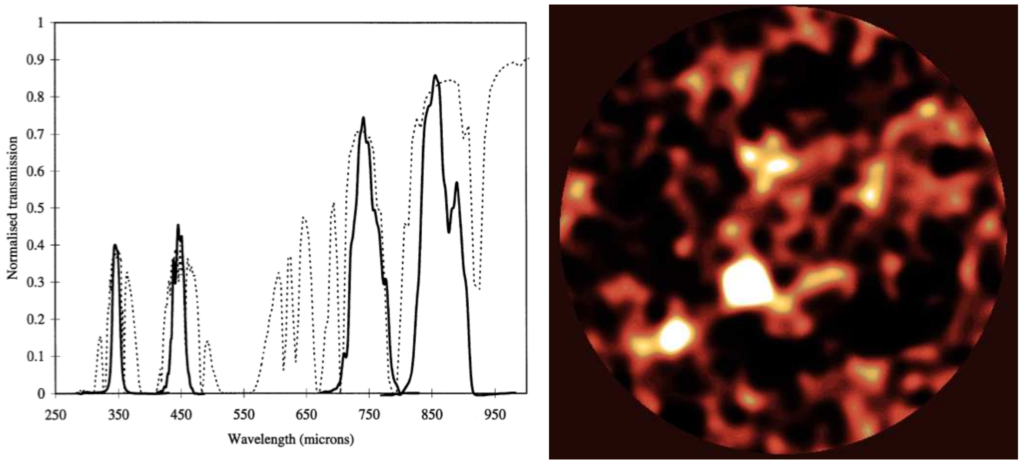

Figure 1.3: **Left:**The measured SCUBA filter profiles (solid lines), superimposed on the sub-millimetre atmospheric transmission curve (dotted) for Mauna Kea for 1 mm of precipitable water vapor (Holland et al. 1999). **Right:** The 850 μm SCUBA image of the Hubble Deep Field. The image shows a radius of $100''$ from the map centre (Hughes et al. 1998)

timate the observed surface density of sub-millimeter sources: this demonstrates that a significant fraction ($> 80\%$) of the star-formation activity in the high-redshift universe may have been missed in previous optical studies (Smail et al. 1997, Hughes et al. 1998). SCUBA has identified a population of high-redshift dusty starburst galaxies which contribute a significant fraction of the extragalactic background at 850 μm (Hughes et al. 1998) and shown that a density of dust-enshrouded star-formation at $z > 2$ which is at least a factor of ~ 5 greater than that deduced from Lyman limit systems.

ISO The Infrared Space Observatory (ISO, Kessler et al. 1996) was the world's first true orbiting infrared observatory. Equipped with four highly-sophisticated and versatile scientific instruments, it was launched by Ariane in November 1995 and provided astronomers world-wide with a facility of unprecedented sensitivity and capabilities for a detailed exploration of the Universe at infrared wavelengths.

Two spectrometers (SWS and LWS), a camera (ISOCAM) and an imaging photo-polarimeter (ISOPHOT) jointly covered wavelengths from 2.5 to around 240 μm with spatial resolutions ranging from $1.5''$(at the shortest wavelengths) to $90''$(at the longer wavelengths). Its 60 cm diameter telescope was cooled by superfluid liquid helium to temperatures of 2-4 K.

The mission was a great technical, operational and scientific success with most satellite sub-systems operating far better than specifications and with its scientific results impacting practically all fields of astronomy. During its routine operational phase, which lasted until April 1998 - almost a year longer than specified, ISO successfully made some 30000 individual imaging, photometric, spectroscopic and polarimetric observations ranging from objects in our own solar system right out to the most distant extragalactic sources.

In the ensuing Post Operational Phases, which ended in 2006, the ISO archive has been improved and enhanced both in functionality and in contents, in order to maximize its long-term value and usability, as a legacy to future generations of astronomers.

ISO allowed for the first time to perform sensitive surveys of distant IR sources in the mid- and far-IR and to characterize in detail the evolution of the IR emissivity of galaxies up to redshift $z \sim 1$ and above. Deep surveys with ISO have been performed in two MIR (5–8.5 μm and 12–18 μm) and two FIR ($\lambda = 90$ and 170 μm) broad-bands (ISO sensitivity limits in the MIR are three orders of magnitude deeper in flux density than at long wavelengths). Thanks to these surveys we were able to determine that happened a very rapid increase of galaxy long-wavelength volume emissivity with redshift, paralleled by an increased incidence in high-redshift sources of dust extinction and thermal dust reprocessing, with respect to locally observed galaxies, that only a minor fraction of their IR flux originates from AGN activity, the bulk of it being likely due to star formation (Franceschini et al. 2001). The ISO data generally supported unified accretion disk+circumnuclear torus/disk models, improved out knowledge about the properties, energy sources, and evolution of (ultra) luminous infrared galaxies (Genzel & Cesarsky 2000). Starting from the ISO data, many model was realized to explain the galaxy formation and evolution (e.g. Franceschini et al. 2001).

Spitzer Space Telescope The Spitzer Space Telescope (Spitzer, Werner et al. 2004) is a space-borne, cryogenically-cooled infrared observatory capable of studying objects ranging from our Solar System to the distant reaches of the Universe. Spitzer is the final element in NASA's Great Observatories Program, and an important scientific and technical cornerstone of the Astronomical Search for Origins Program. Spitzer incorporates an 85 cm diameter telescope primary mirror, cooled to as low as 5.5 K, and three scientific instruments providing imaging and spectroscopy at wavelengths from 3.6 to 160 μm. The launch of the Spitzer opened a new era for infrared astronomy. Its vast leap in sensitivity over previous platforms, both space and ground, has enabled Spitzer to address virtually every aspect of observational astronomy. The Spitzer flight hardware consists of a spacecraft that operates at roughly room temperature and a Cryogenic Telescope Assembly (CTA) that is cooled by a combination of superfluid liquid helium, helium boil-off gas, and radiative cooling and operates at much lower temperatures. The Spitzer spacecraft handles the observatory's power generation, pointing and momentum control, data processing and storage, and telecommunications functions. It also contains the warm electronics portions of the three scientific instruments. Three infrared instruments, the Infrared Array Camera (IRAC), the Infrared Spectrograph (IRS), and the MIPS, share a common focal plane.

IRAC The Infrared Array Camera (IRAC) is a four-channel camera that provides simultaneous $5.2' \times 5.2'$ images at 3.6, 4.5, 5.8, and 8 μm. IRAC was built by the NASA Goddard Space Flight Center (GSFC) with management and scientific leadership by the Smithsonian Astrophysical Observatory (SAO) under principal investigator Giovanni Fazio. IRAC is a powerful survey instrument because of its high sensitivity, large field of view, mapping capabilities, and simultaneous four-color imaging.

IRS The InfraRed Spectrograph (IRS) consisted of four separate modules (Short-Low, Short-High, Long-Low, Long-High) which provided low ($R \sim 60-130$) and moderate ($R \sim 600$) resolution spectroscopic capabilities from 5.2 to 38 μm. Spectra could be obtained in either staring or mapping mode. In addition, the IRS provided imaging in two filters (13-18 and 18-26 μm) and onboard software to autonomously identify point sources and accurately place them (by offsetting the telescope) in any of the IRS slits. The IRS was built by Ball Aerospace under contract to JPL and Cornell University based on designs and prototypes constructed at Cornell under principal investigator James R. Houck.

MIPS The Multi-band Imaging Photometer for Spitzer (MIPS) produced imaging and photometry in three broad spectral bands, centered nominally at 24, 70, and 160 μm, and low-resolution spectroscopy between 55 and 95 μm. The instrument contains three separate detector arrays each of which resolves the telescope Airy disk with pixels of size $\lambda/2D$ or smaller. All three arrays viewed the sky simultaneously; multi-band imaging at a given point was provided via telescope motions.

The Spitzer Space Telescope established a new standard for studying the extragalactic universe at IR wavelengths. Although building on the tremendously successful IRAS and ISO missions, Spitzer's enormous gain in sensitivity has enabled studies of objects literally at the farthest reaches of the universe, has discovered new classes of objects and revealed shifts in galaxy populations at intermediate redshifts, and has yielded insights into the physics of interstellar processes in a variety of environments that drive or modulate galaxy evolution.

About the Spitzer cosmological side is important to remember the two main surveys performed: SWIRE and GOODS.

SWIRE, the Spitzer Wide-area Infra-Red Extragalactic Survey, has imaged nearly 50 degrees^2 divided among 6 different directions on the sky. The first general goal was simply to observe a very large patch of sky so that can detect large numbers of galaxies across large expanses of space. Second general goal was to detect galaxies far enough away that they can reveal how the Universe looked when it was half it's current age, or even younger.
GOODS, the Great Observatories Origins Deep Survey, has survey approximately 300 arcmin^2 divided into two fields: the Hubble Deep Field North and the Chandra Deep Field South. The GOODS IRAC observations was designed to detect rest-frame near-infrared light from the progenitors of galaxies like the Milky Way out to $z \sim 4$, and to enable us to measure the stellar mass distribution of galaxies through most of cosmic history. The smaller, ultra-deep IRAC field probed the faintest sources and highest redshifts. The MIPS observations offered the best opportunity to detect emission from dust-obscured star formation in ordinary galaxies out to $z \sim 2.5$. Overall, the data provided the best lower limits to the extragalactic background light at 3.6-24 μm.

The main Spitzer extragalactic results are summarized here as reported in Soifer et al. (2008) .

- Massive galaxies have been found less than a billion years after the Big Bang. This is a great surprise and challenges current ideas about galaxy formation.

- Sources detected in Spitzer surveys at $\lambda > 20$ μm either via direct detections or statistical coadditions, appear to account for the FIR background radiation out to ~ 200 μm. Studies of the origin of the luminosity in FIR sources suggest that 10-20% of the background radiation is attributable to AGN; the rest is attributed to dust-enshrouded star formation.

- The direct detection of dust-enshrouded star formation allows a measurement of the total SFR in the universe as a function of redshift out to $z > 3$. This validates prior studies that applied significant corrections for dust extinction in the distant galaxies.

- The number counts of FIR sources show strong evolution in the population of FIR emitters as a function of redshift. This reflects the increase in dust-enshrouded SFR with redshift and reveals a shift in the IR luminosity function of galaxies toward LIRG dominance and ULIRG prominence at $z \sim 1-2$. At all FIR wavelengths, particularly at 24 μm where counts reach more than 3 orders of magnitude deeper than previous missions, and 70 μm, where the counts go much deeper than ISO, Spitzer's extensive surveys provide much larger samples than previously available. In particular at 24μm the differential counts peak at $\sim 0.2-0.3$ mJy, where the counts are more than an order of magnitude greater than a Euclidean extrapolation from the IRAS data at 100 mJy. The integral counts show $\sim$ 3000 sources per square degree that are brighter than 0.3 mJy. Below 0.3 mJy, the counts converge rapidly at a sub-Euclidian rate to the faint limit of the surveys, which is below 50 μJy in each case. At 70μm the differential source counts turn over at 8–10 mJy; below this flux level, the counts fall steeply with a slope comparable to that reported at 24 μm.

- At $z \sim 2$, 24 μm-selected samples are rich in embedded AGN and MIR enhanced SEDs. This contrasts with sub-millimeter surveys, which favor star formation as a power source and cooler, aromatics-rich SEDs.
- A population of 24 μm bright sources at redshifts between 1.5 and 2.5 has been identified as heavily obscured or even Compton-thick AGN. This population is perhaps twice as abundant as X-ray detected AGN at these redshifts.
- Aromatic features have been found in galaxy spectra for systems at redshifts up to $\sim$ 3. This indicates that the processes that populate the ISM with carbon-rich materials were well in place $\sim$2 Gyr after the Big Bang.
- Aromatic features, commonplace in gas-rich galaxies, appear to diminish in strength rapidly for galaxies with metallicity $<\sim$ 1/4 solar. This implies that z$\sim$ 2 ULIRGs with aromatic- to-dust ratios similar to today's galaxies already had their ISM at close to solar metallicity.
- Silicate emission is found in quasar spectra. This provides another crucial link to the dust- enshrouded AGN, consistent with unified models for AGN.
- Strong molecular hydrogen emission in pure rotational lines is detected in a wide range of systems ranging from dwarfs to normal galaxies to AGN and ULIRGs. These lines carry from $\sim 3\times10^{-5}$ to $\sim 3\times10^{-3}$ of the IR luminosity from dust. In some cases of intergalactic shocks, molecular H can account for as much as 30% of the total luminosity of a system, demonstrating the potential of H2 as a critical cooling channel in early-universe star formation.
- Spitzer 24 μm and H_α data have been combined linearly into more accurate star-formation measures than previously available; the improved measures have been used to extend the Schmidt law of star formation within disks of galaxies.

These are the main results obtained in the last 15 years in the infrared astronomy. But in May 2009 the *Herschel* Space Observatory was launched and now and for the following years we have the opportunity to exploit its exciting data (the

early *Herschel* results was published in an Astronomy and Astrophysics special issue, Walmsley et al. 2010a). I will describe in detail *Herschel* in the Chapter 2, but I will report also here some main information: *Herschel* is the fourth 'cornerstone' mission in the ESA science program. With a 3.5 m Cassegrain telescope it is the largest space telescope ever launched. It is performing photometry and spectroscopy in approximately the 55-671 μm range, bridging the gap between earlier infrared space missions and ground-based facilities.
Herschel has been designed to observe the 'cool universe'; it is observing the structure formation in the early universe, resolving the far infrared cosmic background, revealing cosmologically evolving AGN/starburst symbiosis and galaxy evolution at the epochs when most stars in the universe were formed, unveiling the physics and chemistry of the interstellar medium and its molecular clouds, the wombs of the stars, and unravelling the mechanisms governing the formation of and evolution of stars and their planetary systems, including our own solar system, putting it into context. In short, *Herschel* is opening a new window to study how the universe has evolved to become the universe we see today, and how our star the sun, our planet the earth, and we ourselves fit in. *Herschel* is operated as an observatory facility. It is available to the worldwide scientific community, roughly two thirds of the observing time is 'open time' allocated through standard competitive calls for observing proposals. *Herschel* has three instruments: Spectral and Photometric Imaging REceiver (SPIRE), Photodetector Array Camera and Spectrometer (PACS) and Heterodyne Instrument for the Far Infrared (HIFI). We can understand the importance of *Herschel* looking at the Figure 1.2: the SPIRE and PACS wavelengths range (70-500 μm) cover the CIRB peak and the *Herschel* sensitivity and spatial resolution will be crucial to resolve it in galaxies. In the Chapter 2 and 3 I will describe largely the telescope, the instruments and the observations modes, focusing principally on the SPIRE instrument.

About the opportunities for the cosmology, the main project that *Herschel* is doing and will do are the Herschel Multi-tiered Extragalactic Survey (HerMES) project and the PACS Evolutionary Probe (PEP).
The project HerMES will be largely described in Chapter 5 where I will report also the early results.
The PEP program use the unprecedented sensitivity and spatial resolution of *Herschel* for a comprehensive far-infrared photometric survey of the extragalactic sky. Blank field surveys using PACS at 170, 110 and 75 μm are supplemented with targeted observations of massive $z \sim 1$ clusters and lensing clusters. The main goals are: resolve the bulk of the CIRB, determine the nature of its constituent sources and trace the evolution of dust-obscured star formation. The survey will study the evolution of galaxies and AGN over a wide range of redshifts and in environments of different density, and provide the crucial FIR measurements lacking for a

full understanding of intermediate and high redshift galaxy populations previously identified at other wavelengths. The chosen fields have excellent multi-wavelength coverage enabling both rapid science results and a lasting legacy value. The PEP program is coordinated with HerMES program.

But to emphasize the importance of IR and sub-mm astronomy, it must be said that the next few years, have other missions already in the pipeline, in particular ALMA.

The Atacama Large Millimeter/sub-millimeter Array (ALMA), one of the largest ground-based astronomy projects of the next decade, is a major new facility for world astronomy. ALMA will be comprised of a giant array of 12-m antennas, with baselines up to 16 km and state-of-the-art receivers that cover all the atmospheric windows up to 1 THz. An additional, compact array of 7-m and 12-m antennas will greatly enhance ALMA's ability to image extended sources. Construction of ALMA started in 2003 and will be completed in 2013. The ALMA project is an international collaboration between Europe, East Asia and North America in cooperation with the Republic of Chile. ALMA is located on the Chajnantor plain of the Chilean Andes in the District of San Pedro de Atacama, 5000 m above sea level. ALMA will enable transformational research into the physics of the cold Universe, regions that are optically dark but shine brightly in the millimeter portion of the electromagnetic spectrum. Providing astronomers a new window on celestial origins, ALMA will probe the first stars and galaxies, and directly image the formation of planets. ALMA will operate at wavelengths of 0.3 to 9.6 millimeters, where the Earth's atmosphere above a high, dry site is largely transparent, and will provide astronomers unprecedented sensitivity and resolution. ALMA will be a complete astronomical imaging and spectroscopic instrument for the millimeter/sub-millimetre.

The relevance of IR and sub-mm astronomy has grown in recent years but the years ahead will be even more packed of discoveries thanks to all facilities that at this time and in the years to come will explore the sky at these wavelengths.

2

The *Herschel* Space Observatory

In this chapter I will report the detailed description of *Herschel* Space Observatory and its instruments. I will focus on mission design, observing opportunities and on SPIRE instrument (my work is mainly done in SPIRE ICC). I will describe briefly also the other instrument on-board: PACS and HIFI.

2.1 Introduction

The ***Herschel* Space Observatory** (see Figure 2.1) was successfully launched on 14 May 2009. However, it was conceived almost 30 years earlier as the Far InfraRed and Submillimetre Space Telescope (FIRST), which was formally proposed to ESA in November 1982. It was incorporated in the ESA ‘Horizon 2000’ long-term plan for implementation and in November 1993 the ESA decided that FIRST would be implemented as the fourth ‘cornerstone’ mission.

The mission, approved in 1993 (a spacecraft design with a 3 m telescope passively cooled to 160 K, two science instruments), was changed in the light of the experience gained from the Infrared Space Observatory (ISO, Kessler et al. 1996, Section 1.2) mission: the current mission is based upon a spacecraft employing a superfluid helium cryostat reusing ISO technology, autonomously operating in a orbit around the 2nd Lagrangian point (L2) in the Sun-Earth/Moon system.

The prime science objectives of *Herschel* are intimately connected to the physics of and processes in the inter-stellar medium (ISM) in the widest sense. Near and far in both space and time, stretching from solar system objects and the relics of the formation of the sun and our solar system, over star formation in and feedback by evolved stars to the ISM, to the star-formation history of the universe, galaxy evolution and cosmology.

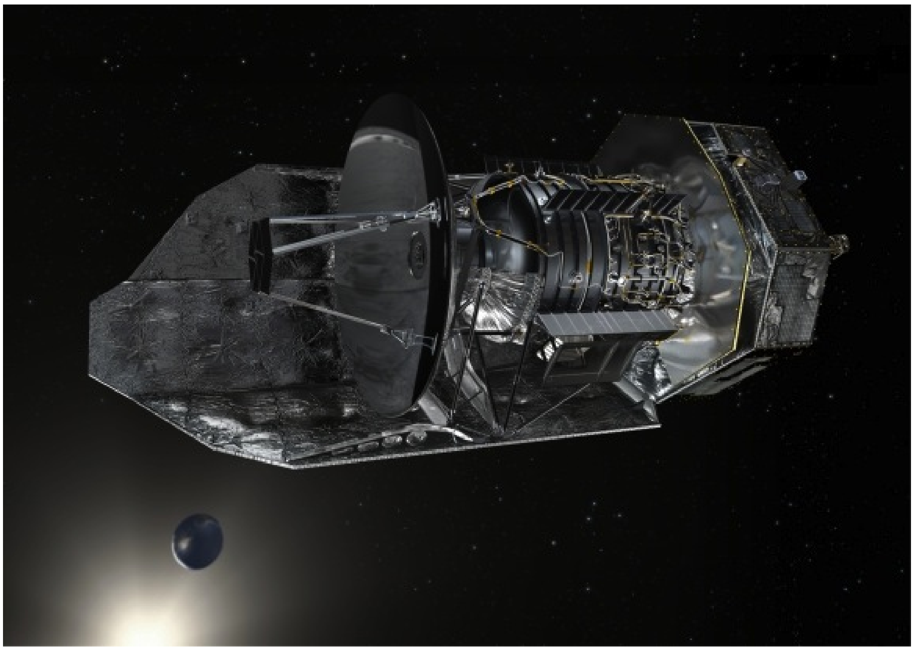

Figure 2.1: The *Herschel* Space Observatory

2.2 Mission design

The *Herschel* mission adopted for implementation had the top level requirement to provide three years of routine science observations, employing a science payload to be provided by Principal Investigator (PI) consortia in exchange for Guaranteed Time (GT) observations. *Herschel* was to be operated as an observatory facility, comprising a space segment - the satellite - and a ground segment, providing mission and science operations.

2.2.1 The Telescope

The *Herschel* telescope (Doyle et al. 2009) was constructed to be as large as possible and still be compatible with no inflight deployable structures, low mass and as cold as possible with passive cooling.

The optical design is that of a classical Cassegrain telescope with a 3.5 m physical diameter primary and an ‘undersized’ secondary, yielding an effective primary diameter of 3.28 m. The primary mirror has been made out of 12 segments, the secondary is a single piece. Similar to ISO, a fully passive design was adopted.

In the Table 2.1 the main characteristic of the telescope are summarized.

Telescope	
Primary physical/effective diameter	3.5 / 3.28 m
Secondary diameter	30.8 cm
System/primary f-number	8.70 / 0.5
Wave front error best-focus (centre/edge)	4.8 / 5.5 μm
Angular resolution	$\sim$7" $\times(\lambda_{\rm obs}/100\ \mu$m)
Operational temperature	$\sim$85 K

Table 2.1: *Herschel* telescope main characteristics.

2.2.2 Science Instruments

The science payload consists of three instruments, provided by consortia of institutes led by PIs:

- The Photodetector Array Camera and Spectrometer (PACS, Poglitsch et al. (2010)), PI: A. Poglitsch, Max-Planck-Institut für extraterrestrische Physik (MPE), Garching.
- The Spectral and Photometric Imaging REceiver (SPIRE, Griffin et al. (2010)), PI: M. J. Griffin, Cardiff University.
- The Heterodyne Instrument for the Far Infrared (HIFI, de Graauw et al. (2010)), PI: T. de Graauw, in late 2008 succeeded by F. Helmich, SRON Netherlands Institute for Space Research, Groningen.

The three instruments enabling *Herschel* to offer its observers broad band photometric imaging capability in six bands with centre wavelengths of 70, 100, 160, 250, 350, and 500 μm, imaging spectroscopy over the entire *Herschel* wavelength coverage, and very high resolution spectroscopy over much of this range. A number of observing modes are provided, including point source photometry, small, and large area photometric imaging, and the observation of a single spectral line, or one or more spectral ranges, in either a single position or in various mapping modes. In the Section 2.5 we will report a detailed description of SPIRE and in Section 2.6 and 2.7 a briefly description of the PACS and HIFI instruments. The SPIRE observation mode was described in Chapter 3. In the Chapter 4 I will describe the *Herschel* software infrastructure.

2.2.3 Ground segment

The *Herschel* ground segment is composed by:

The Mission Operations Centre (MOC): based at the European Space Operations Centre (ESOC), Darmstadt;

The Herschel Science Centre (HSC): based at the European Space Astronomy Centre (ESAC), Madrid;

HIFI ICC: based at SRON, Groningen;

PACS ICC: based at MPE, Garching;

SPIRE ICC: based at Rutherford Appleton Laboratory (RAL), Didcot (SPIRE);

The NASA *Herschel* Science Center (NHSC): based at the Infrared Processing and Analysis Center (IPAC), Pasadena.

The MOC conducts the mission operations, it performs all contact with the spacecraft, monitors all spacecraft systems, safeguards health and safety, and performs orbit maintenance. It generates skeleton schedules for the Science Ground Segment (SGS) to "fill in" with science, calibration, and engineering observations. It creates and uplinks mission timelines and receives, consolidates, and provides telemetry to the SGS.

Science operations are conducted by the SGS, a partnership among the HSC, the three ICCs, and the NHSC. In particular HSC is the link between *Herschel* and science community (proposal, scientific planning, etc).The ICCs are responsible for the successful operation of their respective instruments, developing and maintaining instrument observing modes, and for providing specialized software and procedures for the processing of the data generated. The NHSC is addressed to the science community based in the USA.

The Herschel Common Science System (HCSS) is the common software infrastructure, provided by the ground segment team. The HCSS handles submission of observing proposals, scheduling of observations for execution, generation of commanding requests for the instruments and spacecraft, processing of the resulting scientific data, and the population of the archive with the generated products (see Section 4.1).

Observers are provided with the HSpot tool for observation planning, the Herschel Integrated Processing Environment (HIPE) (see Chapter 4) interactive data processing software, observing data and standard products through the Herschel Science Archive (HSA), and associated documentation including Observers' Manuals and User Guides as well as the Helpdesk interface through the HSC website[1]. A graphical summary is shown in Figure 2.2

2.3 Mission phases

After the launch and early operations phase the inflight mission phases are:

---

[1] HSC website URL: `http://herschel.esac.esa.int/`

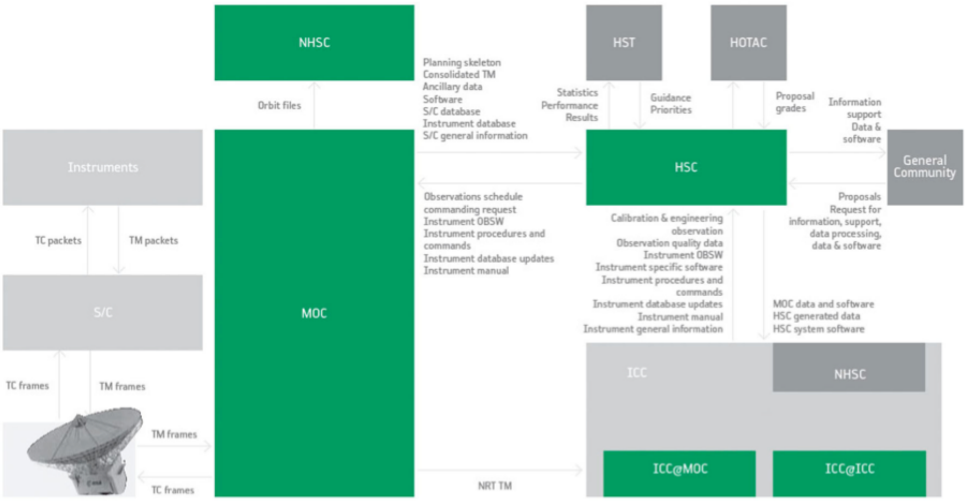

Figure 2.2: The Herschel ground segment elements (green boxes) and information flow. HST stands for the Herschel Science Team, HOTAC for the Herschel Observing Time Allocation Committee, TC for tele-command, TM for telemetry. ICCs receive instrument TM from the HSC in their home locations (ICC@ICC), but can also "intercept" TM on location in the MOC (ICC@MOC) for near real-time (NRT) activities (Pilbratt et al. 2010).

- Commissioning Phase (CoP): Complete check-out of spacecraft functions and performance. Switch-on and functional verification of the instruments. Cryo-cover opening and thermal stabilization. Nominal duration two months.

- Performance verification phase (PVP): Instrument performance, calibration, focal plane geometry, and pointing determination. Test, optimize, verify, and release the various instrument/observing modes for use. Nominal duration three months.

- Science Demonstration Phase (SDP): Use of the released observing modes to execute selected observations from the approved Key programmess (KP, see Section 2.4). Assess, optimize, and release the KPs observations for execution. Nominal duration six weeks.

- Routine science phase (RSP): Execute released observations employing released observing modes. Perform engineering and routine calibration observations to optimize the observing modes and the quality of the data obtained. The RSP will continue until helium exhaustion, and will be followed by archive phases.

The first three phases have been successfully concluded for SPIRE and PACS and the first results was published in a special *Astronomy and Astrophysics* issue (Walmsley et al. 2010a). Some problem have been found in HIFI. In particular, on observational day 81 (August 2, 2009), telemetry from *Herschel* showed that HIFI had entered an anomalous state because of a single event upset, caused by a cosmic particle that damaged the voltage supply for the instrument's control electronics. With HIFI unavailable, the PVP activities had to be re-planned, making more use of PACS and SPIRE and a new phases called HIFI Priority Science Program (PSP) was performed to test the HIFI functionality. Now all work fine and the first results was published in a special *Astronomy and Astrophysics* issue (Walmsley et al. 2010b).

2.4 Observing opportunities

Herschel is an observatory; its observing time is shared between guaranteed and open time (GT and OT). The basic rules were defined in the science management plan (SMP) as part of the Announcement of Opportunity (AO) for the science payload in 1997. In the nominal mission ∼20 000 hours are available for science, 32% is GT (mainly owned by the PI consortia). The remainder is Open Time (OT), which is allocated to the general community (including the GT holders) on the basis of AOs for observing time. In each AO cycle the GT is allocated first, followed by the OT. All observations made in the first year of the RSP will have proprietary times of 12 months, while for all observations made later, the proprietary time will be 6 months, with a simple 'bridging scheme' so that no observation will become public before observations that were executed earlier become public as well. A small amount of the open time can be allocated as discretionary time. All proposals are assessed by the Herschel Observing Time Allocation Committee (HOTAC), and all observing data are archived and will be available to the entire community after the proprietary time has passed.

Given that *Herschel* would not have the benefit of an all sky survey for much of its wavelength coverage, the Science Management Plan (SMP) required that Key programmess (KPs) in the form of "large spatial and spectral surveys" were to be selected and executed early in the mission so that the results could be followed up by *Herschel* itself.

An initial AO limited to KP observing proposals therefore was issued. This process took place from February 2007 to February 2008. There were 21 GT and 62 OT proposals, out of which by coincidence also 21 were awarded observing time (Table 2.2 and Figure 2.3).

The total amount of observing time allocated to KPs constitutes ∼55% of the nominally available observing time. The remainder will be allocated in two

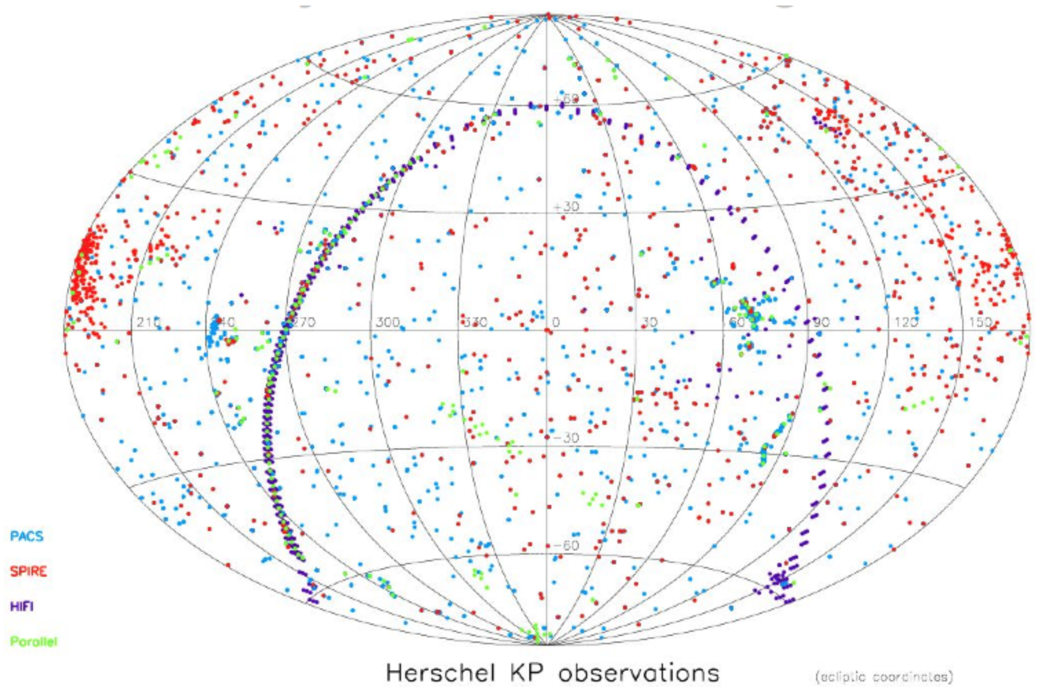

Figure 2.3: Key Programs observations plotted in ecliptic coordinates, with color-coding denoting the instrument. "Parallel" indicates performing 5-band photometric imaging using SPIRE and PACS simultaneously.

Table 2.2: Approved KP proposals by science area (Pilbratt et al. 2010)

Science area	KP GT		KP OT		KP TOTAL	
	#	h	#	h	#	h
Solar System	1	293.7	1	372.7	2	666.4
ISM/SF	10	2337.5	10	2113.2	20	4450.7
Stars	2	544.6	0	0	2	544.6
Gal - AGN	5	983.7	8	1930.3	13	2914.0
Cosmology	3	1719.4	2	962.6	5	2682.0
Total	21	5878.9	21	5378.8	42	11257.7

additional AO cycles. The first of these took place in February 2010 with the GT1 deadline on 31 March 2010. The OT1 was released on 20 May 2010, with proposal submission deadline on 22 July 2010. The final AO (GT2 & OT2) will take place approximately a year later.

2.5 The SPIRE Instrument

The Spectral and Photometric Imaging REceiver (SPIRE), is the *Herschel* submillimeter camera and spectrometer. It contains a three-band imaging photometer and an imaging Fourier Transform Spectrometer (FTS).

2.5.1 General design

The photometer carries out broad-band photometry ($\lambda/\Delta\lambda \approx 3$) in three spectral bands centered on approximately 250, 350 and 500 μm, and the FTS uses two overlapping bands to cover 194-671 μm (447-1550 GHz).

Figure 2.4 shows a block diagram of the instrument. The SPIRE Focal Plane Unit (FPU) is approximately 700 × 400 × 400 mm in size and is supported from the 10-K *Herschel* optical bench by thermally insulating mounts. It contains the optics, detector arrays (three for the photometer, and two for the spectrometer), an internal ^3He cooler to provide the required detector operating temperature of ~ 0.3 K, filters, mechanisms, internal calibrators, and housekeeping thermometers. It has three temperature stages: the *Herschel* cryostat provides temperatures of 4.5 K and 1.7 K via high thermal conductance straps to the instrument, and the ^3He cooler serves all five detector arrays.

Both the photometer and the FTS have cold pupil stops conjugate with the *Herschel* secondary mirror, which is the telescope system pupil, defining a 3.29-m diameter used portion of the primary. Conical feed-horns (Chattopadhyay et al. 2003) provide a roughly Gaussian illumination of the pupil, with an edge taper of around 8 dB in the case of the photometer. The same ^3He cooler design (Duband et al. 2008) is used in SPIRE and in the PACS instrument (Poglitsch et al. 2010). It has two heater-controlled gas gap heat switches; thus one of its main features is the absence of any moving parts. All five detector arrays use hexagonally close-packed feed-horn-coupled spider-web bolometers (see Section 2.5.4). The bolometers are AC-biased with frequency adjustable between 50 and 200 Hz, avoiding $1/f$ noise from the cold JFET readouts. There are three SPIRE warm electronics units: the Detector Control Unit (DCU) provides the bias and signal conditioning for the arrays and cold electronics, and demodulates and digitizes the detector signals; the FPU Control Unit (FCU)controls the cooler and the mechanisms, and reads out all the FPU thermometers; and the Digital Processing Unit (DPU) runs the on-

Table 2.3: SPIRE main characteristics

Sub-Instruments		Photometer		Spectrometer	
Array	PSW	PMW	PLW	SSW	SLW
Band (μm)	250	350	500	194-313	303-671
Resolution ($\lambda/\Delta\lambda$)	3.3	3.4	2.5	$\sim$ 40 - 1000	$\sim$ 40 - 1000
Unvignetted field of view		$4'\times8'$		$2.0'$ (diameter)	
Beam FWHM size (arcsec)	18.1	25.2	36.6	29-42[a]	29-42[a]

[a] The FTS beam size depends on wavelength.

board software and interfaces with the spacecraft for commanding and telemetry (see Section 2.5.3).

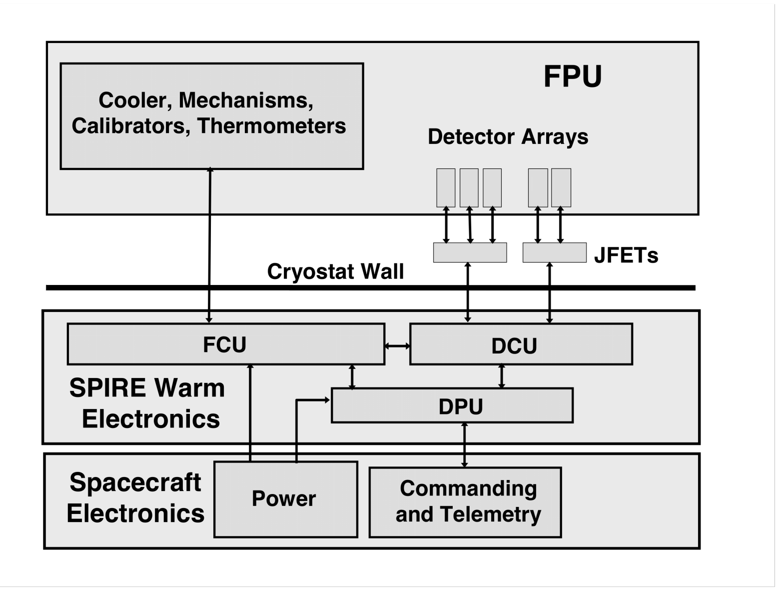

Figure 2.4: The SPIRE instrument architecture

A summary of the most important instrument characteristics are shown in Table 2.1 and the operational parts of SPIRE are presented in the subsequent sections.

SPIRE shares the *Herschel* focal plane with HIFI and PACS and it relative position with respect to the other two instruments is shown in Figure 2.5

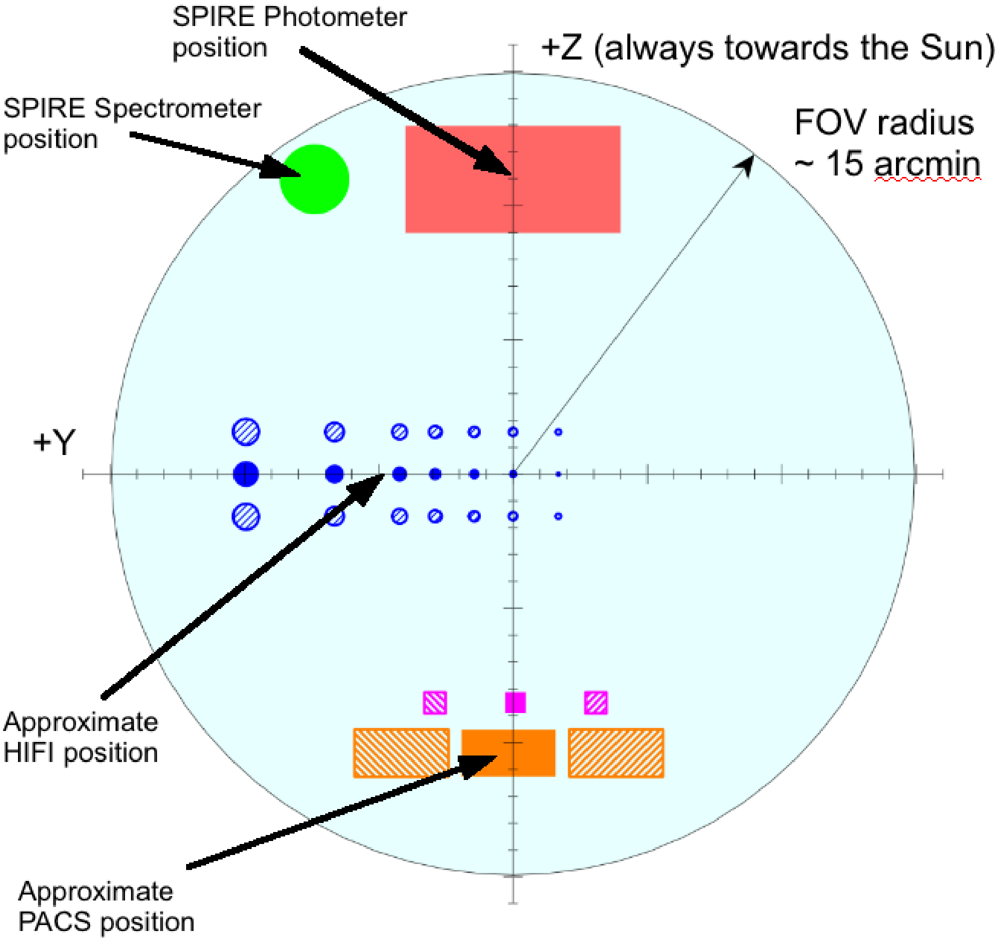

Figure 2.5: SPIRE location on sky with respect to the other two instruments sharing the *Herschel* focal plane. The centre of the SPIRE photometer is offset by ≈ 11 arcmin from the centre of the highly curved focal surface of the *Herschel* telescope, shown by the large shaded circle.

2.5.2 ^3He Cooler and Thermal Strap System

The same ^3He cooler design (Duband et al. 2008) is used for both the SPIRE and PACS instruments. This type of refrigerator consists of a sorption pump and a evaporator and uses porous material which absorbs or releases gas depending on its temperature. The refrigerator contains 6 liters of liquid ^3He . At the beginning of the cold phase, all of this is contained in liquid form in the evaporator. The pump is cooled to ∼2 K, and cryo-pumps the ^3He gas, lowering its vapor pressure and so reducing the liquid temperature. The slow evaporation of the ^3He provides a very stable thermal environment at 300 mK for around 48 hours under constant heat load in normal observing and operational circumstances. Once most of the helium is evaporated and contained in the pump then the refrigerator must be recycled. This is carried out by heating of the sorption pump to ∼40 K in order to expel the absorbed gas. The gas re-condenses as liquid at ∼2 K in the evaporator. Once all of the ^3He has been re-condensed, the pump is cooled down again and starts to cryo-pump the liquid, bringing the temperature down to 0.3 K once again. This recycling takes about 2 hours and is usually performed during the daily telecommunications period. Gas gap heat switches control the cooler and there are no moving parts. For zero-g operation the ^3He liquid confinement in the evaporator is achieved by a porous material which holds the liquid by capillary attraction. A Kevlar wire suspension supports the cooler during launch whilst minimizing the parasitic heat load. Copper straps connect the cooler 0.3 K stage to the five detector arrays, and are held rigidly at various points by Kevlar support modules. The supports at the entries to the spectrometer and photometer 1.7 K boxes are also designed to be light-tight.

2.5.3 SPIRE warm electronics

The warm electronics are physically located on the *Herschel* Service Module (SVM). The temperature of the SVM is conditioned to remain between $-15°C$ and $+45°C$ during operation of the instrument. The principal function of these subsystems is to act as the back end for the instrumentation contained in the Cryostat Vacuum Vessel (CVV) and to interface SPIRE with the *Herschel* spacecraft. This is illustrated in Figure 2.4.

The Warm Electronics consist of the DPU and the Detector Readout and Control Unit (DRCU). The DPU acts as the digital data interface between the instrument and the spacecraft. The DRCU receives low level digital commands from the DPU and carries out the appropriate control function or data acquisition function. Data acquired by the DRCU is digitized and transferred to the DPU.

The DPU is housed in a single enclosure mounted on the SVM. The DRCU is split into two physical enclosures. The first of these contains the DCU electronics.

The second of these boxes contains the FPU Control Unit (FCU) which contains the Sub-systems Control Unit (SCU), the Mechanisms Control Unit (MCU) and the Power Supply Unit (PSU). The FCU controls the ^3He cooler, the Beam Steering Mechanism and the FTS scan mirror, and also reads out all the FPU thermometers.

The DPU interfaces with the DRCU on the instrument side and with the spacecraft Command and Data Management System (CDMS) and the Herschel Power Distribution Unit (PDU). There are two types of data interface between the DPU and the DRCU:

- high-speed, mono directional, serial data links for the transmission of science data (the Fast Science Data Link - FSDL)
- low speed, bi-directional serial links for command transmission (the Low Speed Link - LSL).

The DPU runs the on-board software interfaces with the spacecraft for commanding and telemetry. The MCU, the DCU and the SCU each have one FSDL and one LSL with the DPU.

The DCU provides the bias and signal conditioning for the arrays and cold electronics, and demodulates and digitizes the detector signals. There are three basic board types used in the DCU; the Lock-in Amplifier (LIA) boards, the Bias Boards and the Data Acquisition and Interface (DAQ + I/F) boards.

Bias Boards: Three different biases are provided by the Bias Board, as listed below:

- DC biasing of the JFET modules,
- DC biasing of the JFET heaters,
- AC Biasing of the Photometer BDAs, Spectrometer BDAs and the 300-mK Thermal Control System.

The detectors are differentially biased with an AC voltage, which is provided by the Bias Generator board. Due to the criticality of this component of the detector read out electronics, there is both a prime and redundant board for the bias signals. The amplitude, frequency and phase of the bias signals are all software commandable.

LIA Amplifiers The Lock-in Amplifiers (LIA) are used to read out the AC signals from the detectors and convert them into DC. Each bolometer has a dedicated amplifier. The amplifiers are grouped together in groups of 32 on each LIA board. There are a total of 12 LIA boards; with nine being used for the photometer and three used for the spectrometer.

The DAQ + I/F boards The analogue signals from the 288 photometer channels and the 72 spectrometer channels need to be converted into digital values. To get the required precision, the signals are digitized into at least 19-bit precision. Firstly, the DC offset is removed from the analogue signal. This offset is the three most significant bits of the digitization. The signals are then passed into an analogue multiplexer before being passed to a 16-bit Analogue-to-Digital converter chip. The conversion of all the photometer channels is performed in less than 6.2 ms; the spectrometer channels in less than 1.2 ms. The digitized signals are then passed to the DPU via the FSDL. The board also manages the LSL link and the commanding of the DCU.

2.5.4 SPIRE bolometers

The SPIRE detectors for both the photometer and the spectrometer are semiconductor bolometers. The general theory of bolometer operation is described in Chattopadhyay et al. (2003), but the basic features and the principles are outlined here, and are illustrated in Figure 2.6. The radiant power to be detected is incident on an absorber of heat capacity C. Heat is allowed to flow from the absorber to a heat sink at a fixed temperature T_0 by a thermal conductance, G (the higher G, the more rapidly the heat leaks away). A thermometer is attached to the absorber, to sense its temperature. A bias current, I, is passed throughout the thermometer, and the corresponding voltage, V, is measured. The bias current dissipates electrical power, which heats the bolometer to a temperature, T, slightly higher than T_0. With a certain level of absorbed radiant power, Q, the absorber will be at some temperature T, dictated by the sum of the radiant and electrical power dissipation. If Q changes, the absorber temperature will change accordingly, leading to a corresponding change in resistance and hence in output voltage. In the case of the SPIRE detectors, the absorber is a spider-web mesh composed of silicon nitride with a thin resistive metal coating to absorb and thermalize the incident radiation. The thermometers are crystals of Neutron Transmutation Doped (NTD) germanium (Turner et al. 2001), which has very high temperature coefficient of resistance. A magnified view of a SPIRE bolometer is shown in Figure 2.6.

The bolometers are coupled to the telescope beam by conical feed-horns located directly in front of the detectors on the ^3He stage. Short waveguide sections at the feed-horn exit apertures lead into the detector cavities. The feed-horn entrance aperture diameter is set at $2F\lambda$, where λ is the design wavelength and F is the final optics focal ratio. This provides the maximum aperture efficiency and thus the best possible point source sensitivity (Griffin et al. 2002). The feed-horns are hexagonally close-packed, as shown in Figure 2.9, in order to achieve the highest packing density possible. A centre-centre distance of $2F\lambda$ in the focal plane corresponds to a beam separation on the sky of $2\lambda/D$, where D is the telescope diameter. This is approximately twice the beam FWHM, so that the array does not produce an instantaneously fully sampled image. A suitable scanning or multiple-pointing ("jiggling") scheme is therefore needed for imaging observations. For a detailed analysis of the feed-horns see Griffin et al. (2002).

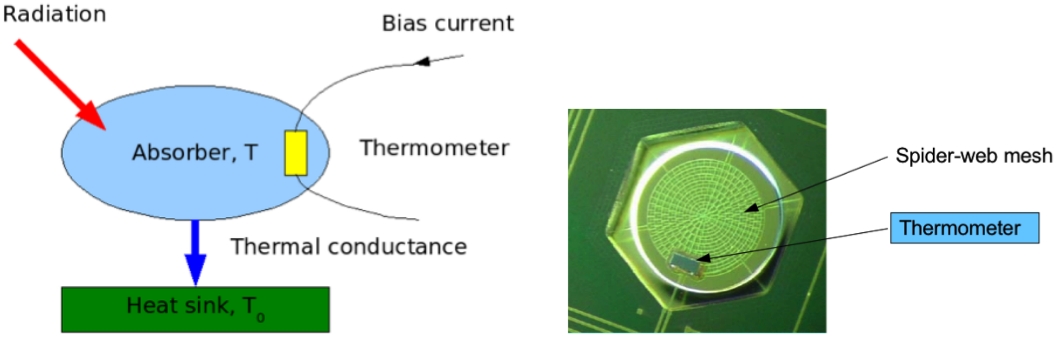

Figure 2.6: **Left**: Basic principles of bolometer operation. **Right**: Magnified view of a SPIRE bolometer, the thermometer size is $10 \times 100 \times 300$ μm.

2.5.5 Photometer design

The photometer opto-mechanical layout is shown in Figure 2.7. It is an all-reflective design (Dohlen et al. 2000) except for the dichroics used to direct the three bands onto the bolometer arrays, and the filters used to define the passbands (Ade et al. 2006). The input mirror M3, lying below the telescope focus, receives the $f/8.7$ telescope beam and forms an image of the secondary at the flat Beam Steering Mechanism (BSM), M4. For photometric observations the BSM is moved on a pattern around the nominal position of the source. It can chop up to ± 2 arcmin along the long axis of the photometer's $4'$x$8'$ field of view and simultaneously chop in the orthogonal direction by up to $30''$. This two-axis motion allows *jiggling* of the pointing to create fully sampled image of the sky. The nominal BSM chop frequency for the photometer is 1 Hz. For scanning observations the BSM is kept at its home position. Mirror M5 converts the focal ratio to $f/5$ and provides an intermediate focus at M6, which re-images the M4 pupil to a cold stop. The input optics are common to the photometer and spectrometer and the separate spectrometer field of view is directed to the other side of the optical bench panel by a pick-off mirror close to M6. The 4.5-K optics are mounted on the SPIRE internal optical bench. Mirrors M7, M8 and a subsequent mirror inside the 1.7-K box form a one-to-one optical relay to bring the M6 focal plane to the detectors.

The 1.7-K enclosure also contains the three detector arrays and two dichroic beam splitters to direct the same field of view onto the arrays so that it can be observed simultaneously in the three bands. The images in each band are diffraction-limited over the $4'$x$8'$ field of view.

The photometric passbands are defined by quasi-optical edge filters (Ade et al. 2006) located at the instrument input, at the 1.7-K cold stop, and directly in front of the detector arrays, the reflection-transmission edges of the dichroics, and the cut-off wavelengths of the feed-horn output waveguides. The filters also serve to minimize the thermal loads on the 1.7-K and 0.3-K stages. The three bands are centered at approximately 250, 350 and 500 μm and their relative spectral response curves are given in Figures 2.8.

The absolute calibration of the instrument is done by observations of standard astronomical sources (see Section 3.5), but to check the health and responsivity of the arrays, the instrument is equipped with the Photometer CALibration source (PCAL). PCAL is a thermal source used to provide a repeatable signal for the bolometers (Pisano et al. 2005). It operates as an inverse bolometer: applied electrical power heats up an emitting element to a temperature of around 80 K, causing it to emit FIR radiation, which is seen by the detectors.

The three arrays contain 139 (PSW - 250 μm), 88 (PMW - 350 μm) and 43 (PLW - 500 μm) detectors, each with its own individual feed-horn. The array feed-horn layouts are shown schematically in Figure 2.9.

The feed-horn-coupled architecture was chosen as the best option given the achievable sensitivity, the requirements for the largest possible field of view and high stray light rejection, and limitations on the number of detectors imposed by spacecraft resource budgets. The detector feed-horns are designed for maximum aperture efficiency, requiring an entrance aperture close to $2F\lambda$, where λ is the wavelength and F is the final optics focal ratio. This corresponds to a beam spacing on the sky of $2\lambda/D$, where D is the telescope diameter.

2.5.6 Spectrometer design

The SPIRE Fourier Transform Spectrometer (FTS, Swinyard et al. 2003, Dohlen et al. 2000) use a Mach-Zehnder configuration: the incident radiation is separated by a beam splitter into two beams that travel different optical paths before recombining. The input and output ports are spatially separated. One port views the a $2.6'$ field of view on the sky, the other an on-board references sources (Spectrometer CALibration source - SCAL[2]). By changing the Optical Path Difference (OPD)

---

[2] SCAL (Hargrave et al. 2006) is available as an input to the second FTS port to allow the background power from the telescope to be nulled. The in-flight FTS calibration measurements of Vesta, Neptune and Uranus with Spectrometer CALibration source (SCAL) off showed that the signal at the peak of the interferogram is not saturated or at most only a few samples are

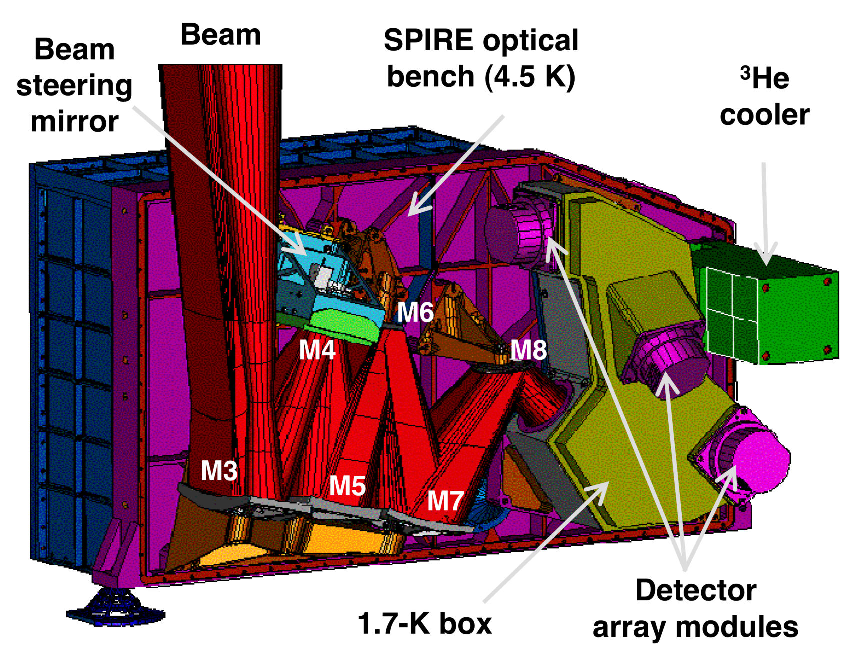

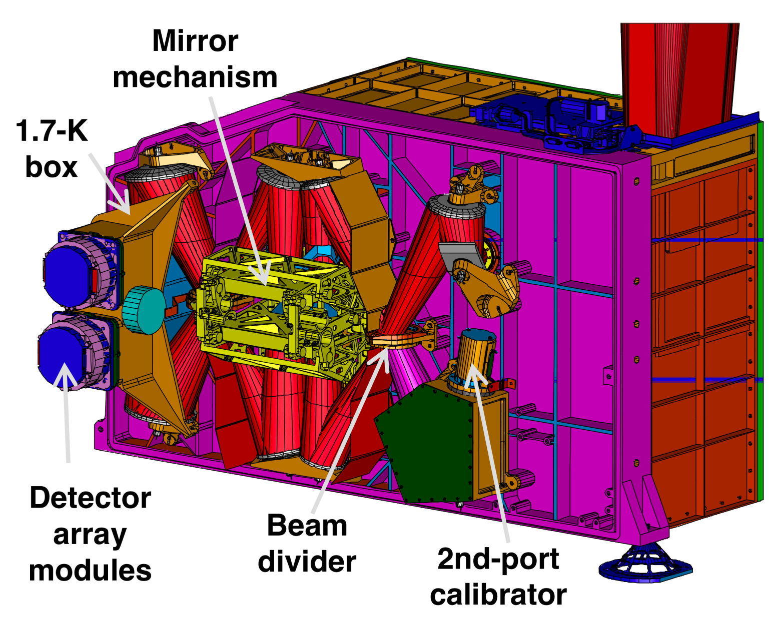

Figure 2.7: SPIRE FPU. **Top**: photometer side layout. **Botton**: spectrometer side layout.

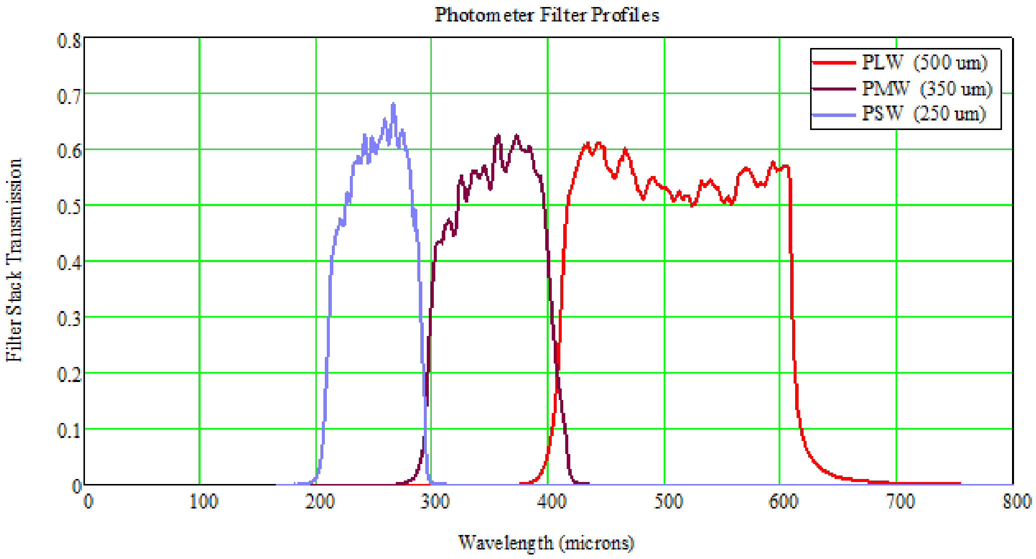

Figure 2.8: Overall filter transmission profiles for the three photometer bands (Spire Observers' Manual 2010).

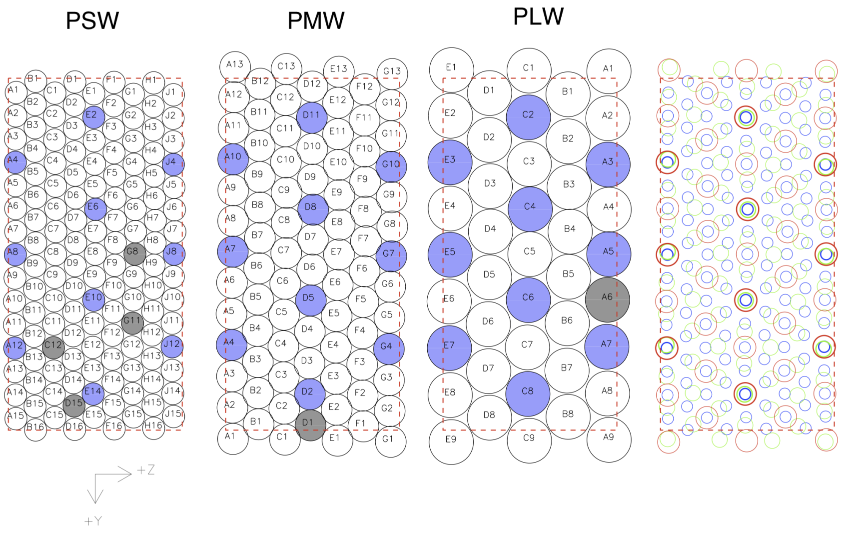

Figure 2.9: A schematic view of the photometer bolometer arrays (PSW - 250 μm PMW - 350 μm PLW - 500 μm). Each circle represents a detector feed-horn. Those detectors centered on same sky positions are shaded in blue, the dead bolometers are shaded in grey. The $4' \mathrm{x} 8'$ unvignetted field of view of each array is delineated by a red dashed rectangle (Spire Observers' Manual 2010).

of the two beams with a moving mirror, an interferogram of signal versus OPD is created. This interferogram is the Fourier transform of the source spectrum. Performing the inverse Fourier transform thus produces the spectrum as a function of the frequency. A single back-to-back scanning roof-top mirror serves both interferometer arms. A filtering scheme similar to the one used in the photometer restricts the passbands of the detector arrays at the two ports, defining the two overlapping FTS bands. In the Figure 2.7 it is possible view the spectrometer focal plane layout.

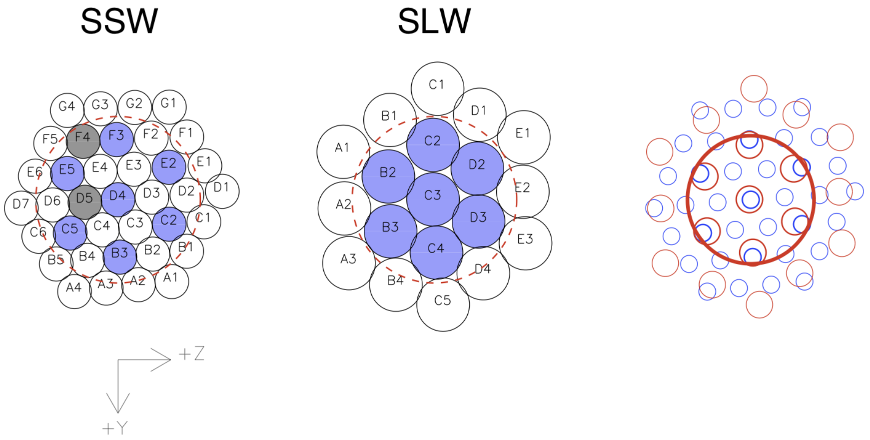

Figure 2.10: A schematic view of the FTS bolometer arrays (94-313 μm - SSW and 303-671 μm - SLW). Those detectors centered on same sky positions are shaded in blue, the dead bolometers are shaded in grey. The $0'2.6$ unvignetted field of view of each array is delineated by a red dashed circle (Spire Observers' Manual 2010).

Two bolometer arrays at the output ports cover overlapping bands of 194-313 μm (Spectrometer Short Wavelength - SSW) and 303-671 μm (Spectrometer Long Wavelength - SLW). The two spectrometer arrays contain 19 (SLW) and 37 (SSW) hexagonally packed detectors, each with its own individual feed-horn, see Figure 2.10. The array modules are similar to those used for the photometer, with an identical interface to the 1.7-K enclosure. The feed-horn and detector cavity designs are optimized to provide good sensitivity across the whole wavelength range of the FTS. The SSW feed-horns are sized to give $2F\lambda$ pixels at 225 μm and the SLW horns are $2F\lambda$ at 389 μm. This arrangement has the advantage that there are many co-aligned pixels in the combined field of view. The SSW beams

---

saturated, which means that SCAL is not required to reduce the dynamic range. On the other hand, using the SCAL adds photon noise to the measurements and it was decided that it will not be used during routine science observations.

on the sky are 33″ apart, and the SLW beams are separated by 51″. Figure 2.10 shows also the overlap of the two arrays on the sky with circles representing the FWHM of the response of each pixel. The unvignetted footprint on the arrays (diameter 2.0′) contains 7 pixels for SLW and 19 pixels for SSW, outside this circle the data is not-well calibrated.

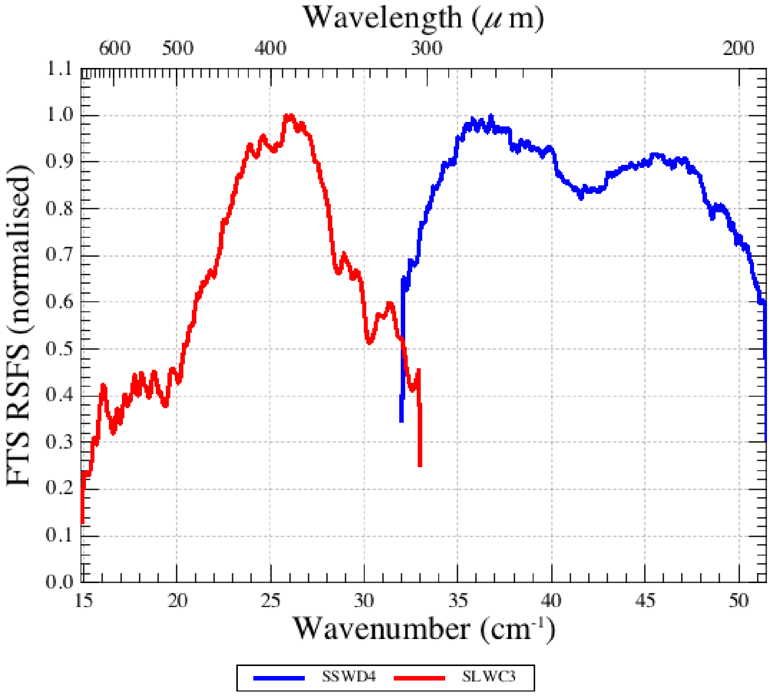

Figure 2.11: SPIRE: The normalized spectrometer relative spectral response curves derived for a point source. The two bands have been normalized independently (Spire Observers' Manual 2010).

As with any FTS, each scan of the moving mirror produces an interferogram in which the spectrum of the entire band is encoded with the spectral resolution corresponding to the maximum mirror travel.

The nominal mode of operation of the FTS involves moving the scan mirror continuously (nominally at 0.5 mms^{-1}, giving an optical path rate of 2 mms^{-1} due to the factor of four folding in the optics). The resolution element is given by $\Delta\sigma = 1/(2 \times OPD_{max})$, where OPD_{max} is the maximum optical path difference of the scan mirror. The maximum mechanical scan length is 3.5 cm, equivalent to an OPD_{max} of 14 cm, thus the highest resolution available is 0.04 cm^{-1} (1.2 GHz).

The spectral passbands are defined by a sequence of metal mesh filters at various locations and by the waveguide cut-offs and provide the overlapping bands.

Their relative spectral response curves are showed in Figure 2.11

2.6 The PACS Instrument

The PACS instrument comprises two sub-instruments which offer two basic and and mutually exclusive modes in the wavelength band 55-210 μm:

- imaging dual-band photometry (60-85 μm or 85-125 μm and 125-210 μm) over a field of view of $1.75' \times 3.5'$, with full sampling of the telescope point spread function (diffraction/wavefront error limited);

- integral-field spectroscopy between 51 and 220 μm with a resolution of ~75-300 km/s and instantaneous coverage of ~1500 km/s, over a field of view of $47'' \times 47''$.

  Figure 2.12 shows an optical circuit block diagram of the major functional parts of PACS. At the top, the entrance and calibration optics is common to all optical paths through the instrument. On the right, the spectrometer serves both, the short-wavelength ("blue"), and long-wavelength ("red") photoconductor arrays.

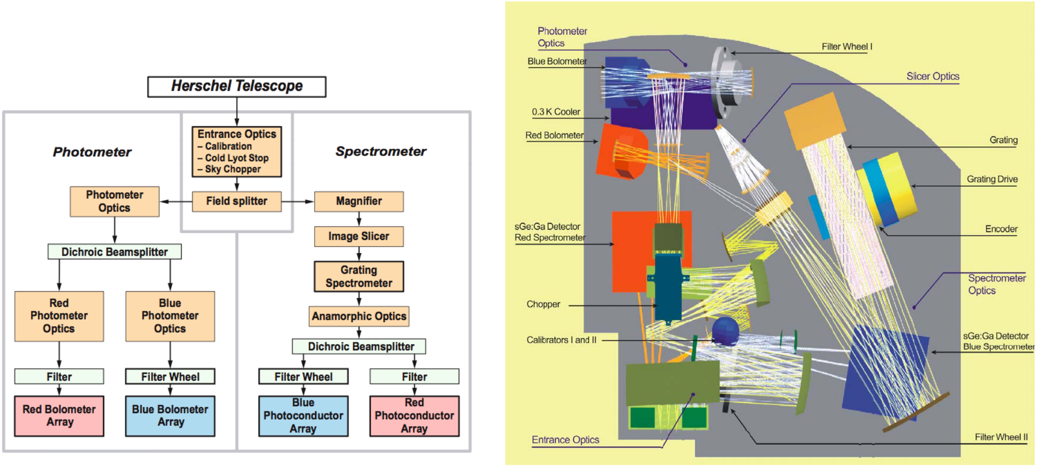

Figure 2.12: PACS FPU. **Left**: PACS focal plane unit functional block diagram **Right**: PACS FPU layout. (Poglitsch et al. 2010)

The photometric bands, which can be observed simultaneously, cover the same field-of-view. The field-of-view of the spectrometer is offset from the photometer field, however, this has no effect on the observing efficiency. The focal plane unit provides photometric and spectroscopic capabilities through five functional units :

- common input optics with the chopper, calibration sources and a focal plane splitter;
- a photometer optical train with a dichroic beam splitter and separate re-imaging optics for the two short-wavelength bands (60-85 μm and 85-125 μm) selectable via a filter wheel and the long-wavelength band (125-210 μm), respectively;
- two bolometer arrays with cryogenic buffers/multiplexers and a common 0.3 K sorption cooler;
- a spectrometer optical train with an image slicer unit for integral field spectroscopy, an anamorphic collimator, a movable diffraction grating in Littrow mount, anamorphic re-imaging optics, and a dichroic beam splitter for separation of diffraction orders. The blue channel contains an additional filter wheel for selecting its short or long wavelength part;
- two photoconductor arrays with attached cryogenic readout electronics (CRE).

The whole instrument, except the detectors is kept at the "Level 1" temperature of ∼3 to 5 K provided by the cryostat.

2.6.1 Photometer design

After the intermediate focus provided by the entrance optics, the light is split into the long-wavelength and short-wavelength channels by a dichroic beam-splitter with a transition wavelength of 125 μm and is re-imaged with different magnification onto the respective Si bolometer arrays. The blue channel offering two filters, 60-85 μm and 85-125 μm, has a 32×64 pixels arrays, while the red channel with a 125-210 μm filter has a 16×32 pixels array. Both channels cover a field-of-view of $\sim 1.75' \times 3.5'$, with full beam sampling in each band. The two short-wavelength bands are selected by two filters via a filter wheel. The field-of-view is nearly filled by the square pixels, however the arrays are made of sub-arrays which have a gap of ∼1 pixel in-between. The incident infrared radiation is registered by each bolometer pixel by causing a tiny temperature difference.

There are in total 3 bands in the PACS photometer: 60-85 μm, 85-125 μm and 125-210 μm. The filter transmission of the photometer filters are showed in Figure 2.13. The reference wavelengths chosen for the 3 photometer filters are 70, 100 and 160 μm. These rounded values (see Figure 2.13) are close to the wavelengths that minimize the color correction terms with the flight model filters. No indications of any near- or mid-infrared filter leakage could be identified. Suitable corrections factors for a wide sample of SED shapes can be found in Poglitsch et al. (2010).

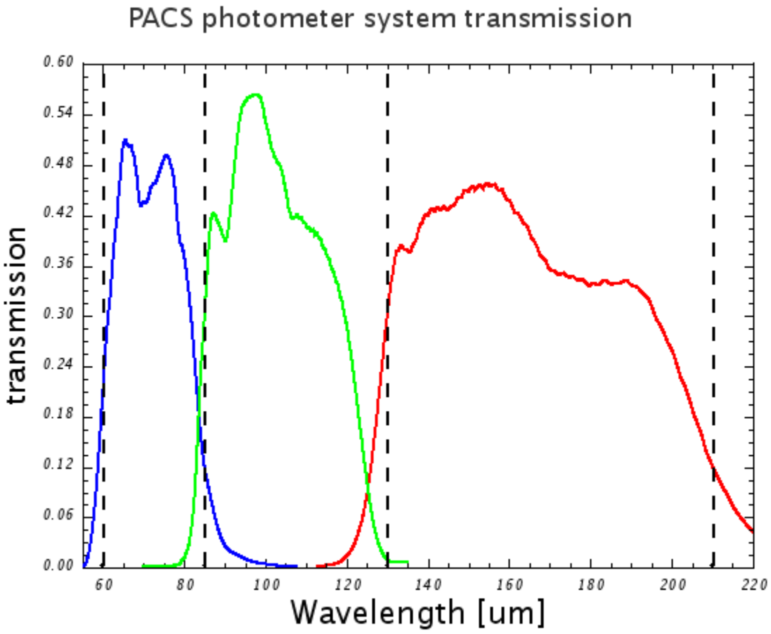

Figure 2.13: Filter transmissions of the PACS photometer filter chains. The graph represents the overall transmission of the combined filters with the dichroic and the detector relative response in each of the three bands of the photometer. The dashed vertical lines mark the original intended (design values) of the band edges (Pacs Observers' Manual 2010).

2.6.2 Spectrometer design

The integral-field spectrometer covers the wavelength range from 51μm to 220 μm, in two channels that operate simultaneously in the blue (51-105 μm) and red (102-220 μm) band. It provides a resolving power between 1000 and 4000 (i.e. a spectral resolution of $\sim$ 75-300km/s) depending on wavelength, for a fixed grating position the instantaneous coverage is $\sim$1500km/s. It allows simultaneous imaging of a $47'' \times 47''$ field of view, resolved into 5×5 pixels. An image slicer employing reflective optics is used to re-arrange the

2 dimensional field-of-view along a 1×25 pixels entrance slit for the grating. This integral-field concept with spectral and spatial multiplexing allows for the most efficient detection of weak individual spectral lines with sufficient baseline coverage and high tolerance to pointing errors without compromising spatial resolution, as well as for spectral mapping of extended sources regardless of their intrinsic velocity structure. For the grating the entrance and exit optical paths coincide. It is operated in first, second or third order, respectively, to cover the full wavelength range. The first order covers the range 102-210 μm, the second order 71-105 μm, and the third order 51-73 μm. It is possible to operate both spectrometer detector arrays simultaneously. For wide scans, full spectra can so be obtained in both selected grating orders. In a spectral line mode in the grating order-of-interest, the other array yields narrow-band continuum data, or in suitably line-rich sources, serendipitous lines.

2.7 The HIFI instrument

HIFI is the Heterodyne Instrument for the Far Infrared (de Graauw et al. 2010). It is designed to provide spectroscopy at high to very high resolution over a frequency range of approximately 480-1250 and 1410-1910 GHz (625-240 and 213-157 μm). This frequency range is covered by 7 "mixer" bands, with dual horizontal and vertical polarizations, which can be used one pair at a time.

The mixers act as detectors that feed either, or both, the two spectrometers on HIFI. An instantaneous frequency coverage of 2.4GHz is provided with the high frequency band 6 and 7 mixers, while for bands 1 to 5 a frequency range of 4GHz is covered. The data is obtained as dual sideband data which means that each channel of the spectrometers reacts to two frequencies (separated by 4.8 to 16 GHz) of radiation at the same time. For many situations, this overlapping of frequencies is not a major problem and science signals are clearly distinguishable. However, particularly for complex sources containing a high density of emission/absorption lines, this can lead to problems with data interpretation. Deconvolution is therefore necessary for the data to create single sideband data. This is especially important for spectral scans covering large frequency ranges on sources with many lines .

There are four spectrometers on board HIFI, two Wide-Band Acousto-Optical Spectrometers (WBS) and two High Resolution Autocorrelation Spectrometers (HRS). One of each spectrometer type is available for each polarization. They can be used either individually or in parallel. The Wide-Band

Spectrometers cover the full intermediate frequency bandwidth of 2.4GHz in the highest frequency bands (bands 6 and 7) and 4GHz in all other bands. The High Resolution Spectrometers have variable resolution with sub-bands sampling up to half the 4GHz intermediate frequency range. Sub-bands have the flexibility of being placed anywhere within the 4GHz range. The HIFI block-diagram and layout are presented in Figure 2.14

The scientific themes for HIFI are mainly related to the understanding of the cyclic interrelation of stars and the interstellar medium in galaxies. On the one hand, stars and planetary systems are formed through gravitational collapse of interstellar molecular clouds. On the other hand, the interstellar medium is composed from the ejecta enriched by newly synthesized elements of dying stars. This complex interplay between stars and the ISM drives the evolution, hence the observational characteristics, of the Milky Way and other galaxies, all the way back to the earliest protogalaxies at high redshift. Although HIFI will have capabilities that address many key topics in modern astrophysics, there are three areas for which HIFIs design was optimized and will be unique:

- Observations of the water lines lines ending in the ground states that are essential for absorption studies of cold water, falling in bands 1 (557 GHz), 4 (1.11 THz), and 6 (1.67 THz);
- Survey of the molecular complexity of the Universe;
- Observations of (redshifted) ionized Carbon ([CII]) at 1.9 THz (band 7).

These three topics required the high spectral resolution and the wide frequency range.

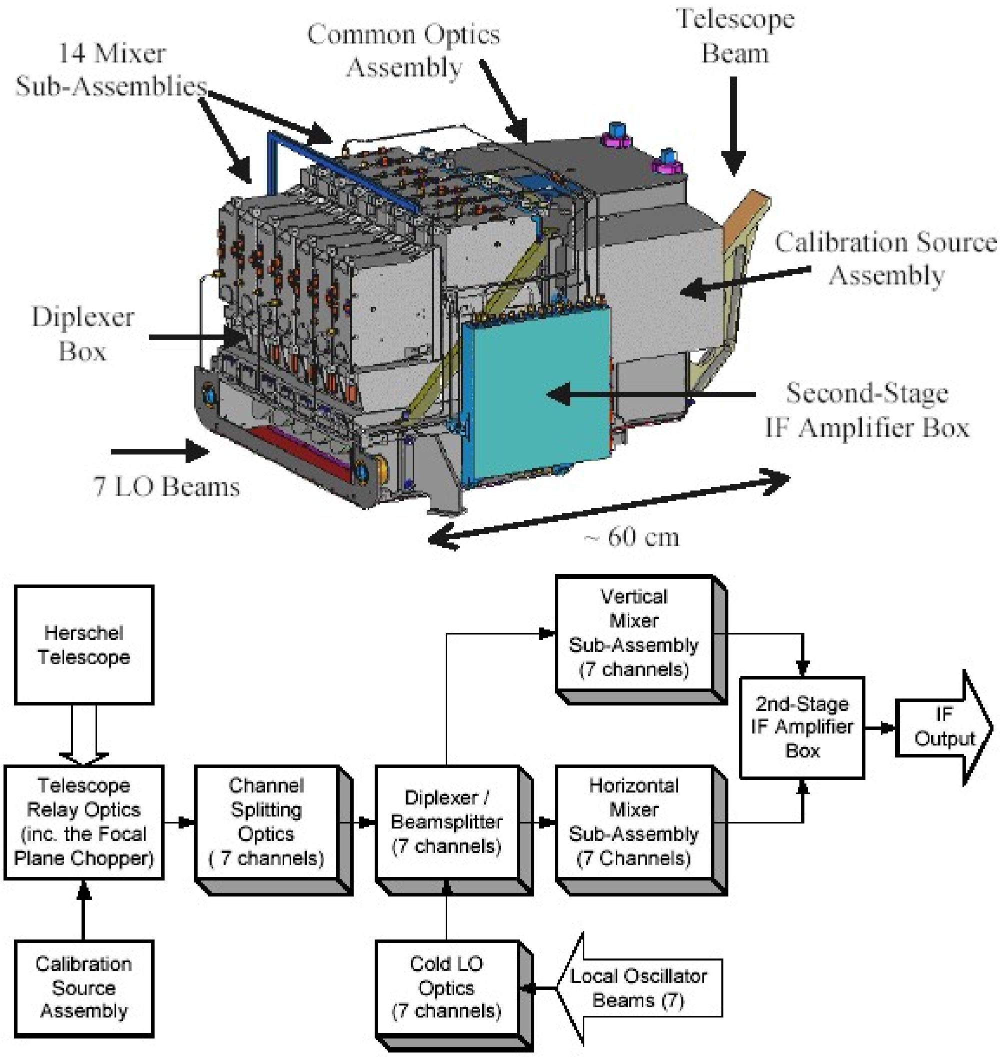

Figure 2.14: The HIFI layout and the block-diagram showing the various subsystems and their interconnections.

3

The SPIRE observing mode and Data Processing Pipeline

In this chapter I will report a detailed analysis of SPIRE Data Processing System (DP) Pipeline. In particular, I will describe the SPIRE observing modes and the steps for the data reduction from engineering conversion to science-ready products (both for photometer and spectrometer).

3.1 Introduction

All SPIRE observations will be processed by pipelines operating fully automatically, which shall produce standard calibrated data products (maps, point source fluxes, spectral data cubes, etc.) with instrument artifacts removed. It will also be possible for users to run the pipelines interactively in order to modify parameters and assumptions if desired. In this chapter I describe the pipeline processes to be used for the standard photometer (point source photometry and scan mapping) and spectrometer observing modes (Griffin et al. 2010 and Fulton et al. 2010).

The pipelines are designed to be modular and flexible, and the algorithmic content of modules has been made as simple as possible, with the associated calibration files containing key parameters. For a graphical overview of the pipeline see Figure 3.8. Because pipeline processing must be carried out automatically for all observations, no a priori assumptions are made about the spatial distribution of the sky brightness distribution, except for point source photometry observations, in which case the fitting of flux density and position assumes that the source is point-like.

3.2 Observing modes

An observation with SPIRE (or with any of the *Herschel* instruments) is performed following an Astronomical Observation Request (AOR) made by the observer. The AOR is constructed by the observer by filling in the so called Astronomical Observing Template (AOT) in the *Herschel* Observation Planning Tool, HSpot. Each template contains options to be selected and parameters to be filled in, such as target name and coordinates, observing mode etc. How to do this is explained in details in the HSpot user's manual[1] while in the following sections we explain the AOT user inputs.

Once the astronomer has made the selections and filled in the parameters on the template, the template becomes a request for a particular observation, i.e. an AOR. If the observation request is accepted via the normal proposal-evaluation-time allocation process then the AOR content is subsequently translated into instrument and telescope/spacecraft commands, which are up-linked to the observatory for the observation to be executed.

There are three Astronomical Observation Templates available for SPIRE: one for doing photometry just using the SPIRE Photometer, one to do photometry in parallel with PACS and one using the Spectrometer to do imaging spectroscopy (this covers all spatial resolutions and high, medium or low spectral resolution).

Observations are made up of logical operations, such as configuring the instrument, initialization and science data taking operations. These logical operations are referred to as building blocks. The latter operations are usually repeated several times in order to build up S/N and/or to map an area of sky. Pipeline data reduction modules work on building blocks.

3.2.1 SPIRE Photometer AOT

The photometer has three principal observing modes: Large Map Mode, Small Map Mode and Point or compact source photometry.

Large Map Mode - POF5: The build up of a map is achieved by scanning the telescope at a given scan speed (Nominal at $30''$/s or Fast at $60''$/s) along lines.

As the SPIRE arrays are not fully filled, the telescope scans are carried out at an angle of ± 42.4 deg with respect to the Z-axis of the arrays and the scan lines are separated by $348''$to provide overlap and good coverage for fully sampled maps in the three bands. This is shown schematically in Figure 3.1. One scan line corresponds to one building block.

As said, cross-linked scanning (or cross scanning) is achieved by scanning at $+42$ deg (Scan A angle) and then at -42 deg (Scan B angle). This angles ("magic

---

[1] HSpot user's manual `http://herschel.esac.esa.int/Docs/HSPOT/html/hspot-help.html`

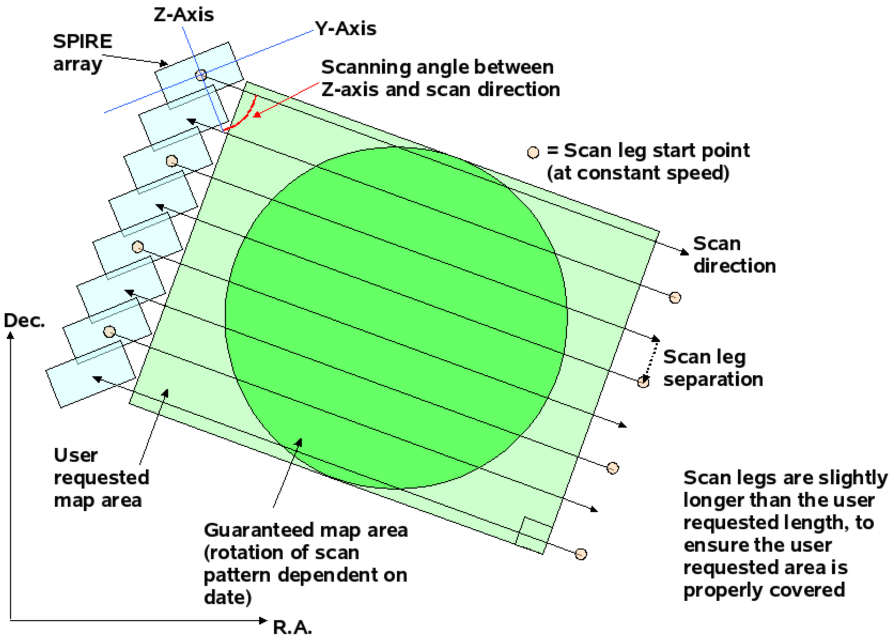

Figure 3.1: Large Map build up with telescope scanning, showing the scan angle, the scan legs and the guaranteed map area. (Spire Observers' Manual 2010).

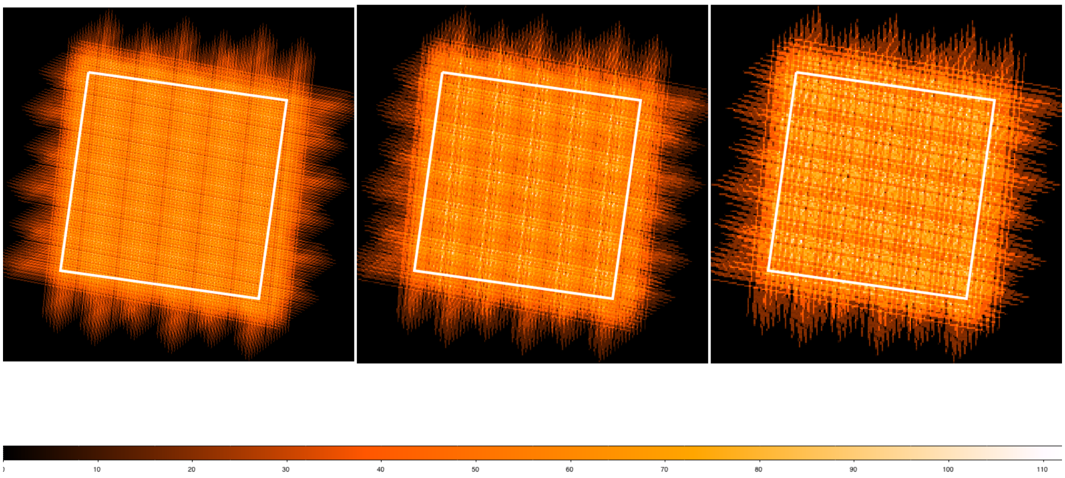

Figure 3.2: Example coverage maps for Large Map mode for the three photometer arrays, PSW (left), PMW (centre) and PLW (right) The pixel size is (6″,10″,14″) for (PSW, PMW, PLW) and the color code represents the number of bolometer hits in each sky pixel (Spire Observers' Manual 2010).

angles") for the scanning have been chosen because it optimizes the observations compared to other methods (e.g. long direction scanning with delayed scheduling with angles of ±77.6). In particular we can perform the observations in a single observing session, with the added advantage that the entire sky is accessible too (Waskett et al. 2007). This cross-scanning at Scan A and B is the default Large Map scan angle option in HSpot. This ensures that the effect of $1/f$ noise on the map can be minimized and also leads to improved map coverage. Note that the $1/f$ noise will be less significant at the faster scan speed.

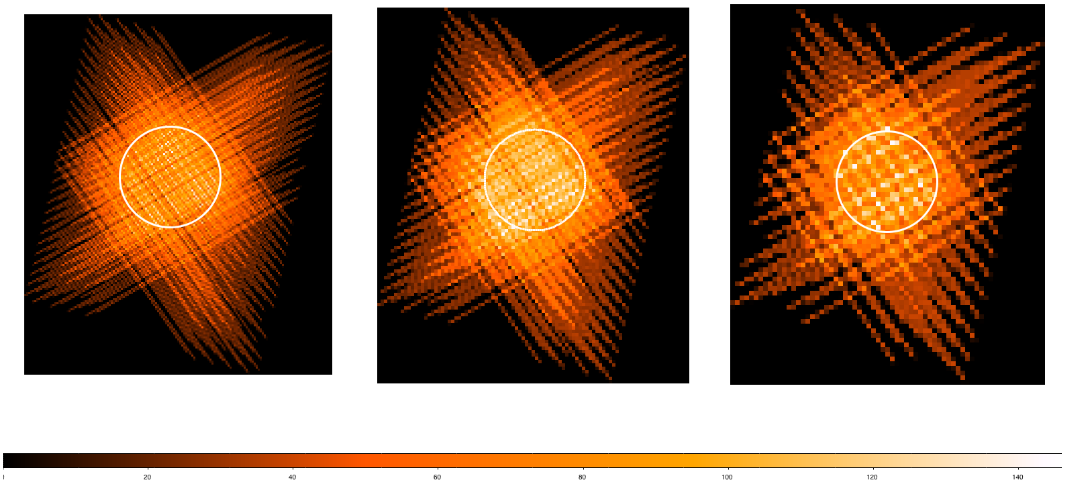

Figure 3.3: Example coverage maps for Small Map mode for the three photometer arrays, PSW (left), PMW (centre) and PLW (right). The white circle is with $5'$ diameter. The pixel size is ($6''$,$10''$,$14''$) for (PSW, PMW, PLW) and the color code represents the number of bolometer hits in each sky pixel.(Spire Observers' Manual 2010).

Real coverage maps for the cross scanning and single direction scanning for the different SPIRE bands it is show in Figure 3.2: the coverage is inhomogeneous due to missing or noisy bolometers.

Large map mode is used to cover large fields, larger than $5'$ diameter, in the three SPIRE photometer bands. Note that the mode can still be used even for input height and width of $5'$, however the efficiency is low and the map size will be much larger than the requested $5' \times 5'$ field.

Small Map Mode - POF10: Used for observations of small fields ($< 4' \times 4'$). The original SPIRE Small Map mode was initially a 64-point Jiggle Map, the POF3 mode[2]. However, after analysis and investigation it has been decided that

---

[2] The Jiggle mapping mode is similar to the standard jiggle-map observing mode used with

the original 64-point Jiggle Map should be replaced by a Small Map. The two small map modes have been compared using metrics for map coverage, quality and sensitivity with the new Small Map mode either outperforming or meeting the performance of the original 64-point Jiggle Map in all areas: increases the total mapping area, improves the observer flexibility and the data quality, improves redundancy and reduces the confusion limit. The Small Map mode consists of 2 orthogonal scan lines of fixed length. The mode operation and processing is essentially the same as the Large Map mode. For a given observation, the area covered by both scan legs defines a central square of side $5'$ although the length of the two orthogonal scan paths are somewhat longer than this. In practice, due to the position of the arrays on the sky at the time of a given observation, the guaranteed area for scientific use is a circle of diameter $5'$ (see Figure 3.3).

This mode has the same sensitivity as the large map mode but for small areas this mode uses less time.

Point or compact source photometry - POF2:

This observing mode is optimized for observations of isolated point sources with accurate astrometry. The mode is not suitable for the observation of faint sources close to the confusion limit. This observing mode use two particular sets of three detectors with overlapping beams on the sky in order to take data in the three bands simultaneously. The Beam Steering Mechanism (BSM) (see Section 2.5.5) will be used to make a seven-point map in which the nominal position and six hexagonally arranged neighboring positions with an angular offset of $6''$($\sim$ 1/3 of the smallest beam) will be observed in turn, with the central position observed twice, at the beginning of and the end of the sequence. Due to small asymmetries in the optical system, the ambient background power in the two chop positions will be slightly different. In order to subtract the resulting offset, the telescope will be nodded in the standard manner adopted on ground-based telescopes: during an observation, 3 co-aligned detectors see the source and the central co-aligned detector sees the source on both Nods (with positive signal in prime central detector and 2 half negative signals in the off source detectors). The data will be fitted with a 2-D beam profile to determine the peak flux density and positional offset from the telescope pointed position, assuring that pointing or source position errors do not result in flux density errors. The data from all detectors in all of the arrays will also be available, providing sparsely sampled maps of the field around the object. The standard point source observation involves an

---

SCUBA on the James Clerk Maxwell Telescope (Holland et al. 1999). For mapping of regions up to few arcmin. In size, the BSM will perform a 64-point jiggle map, needed to achieve full spatial sampling in all bands simultaneously, with a step size of $9''$(half-beam spacing at 250 μm). The jiggle-map field size is $0'4 \times 0'4$ as the 2-arcmin. Regions at each end of the array will be chopped outside the field of view admitted by the photometer optics. Nodding is carried out as for point source observations.

A-B-B-A sequence where A and B are the two telescope nod positions. The on-source integration time for each of the four steps is 64 seconds, comprising eight seconds in each of the eight map positions. With the standard 1-Hz chop frequency, each of these eight-second sequences comprises 8 chop cycles. See Figure 3.4 for a graphical description of this process.

The SPIRE Point Source mode is recommended for bright isolated sources in the range 0.2-4 Jy where the astrometry is accurately known and accurate flux measurement is required. For sources fainter than 200mJy (where the background produces a significant contribution) or at fluxes higher than ∼4 Jy (where pointing jitter can introduce large errors) the Small Map mode is preferable.

Parallel Mode - Parallel: In Parallel Mode, SPIRE and PACS are operating in photometry mode simultaneously, carrying out large-area mapping observations. SPIRE is observing in its three photometric bands, while PACS is taking data in its red band (130-210 μm) and in one of the blue bands (60-85 μm or 85-130 μm). The advantage of Parallel Mode is ensured by the compatibility of the two instruments and their operating modes. In practice, simultaneous observations in five bands are made possible without significant degradation in instrument performance. However, considering the fact that the PACS and SPIRE integration times are identical, the relative instrument sensitivities have to be carefully inspected to judge the real scientific benefit of using Parallel Mode. The SPIRE observations performed in Parallel Mode are essentially equivalent to the Large Map observations.

3.2.2 SPIRE Spectrometer AOT

This observing mode is used to make spectroscopic observations with the SPIRE Fourier Transform Spectrometer (FTS) (Section 2.5.6). Spectra can be measured in a single pointing (using a set of detectors to sample the field of view of the instrument) or in larger maps which are made by moving the telescope in a raster. For either of these, it is possible to choose sparse, intermediate, or full Nyquist spatial sampling. In summary, to define an observation, we need to select a spectral resolution (high, medium, low, high and low), an image sampling (sparse, intermediate, full) and a pointing mode (single or raster).

The Spectrometer Mirror Mechanism (SMEC) is scanned continuously at constant speed over different distances to give different spectral resolutions. For every repetition, two scans of the SMEC are done: one in the forward direction and one in the backward direction, making one scan pair. Two scan pairs are deemed essential for redundancy in the data. The desired integration time is set by increasing the number of scan pairs performed (corresponding to the number of repetitions entered in HSpot).

The Spectrometer can be used to take spectra with different spectral resolutions:

High resolution, Medium resolution, Low resolution and High and Low resolutions.

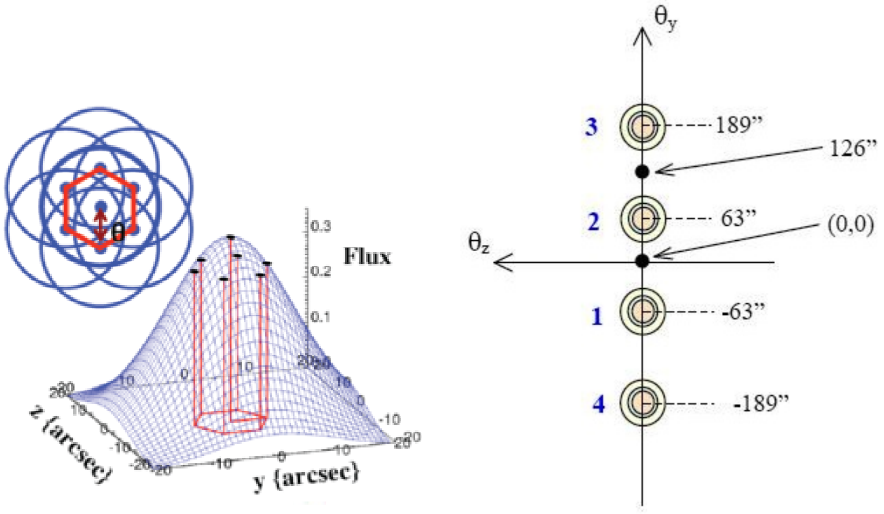

Figure 3.4: SPIRE Photometer Point Source Mode: a mini-map (**left**) is made around the nominal position to make sure that the source signal and position can be estimated. This mini-map is made by moving the BSM around to make the map for one detector. The 7-point map is made by observing the central position and then moving the BSM to observe six symmetrically arranged positions, offset from the central position by a fixed angle (nominally 6″), and then returning to the central point once more (note that the 7 in 7-point refers to the number of different positions). At each of these positions, chopping (**right**) is performed between sets of co-aligned detectors to provide spatial modulation and coverage in all three wavelength bands.

High resolution The high resolution mode gives spectra at the highest resolution available with the SPIRE spectrometer, $\Delta\sigma = 0.04\ cm^{-1}$ which corresponds to $\lambda/\Delta\lambda = 1000$ at $\lambda = 250\ \mu$m. High resolution scans are made by scanning the SMEC to the maximum possible distance from Zero Optical Path Difference (ZPD) (the SMEC point of symmetry). It takes 66.6 s to perform one scan in one direction at high resolution. This mode is best for discovery spectral surveys where the whole range from 194 to 671 μm can be surveyed for new lines. It is also useful for simultaneously observing sequences of spectral lines across the band (e.g. the CO rotational ladder). In this way, a relatively wide spectral range can be covered in a short amount of time compared to using HIFI (although with much lower spectral resolution than achieved by HIFI).
The Instrumental Line Shape of the SPIRE spectrometer is a *sinc* function and the

FWHM of an unresolved spectral line will be 1.207 times the spectral resolution, i.e. 0.048 cm^{-1} for a high resolution spectrum.

Medium resolution The intermediate resolution of $\Delta\sigma = 0.24$ cm^{-1} ($\lambda/\Delta\lambda = 160$ at $\lambda = 250$ μm) will be more suited to broad features. Medium resolution scans are made by scanning the SMEC again symmetrically about ZPD, but over a larger distance than in the low resolution mode. It takes 24.4 s to perform one scan in one direction at medium resolution. This mode is intended for surveys where the user may require a significant amount of spatial coverage and also wishes to survey bright, isolated lines. For these cases the high resolution mode may take up too much observing time. This mode may also be useful to characterize the SED with more data points than available with low spectral resolution.;

Low resolution Low resolution provide continuum measurements at the resolution of 0.83 cm^{-1} ($\lambda/\Delta\lambda = 48$ at $\lambda = 250$ μm). The SMEC is scanned symmetrically about ZPD over a short distance. It takes 6.4 s to perform one scan in one direction at low resolution. This mode is intended to survey sources without spectral lines or very faint sources where only a SED is required.

High and Low resolutions High and Low resolutions mode allows to observe a high resolution spectrum as well as using additional integration time to increase the S/N of the low resolution continuum to a higher value than would be available from using a high resolution observation on its own. This mode saves overhead time over doing two separate observations. The number of high resolution and low resolution scans can differ, and will depend on the required S/N for each resolution. If the number of repetitions for the high and low resolution parts are nH and nL respectively, then the achieved low resolution continuum sensitivity will correspond to nH+nL repetitions, because low resolution data can also be extracted from every high resolution scan.

The spectrometer combine a pointing mode and an image sampling to produce the required sky coverage.
The pointing mode available are:

Single Pointing Mode is used to take spectra of a region covered by the instrument field of view (2.0′ diameter circle unvignetted). With one pointing of the telescope only the field of view of the arrays on the sky is observed;

Raster Pointing Mode is used to take spectra of a region larger than the field of view of the instrument. The telescope is pointed to various positions making a hexagonally packed map (see Figure 3.5). At each position, spectra are taken at one or more BSM positions depending on the image sampling chosen.

The image sampling available are:

Sparse Image Sampling is used in conjunction with a single pointing, to measure the spectrum of a point or compact source well centered on the central detectors of the Spectrometer. The BSM is not moved during the observation,

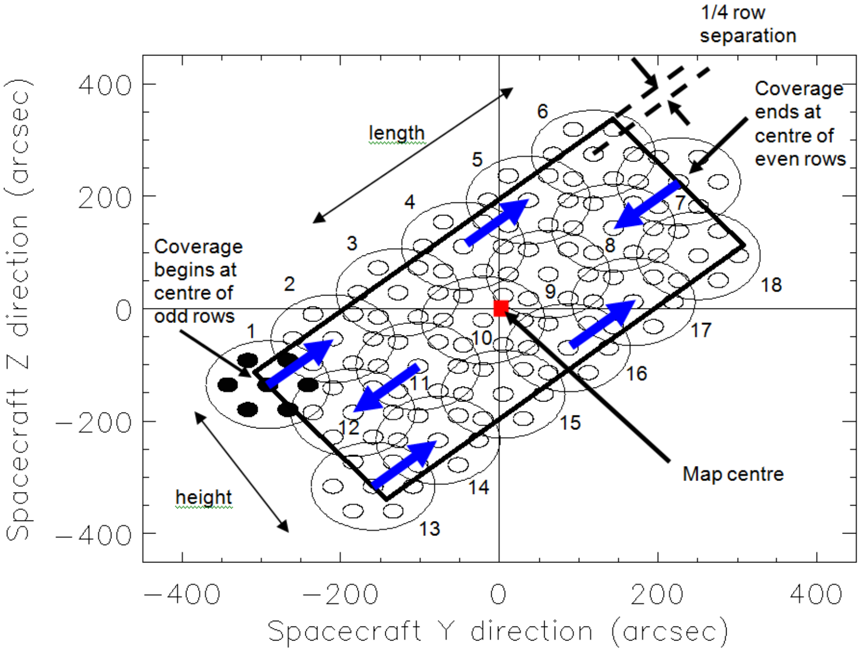

Figure 3.5: Ratser map with the SPIRE FTS (Spire Observers' Manual 2010).

producing a single array footprint on the sky. The result is an observation of the selected source position plus a hexagonal-pattern sparse map of the surrounding region with beam centre spacing of 32.5″ in the SSW band and 50.5″ in the SLW band as shown in Figure 3.6. For a point source this requires accurate pointing and reliable knowledge of the source position to be sure to have the source well centered in the central detector beam.

Intermediate Image Sampling is used to produce imaging spectroscopy with intermediate spatial sampling (1 beam spacing). This gives intermediate spatial sampling without taking as long as a fully Nyquist sampled map. This is achieved by moving the BSM in a 4-point low frequency jiggle, giving a beam spacing of 16.3″ in SSW band and 25.3″ in SLW band as shown in Figure 3.6. The input number of repetitions is performed at each of the 4 positions to produce the spectra.

Full Image Sampling allows fully Nyquist sampled imaging spectroscopy of a region of the sky or an extended source. This is achieved by moving the BSM in a 16-point jiggle to provide complete Nyquist sampling (1/2 beam spacing) of the required area. The beam spacing in the final map is 8.1″ for PSW band and 12.7″ in PLW band as shown in Figure 3.6. The input number of repetitions is performed at each one of the 16 positions to produce the spectra.

In the following section I will describe briefly the engineering conversion pipeline

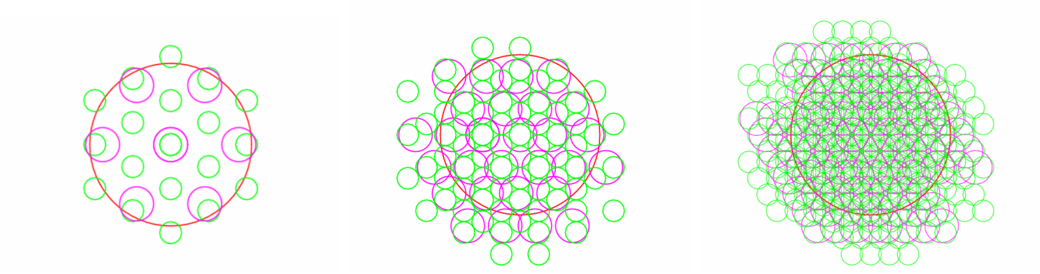

Figure 3.6: SPIRE Spectrometer spatial sampling: sparse (left), intermediate (centre) and full (right). The small green and magenta circles indicate the regions where spectra will be observed for different spatial samplings. The green circles show SSW and the magenta show SLW, the large red circle of $2'$ diameter is to guide the eye for the unvignetted field of view (Spire Observers' Manual 2010).

and all the SPIRE data processing pipeline.

3.3 SPIRE data processing pipelines

In this section I will briefly describe the data products and the data structure coming from SPIRE observations, as well as the standard pipeline processing that this data was subject to.

SPIRE observations are supplied in a highly organized structure that may be unfamiliar compared to previous astronomical datasets. In addition, with this new structure comes a host of new terminology which will be introduced and described in this section. All data within the HCSS processing system (see Section 4.1) are passed around in containers referred to as Products. There are Products for every kind of data. The product contains datasets, metadata and information about the process (history). A dataset can contains array tables, nested tables or image arrays.

Astronomer users will receive data that has already been processed through the standard pipelines to several Levels. The processing levels of the SPIRE pipeline and user deliverables are outlined below in Figure 3.8. In general, data Level 0 corresponds to the raw data, formatted from the raw telemetry by an external pre-processing stage. These Level 0 Data Products are then passed through a processing stage referred to as the Engineering Conversion (see 3.3.1) that creates the Level 0.5 data products in a meaningful and manageable form. The SPIRE AOT specific pipelines then process these Level 0.5 Data Products to produce the science usable, calibrated Level 1 Data Products. Further advanced processing to create products such as maps produce the high-level Level 2 Data Products.

Quality Control is carried out by the HSC and delivered to the user.
The smallest “piece” of SPIRE observational data is called "Building Block". These Building Blocks correspond to basic operations within an observation and as the name suggests every SPIRE AOT is built up from a combination of these building blocks. Building Blocks are usually in the form of Timeline Data Products (e.g. a scan line in a map, a set of Spectrometer scans, a motion of the BSM, etc).

Building Blocks and other Products are grouped into a context. A context is a special kind of product linking other products in a coherent description and can be thought of as an inventory or catalogue of products. The SPIRE processed observation consists of many such contexts within a general Observation context. Therefore, each set of building blocks have a context. Each Processing Level in the SPIRE pipeline has a context and the entire Observation has a context. Moreover, contexts are not just for building block products and higher processed data products, there are contexts for Calibration Products and contexts for Auxiliary Products (e.g. pointing) and even a context for Quality Control. This is the structure and content that you should receive for your SPIRE observation from the HSA (see Section 4.2.1). The Figure 3.7 show the complete Observation Context of a SPIRE observation, here described:

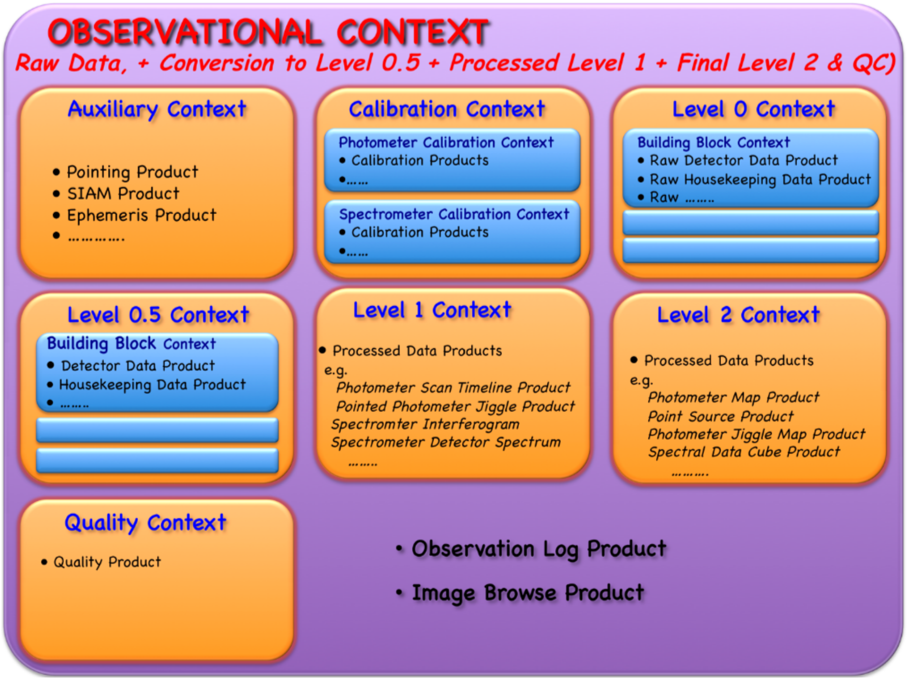

Figure 3.7: The complete Observation Context of a SPIRE observation (Spire Observers’ Manual 2010).

level 0 The Level 0 context contain links to the Level 0 raw data before any pipeline processing.

level 0.5 The Level 0.5 context contain links to the Level 0.5 data products after the common engineering conversion has been made.

level 1 The Level 1 context contain links to the Level 1 data products after AOT specific pipeline processing.

level 2 The Level 2 context contain links to the final Level 2 data products from the pipeline.

calibration: The Calibration context point to all calibration products required for the processing of SPIRE data.

auxiliary All *Herschel* non-science spacecraft data required directly or indirectly in the processing and analysis of the scientific data.

logObsContext The context point to the reduction log that records the processing history of the data.

quality The Quality context point to the quality control products for this observation.

browseImageProduct The context point to thumbnail products.

browseProduct The context provides a quick look to the products.

level 3 (optional) Publishable science products with level 2 data products as input. Possibly combined with theoretical models, other observations, laboratory data, catalogues, etc. Formats should be Virtual Observatory compatible.

Therefore, any Observation context contains the results from the all data reduction pipeline stages. In the following section I will describe these stages.

3.3.1 The Engineering Conversion Pipeline

This part of the SPIRE processing pipeline is common to both the photometer and spectrometer and converts the Level 0 raw data products into the processed Level 0.5 data products. The first step, before running the Engineering Conversion Pipeline, consist in extract the telemetry data (specified by a user selected range) from a database and to compile them into a set of Level-0 SPIRE data products for the use of further data processing steps. The data from the spacecraft arrives

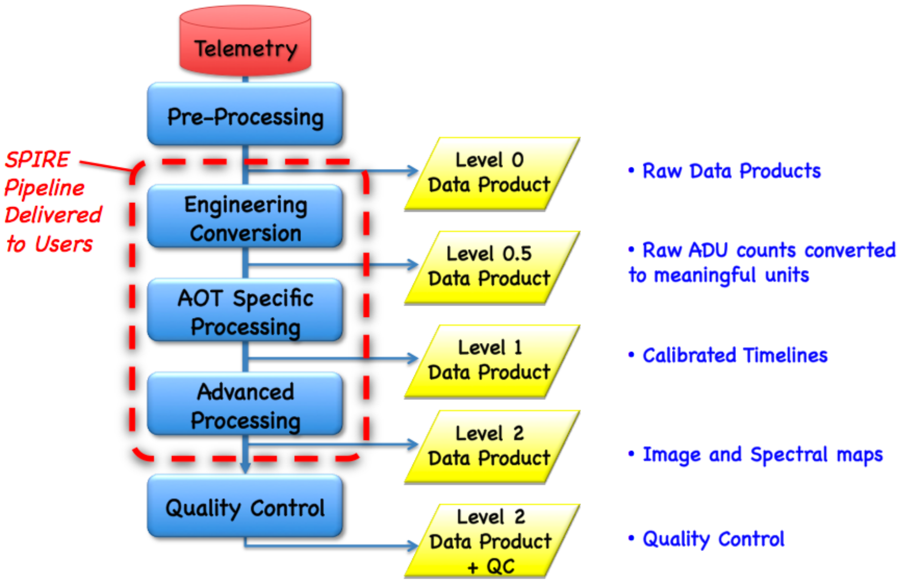

Figure 3.8: The processing levels of the SPIRE pipeline and user deliverables (Spire Observers' Manual 2010).

in telemetry packets that are reordered into the Level 0 data Products in the form of timelines. In addition to producing the Level 0 products this step also produces the DPU reset history calibration product. Before any AOT specific processing is carried out, all SPIRE data goes through an Engineering Conversion processing stage which converts the Level 0 Products to a more manageable structure in the form of Level 0.5 Data Products.

The pipeline flow is described in Figure 3.9. Note that in general it is expected that users will start any reprocessing or interactive analysis from Level 0.5 and thus will rarely, if ever need to use the Engineering Conversion.

The first step in the Engineering Conversion pipeline is to reformat the raw Level 0 products into a more intuitive and workable form. The input Level 0 products consist of single tables with the name of the packet type that originated them. Each column in this table has the name of the corresponding telemetry parameter (e.g. PHOTFARRAY123 for a channel, see Figure 3.10). For the detector timelines, this stage creates Level 0.5 format products with separate tables for "Signal", "Mask" and "Quality" data. At this stage, all columns are copied to the Level 0.5 format however the columns use a more intuitive naming convention such as the names of channels within detector arrays[3]. For other raw non-detector timelines the names of the columns are changed using a set of telemetry dictionary

---

[3] The first column in the tables is the "sampleTime", which is the renamed "sdfTime" (SPIRE Data Frame Time) column in the Level 0 table.

Figure 3.9: Level 0.5 Engineering Conversion Pipeline.Data products delivered to the user are shown in yellow. Processing steps are shown in blue and calibration files in orange (Spire Observers' Manual 2010).

lookup tables.

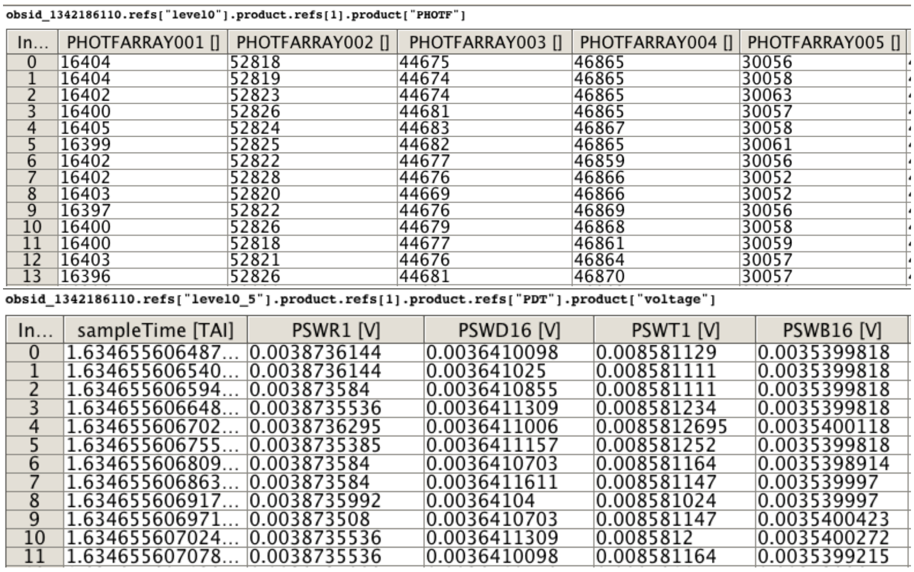

`obsid_1342186110.refs["level0"].product.refs[1].product["PHOTF"]`

In...	PHOTFARRAY001 []	PHOTFARRAY002 []	PHOTFARRAY003 []	PHOTFARRAY004 []	PHOTFARRAY005 []
0	16404	52818	44675	46865	30056
1	16404	52819	44674	46865	30058
2	16402	52823	44674	46865	30063
3	16400	52826	44681	46865	30057
4	16405	52824	44683	46867	30058
5	16399	52825	44682	46865	30061
6	16402	52822	44677	46859	30056
7	16402	52828	44676	46866	30052
8	16403	52820	44669	46866	30052
9	16397	52822	44676	46869	30056
10	16400	52826	44679	46868	30058
11	16400	52818	44677	46861	30059
12	16403	52821	44676	46864	30057
13	16396	52826	44681	46870	30057

`obsid_1342186110.refs["level0_5"].product.refs[1].product.refs["PDT"].product["voltage"]`

In...	sampleTime [TAI]	PSWR1 [V]	PSWD16 [V]	PSWT1 [V]	PSWB16 [V]
0	1.634655606487...	0.0038736144	0.0036410098	0.008581129	0.0035399818
1	1.634655606540...	0.0038736144	0.003641025	0.008581111	0.0035399818
2	1.634655606594...	0.003873584	0.0036410855	0.008581111	0.0035399818
3	1.634655606648...	0.0038735536	0.0036411309	0.008581234	0.0035399818
4	1.634655606702...	0.0038736295	0.0036411006	0.0085812695	0.0035400118
5	1.634655606755...	0.0038735385	0.0036411157	0.008581252	0.0035399818
6	1.634655606809...	0.003873584	0.0036410703	0.008581164	0.0035398914
7	1.634655606863...	0.003873584	0.0036411611	0.008581147	0.003539997
8	1.634655606917...	0.0038735992	0.00364104	0.008581024	0.003539997
9	1.634655606971...	0.003873508	0.0036410703	0.008581147	0.0035400423
10	1.634655607024...	0.0038735536	0.0036411309	0.0085812	0.0035400272
11	1.634655607078...	0.0038735536	0.0036410098	0.008581164	0.0035399215

Figure 3.10: Reformatting of Level 0 Product into Level 0.5 format. Signal Table (**bottom**) is created from the Raw PDT (**top**). Column names are renamed to more intuitive labels.

The next step is flagging out of range detectors. The impact of Cosmic rays on the Analogue to Digital Converter (ADC) can generate a change in the electronics that may corrupt the ADC reading (referred to as an analogue to digital converter latch-up). The electronics however detect these events and set a flag corresponding to the affected ADC channel. These flags inform the DPU of the occurrence of ADC latch-up and that the ADC was not made correctly, or a Spacecraft Subsystem to DPU interface fault, and therefore of the risk of propagation of corrupted data. When one flag or more is set, the related data have to be masked so that they will not be used in the following data processing steps. The occurrence of this error will be stored in a metadata keyword. This flags column in the Level 0.5 format data signal table is thus translated into the mask and then deleted. Another problem is the truncation of detector channel values, i.e. if the voltage is out of the ADC range. When a detector channel voltage is out of the ADC range, the Analogue Data Unit (ADU)[4] measured value is 0 or 65535; when these values are found in the "signal" table, the sampling shall be flagged as invalid by setting the appropriate bit in the value contained in the "mask" table corresponding to the affected sample.

---

[4] The (usually 16 bit) value returned from the Analogue to Digital Converter (ADC) in the instrument electronics.

In general, the SPIRE data processing supports three general categories of masks:

Channel Masks: are applied to all data from a given channel (bolometer, thermistor, resistor, etc.) and thus affects all time samples for that channel. They indicate whether a signal channel is useful or not, such as whether that particular channel is dead.

Instrument Mode Masks: are effectively channel masks that are applied only to data from specific observing modes. Following the same procedure as for Channel Masks, they indicate whether a signal channel is useful or not for that specific observing mode.

Sample Masks: All data products contain a sample mask table added at the Reformat Level 0 Product stage. In this table, a 32-bit integer is reserved for each sample for each detector, referred to as a Sample Mask. Mask information is represented by bits in a Sample Mask, with different bits representing different mask conditions.

The Sample Masks table of Level 0.5 is populated using the information from the Channel Masks table and the Instrument Mode Masks table. The mask table contains an integer mask for every detector for every time step. A flag is raised (bit set equal to 1) in the mask to indicate that a given status is "TRUE". If the mask is set in the calibration products then the relevant bit is raised in the mask table for every single time sample for that channel. Furthermore, the masks contain three subsets of flags that can be raised within them.

Unusable: reserved for samples that are afflicted with critical problems to the degree that the data samples should not be considered scientifically valid and are ignored by the pipeline modules which simply propagate the Sample Mask Table. There is also a Master Bit to provide a quick reference as to whether a data sample is or is not scientifically valid which is set if any "unusable" flag is raised.

Informational: represent non-critical problems with the detector data samples for which there exists no correcting data processing module. Data processing modules that encounter a Information condition should process the sample as normal and propagate the Sample Mask Table.

Correctable: conditions for which a data processing module exists that may be able to correct the condition. These masks always come in pairs: one mask will denote the identification of the condition; the second will denote whether the condition has been corrected.

A list of the sample masks that are currently defined in SPIRE data processing pipeline is given in Appendix B.

After the “mask” step, the Engineering Conversion Pipeline calculates an accurate absolute time for all samples in both detector and non-detector timelines. Note that the “sampleTime” in the Level 0.5 format products was originally copied from the SPIRE Data Frame Time (DFT) in the Level 0 products and the DFT was measured in microseconds since 1st January 1958, stored as a 64-bit integer. It is computed via the following equation:

$$DFT = T_{reset} \times \frac{1 \cdot 10^6}{65536} + F_{time} \times 3.2 \tag{3.1}$$

where, T_{reset} is the DPU reset time and F_{time} is the number of (3.2 microsecond) clock ticks since the last DPU reset time. The DPU reset time is the onboard time at which the DPU counter reset event occurred. The value is represented as a raw time code in 1/65536 seconds ($65536 = 2^{16}$) since 1st January 1958, and F_{time} is the number of (3.2 microsecond) clock ticks since the last DPU reset time.

Re-ordering is now implemented so that each data sample in a timeline has an associated absolute time and at this stage the additional time information in the Level 0.5 products is removed: only the Sample Time, now measured in seconds, remains. The next stage is the conversion: conversion of the data from ADU to meaningful units in the raw non- detector timelines (e.g. Raw Nominal Housekeeping Timeline) and conversion from ADU to JFET voltage. Using the RMS Voltage at the JFET output, we can derive the RMS voltage at the bolometer and the bolometer resistance, by an iterative procedure designed to take into account the RC roll-off due to the harness transfer function and also any changes in the phasing of the bias demodulator.

The last two stages are the calculation of bath temperature and association of the position to the appropriate building block. The thermistor temperature timelines are derived for each detector array (this is in addition to the thermistor signals contained in the detector signals table). These timelines will contain the calculated bolometer bath temperatures T_{bath} in Kelvin, as measured by the thermistors. The bath temperature is calculated from the parameters T_R and R_0contained in a calibration file:

$$T_{bath} = \frac{T_R}{ln(R_T/R_0)^2} \tag{3.2}$$

where, T_R is the Reference Temperature for Bolometer Resistance, R_0 is the Bolometer Resistance at theReference Temperature, and R_T is the resistance of the Thermistor from the Detector Timeline Product.

About the pointing, the Engineering Conversion Pipeline associates the nodding ID for the photometer Point Source observations, the scan line number for

Large Map, Small Map and parallel observations and the jiggle ID and pointing number for spectrometer observations, with the appropriate building blocks. Note that this is the addition of identifiers rather than actual positions: after, any AOT pipeline will associate the correct position to the observation (see e.g. Section 3.3.2.9).

The output from the Engineering Conversion Pipeline are calibrated voltage detector and auxiliary data timelines as Level 0.5 products. These Level 0.5 products form the input into the AOT specific pipelines.

3.3.2 The Large Map and the Small Map pipelines

The SPIRE Large Map and Small Map data processing pipeline (also used for processing parallel mode data) takes as input individual scan lines in the form of timeline data. However, for the purposes of efficient processing, all scan lines for a given observation (including the end of scan turnarounds) are concatenated into a single timeline (see Section 4.7). After the processing has been completed this single timeline is then dissected into the individual scan lines for map making. The standard processing pipeline for Large/Small Map mode is shown below in Figure 3.11. The workflow start with the level 0.5 products (Photometer Detector Timeline (PDT)) and finish with the Level 2 products (Photometer Map). In the following, I try to explain in details some of this step.

3.3.2.1 Conversion of the Beam Steering Mirror (BSM) telemetry into Angles on the Sky

The first step to do in the pipeline is convert the telemetry of BSM (that contains all the informations about the position, see Section 2.5.5) in angle on the sky. The method is simple: we need to realize an interpolation from a calibration table containing the two converted angles (spacecraft Y and Z axes) versus the two raw signal values (in the BSM chop and jiggle axes). Note that for scan map observations there is no chopping, and therefore there is no need to create a "chop-jiggle timeline" as in the case of Jiggle observations. However, it is still necessary to create a BSM angle timeline because it is important to know where the BSM is pointing even if it supposed be at a fixed position. For scan map observations, the instrument does not produce BSM telemetry packets at all, but rather the input comes from the Nominal Housekeeping Timeline (NHK) which contains the BSM sensor signal values at a lower sampling rate. The process is shown pictorially in the Figure 3.12

Figure 3.11: Flowchart for the Large Map, Small Map and Parallel mode data processing pipelines. Data products delivered to the user are shown in yellow, intermediate data products in green. Processing steps are shown as light-blue boxes while calibration files are shown in orange (Spire Observers' Manual 2010).

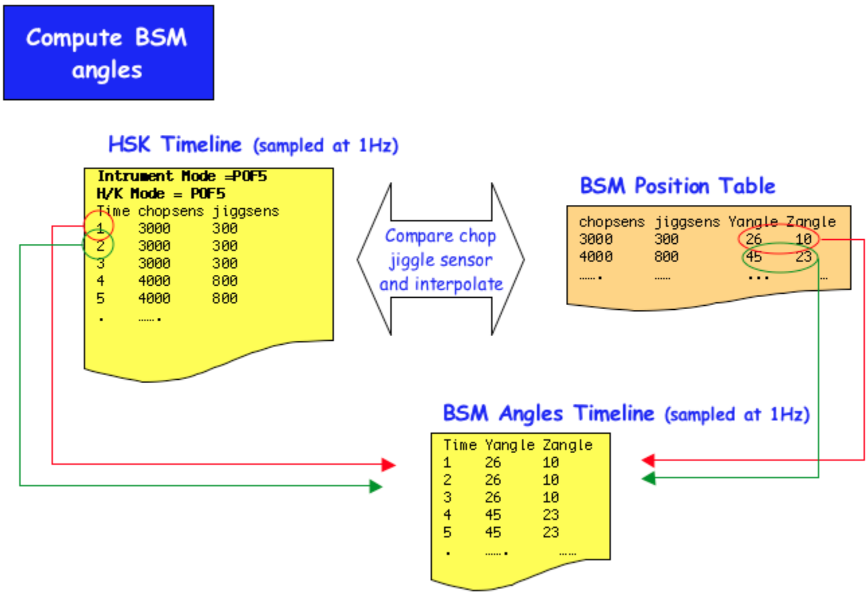

Figure 3.12: Creation of BSM Angles Timeline by the Compute BSM Angles module in the Scan Map Pipeline

3.3.2.2 Deglitching the Timeline Data

Before further processing of the measured detector voltage timeline glitches due to cosmic ray hits or other impulse-like events in the detectors is removed by a method involving a wavelet-based local regularity analysis. The basic assumption is that the glitch signature is similar to a Dirac delta function. This process consist of two steps: the first step implements a wavelet-based local regularity analysis to detect glitch signatures in the measured signal; the second step locally reconstructs a signal free of such glitch signatures.

Glitch Identification: Glitches are detected in the input Detector Timeline product by wavelet analysis assuming that the glitch signature is similar to the signature of a Dirac delta function. Each sample that is identified as a glitch will have its mask modified in accordance with the SPIRE pipeline mask policy (see Section 3.3.1 and Appendix B).

Glitch Reconstruction: actually the reconstruction is performed via polynomial interpolation. The samples identified as glitches are replaced by way of polynomial interpolation.

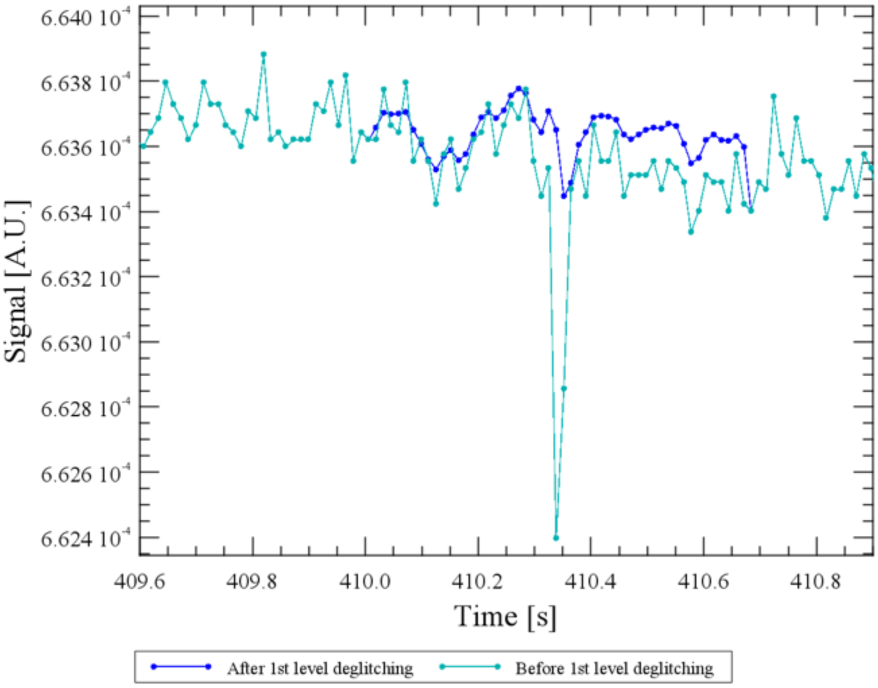

Figure 3.13: An example for glitch removal in a the detector timeline. An original detector timeline (green) is shown after removal of the glitch (blue).

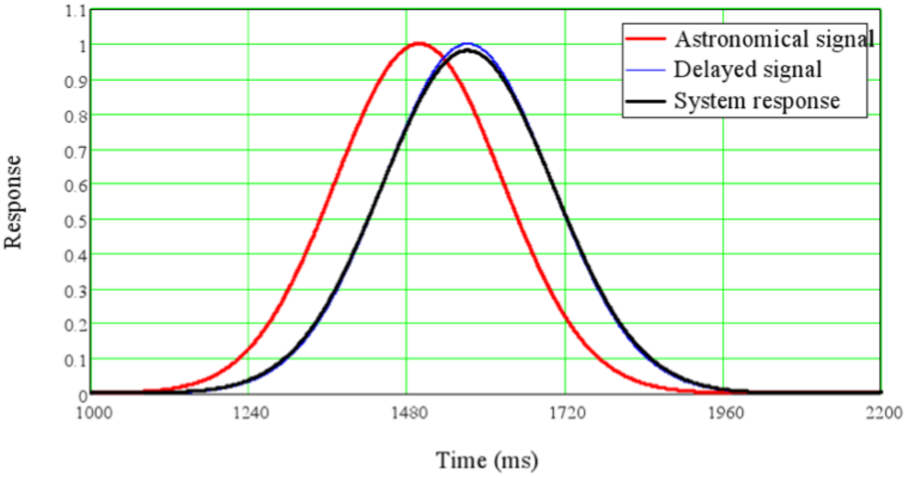

Figure 3.14: Effects of the electrical low pass filter transient response

3.3.2.3 Removal of electrical crosstalk

The deglitched timeline may contain contributions that depend on the signals from other detectors due to either electrical or optical crosstalk. Electrical crosstalk arises after the detector and is due to capacitative or inductive coupling between the detector readout channels. Optical crosstalk occurs before the detector and is due to diffraction or aberrations in the optical system causing some of the power from an astronomical source to fall on inappropriate detectors. Electrical crosstalk can be removed if the coupling between the detectors is known. We assume that 1) electrical crosstalk is linear, so that the effects can be characterized by a crosstalk matrix with constant elements; 2) crosstalk from one detector to another involves negligible diminution of the signal in the primary detector, so that the diagonal elements of the crosstalk matrix are unity; 3) there is no crosstalk between different arrays. For a particular time-step, the vector of electrical crosstalk-corrected signals is given by a simple matrix multiplication:

$$V_f = C_{elec} V_0. \tag{3.3}$$

Determination of the electrical crosstalk matrix elements in flight is carried out using ionizing radiation hits that the bolometers will experience. Ideally, a single event in a bolometer produces a spike only in its own output; crosstalk results in this being accompanied by lower-level responses from other detectors. In the absence of crosstalk, or if the crosstalk correction is to be left out, then the non-diagonal coefficients of C_{elec} are set to zero.

3.3.2.4 Correction for Electrical Filter Response

The electronics chain imposes a delay on the data with respect to the telescope position along the scan: this is due to the electrical filter (Low pass filter - LPF) transient response (as shown in Figure 3.14). This effect must be taken into account to ensure that the astrometric pointing timeline be properly matched to the detector data timeline. To correct for the effect of the electrical filter a digital filtering technique is applied to the pipeline:

1. Transforming the signal timelines of individual detectors in to the Fourier domain;

2. Dividing by the electrical filter transfer function;

3. Transforming the result back to the time domain.

The electrical filter transfer function is derived from the LPF parameters (nominally the same for all detectors). To a close approximation, the overall effect of this step is to shift the data timeline by 74 ms with respect to the pointing timeline.

This correction is applied to the complete detector timeline (from the start of telescope acceleration to the end of the deceleration) since the acceleration and deceleration periods may be used later for scientific purposes, and to make sure that any ringing effects at the start and end of the scan caused by the Fourier transformations are well clear of the nominal map area.

3.3.2.5 Conversion to flux density

Signal conversion from voltage to flux in Jy/beam use a parameterization of the relationship between the voltage and flux based on observed calibration sources. The conversion also incorporates flat fielding and strong source corrections. For the SPIRE bolometers, whose behavior is accurately described by an ideal bolometer model, the small-signal responsivity for a given applied bias voltage varies with the voltage across the bolometer with a near-linear relationship over a wide range of background loading and bath temperature conditions. This translates to a corresponding relationship for the differential sensitivity of the system to flux density. To allow for the fact that the responsivity–operating point voltage relationship will not be exactly linear, we let

$$\frac{dS}{dV} = f(V). \tag{3.4}$$

it is demonstrated (Griffin et al. 2008) that an accurate fit to the shape of $f(V)$ can be made using a function of the form:

$$f(V) = K_1 + \frac{K_2}{V - K_3}, \tag{3.5}$$

where K_1, K_2 and K_3 are constants. K_3 and the ratio K_1/K_2 can be found by pointing the telescope at a selection of bright sources (without chopping) and measuring the relative change in responsivity as a function of bolometer voltage using the internal calibration source PCAL. It is not necessary to know how bright these sources are: they are just being used to establish a range of backgrounds on the detectors. The absolute values of K_1 and K_2 can be determined by observation of a single suitable astronomical calibrator.

A flux density corresponding to the measured RMS detector voltage, V_m, can be derived by integrating the above expression between some fixed detector voltage, V_0, and V_m:

$$S_f = \int_{V_0}^{V_m} (K_1 + \frac{K_2}{V - K_3}) dV = K_1(V_m - V_0) + K_2 \ln(\frac{V_m - K_3}{V_0 - K_3}). \tag{3.6}$$

Ideally, V_0 would be the bolometer voltage in the absence of any astronomical signal (i.e., what would be measured when observing blank sky in otherwise identical conditions). The resulting flux density would correspond to that from the sky calibrated with respect to the dark sky level. V_0 will therefore be derived from standard calibration observations of a "dark" area of sky in scan-map mode, to determine the offset voltages for the detectors under the nominal conditions: bias voltage and frequency, detector and FPU temperature, and telescope temperature. Although ideally the conditions would be the same for the calibration and science observations, small differences are likely in practice. We therefore expect that, even for dark sky, V will differ from the ideal value V_0 (by an amount much larger than most astronomical signals). This means that the initial flux density values produced in this step will include offsets that must be removed later to derive the flux density from the sky. This is done naturally as part of the map-making routine. After this step we have a set of timelines corresponding to the first estimates of flux densities, $S_f(t)$. For the photometer calibration see Section 3.5.

3.3.2.6 Removal of correlated noise due to bath temperature fluctuations

To first order, bath temperature fluctuations will influence all bolometers in an array coherently – the temperature and corresponding output voltages will go up and down in synchronism. The ^3He bath temperature, T_0, may fluctuate due to temperature drifts within the instrument. For the level of fluctuations in SPIRE, the most important effect of bath temperature variations will be the direct response of the bolometer output voltage. Because bath temperature fluctuations replicate the effect of absorbed power fluctuations on the bolometer output, it is best to correct for them after the conversion to flux density (which is proportional to power). There be a small second-order effect on the bolometer small-signal responsivity. Fluctuations in T_0 are expected to be much slower than the nominal chopping frequency of 2 Hz, so that the correction will only be needed for scan-map observations. The procedure is based on the empirical correlations between detectors and thermistors (or, in case of high bias voltages when thermistors are saturated, the correlations between detectors and dark pixels) and involves generating a voltage timeline $V_{h-i}(t)$ from the array thermistor timelines. A scaled version of this is then subtracted from that bolometer's signal timeline. To avoid introducing additional noise, the thermometry timeline will need to be significantly less noisy than the bolometer signals. It will therefore need to be averaged over a period of time such that it becomes a negligible fraction (say 10%) of the bolometer noise. This will require a suitable averaging period. Thermal fluctuations on timescales shorter than this will not be tracked.The correction scheme, and the results of its application to instrument test data are described in Schulz et al. (2008).

The correction will be implemented in the following way: let $\bar{V}_{T1}$ and $\bar{V}_{T2}$ be the smoothed voltage timelines of thermistors T_1 and T_2 for a given array. These are converted to flux density timeline for bolometer i as follows:

$$S_{T1-i}(t) = A_{1-i}(\bar{V}_{T1} - V_{o1}) + 0.5B_{1-i}(\bar{V}_{T1} - V_{o1})^2, \tag{3.7}$$
$$S_{T2-i}(t) = A_{2-i}(\bar{V}_{T2} - V_{o2}) + 0.5B_{2-i}(\bar{V}_{T2} - V_{o2})^2, \tag{3.8}$$

where V_{o1} and V_{o2} are reference signals of T_1 and T_2, measured during calibration observations, and A_{1-i}, B_{1-i} and A_{2-i}, B_{2-i} are correlation coefficients for bolometer i.

These timelines can be used individually or averaged to generate the final correction timeline :

$$S_{T-1} = S_{T1-i}(t) \quad S_{T-1} = S_{T2-i}(t) \quad S_{T-i} = 1/2(S_{T1-i}(t) + S_{T2-i}(t)). \tag{3.9}$$

The best choice will depend on the detailed performance of the thermistors on the different arrays. The corrected bolometer timeline for bolometer i is given by:

$$S_{F-i}(t) = S_{0-i}(t) - S_{T-i}(t) \tag{3.10}$$

At the high bias voltage setting, the thermistors will be saturated, and the temperature drift will be traced by dark bolometers. Therefore, for the high bias voltage, the dark bolometer voltages V_{DK} will be used instead of the thermistor voltages V_T. The output of this module is a set of timelines of astronomical flux densities corrected for low-frequency thermal drifts: $S_{F-i}(t)$ for bolometer i.

3.3.2.7 Correction for bolometer time response

The photometer detectors are designed to have first-order time constants of typically 6 ms, and this has been verified in unit-level and instrument-level testing of the arrays. There is evidence from measurements on similar detectors that SPIRE-like bolometers may not exhibit a pure first-order response (characterized by a single time constant), but can also have a low-level slow response, with variation of detector responsivity with signal frequency, ω_s, characterized by a transfer function of the following form:

$$H(\omega_s) = \frac{1-a}{1 + j\omega_s\tau_1} + \frac{a}{1 + j\omega_s\tau_2} \tag{3.11}$$

The procedure for correcting the timelines is essentially the same as for the electrical filter correction:

1. Transforming the signal timelines of individual detectors in to the Fourier domain;

2. Dividing by the bolometer transient response transfer function (based on the parameters τ_1, τ_2, and a);
3. Transforming the result back to the time domain.

The values of the parameters of the transfer function will be derived from calibration file parameters stored for each detector:

- nominal detector time constant, τ_1
- slow detector time constant, τ_2
- time constant amplitude factor, a

The output of this module is a set of timelines of astronomical flux densities corrected for the bolometer time response.

3.3.2.8 Removal of optical crosstalk

Optical crosstalk is here defined as power from the astronomical sky that should be incident on one detector actually falling on another. It is important to note that in the case of SPIRE, neighboring detectors are separated by an angle of $2\lambda/D$ on the sky, and even if a source is on-axis for a given pixel, a small fraction of the source power will be incident on the neighboring detectors due to telescope diffraction. Non-neighboring detectors are sufficiently far apart that they should not pick up any power from an on-axis source. Optical crosstalk can be characterized by a crosstalk matrix, C_{opt}, analogous to the electrical crosstalk matrix described above. The vector of optical crosstalk-corrected flux densities is then given by

$$\mathbf{S_f} = \mathbf{C_{opt}} \mathbf{S_0} \tag{3.12}$$

Unlike the case of electrical crosstalk, the diagonal elements are not equal to unity since optical crosstalk involves loss of power from the primary detector. The optical crosstalk matrix coefficients must be determined from calibration observations involving scanning a strong point source across each of the detectors in the array. In the absence of optical crosstalk, or if the crosstalk correction is to be left out, then the non-diagonal coefficients are set to zero and the diagonal coefficients are set to unity. The output of this module is a set of flux density timelines, $S_f(t)$, suitable for input to the map-making module.

3.3.2.9 Associate Sky Position

The RA and Dec position of any bolometer at any given time during the observation are finally calculated using information provided by the SPIRE Pointing

Product.
The astrometry is calculated from various offsets (detector positions, BSM position, etc) that map a single detector to a position on the sky. This step is achieved via:

- Conversion of the BSM telemetry into angles on the sky (see Section 3.3.2.1);
- Extraction from the raw values of the angles of the BSM or the position of the jiggle map and the chopper information. The BSM has a definite position, then move to another one. We have a start time and an end time for each position. The method to obtain this is simple: each couple (chopper angle, jiggle angle) is compared to each position of the Operation Calibration table with a tolerance. If it falls inside the rectangle defined by the tolerance, it is in this position.

The entire process is showed in Figure 3.15

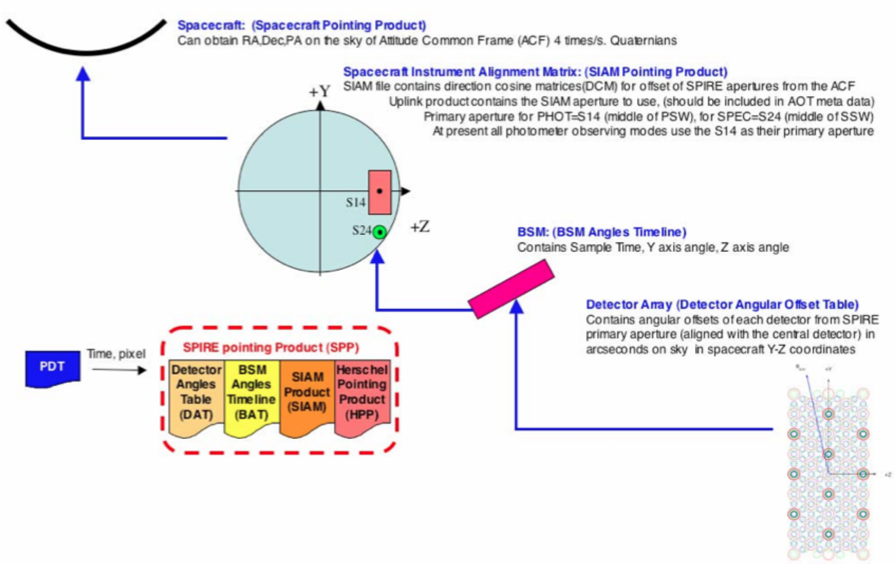

Figure 3.15: Steps to obtaining the absolute position on the sky for the timeline data for a given pixel.

3.3.2.10 Map-making

The map-making module of the pipeline contains 2 mappers for the scan mode:

Naive Mapper The Naive Mapper use an algorithm that combine the timelines using a direct coaddiction: i.e.. this technique performs no additional data-processing on the timelines. The data are simply re-mapped onto the image plane, by projecting the full power seen by a detector onto the nearest sky map pixel. For each bolometer timeline at each time step, the signal measurement is added to the total signal map, the square of the signal is added to the total signal squared map, and 1 is added into the coverage map. After all bolometer signals have been mapped, the total signal map is divided by the coverage map to produce a flux density map, and the standard deviations are calculated using the total signal, total signal squared, and coverage map.

MADmap Mapper MADmap Mapper use a maximum-likelihood estimate to combine the timelines derived from MadMap algorithm. MADmap is a maximum-likelihood based method of estimating a final sky map from the input data. It uses a 'brute- force' approach to solve the system of linear equations

$$d_t = A_{tp} s_p + n_t \tag{3.13}$$

where d_t is the time-ordered data (TOD) set $(t = 1..m)$, s_p is the pixelized map $(p = 1..n)$. A_{tp} is the m-by-n pointing matrix which projects the pixel domain onto the time domain. The noise vector n_t is a m-sample of random variables drawn from a multivariate Gaussian distribution of mean zero, not independent (because of the $1/f$ noise) but of finite correlation length and piecewise stationary.
The maximum likelihood estimate of the map is

$$s = (A^T N^{-1} A) A^T N^{-1} d \tag{3.14}$$

where $N =< nn^T >$ is the time-time noise covariance matrix, A is the pointing matrix, d is the TOD, and s is the map estimate.

These are the implemented mapper but it's possible use personal tools: e.g., the SPIRE HerMES team has designed and implemented a map-making pipeline, called *SPIRE-HerMES Iterative Mapper* (SHIM), because the implemented mapper are not optimal for SPIRE data due to the large number of detectors with correlated noise (Levenson et al. 2010). *SHIM* exploits the redundant observations of each point on the sky with multiple detectors in cross-linked scan directions to determine both the sky signal and the weighting of the data samples for binning into map pixels while simultaneously producing an accurate error map.The results show that *SHIM* reproduces both point source and diffuse extended emission with the highest possible fidelity for the most sensitive statistical analyses. A rigorous program of investigation into the noise properties of the *SHIM* maps, their relative and absolute astrometry, the map transfer function and low-level residual effects, shows that the HerMES SDP maps are reliable on scales from the beam diameter up to at least 1°.

The final product of the SPIRE Large/Small Map & Parallel pipelines are calibrated images maps for the 3 SPIRE bands and their associated error and weight maps. The Table 3.1 report the standard generated products in the Large/Small map observations.

Table 3.1: Standard generated products in Large/Small map observations.

Product Level	**Name**
Level 0	Raw Photometer Detector Timeline[a]
Level 0.5	Photometer Detector Timeline[b]
Level 1	Photometer Scan Product[c]
Level 2	Photometer Map Product[d]

[a] Raw data directly reformatted from telemetry
[b] Formatted voltage timelines
[c] Calibrated detector scan timelines in Jy in beam
[d] Image (error and coverage) maps in Jy in beam

3.4 The point source pipeline

The SPIRE Point Source data processing pipeline takes as input sets of 7-point Jiggle observations in the form of modulated timeline data. The standard processing pipeline for Point Source mode is shown below in Figure 3.16.

The pipeline processing from Level 0.5 to Level 1 corrects for electrical, detector and instrumental effects and in addition demodulates and De-Nods the data to remove asymmetric effects due to the telescope emission and optics produce calibrated estimations of the flux at each of the 7 Jiggle positions for all detectors in the array in Jy/beam (referred to as the Level 1 Averaged Pointed Photometer Product). A brief outline of the Level 0.5 to Level 1 pipeline module steps is given in the following pages.

The chopping/nodding principles are showed in Figure 3.17 (Griffin et al. 2008). The idea is the following: let S_{0R} and S_{0L} be the flux densities measured in the right and left beams for blank sky. Let S_{b1}, S_{b2} and S_{b3} be the sky background levels in the three positions, and let S_S be source flux density. The de-modulated chopped signal $(R-L)$ for nod position A is $S_A = (S_{0R}+S_{b1}+S_S)-(S_{0L}+S_{b1})$,whilst that for position B is $S_B = (S_{0R}+S_{b3})-(S_{0L}+S_{b2}-S_S)$. The difference (de-modulated nod signal) is this $S_A - S_B = 2S_S + (S_{b2} - S_{b1}) + (S_{b3} - S_{b2})$. Thus, if the sky background is uniform or varying linearly, it is removed. If there is a higher order variation in sky brightness, then it will not be completely subtracted.

Some artifacts corrections performed in this pipeline are the same performed in the Large/Small map pipeline, for this reason refer to those sections for details (Section 3.3.2.2 for the First Level Deglitching, Section 3.3.2.3 for the Removal Electrical Crosstalk, Section 3.3.2.5 for the Flux Conversion, Section 3.3.2.8 for the Remove Optical Crosstalk)

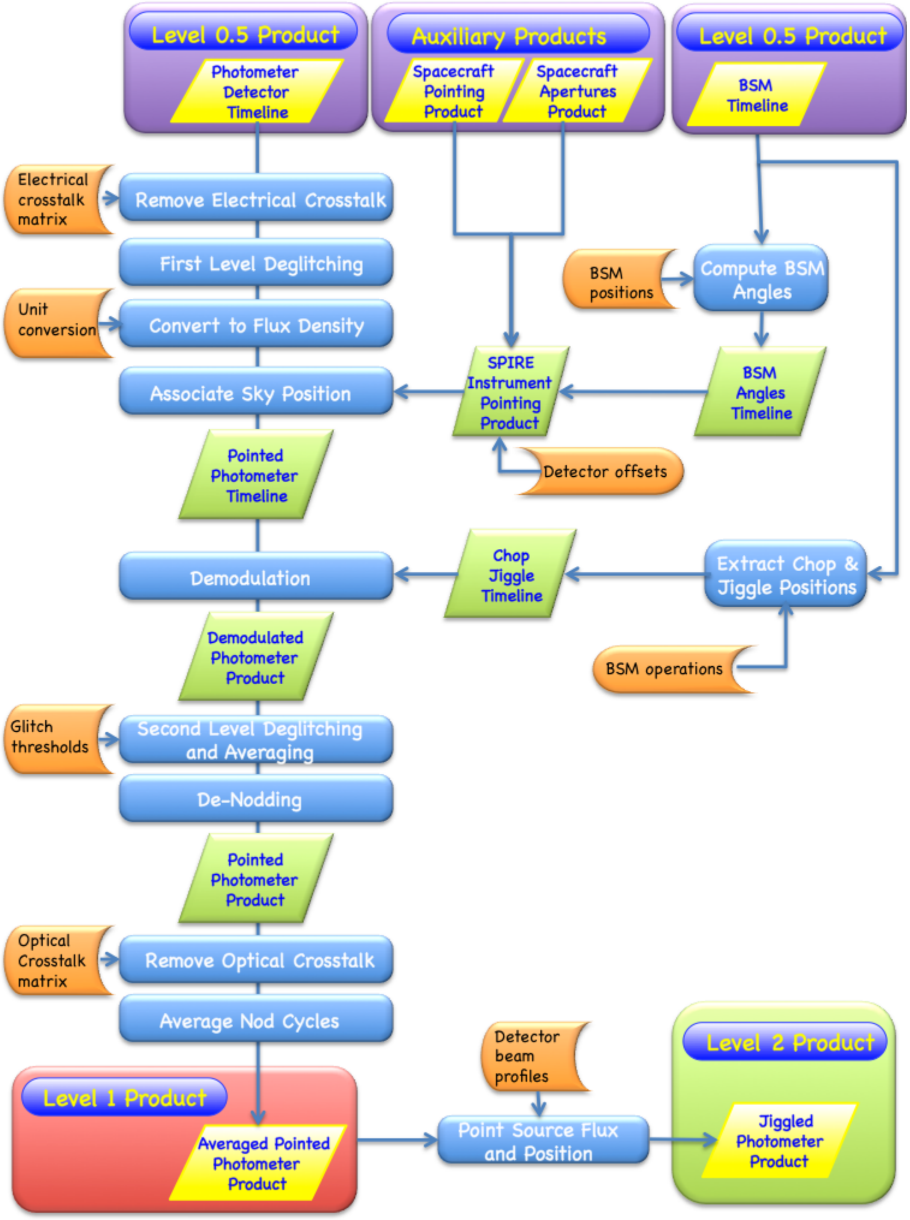

Figure 3.16: SPIRE Point Source pipeline flow. Data products delivered to the user are shown in yellow, intermediate data products in green. Processing steps are shown as light-blue boxes while calibration files are shown in orange(Spire Observers' Manual 2010).

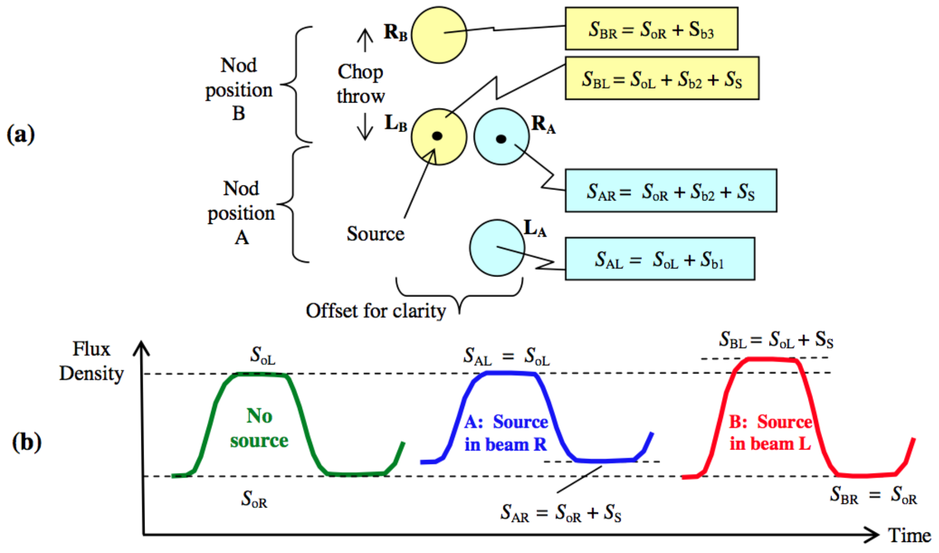

Figure 3.17: Flux density levels measured during chopping and nodding. (b) Example timelines for nod positions A and B (with the source in the right beam for position A), where for simplicity the sky background is taken to be uniform. (Griffin et al. 2008).

3.4.0.11 Demodulation

As drawn in Figure 3.17 , most of the difference between the chop positions is due to the asymmetric telescope background. In nod position A, the source decreases the magnitude of the difference and in nod position B it increases it. There is one point per chopper cycle per bolometer. The de-nod process merely takes the difference between the flux densities in the two nod positions to derive the first estimate of the source flux density and the demodulated flux densities for nod positions A and B are calculated as:

$$S_A = \bar{S}_{AR} - \bar{S}_{AL} \;\; and \;\; S_B = \bar{S}_{BR} - \bar{S}_{BL} \qquad (3.15)$$

where $\bar{S}$ is the average of data for the relevant half-cycle. For a given jiggle position with N_{chop} chop cycles, the output of this module is thus N_{chop} estimates of both S_A and S_B for each nod cycle: $S_{Aj,k}$ and $S_{Bj,k}$ where $j = 1 - N_{chop}$ and $k = 1 - N_{nod}$. Note that for most practical cases $N_{nod} = 1$ since the nominal jiggle map observation incorporates four nod cycles, each covering 16 different jiggle positions, so that there is only one nod cycle for a given jiggle position..

3.4.0.12 Second Level Deglitching and Averaging

For each nod cycle, the N_{chop} estimates of the demodulated flux densities in each of the two nod positions can be deglitched by rejecting outliers and averaging the remaining samples, to produce mean values and an associated uncertainty. The deglitching scheme employed here is a median clipping, operating as follows (note that this procedure requires a minimum of five data points, always available in the case of standard SPIRE AOTs):

- the median of the N_{chop} points is calculated;
- the standard deviation of the N_{chop} points is calculated, leaving out the highest and lowest values
- any points that are different from the median by more than a preset number of standard deviations (e.g., 3) are rejected;
- the process is repeated until no more outliers are identified or until there are not enough data points to continue.

The mean S and standard error ΔS of the deglitched data set can then be computed in the normal way. Note that if N_{chop} is small, then by chance the calculated uncertainty ΔS will occasionally be inappropriately small. A minimum uncertainty per bolometer, based on the average uncertainty over the observation or based on previous observations, could be defined but this is not baselined at present. For a given bolometer and jiggle position, the outputs of this module are, for each nod cycle, values of flux density and their associated uncertainties: $S_{A,k} \pm \Delta S_{A,k}$ and $S_{B,k} \pm \Delta S_{B,k}$.

3.4.0.13 DeNodding

The demodulated signal is de-nodded to remove any asymmetric contribution from the telescope by simply taking the difference between the flux densities at the 2 nod positions to derive the first estimation of the source flux. For each of the N_{nod} nod cycles, we have:

$$\begin{aligned} S_{S,k} &= \tfrac{1}{2}(\bar{S}_{A,k} - \bar{S}_{B,k}) \\ \Delta S_{S,k} &= \tfrac{1}{2}(\Delta S^2_{A,k} + \Delta S^2_{b,k})^{1/2} \end{aligned} \tag{3.16}$$

The final output of this module is a value of in-beam source flux density, S_S, with an associated statistical uncertainty for each jiggle position of each detector. If the sky background is uniform or varying linearly, it is also removed; but if there is a higher order variation in sky brightness, then it will not be completely subtracted.

Table 3.2: Data Products from the SPIRE Point Source Mode pipeline.

Product Level	**Name**
Level 0	Raw Photometer Detector Timeline[a]
Level 0.5	Photometer Detector Timeline[b]
Level 1	Averaged Pointed Photometer Product[c]
Level 2	Jiggled Photometer Product[d]

[a] Raw data directly reformatted from telemetry

[b] Formatted voltage timelines

[c] Calibrated flux for each detector at each individual jiggle position

[d] Fitted flux, error and position for the target

3.4.0.14 Average Nod Cycles

If $N_{nod} > 1$, then a weighted mean of the separate estimates of S_S is be calculated as the final value.

$$\bar{S}_S = \frac{\sum_{k=1}^{N_{nod}} \frac{S_{S,k}}{(\Delta S_{S,k})^2}}{\sum_{k=1}^{N_{nod}} (\frac{1}{\Delta S_{S,k}})^2} \qquad \Delta S_s = [\frac{1}{\sum_{k=1}^{N_{nod}} (\frac{1}{\Delta S_{S,k}})^2}]^{1/2} \tag{3.17}$$

The output from the Level 0.5 to Level 1 pipeline are calibrated, demodulated/denodded measurements of the sky (in Jy/beam) at each of the 7 Jiggle positions in the 7-point pattern for each detector in all arrays with associated errors and astrometry.

The Level 2 Product is produced by fitting a Gaussian profile to the measured signal over the 7-point Jiggle pattern, independently for both the signal and position. The final output of the pipeline (the Level 2 product) is the fitted flux, position and associated uncertainties for the source itself measured from the central co-aligned detectors on each array.

The Table 3.2 report the standard generated products in the Point Source mode observations.

3.5 Photometer flux calibration

The photometer pipeline produces monochromatic in-beam flux densities (Jy/beam) at standard frequencies corresponding to 250, 350 and 500 μm, and calculated under the assumptions of 1) a point source observation and 2) a flat νS_ν spectrum. The calibration is carried out at the level of Level-1 data products. SPIRE flux calibration for the photometer is based on Neptune (Moreno 2010) which has an estimated absolute uncertainty of 5%. The SPIRE calibration program also includes observations of Mars, asteroids, and stars to enable a consistent and reliable flux calibration to be developed over the course of the mission, and to ensure that cross calibration with PACS and HIFI, and with other facilities, is well established.

The SPIRE maps are calibrated in terms of in-beam flux density (Jy/beam) rather than surface brightness (Jy/pixel or /sr). The in-beam astronomical flux density at a given frequency, ν, is defined as:

$$S(\nu) = \oint_{4\pi} B(\theta,\phi) I_\nu(\theta,\phi) d\Omega \tag{3.18}$$

where $\theta \in [0,\pi]$ is a radial angular offset from the beam centre, $\phi \in [0,2\pi]$ is an azimuthal angular offset, $B(\theta,\phi)$ is the normalized beam profile, $I_\nu(\theta,\phi)$ is the sky intensity (surface brightness) profile, and $d\Omega$ is a solid angle element in the direction defined by (θ,ϕ). Note that we assume here that the beam profile can be regarded as uniform across the spectral passband.

As said, the photometer pipeline produced flux densities in terms of Jy/beam. For an extended sources which is uniformly bright over the beam area (solid angle), the surface brightness (Jy arcsec^{-2} or Jy sr^{-1}) can be obtained from the flux density by dividing it by the beam area. The beam area is:

$$A_{beam} = \oint_{4\pi} B(\theta,\phi) d\Omega \tag{3.19}$$

For a Gaussian beam profile with FWHM θ_{beam}, the beam area is given by

$$A_{beam} = \frac{\pi\theta_{beam}^2}{4ln(2)}. \tag{3.20}$$

However, the SPIRE beams exhibit departures from gaussianity at low levels due to the diffraction effects of the central obscuration and the secondary supports, and it is important to use the full beam area in the conversion.

3.5.1 Calibration accuracy

SPIRE photometer observations are subject to several kinds of uncertainty.

Absolute calibration uncertainty This component is associated with the knowledge of the brightness of the primary calibrator, Neptune, and is estimated at ±5%. It is correlated across the three bands, i.e., flux densities in the three bands will move up or down systematically in the event of this calibration being revised.

Relative calibration uncertainty This uncertainty arises from the process of comparing a source observation with Neptune (using the Neptune-derived voltage to flux density parameters that are implemented in the pipeline). This is a random contribution and has been estimated by careful analysis of repeated measurements of a bright source (actually Neptune itself). The results show that this component is less than 2% in all bands. At present, the overall calibration uncertainty for the SPIRE photometer, taking these two contributions into account, should be taken conservatively as ±7% (the direct rather than quadrature sum of the absolute and relative calibration uncertainties). It should be noted that this is dominated by the absolute component and is thus largely correlated across the three bands.

Photometric uncertainty This component is due to the source measurement errors. The photometer pipeline produces timelines representing the the in-beam flux density, and some random detector noise will be present in the timelines. Any astrometric errors will also introduce additional noise when timelines are combined in mapmaking. In addition, in order to derive estimates of, for example, the flux density of a point or compact source, users will need to employ some suitable fitting or aperture photometry technique, and additional uncertainties can be introduced due to confusion or source crowding. Except for bright sources in uncrowded regions, such photometric uncertainties will be significant or dominant. The assessment of these uncertainties depends on the sky brightness distribution and on the source extraction or background subtraction methods.

3.6 The spectrometer pipeline

The SPIRE Spectrometer data processing pipeline for both point source spectroscopy and mapping takes as input signal timeline data created by scanning the spectrometer mirror (SMEC) back and forth. The standard processing pipeline for Spectrometer mode is shown below in Figure 3.18 (see Spire Observers' Manual 2010 and Fulton et al. (2010)).

The spectrometer pipeline processing modules can be segregated into five fundamental operations, listed below:

- **Modify Timelines:** These processing modules perform time domain operations on the spectrometer detector timelines;

- **Create Interferograms:** This processing module merges the timelines of the spectrometer detectors and spectrometer mirror mechanism into interferograms;

- **Modify Interferograms:** These processing modules operate on the Spectrometer Detector Interferograms and differ from those in the ”Modify Timelines” group in that they are designed to act on spatial domain data rather than time domain data;

- **Transform Interferograms:** This processing module transforms the interferograms into a set of spectra;
- **Modify Spectra:** These processing modules perform operations on the spectrometer detector spectra.

3.6.0.1 Modify Timelines

First Level Deglitching & Remove Electrical Crosstalk Deglitching and removing of electrical crosstalk are performed following what just said about photometer pipeline(see Section 3.3.2.2 and Section 3.3.2.3 respectively).

Non-linearity Correction Changes in the responsivity of the detectors are corrected using a parameterized calibration table. Even though bolometric detectors are commonly fabricated with highly linear response characteristics, the detectors of the SPIRE spectrometer will be subject to a wide dynamic range which makes a non-linear response likely. The correction for the nonlinear bolometer responsivity applied to a spectrometer detector voltage timeline V is derived by integrating the function:

$$f(V) = K_1 + K_2/(V - K_3) \tag{3.21}$$

from V_0 to V, where the parameters V_0, K_1, K_2, and K_3 are given for each and every detector channel in a calibration product. The result is a voltage timeline Spectrometer Detector Timeline (SDT) where the voltage is directly proportional to the power incident on a detector.

Bath Temperature Correction To first order, bath temperature fluctuations will influence, coherently, all detectors in an array; the temperature and corresponding output voltages will vary in synchronism. The corrections applied are the same explained in Section 3.3.2.6.

Clipping Correction The 16-bit Analogue-to-Digital Converter (ADC) to read the detector voltages into SPIRE's on-board digital processing unit imposes a minimum (0) and maximum (65535) value to the detector ADU readings. The two extreme samples are flagged as truncated by the Check ADC Flags and Truncation module in Engineering Conversion Pipeline (see Section 3.3.1). The clipping correction module reconstructs those samples of the SDT which are flagged as truncated. Samples are reconstructed by using a polynomial fitting routine for each data range affected by truncation, see Figure 3.19.

Correct Time Domain Phase Some filtering effects are introduced by the read-out electronics and the thermal behavior of the bolometer detectors. The phase shift is characterized by comparing forward and reverse interferograms and a thermal detector-specific time constant τ is derived. The thermal time constants

Figure 3.18: SPIRE Spectrometer pipeline flow. Data products delivered to the user are shown in yellow, intermediate data products in green. Processing steps are shown as light-blue boxes while calibration files are shown in orange (Spire Observers' Manual 2010).

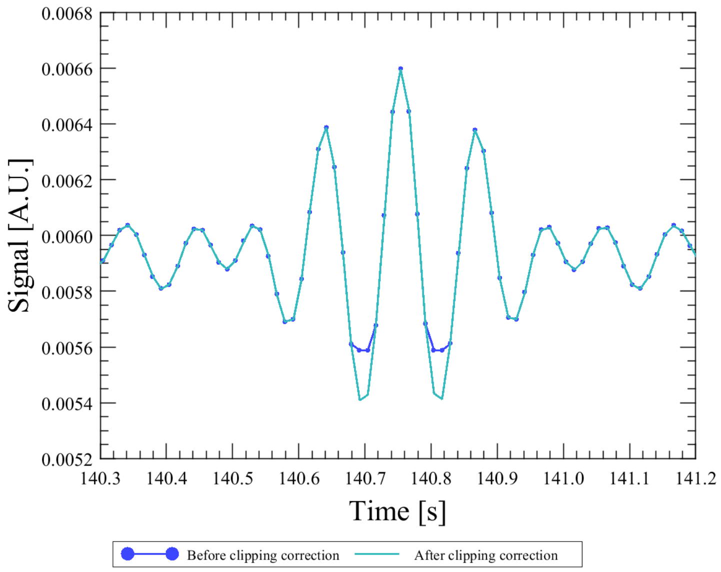

Figure 3.19: Detector Timeline before and after correcting for clipped data (Spire Observers' Manual 2010).

are retrieved from a calibration product and time domain phase correction functions are computed accordingly. The measured detector timelines are corrected by a convolution with the derived time domain phase correction function. The edges of the timelines, invalidated by the convolution operation are truncated. The process is illustrated in Figure 3.20

3.6.0.2 Create Interferograms

A single building block of a SPIRE spectrometer observation in scanning mode consists of a series of scans of the SMEC while the instrument is pointed at a given target. The sampling of the SPIRE spectrometer detectors and the spectrometer mechanism is not synchronized; the two subsystems are sampled at different rates and at different times. In order to derive the source spectrum from the measured data, the spectrometer detector samples must be linked with the position of the SMEC in the form of interferograms, i.e. signal as a function of Optical Path Difference (OPD). Additionally, the spectrometer detector signal timelines are interpolated onto timelines where the SMEC positions are equidistantly spaced to ensure accurate transformation of the interferogram with the Discrete Fourier Transform. First, the SMEC timeline is interpolated from one that is non-equidistant in position to one that is equidistant in position. Then, the detector signal timelines are interpolated onto the times which correspond to

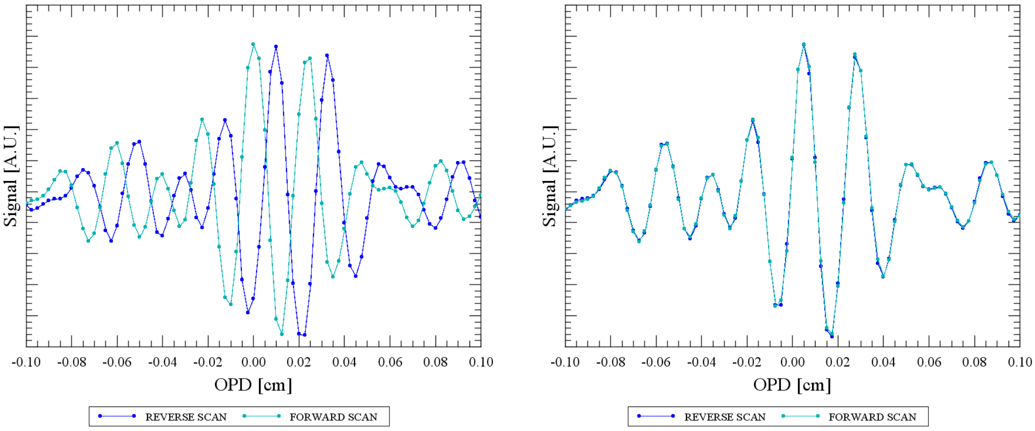

Figure 3.20: **Left:**Forward and reverse interferograms do not line up well without applying time domain phase correction. A forward (green) and a reverse (blue) scan are slightly shifted with respect to one another. **Right:**Forward (green) and reverse (blue) interferograms line up much better after applying time domain phase correction to the SDT (Spire Observers' Manual 2010).

the equidistant SMEC position grid. The mean value of the sky position during a given scan is assigned to the interferograms in the output Spectrometer Detector Interferogram (SDI) product.

3.6.0.3 Modify Interferograms

These processing steps operate on the Spectrometer Detector Interferograms and differ from those in the Section 3.6.0.1 group in that they are designed to act on spatial domain data rather than time domain data.

Baseline correction The intensity incident on the SPIRE spectrometer detectors can be separated into two components: a component that is constant as a function of OPD and a component that is modulated as a function of OPD. As the first baseline term does not contain relevant spectral information, it may be removed without affecting the source spectrum. Frequency components outside of the optical passband can also be removed from the second term. On a detector-by-detector and scan-by-scan basis, the baseline correction algorithm evaluates and removes the baseline of the interferogram. The baseline are defined by a polynomial fit or by the inverse Fourier transform of the spectrum including only low frequencies. The results are show in Figure 3.21.

Second Level Deglitching Repeated FTS measurements of the same astronomical source should not deviate from one another beyond random noise. This

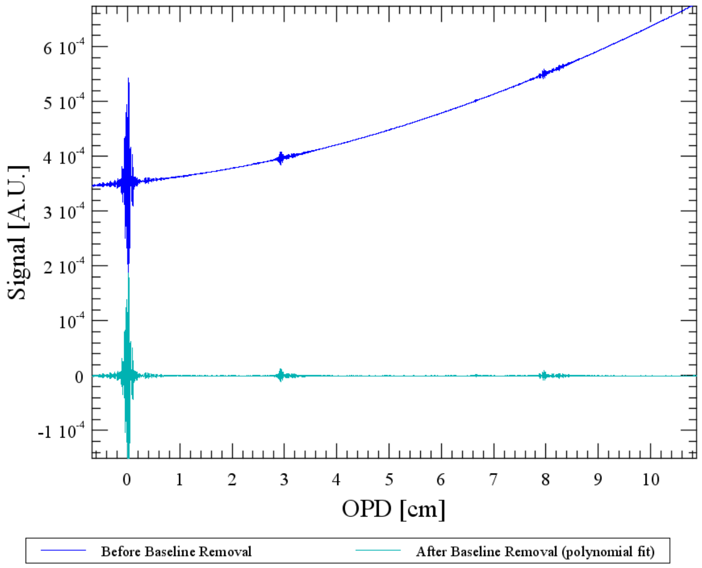

Figure 3.21: An example for removing the baseline with a 4th order polynomial fit to the interferogram. The interferogram before (blue) and after (green) baseline removal (Spire Observers' Manual 2010).

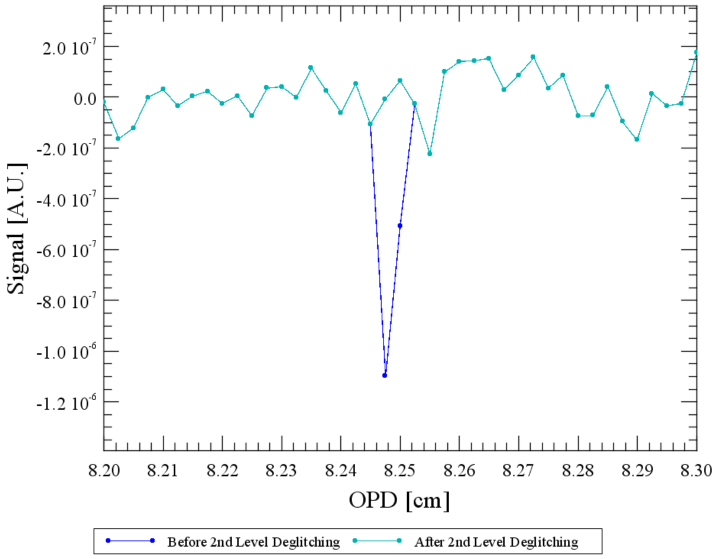

Figure 3.22: An example for glitch removal in an interferogram. An interferogram before (blue) and after glitch removal (green) (Spire Observers' Manual 2010).

principle is be used to identify and remove glitches without having to make any assumptions about the shape of the glitches. Glitches are identified for each spectrometer detector by comparing, on an OPD position by OPD position basis, the samples from one scan to those from all other scans in the same building block. In the pipeline two different methods are available to compare the data and flag outliers. The baseline approach is to use the median of the spectral data across scans and a threshold factor times the standard deviation or the median absolute deviation to define a range for outliers. The alternative approach uses a window of a user-defined length within which the standard deviation is computed and outliers are flagged based on a standard deviation or median absolute deviation. The scan with the largest absolute deviation will then be discarded and the procedure repeated until no further outliers are flagged. The flagged samples are then replaced by the average of the non-glitch samples from the other observed interferograms at that position (see Figure 3.22).

Phase Correction It's important correct the interferograms for asymmetry (non-zero phase) about Zero Optical Path Difference (ZPD). The symmetry of the optical layout of a Fourier transform spectrometer theoretically implies that the recorded interferograms also exhibit even symmetry. The Fourier transform of an evenly symmetric interferogram contains only real components. The presence of dispersive elements and imperfect time domain phase correction can result in an interferogram with signal samples that are not symmetric about ZPD. The resulting spectrum will contain both real and imaginary components and therefore a non-zero phase. The pipeline offers two different options to remove the phase:

- If the user supplies a calibration file with a characterization of the phase, then the task will only remove that calibrated phase without further inspection of other possibly existing asymmetries.

- If the user does not supply that calibration file, then the task will first characterize the phase of the measured interferogram and then remove the phase.

An example of this correction is showed in Figure 3.23.

Apodization the natural instrument line shape (ILS) for a Fourier Transform spectrometer is a cardinal sine, or *Sinc* function. If the source signal contains features at or near the resolution of the spectrometer, the ILS can introduce secondary maxima in the spectra. Using an apodization functions it's possible to reduce these secondary maxima at the cost of reducing the resolution of the resultant spectrum. The pipeline offers a number of apodizing functions that to allow for an optimal trade-off between reduction in the secondary maxima and reduced resolution. These are the apodization functions implemented in this module:

- **Gaussian**, "aGauss-19";

- **Hamming** [5], "aHM-15";
- **Hanning** [6], "aHN-17";
- ten adjusted **Norton Beer**[7] functions , "aNB-11" - "aNB-20" (aNB-15 is default)

The Figure 3.24 shows an example of the apodization functions and the results for the corrections.

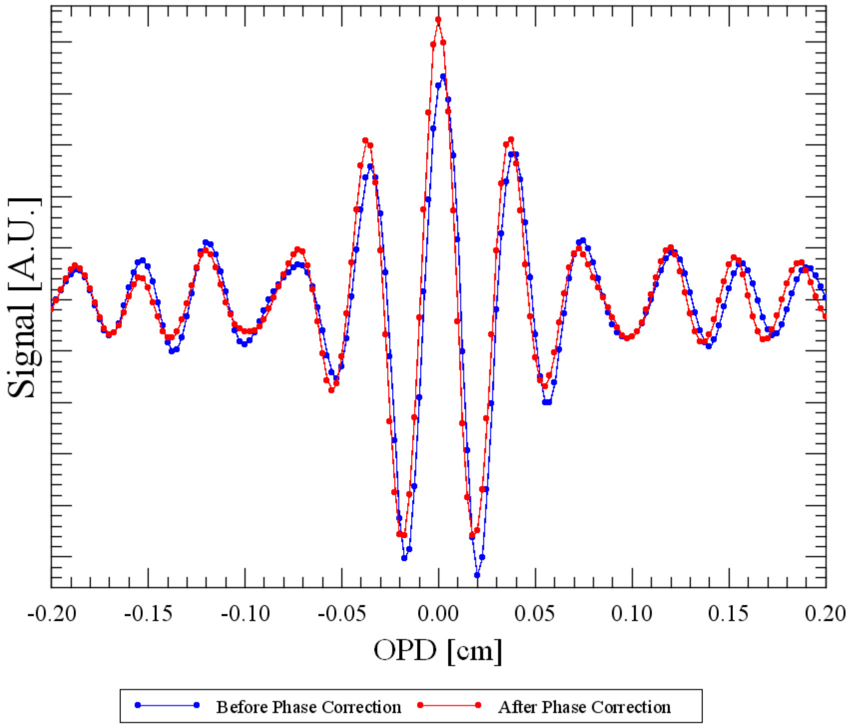

Figure 3.23: An example for phase-correction: The original interferogram (blue) shows a slight displacement from ZPD and asymmetries with respect to the center burst. Note how the first side-lobes at plus and minus 0.02 cm have different amplitudes. The phase-corrected interferogram (red) is well centered about ZPD and its first side-lobes have very similar amplitudes (Spire Observers' Manual 2010).

---

[5] `http://mathworld.wolfram.com/HammingFunction.html`

[6] `http://mathworld.wolfram.com/HanningFunction.html`

[7] Naylor & Tahic (2007)

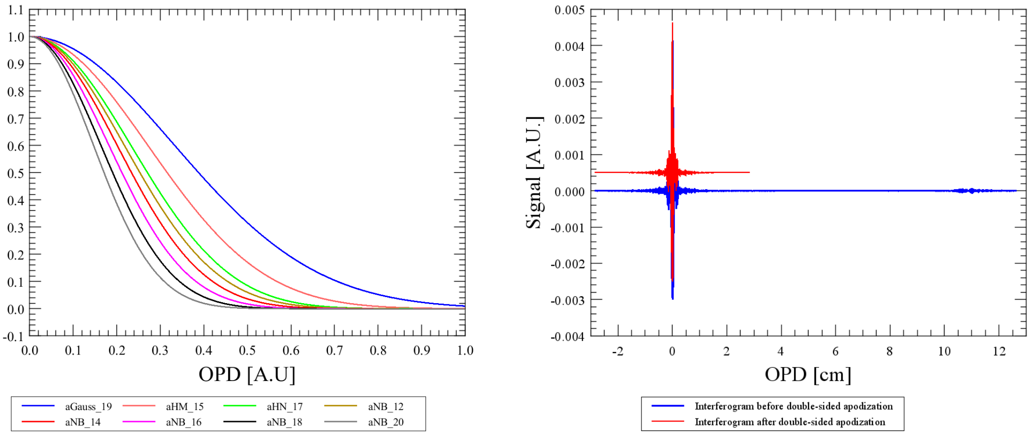

Figure 3.24: **Left:**A selection of the available apodizing functions. **Right:**An example for double-sided apodization: The original interferogram (blue) and the apodized interferogram (red), offset by 0.0005 for clarity. The apodizing function aNB-15 was used. (Spire Observers' Manual 2010).

3.6.0.4 Transform Interferograms

The set of interferograms from a SPIRE spectrometer observational building block must be transformed into a set of spectra both double-sided[8] and single-sided interferograms[9].

Double-sided Transform. For the double-sided transform, each interferogram in the SDI is examined and only the double-sided portion of the interferogram, where data are available between $-OPD_{max}$ and $+OPD_{max}$, is used to compute the resultant spectrum. The resultant spectra will contain both real and imaginary components.

Single-sided Transform. For the single-sided transform, only those interferogram samples to one side of the position of ZPD are considered. The spectra that result from the single-sided transform contain only real components as perfect even symmetry with respect to ZPD is assumed.

---

[8] The low and medium-resolution AOTs lead to double-sided interferograms. In these cases, each interferogram in the SDI is examined and the entire recorded interferogram is used to compute the resultant spectrum

[9] The high-resolution AOT leads to single-sided interferograms, whose samples are asymmetric with respect to the position of ZPD

3.6.0.5 Modify Spectra

Spectra average The spectra average process compute, on a wavenumber-by-wavenumber basis for each spectrometer detector, the average and the uncertainty of the spectral intensities across all scans. The average is calculated as the arithmetic mean of the spectral components. The uncertainty is calculated as the standard deviation of the spectral components. This allows to average all scans or to keep scans from different directions separate. The module rejects outliers by default. The data outside of the optical passband are removed by default in order to reduce data volume. The data product that results from this processing step will be made available to observers as a Level-1 Spectrometer Detector Spectrum (SDS) product.

Flux conversion The flux conversion perform the absolute flux calibration for the SPIRE spectrometer pipeline. Based on measurements of the telescope, an extended source flux calibration is applied. It can also be used to convert the flux calibration for extended sources to the flux calibration for point sources. The process is based on a characterization of the beam shape, and a deep measurement and detailed model of Uranus. The values in the Spectrometer Detector Spectrum (SDS) product are converted from Volts per cm^{-1} to Jy as a function of wavenumber.

Removal of optical crosstalk The procedure to remove optical crosstalk due to diffraction or aberrations in the optical system from the spectrometer detectors is functionally equivalent to that for the photometer detectors (see Section 3.3.2.8).

3.6.0.6 Conclusion

The Table 3.3 report the standard generated products in the spectrometer pipeline.

The output from the Level 0.5 to Level 1 pipeline are calibrated, spectra in units of Jy versus wavenumber in cm^{-1}. For a point source observation there will be a single spectrum for each detector (in addition to the Spectrometer Detector Interferogram Level 1 Product). For a spectrometer mapping observation, the Level 1 product corresponds to a detector spectrum for each detector at each position on the sky. The Level 2 Product consists of the Level 1 Product spectra interpolated onto a spectral data cube that is equidistantly sampled in the two spatial dimensions while leaving the grid along the spectral dimension unchanged. The final Level 2 Product is a 3-dimensional data structure for the signal with axes of Ra, Dec and wavenumber, referred to as a Spectral Simple Cube. This pipeline performs the same data processing steps for spectral maps as for point source observations. Data processing for spectral mapping adds a projection of the point spectra onto a Level-2 data product, a regularly gridded, spectral cube.

Table 3.3: Data Products from the SPIRE Spectrometer pipeline.

Product Level	**Name**
Level 0	Raw Photometer Detector Timeline[a]
Level 0.5	Spectrometer Detector Timeline[b]
Level 1a	Spectrometer Detector Interferogram[c]
Level 1b	Spectrometer Detector Spectrum[d]
Level 2	Spectral Simple Cube[e]

[a] Raw data directly reformatted from telemetry
[b] Formatted voltage timelines
[c] Processed interferograms for each scan
[d] Final calibrated spectrum for each detector
[e] Signal cube (RA, Dec, wavelength, signal)

The current projection algorithm employs a simple nearest neighbor interpolation which does not average the spectra within one map pixel but assigns the single spectrum closest to pixel centre. It also does not flag those map pixels where no single spectrum was observed within its footprint, but assigns the nearest neighbor (even if it is outside the pixel boundary).

3.7 Spectrometer flux calibration

The calibration of the spectrometer follows a different method to that adopted for the photometer. The FTS detector output is not a direct measurement of the flux density integrated over the passband as in the photometer, but depends on the Fourier components of the spectral content. The spectrometer bolometers receive radiation from the combination of the astronomical source, the telescope, and the instrument itself. It is therefore necessary to subtract the excess emission to recover the source spectrum. This is done using the following model:

$$Measure = R_{Source}B_{Source} + R_{Tel}B_{Tel} + R_{Inst}B_{Inst} \tag{3.22}$$

where R_{Source}, R_{Tel} and R_{Inst} are the Relative Spectral Response Functions (RSRF) applicable to the source, telescope and instrument contributions, and B_{Source}, B_{Tel} and B_{Inst} are the corresponding intensities (in the case of the instrument, B_{Inst} is due to the thermal emission from within the $\sim 5-$K Focal Plane Unit enclosure).

The emission from the telescope is determined using its emissivity (Fischer et al. 2004):

$$\varepsilon_{Tel} = 0.0336\lambda^{-0.5} + 0.273\lambda^{-1}, \tag{3.23}$$

where λ is the wavelength in μm. The final emission from the telescope, assuming that there is no stray light, and taking account of emission from both the primary and secondary mirrors, and reflection from the secondary, is taken to be

$$B_{Tel} = (1 - \varepsilon_{Tel})\varepsilon_{Tel}B(T_{M1}, \nu) + \varepsilon_{Tel}B(T_{M2}, \nu) \tag{3.24}$$

where $B(T, \nu)$ is the Planck function.

The temperatures of the telescope primary and secondary mirrors, T_{M1} and T_{M2}, are measured by thermistors on the spacecraft and are available as auxiliary products in the observation context.

4

The SPIRE Data Processing: Pipeline task and visualization tools

In this chapter I will report my work within SPIRE Instrument Control Center (ICC). I will briefly introduce how is structured the *Herschel* software, what are the main instruments for the users and what is the way to get the *Herschel* data. But, in particular I will describe the Graphical User Interface (GUI) developed to visualize the SPIRE data and the, so called, "tasks" used in the SPIRE pipeline. The GUI, contained in the *herschel.spire.ia.gui* package, are important tools to explore the data from level 0.5 to level 2, then to understand if the data are well processed etc. The "tasks" , contained in the *herschel.spire.ia.pipeline.common.util* package, are used in the SPIRE data processing pipeline.

4.1 The *Herschel* software

In the Chapter 3 I described the SPIRE data processing pipeline. I also introduced the definition of products and how they are created during the data reduction pipeline. To explain the importances of the SPIRE visualization tools, I need briefly describe, in the next sections, how we can get these products using Herschel Integrated Processing Environment (HIPE).

All the *Herschel* software was developed in Java language, one of the most popular programming languages. For the Interactive Analysis (IA) the language used is Jython[1]: it is an implementation of the high-level, dynamic, object-oriented language Python, which is already heavily used for scientific purposes. Jython is written entirely in Java, and seamlessly integrated with the Java platform. It thus allows you to combine the power of both Java and Python.

The choice of Java is due mainly to:

---

[1] `http://www.jython.org`

- much simpler language than C++ to write, understand and maintain;
- extensive standard class library, allowing considerable reuse of existing code;
- package mechanism, important for structuring complex applications;
- portable across many hardware platforms;
- excellent for networked and inter/intra-net applications;
- automatic generation of source code documentation;
- deprecation mechanism to cope with evolving interfaces.

All the software was developed by the HCSS and ICC Team: the HCSS consists of software for the *Herschel* Science Ground Segment (Commanding, Proposal handling, Mission Planning, etc), in addition to the DP system (that contains the software for Standard Product Generation (SPG), Quality Control Pipeline (QCP), Quick Look Analysis (QLA) and Interactive Analysis (IA)).
The main gateway to the DP is HIPE: I will describe it in Section 4.2.

The *Herschel* software is divided in module or package. All the software has a common repository: the Concurrent Version System (CVS) is used for version control of source code and other related files: this allows remote (and local) developers to check their source code in and out of the repository, using the 'pserver' mode of CVS. The *Herschel* CVS repository has the following directory:

- **/documents** The top level documents directory is for development of general documents that may not need to be included in the build, but the author would like to keep track of their work in CVS;
- **/develop/main** The "main" directory contains code that is part of the evolving HCSS system;
- **/develop/proto** The "proto" directory is provided so that developers can check in their own prototype code, if they wish, either to share it with other developers or simply as a means of backup. Code in the 'proto' directory may make use of classes in the 'main' tree, but not vice versa. Developers who wish to use the "proto" area should use Java package prefixes that follow the naming convention illustrated in the following examples: *herschel.proto.someproject*;
- **/develop/test** The "test" directory contains the test code, where all the test harness code should be committed. This is a directory structure that parallels the main structure, but allows developers to keep their test code separate from the main source code;

- **/develop/data** The “data” directory contains data used by the system, including mibdata, observingmodes etc;
- **/develop/user** The “user” directory is used as a personal repository by the users.

All Java packages that form part of the evolving HCSS system have the package prefix 'herschel' (e.g. *herschel.spire.ia.gui*)

All Java source files are contained in a directory tree that is isomorphic with the package tree. For example, *herschel.spire.ia.gui.DetectorTimelineExplorer.java* is in the directory herschel/spire/ia/gui in the develop/main tree.

Each package in the HCSS has an owner and a custodian, who is responsible for its development. This helps to ensure that the package maintains a coherent concept, which might not be the case if several developers tried to modify the same package. This principle applies to all packages, including those that only contain documentation. Each developer is responsible for the evolution of his packages. This includes keeping them in a consistent state, with up-to-date test harnesses and documentation, and making periodic releases of the packages.

When you need to make use of other subsystems or packages, the preferred way is to consult the JavaDoc documentation, rather than looking at the source code. The JavaDoc only shows public interfaces of the package that you are allowed to use.

Each package that contains code will have a test harness (this includes Java as well as Jython code). Where possible, these should provide a "go/no-go" indication, so that the system may be tested automatically as part of the build procedure. Packages should have a test harness that tests the package at the level of its public interfaces. Individual classes may also have test harnesses, which test their public interfaces and/or private classes and methods. It is often impossible or very difficult to literally test every single line of code. Some block for catching exceptions can be impossible to reach from a test, but most of them can be tested by reproducing the appropriate circumstance in the test. The package developer is responsible for running test harnesses before submitting a new release of a package. The developer may design and implement test harnesses, but the test cases should be subject to independent review. The test harnesses should cover both normal operation (e.g. derived from use-cases) and abnormal conditions. In general, a developer should try to write tests for 80% of his code (the coverage for *herschel.spire* is 86%).

Herschel uses JIRA[2] for tracking general issues, bugs in the code, and change requests for additional functionality. All work on DP software starts with an issue

---

[2] JIRA provides issue tracking and project tracking for software development teams to improve code quality and the speed of development (`http://www.atlassian.com/software/jira/`)

in JIRA; whether this is a request for completely new functionality, an extension of existing functionality, or bug or anomaly report. *Herschel* has configured JIRA with the following issue types:

SPR An SPR is a System Problem Report, and is raised when the code does not behave according to the requirements for the software. This includes errors in the documentation, as well as problems arising from design errors or coding errors.

SCR An SCR, System Change Request, should be used to request changes or additions to existing functionality.

action An action is a work item that does not require a code change. Actions are normally raised as part of an SPR or an SCR (a kind of sub-process).

The package developer is responsible also for all the documentation. The package documentation contains:

JavaDoc The JavaDoc documentation is the automatic documentation generate by Java.

User's Reference Manual: The User Reference Manual contains information about all the main tasks and classes that we can use within our scripts.

SPIRE Pipeline Design Document The SPIRE Pipeline Design Document describe the implementation of modules (an example of this is showed in Appendix C).

SPIRE Pipeline Test Plan The SPIRE Pipeline Test Plan Document describe the implementation of the test for the pipeline modules (an example of this is showed in Appendix D).

I'm member of SPIRE ICC and I'm owner of two packages:

herschel.spire.ia.gui This package contains some tools (GUI) to explore the data from level 0 to level 2.

herschel.spire.ia.pipeline.common.util This package contains some "task" used in the SPIRE data reduction pipeline.

4.2 HIPE, the *Herschel* Integrated Processing Environment

What it is HIPE? HIPE it is a graphical application which includes Jython scripting, data analysis, plotting, communication with the Herschel Science Archive (HSA) and much more.
HIPE provides an integrated suite of graphical interfaces that can interact with each other. It allows for interactively choosing your active data in your session, visualizing that data in various ways and selecting tools that can operate on the data: from raw data fresh off the HSA to publication-ready plots, all we need to get science out of our observations. HIPE is based on Java. The multi-platform nature of Java allows HIPE to work flawlessly under Window, Mac OS and many Linux and UNIX flavors. HIPE implement also Jython. Both Jython command-line and GUI are available. High-level interactions, which can involve GUIs, are also echoed as commands on the command-line that allow the saving of commands used in a session and the generation of scripts from these interactions. There are several good reasons why HIPE is the best choice for reducing *Herschel* data: it was especially developed to handle *Herschel* data types, it includes all the routines you need to go from off-the-satellite data format to publication-ready results, it's the best place to develop your own reduction routines, thanks to the Jython language and the wealth of available functions, it is a modern and actively developed application: this ensures fast help and resolution of problems. The HIPE "Welcome" screen is showed in Figure 4.1.

HIPE is based on *Perspective*: a perspective is a collection of related views. You can customize a perspective by adding, deleting and moving views. To save space, you can also rearrange different views as tabs of the same window.

The main perspectives are the:

- **The Product Browser perspective** The Product Browser perspective provides a way of getting and briefly viewing data from databases and data stores, both locally and remotely stored.

- **The *Herschel* Science Archive perspective** The *Herschel* Science Archive perspective provides a convenient means of querying and obtaining data from the HSA (see Section 4.2.1).

- **The Work Bench perspective** The Work Bench perspective provides many views for working with tasks, variables, scripts and command-line inputs. You can also navigate in your file system and check log messages and the command history.

Figure 4.1: HIPE Welcome perspective

You can modify a perspective by deleting and adding views, and by moving, resizing and rearranging existing views.

4.2.1 Get the data

How explained in Section 3.3, the smallest “piece” of SPIRE observational data is called a **Building Block**. Building Blocks and other Products are grouped into a context. A context is a special kind of product linking other products in a coherent description and can be thought of as an inventory or catalogue of products. The SPIRE processed observation consists of many such contexts within one giant Observation context.
These Observation contexts are accessed/downloaded and stored as a **Pool** of these products. A Pool is basically a directory that contains then the original raw data, the results of the automatic pipeline processing and everything you need to process your observations again yourself (e.g. spacecraft pointing, the parameters you entered in HSPOT when you submitted the proposal, and the pipeline calibration tables). Data that you reprocess yourself can also be stored into the same Pool or you may alternatively wish to save the results in a new Pool. If you wish to send someone a set of processed data for example, the entire Pool

directory should be archived and sent.

To get these data you can use the HSA perspective within HIPE or the HSA web portal[3]. To get the data you need to have an account. It's possible require an account at the same web page of the HSA: when you have an account you can get all the public data[4]. The HIPE HSA interface and the web interface are the same. All the observation are identified with a Observation ID. The Observing Log[5] reports all the *Herschel* observations information (Observation ID, observation day, proposal, AOT, etc.). Using this information is possible retrieve the data from the HSA. An example of query is showed in Figure 4.2.

After the query it's possible load the data directly in HIPE. But are the data well processed? To understand this, we need to explore these data. And for this reason we need tools that allow us to quickly understand the quality of these products. In particular, the level 0.5 and level 1 products consist of a large number of datasets that are difficult to explore. This dataset are in the form of timelines, as showed in Figure 4.3. I developed a GUIs to explore some of these timeline-type products: the PDT and SDT products. These tools are described in the following sections.

4.3 Detector Timeline Explorer

The Detector Timeline Explorer (DTE) is a GUI allowing a user-friendly view of SPIRE (both photometer and spectrometer) Timeline-type Products. DTE consist of three class but the kernel of the software is the DTEEngine class. This class is called by DetectorTimelineExplorer class (class used to launch DTE from HIPE command line) and from DetectorTimelineExplorerComponent (class used to launch DTE as explorer in HIPE). DTE is the default viewer within HIPE for the SPIRE Detector Timeline Product (both SDT and PDT). The documentation for these class is up to date and the test harness coverage is over 81%.

4.3.1 Starting DTE

DTE is an application that can be called from the HIPE. At least one instance of Timeline-type products must already be available in memory to launch DTE (e.g. output from pipeline script or product loaded from local store).

---

[3] `http://herschel.esac.esa.int/Science_Archive.shtml`

[4] All observations made in the first year of the routine phase will have proprietary times of 12 months, while for all observations made later, the proprietary time will be 6 months, with a simple 'bridging scheme' so that no observation will become public before observations that were executed earlier become public as well.

[5] `http://herschel.esac.esa.int/observing/LogReport.html`

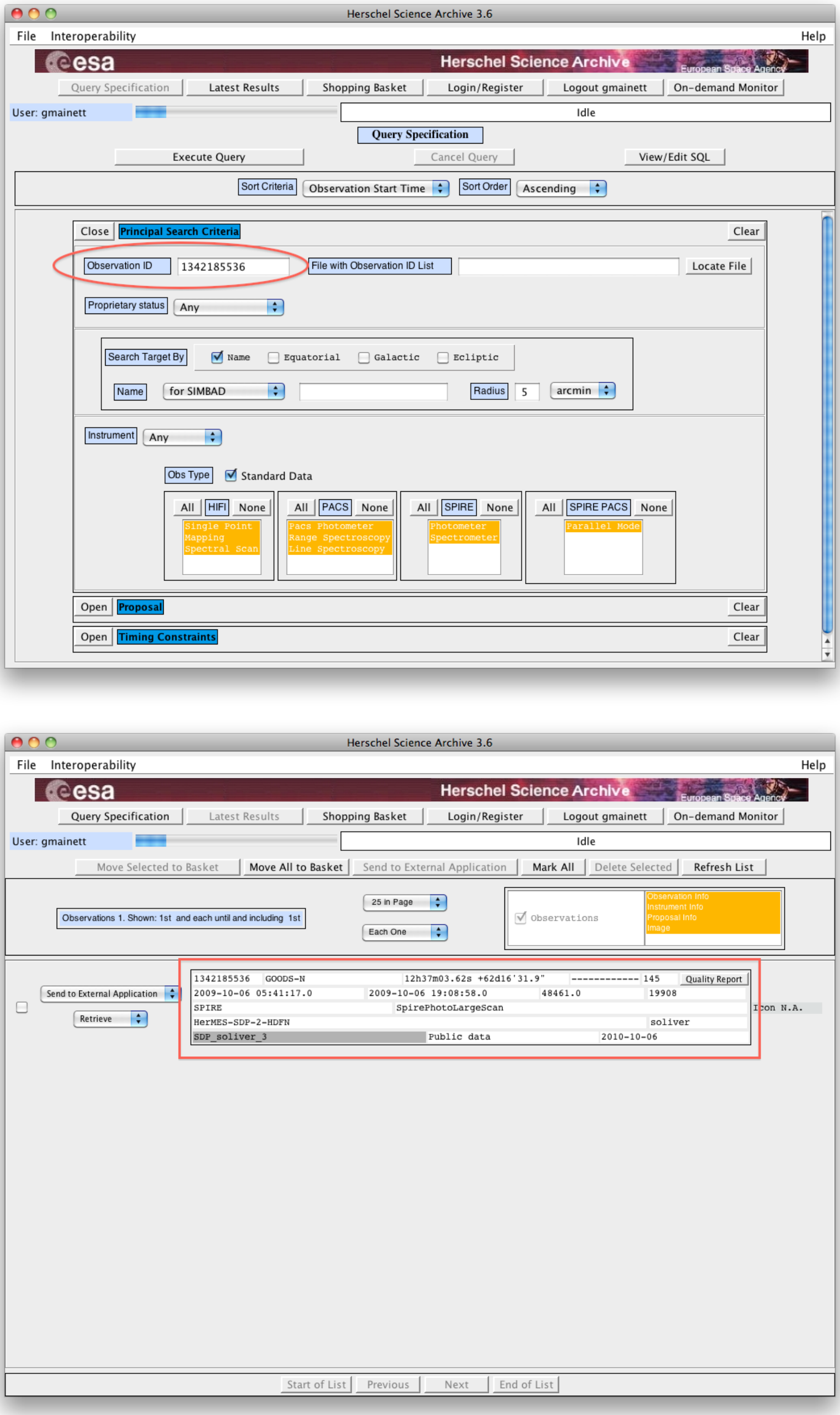

User: gmainett

Idle

Sort Criteria: Observation Start Time

Sort Order: Ascending

Observation ID: 1342185536

Proprietary status: Any

Search Target By: ☑ Name ☐ Equatorial ☐ Galactic ☐ Ecliptic

Name: for SIMBAD

Radius: 5 arcmin

Instrument: Any

Obs Type: ☑ Standard Data

User: gmainett

Idle

Observations 1. Shown: 1st and each until and including 1st

25 in Page

Each One

☑ Observations

☐ Send to External Application

```
1342185536  GOODS-N          12h37m03.62s +62d16'31.9"   ------------ 145
2009-10-06 05:41:17.0    2009-10-06 19:08:58.0     48461.0      19908
SPIRE                    SpirePhotoLargeScan
HerMES-SDP-2-HDFN                                               soliver
SDP_soliver_3                    Public data              2010-10-06
```

Figure 4.2: The HSA perspective. **Top:** the query interface. In this example I want get the observation id 1342185536, an observation of GOODS-N field performed in SDP **Bottom:** the results of the query: all the main information are reported and now I can save the data in many ways.

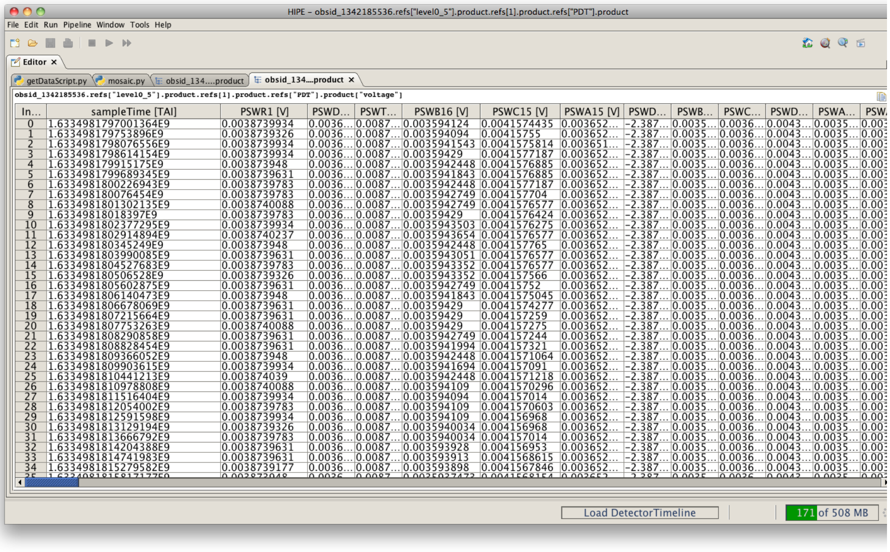

HIPE – obsid_1342185536.refs["level0_5"].product.refs[1].product.refs["PDT"].product

obsid_1342185536.refs["level0_5"].product.refs[1].product.refs["PDT"].product["voltage"]

In...	sampleTime [TAI]	PSWR1 [V]	PSWD...	PSWT...	PSWB16 [V]	PSWC15 [V]	PSWA15 [V]	PSWD...	PSWB...	PSWC...	PSWD...	PSWA...	PSW
0	1.6334981797001364E9	0.0038739934	0.0036...	0.0087...	0.003594124	0.0041574435	0.003652...	-2.387...	0.0035...	0.0036...	0.0043...	0.0035...	0.00
1	1.633498179753896E9	0.0038739326	0.0036...	0.0087...	0.003594094	0.00415755	0.003652...	-2.387...	0.0035...	0.0036...	0.0043...	0.0035...	0.00
2	1.6334981798076556E9	0.0038739934	0.0036...	0.0087...	0.0035941543	0.0041575814	0.003651...	-2.387...	0.0035...	0.0036...	0.0043...	0.0035...	0.00
3	1.6334981798614154E9	0.0038739934	0.0036...	0.0087...	0.00359429	0.0041577187	0.003652...	-2.387...	0.0035...	0.0036...	0.0043...	0.0035...	0.00
4	1.633498179915175E9	0.003873948	0.0036...	0.0087...	0.0035942448	0.0041576885	0.003652...	-2.387...	0.0035...	0.0036...	0.0043...	0.0035...	0.00
5	1.6334981799689345E9	0.0038739631	0.0036...	0.0087...	0.0035941843	0.0041576885	0.003652...	-2.387...	0.0035...	0.0036...	0.0043...	0.0035...	0.00
6	1.6334981800226943E9	0.0038739783	0.0036...	0.0087...	0.0035942448	0.0041577187	0.003652...	-2.387...	0.0035...	0.0036...	0.0043...	0.0035...	0.00
7	1.633498180076454E9	0.0038739783	0.0036...	0.0087...	0.0035942749	0.004157704	0.003652...	-2.387...	0.0035...	0.0036...	0.0043...	0.0035...	0.00
8	1.6334981801302135E9	0.0038740088	0.0036...	0.0087...	0.0035942749	0.0041576577	0.003652...	-2.387...	0.0035...	0.0036...	0.0043...	0.0035...	0.00
9	1.63349818018397E9	0.0038739783	0.0036...	0.0087...	0.00359429	0.0041576424	0.003652...	-2.387...	0.0035...	0.0036...	0.0043...	0.0035...	0.00
10	1.6334981802377295E9	0.0038739934	0.0036...	0.0087...	0.0035943503	0.0041576275	0.003652...	-2.387...	0.0035...	0.0036...	0.0043...	0.0035...	0.00
11	1.6334981802914894E9	0.0038740237	0.0036...	0.0087...	0.0035943654	0.0041576577	0.003652...	-2.387...	0.0035...	0.0036...	0.0043...	0.0035...	0.00
12	1.633498180345249E9	0.003873948	0.0036...	0.0087...	0.0035942448	0.004157765	0.003652...	-2.387...	0.0035...	0.0036...	0.0043...	0.0035...	0.00
13	1.6334981803990085E9	0.0038739631	0.0036...	0.0087...	0.0035943051	0.0041576577	0.003652...	-2.387...	0.0035...	0.0036...	0.0043...	0.0035...	0.00
14	1.6334981804527683E9	0.0038739783	0.0036...	0.0087...	0.0035943352	0.0041576577	0.003652...	-2.387...	0.0035...	0.0036...	0.0043...	0.0035...	0.00
15	1.633498180506528E9	0.0038739326	0.0036...	0.0087...	0.0035943352	0.004157566	0.003652...	-2.387...	0.0035...	0.0036...	0.0043...	0.0035...	0.00
16	1.6334981805602875E9	0.0038739631	0.0036...	0.0087...	0.0035942749	0.00415752	0.003652...	-2.387...	0.0035...	0.0036...	0.0043...	0.0035...	0.00
17	1.6334981806140473E9	0.003873948	0.0036...	0.0087...	0.0035941843	0.0041575045	0.003652...	-2.387...	0.0035...	0.0036...	0.0043...	0.0035...	0.00
18	1.6334981806678069E9	0.0038739631	0.0036...	0.0087...	0.00359429	0.0041574277	0.003652...	-2.387...	0.0035...	0.0036...	0.0043...	0.0035...	0.00
19	1.6334981807215664E9	0.0038739631	0.0036...	0.0087...	0.00359429	0.004157259	0.003652...	-2.387...	0.0035...	0.0036...	0.0043...	0.0035...	0.00
20	1.6334981807753263E9	0.0038740088	0.0036...	0.0087...	0.00359429	0.004157275	0.003652...	-2.387...	0.0035...	0.0036...	0.0043...	0.0035...	0.00
21	1.6334981808290858E9	0.0038739631	0.0036...	0.0087...	0.0035942749	0.004157244	0.003652...	-2.387...	0.0035...	0.0036...	0.0043...	0.0035...	0.00
22	1.6334981808828454E9	0.0038739631	0.0036...	0.0087...	0.0035941994	0.004157321	0.003652...	-2.387...	0.0035...	0.0036...	0.0043...	0.0035...	0.00
23	1.6334981809366052E9	0.003873948	0.0036...	0.0087...	0.0035942448	0.0041571064	0.003652...	-2.387...	0.0035...	0.0036...	0.0043...	0.0035...	0.00
24	1.6334981809903615E9	0.0038739934	0.0036...	0.0087...	0.0035941694	0.004157091	0.003652...	-2.387...	0.0035...	0.0036...	0.0043...	0.0035...	0.00
25	1.6334981810441213E9	0.003874039	0.0036...	0.0087...	0.0035942448	0.0041571218	0.003652...	-2.387...	0.0035...	0.0036...	0.0043...	0.0035...	0.00
26	1.6334981810978808E9	0.0038740088	0.0036...	0.0087...	0.003594109	0.0041570296	0.003652...	-2.387...	0.0035...	0.0036...	0.0043...	0.0035...	0.00
27	1.6334981811516404E9	0.0038739934	0.0036...	0.0087...	0.003594094	0.004157014	0.003652...	-2.387...	0.0035...	0.0036...	0.0043...	0.0035...	0.00
28	1.6334981812054002E9	0.0038739783	0.0036...	0.0087...	0.003594109	0.0041570603	0.003652...	-2.387...	0.0035...	0.0036...	0.0043...	0.0035...	0.00
29	1.6334981812591598E9	0.0038739934	0.0036...	0.0087...	0.003594109	0.004156968	0.003652...	-2.387...	0.0035...	0.0036...	0.0043...	0.0035...	0.00
30	1.6334981813129194E9	0.0038739326	0.0036...	0.0087...	0.0035940034	0.004156968	0.003652...	-2.387...	0.0035...	0.0036...	0.0043...	0.0035...	0.00
31	1.6334981813666792E9	0.0038739783	0.0036...	0.0087...	0.0035940034	0.004157014	0.003652...	-2.387...	0.0035...	0.0036...	0.0043...	0.0035...	0.00
32	1.6334981814204388E9	0.0038739631	0.0036...	0.0087...	0.003593928	0.004156953	0.003652...	-2.387...	0.0035...	0.0036...	0.0043...	0.0035...	0.00
33	1.6334981814741983E9	0.0038739631	0.0036...	0.0087...	0.003593913	0.0041568615	0.003652...	-2.387...	0.0035...	0.0036...	0.0043...	0.0035...	0.00
34	1.6334981815279582E9	0.0038739177	0.0036...	0.0087...	0.003593898	0.0041567846	0.003652...	-2.387...	0.0035...	0.0036...	0.0043...	0.0035...	0.00

Figure 4.3: The contents of a PDT product: any column report the signal voltage registered by a single detector. The first column report the time.

To launch DTE in HIPE: identify the product for visualization from Variables list and right-click the timeline-type product, follow the "Open With" menu entry and select Detector Timeline Viewer from the drop-down menu (Figure 4.4).

DTE can also be called from the HIPE command line:

```
from herschel.spire.ia.gui import DetectorTimelineExplorer
dte=DetectorTimelineExplorer()
p=dte.createFrame(yourProduct)
```

The DTE was originally develop for DatasetInspector, a old environment for SPIRE data analysis.

4.3.2 DTE Layout

The Display Panel is divided in three section (see Figure 4.5):

LEFT - Array Display This area is used to display the arrays of bolometers (three arrays for photometer, two for spectrometer).

RIGHT - Quick View This area is used to display the plot.

BOTTOM - Control Panel This section contains menu to select the array and the type of sub-products that you want view. In this area we have also the

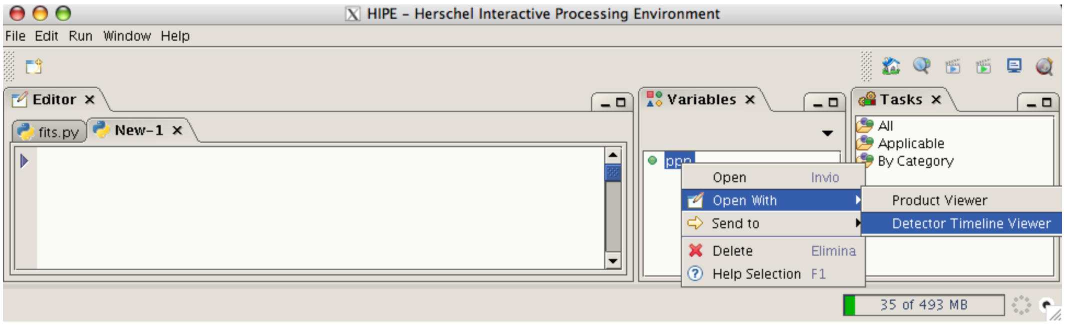

Figure 4.4: Starting DTE via HIPE.

slider and play-stop button for browsing trough time across the timeline and we can select color scheme, time scale, etc.

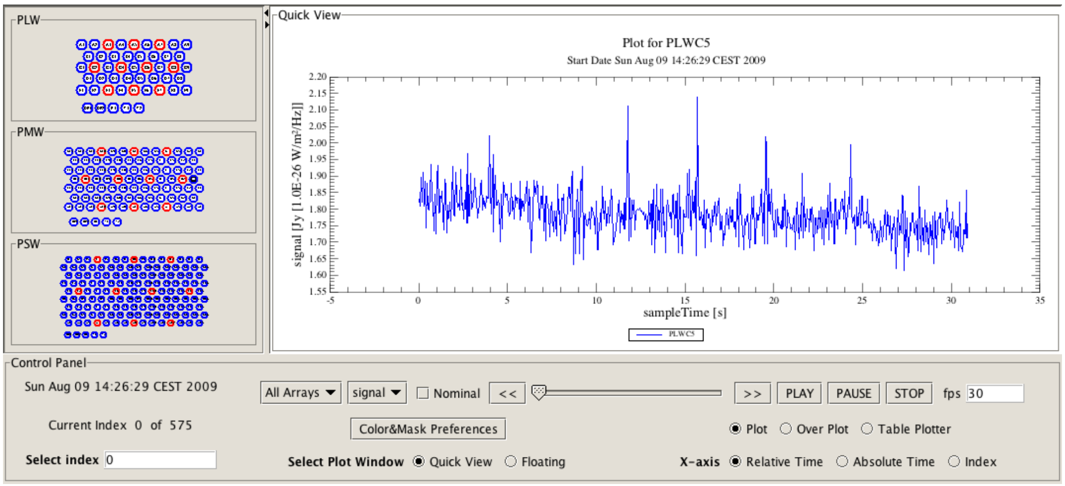

Sun Aug 09 14:26:29 CEST 2009

Current Index 0 of 575

Select index 0

☐ Nominal

fps 30

● Plot ○ Over Plot ○ Table Plotter

Select Plot Window ● Quick View ○ Floating

X-axis ● Relative Time ○ Absolute Time ○ Index

Figure 4.5: DTE Layout.

4.3.3 Array Display

Array Display area shows the bolometer's arrays (Figure 4.6), Control Panel contains drop-down menu to select if visualize all the arrays or only one (Figure 4.10). The implemented color scheme for bolometer's arrays are two (heat and grey) and we can select which to use into "Color&Mask Preferences" Panel (Section 4.3.6). The value for both color scheme are based upon intensity at current index of the channel. The co-alligned detectors are displayed with a red border.

It is possible visualize only the nominal bolometers (i.e. the bolometers that see the sky and not the bolometers that measure the performance of the instrument) selecting the "Nominal" checkbox in the Control Panel (Section 4.3.5). The value registered by the bolometer is showed via tooltip when the mouse is placed over.

DTE implement some plotting function, in particular it is possible plot a timeline with a single click on desired detector but it is also possible to use DTE to plot data recorded by many detectors during one observation on a single page to compare data more effectively (“mosaic plot”). The plots are arranged in the same pattern as the detectors are presented in the Bolometer Detector Array display, a honeycomb pattern. The mosaic plot is available via right-click on the desired array and selecting "Create Mosaic" (see Figure 4.7) from contextual menu. This functionality is obtained using Detector Timeline Mosaic (DTM) class, see Section 4.5.

4.3.4 Quick View Area

"Quick View" area is used to visualize the plots (Figure 4.8).

When DTE start, the “Quick View” area is filled with a plot: an array’s central detector is plotted, otherwise, if no one central detector is good (e.g. the channel is missing), the first valid detector is plotted. We can visualize the plot not only in the Quick View area but also in a new floating window (see Section 4.3.5). When the “floating windows” method is selected, each plot creates a new window (Figure 4.8) and erases the "Quick View" area.

Using “Quick View” area we can also create over-plot (see Section 4.3.5.1) and visualize the data with Table Plotter (an external tool developed by IPAC Team, see Section 4.3.5.2). All plot properties (axis scale, title, label, etc.) are accessible via simple right-click over the selected plot.

4.3.5 Control Panel

Via “Control Panel” we can change/select/modify the data visualization. It contains (Figure 4.9):

- Data of the observation;
- "Current Index" label that shows row/readout number;
- "Select Index" writable field allowing to choose the row/readout number. A warning message appears if selected index is out of range;
- Drop-down menu to select the array and the dataset (Figure 4.10);

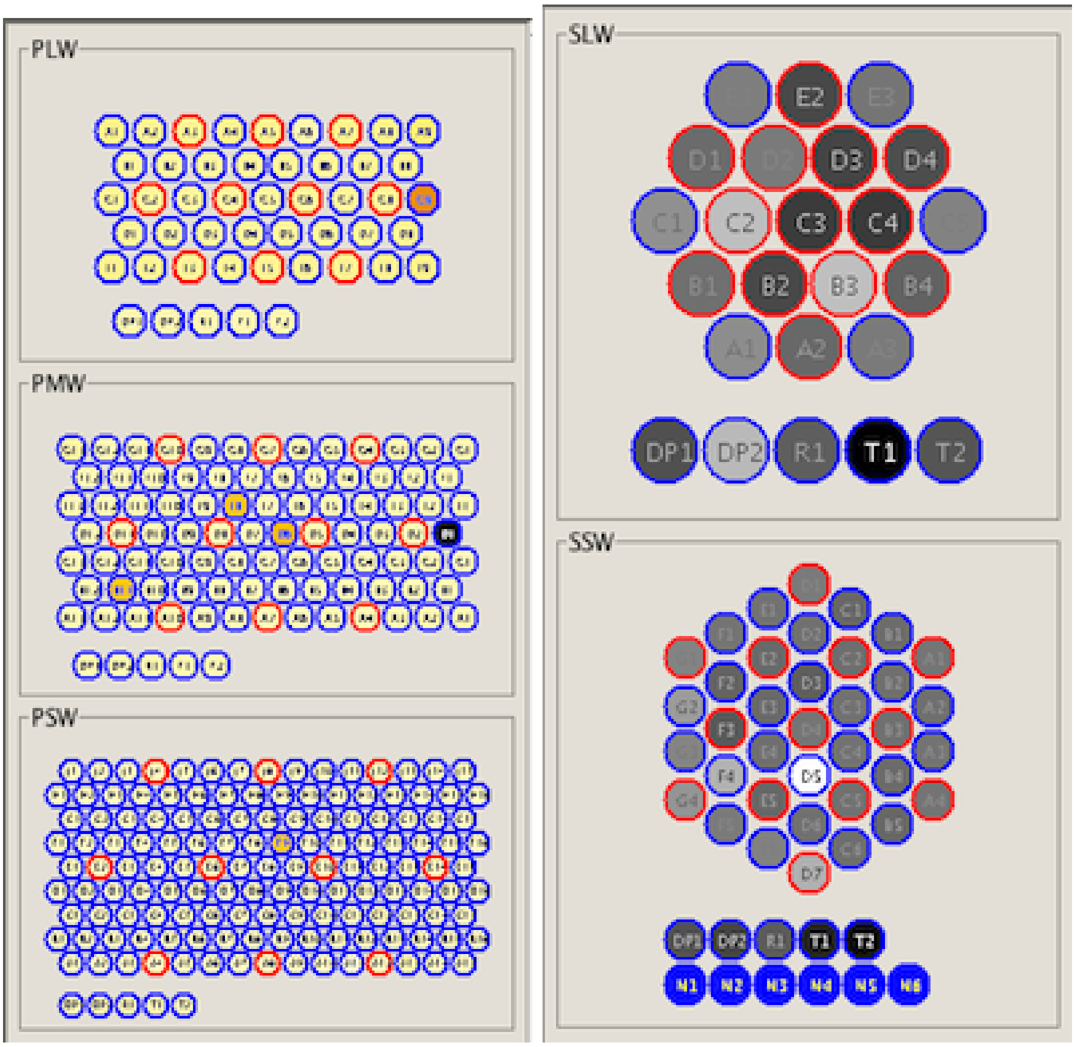

Figure 4.6: Array Display: on the left the visualization for the photometer using the "heat" color scheme, on the right for the spectrometer using the "gray" color scheme.

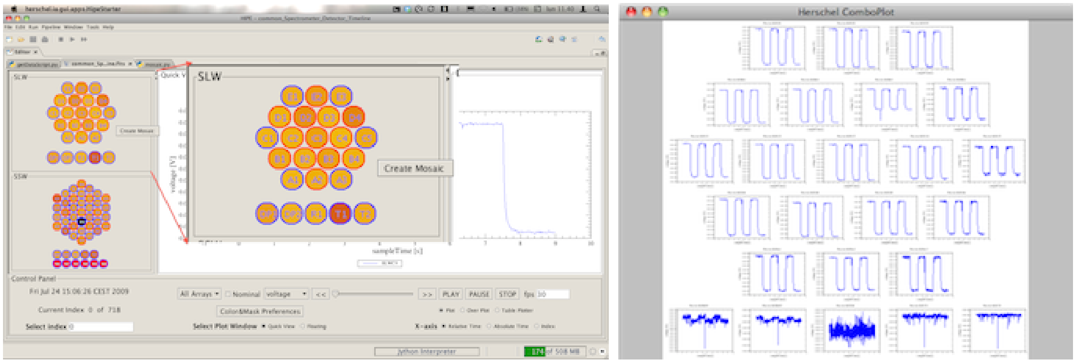

Figure 4.7: Mosaic Plot in DTE **Left:** how to create a mosaic plot with a simple right-click on the desired array. **Right:** the mosaic plot.

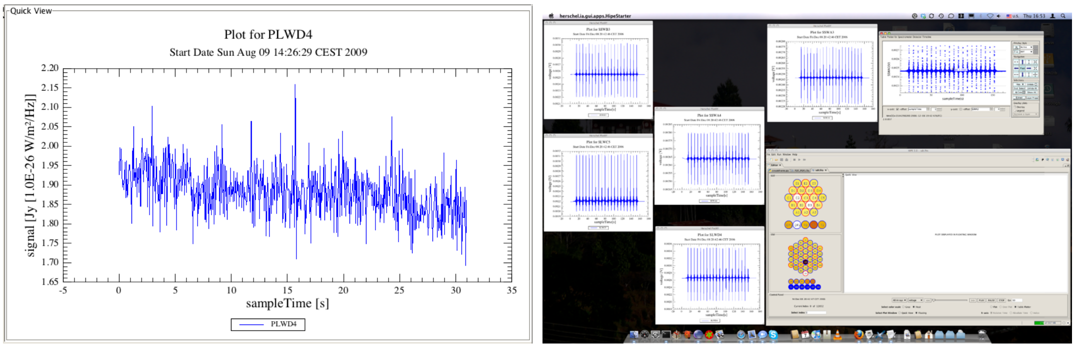

Figure 4.8: Plot visualized in the "Quick View Area" (left) and in the floating windows (right).

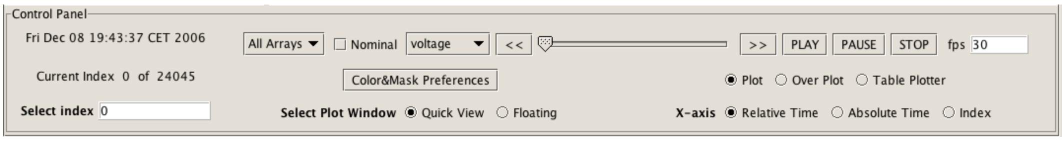
Control Panel

Fri Dec 08 19:43:37 CET 2006

Current Index 0 of 24045

Select index 0

All Arrays ☐ Nominal voltage

fps 30

● Plot ○ Over Plot ○ Table Plotter

Select Plot Window ● Quick View ○ Floating

X-axis ● Relative Time ○ Absolute Time ○ Index

Figure 4.9: Control Panel.

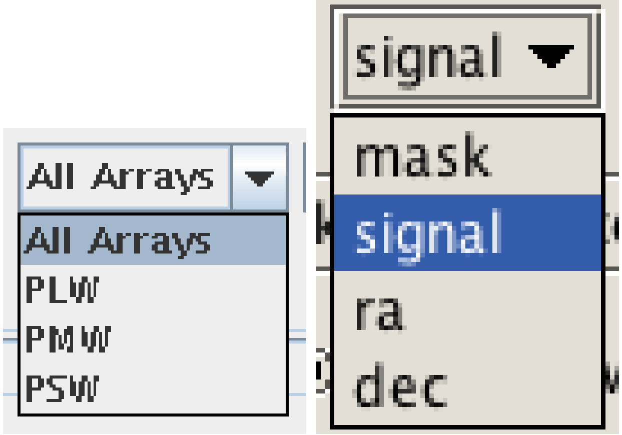

Figure 4.10: Drop-down menu to select the array (on the left) and the dataset (on the right).

- "Nominal" checkbox to visualize only the nominal bolometers;
- "Color&Mask preferences" button to open the preferences panel for color and mask (Section 4.3.6);
- "Select Plot Window" radio-buttons to select the plotting area (“Quick View” area or new floating window).
- A slider and play/stop button for browsing trough time across the timeline (Figure 4.11). We can also choose the speed for the browsing via the frame per second (fps) text box;

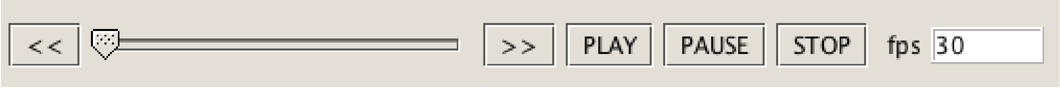

fps 30

Figure 4.11: Slider for browsing trough time across the timeline.

- Three radiobuttons ("Plot", "Over Plot" and "Table Plotter") that allow creation of plot, overplot (see Figure 4.12 and Section 4.3.5.1) or data visualization using Table Plotter (see Figure 4.12 and Section 4.3.5.2). When "Over Plot" checkbox is selected, the plot is always create into QuickView area and "Floating" button (to display the plot in a floating window) is disabled.

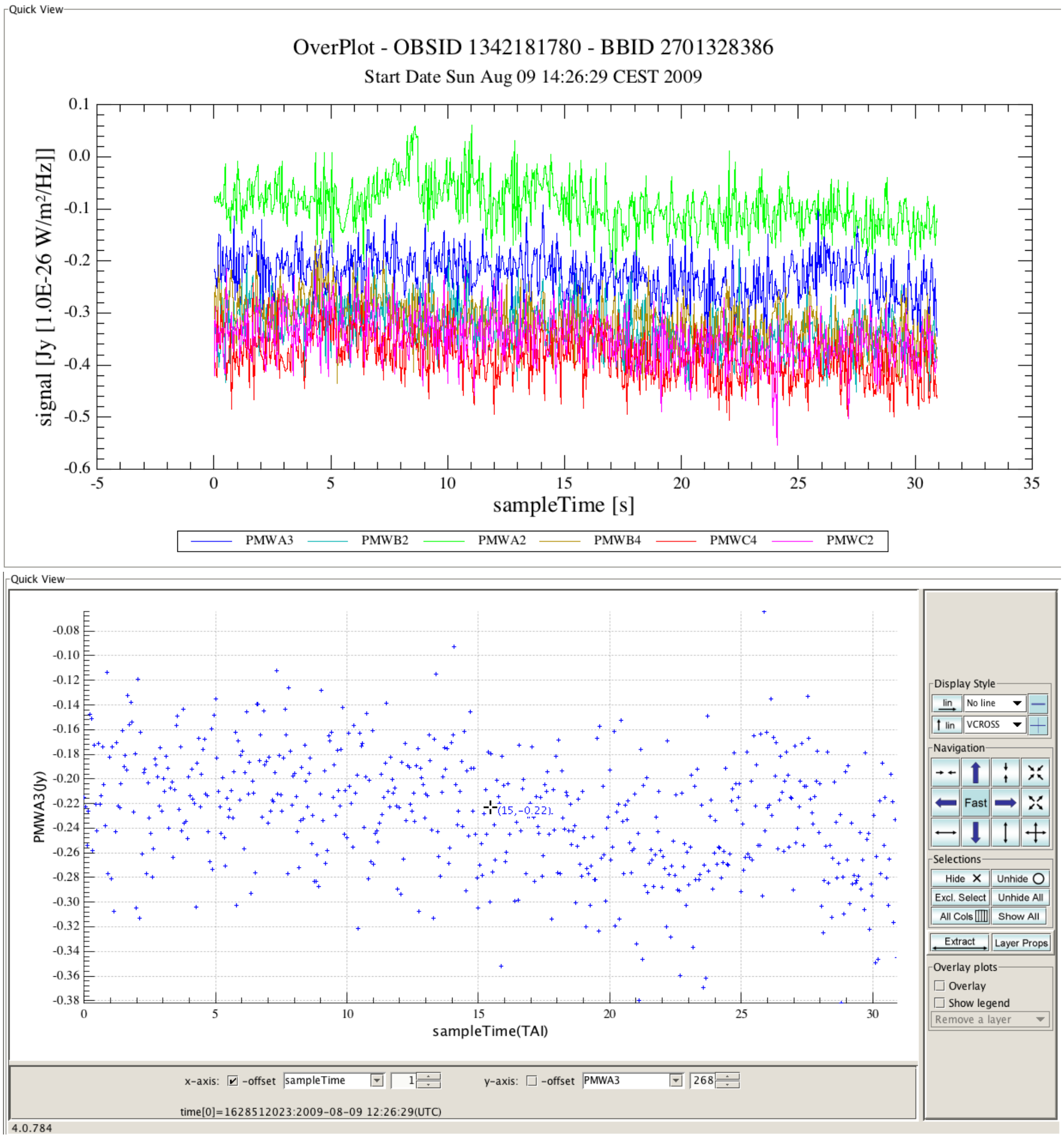

x-axis: ☑ -offset sampleTime 1 y-axis: ☐ -offset PMWA3 268

time[0]=1628512023:2009-08-09 12:26:29(UTC)

Figure 4.12: Plot Visualization: Over Plot (top) and Table Plotter (bottom).

4.3.5.1 Overplot

To enable over-plotting we need check the "Over Plot" radio-button within Control Panel area (Section 4.3.5). Over-plotting is allowed only within "Quick View" area. When floating plot window is selected and we check "Over Plot" checkbox, a info-window shows this message: "Over-plotting not allowed in floating windows" and the last plot is redraw within "Quick View" area. During over-plotting is not possible change "X axis" scale.

4.3.5.2 Table Plotter

To visualize the data with Table Plotter we need check the "Table Plotter" radio-button within Control Panel area (Section 4.3.5). When TablePlotter radio-button is selected, we can click on the desired detector inside Array Display area to visualize it. It is possible create a Table Plotter object both in "Quick View" area and in floating window.

4.3.6 Color&Mask Preferences

To improve the user experience in data analysis, DTE make a large use of the colors. All the colors properties and functionality are regulated by the Color&Mask Preferences panel. The Color&Mask Preferences panel allows to:

1. Select the scale color for the bolometer's array visualization: heat or gray scheme are available;

2. Select the Max/Min value for the color scale;

3. Work with the mask.

Color Preferences Using "Select color scale" radio-buttons it's possible to choose the color scheme between gray (default) and heat. The colors associated at the bolometers are based upon the RGB scale; the RGB scale is based upon three primary color (Red, Green and Blue) called components. The component values are stored as integer numbers in the range 0 to 255. The value associate to the component is calculated using

$$R_{level} = V_C \times 255 \tag{4.1}$$

$$G_{level} = V_C \times 255 \tag{4.2}$$

$$B_{level} = V_C \times 255 \tag{4.3}$$

for the grey scale and

$$R_{level} = V_C^{1/r} \times 255 \tag{4.4}$$
$$G_{level} = V_C^{1/g} \times 255 \tag{4.5}$$
$$B_{level} = V_C^{1/b} \times 255 \tag{4.6}$$

for the heat scale. Here, r, g, b are constants and V_C is derived from the value V_i registered by the bolometer at showed row/readout number of the timeline:

$$V_C = V_{Max} - V_i / V_{Max} - V_{Min}. \tag{4.7}$$

V_{Max} and V_{Min} are the max/min value registered by all the bolometers displayed.

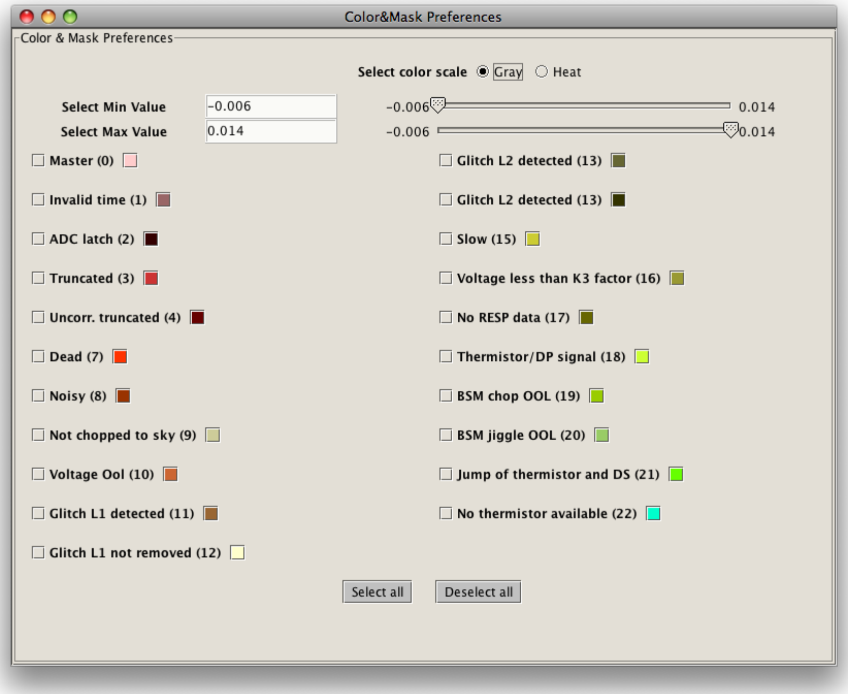

Select color scale ● Gray ○ Heat

Select Min Value -0.006 (slider: -0.006 … 0.014)

Select Max Value 0.014 (slider: -0.006 … 0.014)

☐ Master (0)
☐ Invalid time (1)
☐ ADC latch (2)
☐ Truncated (3)
☐ Uncorr. truncated (4)
☐ Dead (7)
☐ Noisy (8)
☐ Not chopped to sky (9)
☐ Voltage Ool (10)
☐ Glitch L1 detected (11)
☐ Glitch L1 not removed (12)
☐ Glitch L2 detected (13)
☐ Glitch L2 detected (13)
☐ Slow (15)
☐ Voltage less than K3 factor (16)
☐ No RESP data (17)
☐ Thermistor/DP signal (18)
☐ BSM chop OOL (19)
☐ BSM jiggle OOL (20)
☐ Jump of thermistor and DS (21)
☐ No thermistor available (22)

Figure 4.13: Color&Mask Preferences panel.

It is possible change the min/max value for the color scale using either writable fields or sliders. Changing in the min value implies that all bolometers with a registered value below this limit are colored white, changing in the max value implies that all the bolometers with a registered value over this limit are colored black. For the others bolometers, the colors are re-calculated using this new limits for V_{Max} and V_{Min} (Figure 4.14).

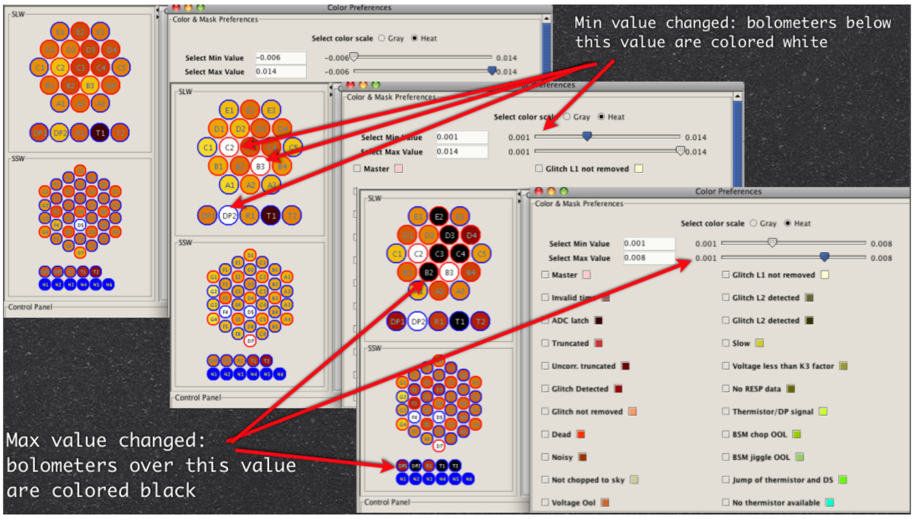

Min value changed: bolometers below this value are colored white

Max value changed: bolometers over this value are colored black

Select color scale ○ Gray ● Heat
Select Min Value -0.006
Select Max Value 0.014

Select color scale ○ Gray ● Heat
Select Min Value 0.001
Select Max Value 0.014

Select color scale ○ Gray ● Heat
Select Min Value 0.001
Select Max Value 0.008

Figure 4.14: Color scale Min/Max value example.

Mask Preferences It's possible that some detectors in the dataset are flagged because they have an error or a problem (as explained in Section 3.3.1). This information is contained in the "Mask" dataset and via DTE we can use this information to optimize the visualization of the data. The mask preferences show a list of masks values as defined by SpireMask (see Figure 4.13 and Appendix B).For each of this values we have a checkbox and a colored button: the checkboxs allow to select a specific mask value and colored buttons to assign a color to the specific mask value.

The selection of a checkbox associated with a specific mask value cause the update of:

- **Display array** The bolometers flagged (at the displayed readout number) by the mask value selected are colored with the associated color (Figure 4.15 top).
- **Displayed plot** If the displayed plot is flagged by the selected mask value, the mask value is over-plotted (Figure 4.15 bottom) and the right Y axis show the mask bit number.

The style of the mask value over-plotting is linked to the mask preferences: if we change the color associated at the specific mask value, we change also the layer color. Different mask value have also different plot symbol.

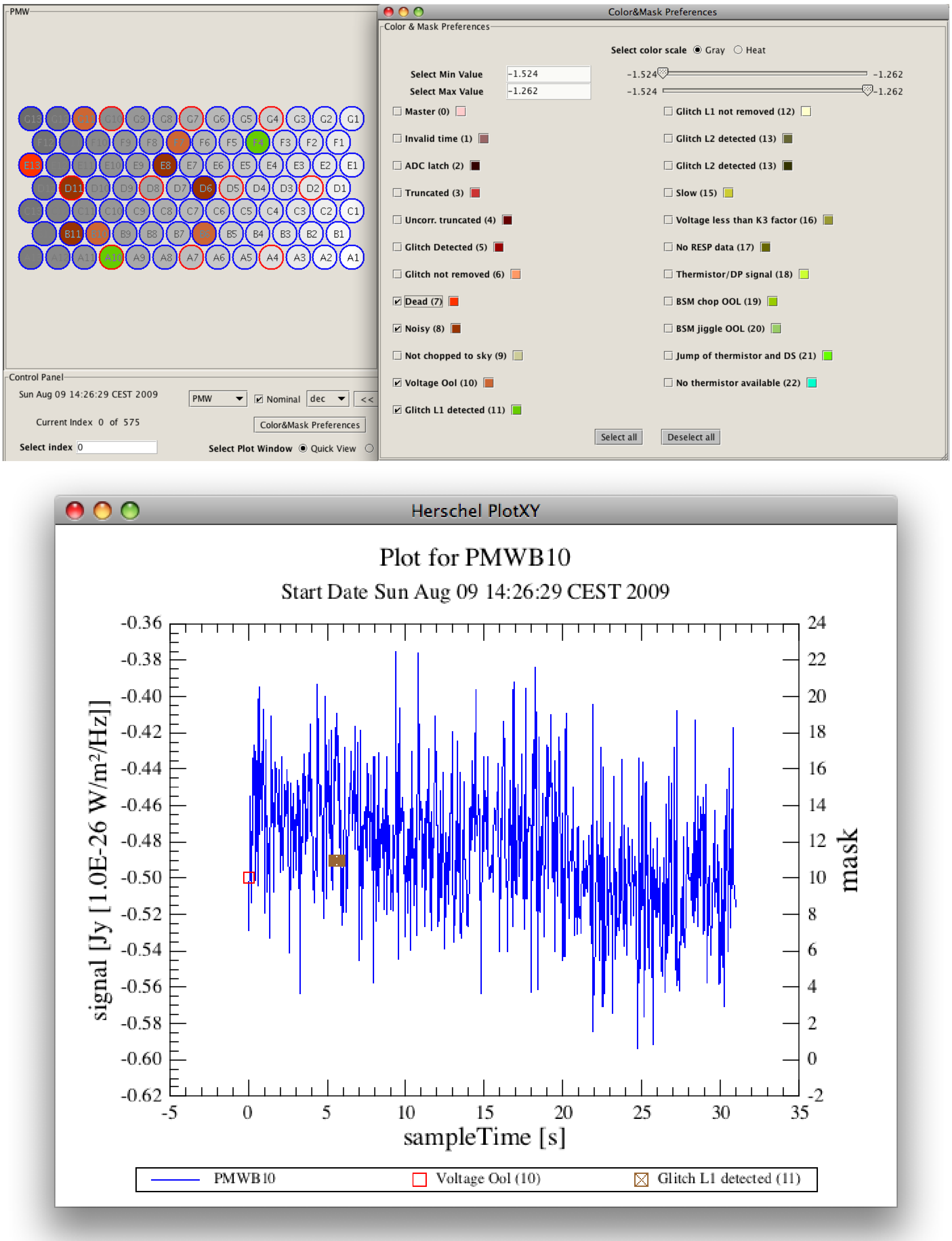

Control Panel

Sun Aug 09 14:26:29 CEST 2009

PMW ☑ Nominal dec

Current Index 0 of 575

Select index 0

Select Plot Window ● Quick View ○

Color & Mask Preferences

Select color scale ● Gray ○ Heat

Select Min Value -1.524

Select Max Value -1.262

☐ Master (0)
☐ Invalid time (1)
☐ ADC latch (2)
☐ Truncated (3)
☐ Uncorr. truncated (4)
☐ Glitch Detected (5)
☐ Glitch not removed (6)
☑ Dead (7)
☑ Noisy (8)
☐ Not chopped to sky (9)
☑ Voltage Ool (10)
☑ Glitch L1 detected (11)
☐ Glitch L1 not removed (12)
☐ Glitch L2 detected (13)
☐ Glitch L2 detected (13)
☐ Slow (15)
☐ Voltage less than K3 factor (16)
☐ No RESP data (17)
☐ Thermistor/DP signal (18)
☐ BSM chop OOL (19)
☐ BSM jiggle OOL (20)
☐ Jump of thermistor and DS (21)
☐ No thermistor available (22)

Figure 4.15: Mask preferences. **Top:** the selection of a specific mask value cause the update of the Array Display. **Bottom:** the mask value is over-plotted to the data.

4.3.7 Example of the use of DTE

In this section I will report some examples about the use of DTE.

Example: Plotting functions

In order to inspect detectors from a specific product using the DetectorTimelineExplorer plotting functions perform the following steps:

1. Start the DTE for the product in question.
2. Click on the desired detector to create the plot.
3. Click on another detector to change the displayed plot.
4. Select "Over Plot" radio button within "Control Panel" to allow the overplotting (see Figure 4.16).
5. Click on another detector to overplot the data (see Figure 4.12).
6. To see the last plotted data within TablePlotter (Figure 4.12) select "Table Plotter" radio button within "Control Panel" (see Figure 4.16).
7. To change the detector displayed with Table Plotter, simply click on the desired detector in the Array Display.

Figure 4.16: Radio buttons to select the plotting options.

Example: Browse trough time across the timeline.

In order to browse trough time across the timeline perform the following steps:

1. Start the DTE for the product in question.
2. In the Control Panel click on the ">>" button to go on the next step of the timeline readout. (Figure 4.11)
3. To automatize the browsing, click on the "PLAY" button. (Figure 4.11)

4. Use "PAUSE" button to block the automatic browsing and "STOP" button to come back at the beginning of the timelines. (Figure 4.11)

5. To change the speed of the automatic browsing change the value in the "FPS" (frame per second) textfield (default value = 30 fps, Figure 4.11).

Example: Visualize the flagged detectors in Array Display

In order to Visualize the flagged detectors perform the following steps:

1. Start the DTE for the product in question.

2. In the Control Panel click on the "Color&Mask Preferences" button to open the preferences panel (Figure 4.9).

3. Select the checkbox associated to the desired mask value: if a detector is flagged by this mask (at the selected timeline readout number) its color in Array Display change according with associated color (Figure 4.17). You can select all the mask value simply clicking on the "Select all" button (and deselect all the mask value clicking on the "Deselect all" button, Figure 4.13).

4. You can change the color associated at the mask clicking on the colored button and selecting the new color from color selector.

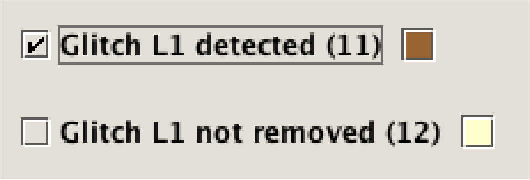

☑ Glitch L1 detected (11)

☐ Glitch L1 not removed (12)

Figure 4.17: Mask preferences: two mask values with associated checkboxs and color buttons.

4.4 Timeline Simple Plot

Timeline Simple Plot (TSP) was developed after a specific request from users:

> SPIRE-2244:The DetectorTimelineViewer provides plots displaying timelines for individual channels. It would be helpful if such plots could be created from the HIPE/Jython command line.

TimelineSimplePlot class allows to create simple SPIRE Detector Timeline plots from HIPE command line. Also for this class the documentation is up to date and the test harness coverage is 100%.

4.4.1 Using TSP

TSP is an application that can be called from HIPE command line.

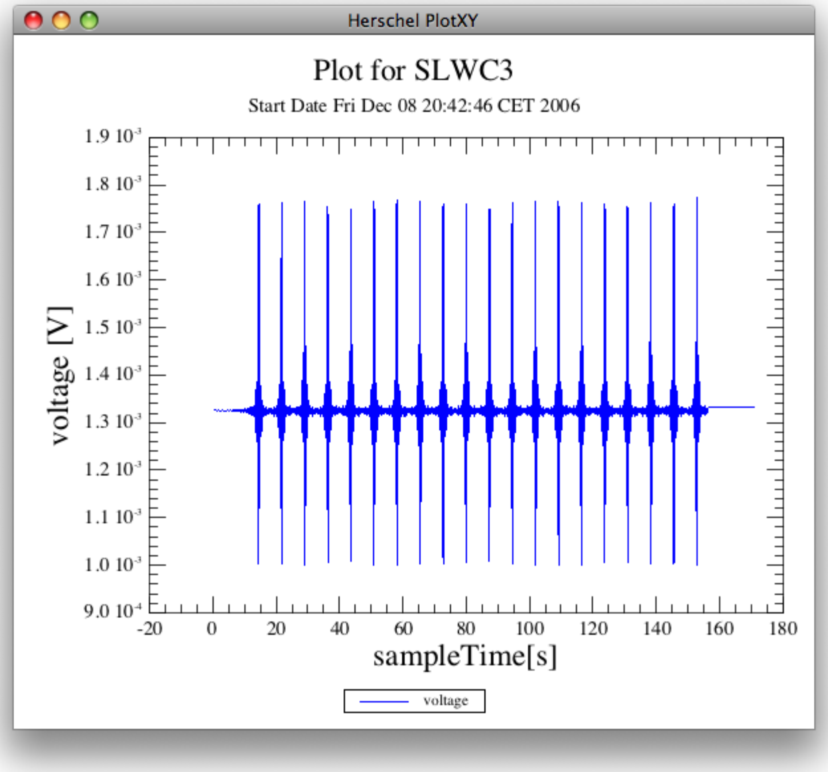

Figure 4.18: Example of default TSP plot

It is possible call TSP in two way from HIPE command line:

```
from herschel.spire.ia.gui import TimelineSimplePlot
c=TimelineSimplePlot(my_products, "my_dataset", "my_channel")
```

or

```
from herschel.spire.ia.gui import TimelineSimplePlot
sp=TimelineSimplePlot()
sp.setObject(my_products, "my_dataset", "my_channel")
```

where:

my_products is a DetectorTimeline object already available in memory (Object: DetectorTimeline, MANDATORY)

"my_dataset" is the name of the dataset that we want use, for example signal, voltage, mask, ... (Object: String, MANDATORY)

"my_channel" is the name of the channel that we want plot, for example PSWC5, SLWC5, ... (Object: String, MANDATORY)

Some public methods allow to customize the plot. In particular:

- changeObject(DetectorTimeline _product)
- changeDataset(String _dataset)
- changeChannel(String _channel)
- clearObject()
- setScale(int n)
- setMask()
- clearMask()
- setColorMask(java.awt.Color color)

changeObject(DetectorTimeline _product) The public method changeObject(DetectorTimeline dt) allow to change the product but don't change the dataset and the channel. The plot is updated immediately.

```
sp.setObjects(my_first_product, "my_dataset", "my_channel")
sp.changeObject(my_second_product)}
```

changeDataset(String _dataset) This method allow to change the dataset (for example we can change from voltage to resistance) but don't change the product and the channel. The plot is updated immediately.

```
sp.changeDataset("resistance")
```

changeChannel(String _channel) This method allow to change the channel(for example we can change from PLWC5 to PSWC10) but don't change the product and the dataset. The plot is updated immediately.

```
sp.changeChannel("PLWC5")
```

clearObject() This method allow to set all the objects (product, dataset and channel) to null and close the plot's frame. To visualize the plot we need to reuse setObject() method.

```
sp.clearObject()
```

setScale(int n) This method allow to select the x axis scale. We have three possible choices:

- **n=0** (default) relative time scale
- **n=1** absolute time scale
- **n=2** index

```
sp.setScale(1)
```

setMask() This method allow to overplot the mask value for the selected channel (see Figure 4.19).

```
sp.setMask()
```

clearMask() This method allow to remove the over-plotted mask.

```
sp.clearMask()
```

setColorMask(java.awt.Color color) The public method setColorMask(java.awt.Color color) allow to set the color to use to display the mask (java.awt.Color.RED, java.awt.Color.CYAN, etc).

```
sp.setColorMask(java.awt.Color.yellow)
```

4.5 Detector Timeline Mosaic

DTM ia a useful tool allowing creation of "mosaic plot" of data from PDT and SDT products. In a mosaic plot, the plots are arranged in the same pattern as the detectors are presented in the Array Display, a honeycomb pattern. An example of mosaic plot is showed in Figure 4.20.

DTM is used by DTE to create mosaic plot (see Section 4.3.3) but it's possible to launch also from HIPE command line. DTM use TimelineSimplePlot to create the single plot.

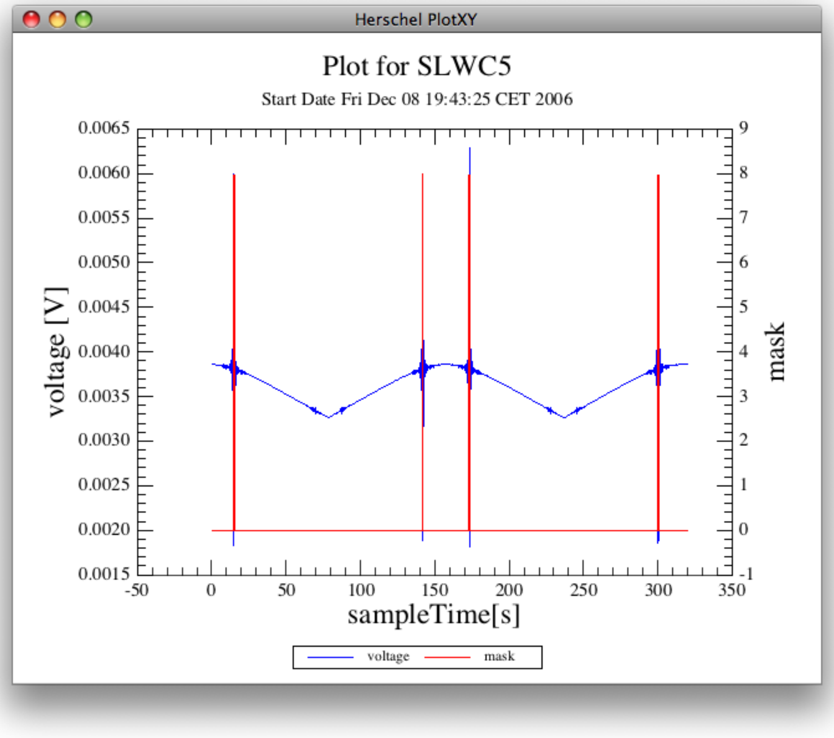

Figure 4.19: useMask(): voltage and mask over-plotted

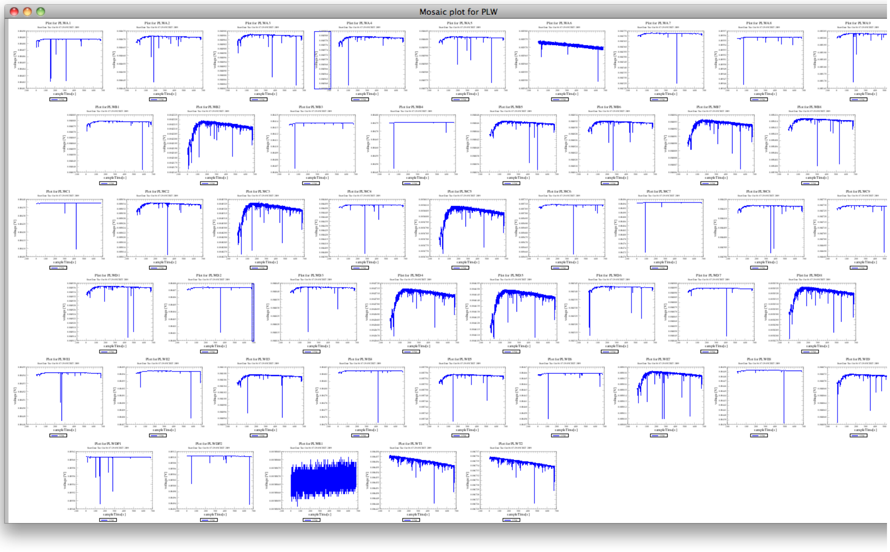

Figure 4.20: An example of DTM.

4.5.1 Using DTM

I have already explained how launch DTM in DTE (Section 4.3.3). It's possible to call DTM in many way from HIPE command line. The simpler way is the following:

```
from herschel.spire.ia.gui import DTMosaic
dtm=DTMosaic()
dtm.setMosaicType(DetectorTimeline my_product,
                        String "my_dataset",  String "my_array")
```

where:

my_products is a DetectorTimeline object already available in memory (Object: DetectorTimeline, MANDATORY)

"my_dataset" is the name of the dataset that we want use, for example signal, voltage, mask, ... (Object: String, MANDATORY)

"my_array" is the name of the array that we want plot, for example PSW, SLW, SSW, ... (Object: String, MANDATORY)

An other way to launch DTM is the following:

```
from herschel.spire.ia.gui import DTMosaic
dm=DTMosaic(DetectorTimeline my_product,
               String "my_dataset", String "my_array", int n)
```

In this case we have also the parameter **n**: the parameter **n** is used to set the X-axis scale for all the plot contained in the mosaic. We have three possible chooses:

- **n=0** (default) relative time scale;
- **n=1** absolute time scale;
- **n=2** index.

The choice of X-axis scale is possible also via *setXScale(int n)* method

```
from herschel.spire.ia.gui import DTMosaic
dm=DTMosaic()
dm.setXscale(n)
# E.G. n=0 ---> Relative time scale
# E.G. n=1 ---> Absolute time scale
# E.G. n=2 ---> Index scale
# default n=0
dm.setMosaicType(DetectorTimeline my_product,
                    String "my_dataset", String "my_array")
# E.G. my_dataset=voltage , signal , mask...
# E.G. my_array=PLW, SLW, ...
```

The last way to launch DTM is:

```
from herschel.spire.ia.gui import DTMosaic
dm=DTMosaic(DetectorTimeline my_product,
               String "my_dataset", String "my_array", int n,
                boolean nominal)
```

The new parameter **nominal** allows the creation of mosaic plot containing only the nominal detectors, i.e. the bolometers that see the sky (not the bolometers that measure the performance of the instrument).

A comparison between the normal mosaic plot and "nominal" mosaic plot is showed in Figure 4.21.

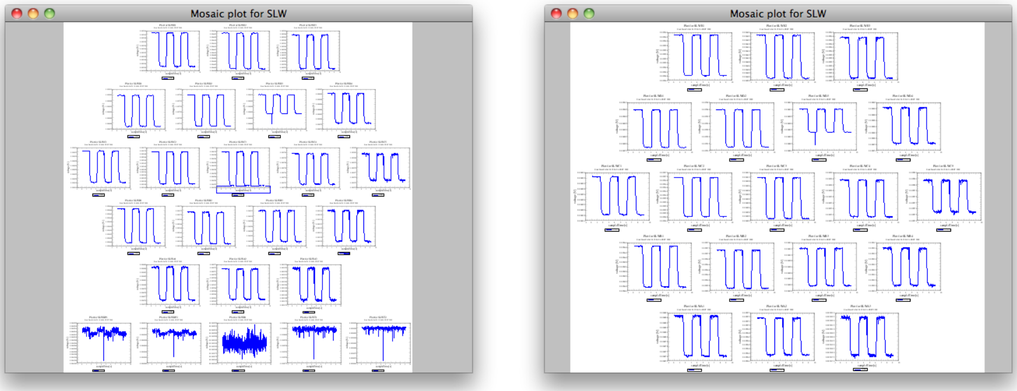

Figure 4.21: **Left:** a normal mosaic plot. **Right:** a "nominal" mosaic plot.

Also in this case it's possible set the **nominal** parameter using the method *setNominal(boolean nominal)*.

```
from herschel.spire.ia.gui import DTMosaic
dm=DTMosaic()
dm.setNominal(nominal)
# E.G. nominal ---> If True, only the nominal detectors
#are plotted.
# If False, all the detectors are plotted.
dm.setMosaicType(DetectorTimeline my_product,
                     String "my_dataset", String "my_array")
```

The documentation for DTM is up to date and the test harness coverage is 100%.

4.6 Others tools

The *herschel.spire.ia.gui* package contains also other tools not developed by me:

- SpecExplorer, developed by BlueSky Inc., Lethbridge (CA)
- Mosaic, developed by BlueSky Inc., Lethbridge (CA)

- SpireMaskEditorTool, developed by IPAC team, Pasadena (US)

The **SpecExplorer** (see Figure 4.22) and **Mosaic** tools are addressed to explore the SPIRE spectrometer data. In particular SpecExplorer is a GUI-based visualization tool that allows efficient inspection of the contents of the two SPIRE products: Spectrometer Detector Interferogram (SDI) and Spectrometer Detector Spectrum (SDS).

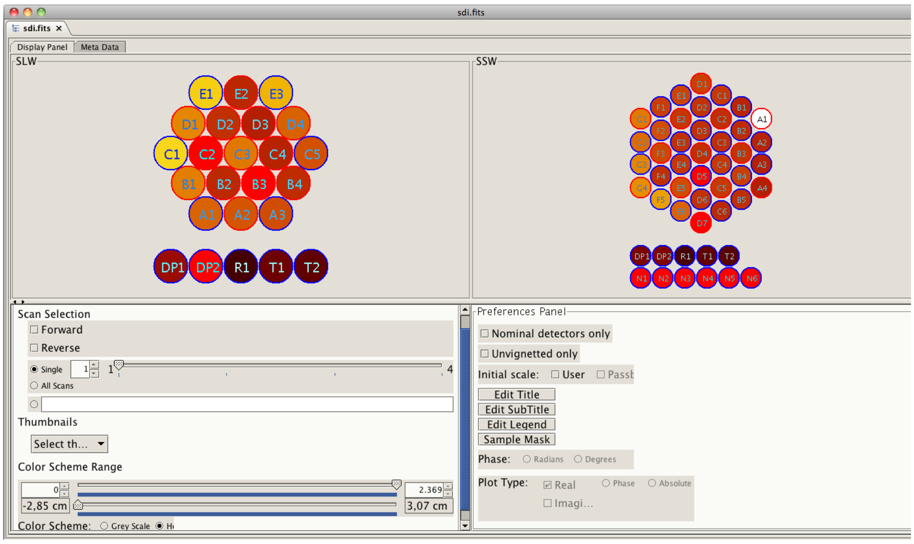

Figure 4.22: SpecExplorer Graphical User Interface.

As DTE SpecExplorer run within HIPE and allows allows users to:

- Select a subset of the scans within the data product (Scan Selection).
- Create plots of many datasets on one page (mosaic plot).
- Define the fill colors for the detectors (Color Scheme Range).

To create the mosaic plot, SpecExplorer use the Mosaic class, written specifically for SDI and SDS products.

The **SpireMaskEditorTool** is a tool which will be used to change, edit and display the SPIRE Mask. The tool is a HIPE component and can be invoked in HIPE by right click a SPIRE Detector Timeline product or a SPIRE Observation Context .

The total test harness coverage for *herschel.spire.ia.gui* is 83%: this is a great results for a GUI package.

4.7 The pipeline tasks

I explained in the previously sections how the *Herschel* software is structured and how is subdivided in package. I said that I am responsible for two packages, the *herschel.spire.ia.gui* and the *herschel.spire.ia.pipeline.common.util*. I just described my work about the visualization tools contained in the first package, I will describe now my work about the second package. This package contains some task used in the SPIRE pipeline (see Chapter 3), used in particular in the scan map pipeline. I will describe how this task work and how was developed. I report in Appendix the design documentation and the test plan.

The *herschel.spire.ia.pipeline.common.util* contains the following class:

JoinPhotDetTimelinesTask Task to join scan line detector timelines with the detector timelines of the leading and trailing turnaround building block in scan maps.

CutPhotDetTimelinesTask Task to cut a Pointed Photometer Timelines that were previously joined with the detector timelines of the trailing and following turnaround building block in scan maps.

JoinNhkTimelinesTask Task to join scan line NHK timelines with the NHK timelines of the leading and trailing turnaround building block in scan maps.

RemoveBaselineTask Task to remove the baseline from Pointed Photometer Timeline. The baseline corresponds to the median value.

4.7.1 JoinPhotDetTimelinesTask

The purpose of this module/task is to join scan line detector timelines with the detector timelines of the leading and trailing turnaround building block in scan map. This task is used in all the Photometer scan map pipeline (Parallel, Large and Small Map, see Section 3.3.2).

The module use three input PDT:

1. pdt: PDT of the scan line;
2. leading: PDT of the leading turnaround building block;
3. trailing: PDT of the trailing turnaround building block.

The only mandatory parameter is the scan line PDT: if the leading and trailing input are not set, the output of the module is equal to the input.

The module reads the scan line PDT and propagates the meta data to the output. Finally, the module combines in the output the dataset of the three input

PDT.

To use this task in HIPE command line or in a script:

```
my_output = joinPhotDetTimelines(pdt=my_pdt,leading=my_leading,trailing=my_trailing)
```

The module design plan is reported in Appendix C and the module test plan in Appendix D. The test harness coverage for this task is 100%.

4.7.2 Cut turnaround for PDT task

The purpose of this module/task is to cut the Photometer Scan Product (PSP) timelines that were previously joined with the detector timelines of the leading and trailing turnaround building block in scan maps. The module will take as mandatory input an PSP and use a optional parameter *extend* to to keep half of turnaround data.
This task is used in all the Photometer scan map pipeline (Parallel, Large and Small Map).

To use this task in HIPE command line or in a script:

```
my_output = cutPhotDetTimelines(pdt=my_ppt,extend=True)
```

The module design plan is reported in Appendix G and the module test plan in Appendix H. The test harness coverage for this task is 100%.

4.7.3 Add turnaround for NHKT task

The purpose of this module is to join scan line detector timelines with the detector timelines of the leading and trailing turnaround building block in scan map. This task is used in all the Photometer scan map pipeline (Parallel, Large and Small Map).

The module use three input Nominal House Keeping Timeline (NHK) Timelines (this product contains the timelines for the nominal housekeeping telemetry parameters):

1. nhkt: NHK Timeline of the scan line;
2. leading: NHK Timeline of the leading turnaround building block;
3. trailing: NHK Timeline of the trailing turnaround building block.

The only mandatory parameter is the scan line NHK: if the leading and trailing input are not set, the output of the module is equal to the input.

To use this task in HIPE command line or in a script:

```
my_output = joinNhkTimelines(nhkt=my_nhkt,leading=my_leading,trailing=my_trailing)
```

The module design plan is reported in Appendix E and the module test plan in Appendix F. The test harness coverage for this task is 100%.

4.7.4 Remove baseline task

The purpose of this module is to remove the baseline from Pointed Photometer Timeline (PPT). The baseline corresponds to the median. This task is used in all the Photometer scan map pipeline (Parallel, Large and Small Map). This task require two mandatory input, the PPT and a Channel Number Mapping Table.

To use this task in HIPE command line or in a script:

```
my_output = removeBaseline(pdt=my_ppt,chanNum=my_chanNum)
```

The test harness coverage for this task is 100%.

5

HerMES: The *Herschel* Multi-tiered Extragalactic Survey

In this chapter I will describe the Herschel Multi-tiered Extragalactic Survey (HerMES) project, the largest project on *Herschel* to study the evolution of galaxies in the distant Universe. I will report a briefly description of the project, the main objective and a selection of the first results from the papers in which I participated focusing in particular on the study of the confusion limits and number counts.

5.1 Description and aim

HerMES is the Herschel Multi-tiered Extragalactic Survey, an astronomical project to study the evolution of galaxies in the distant Universe. It is the largest project in term of time on *Herschel*. The project is carried out by a large team, made up primarily of people in SPIRE ICC.

A central challenge in astrophysics today is to understand the complex processes of galaxy formation: the development of galactic structure, the conversion of gas into stars, and the growth of supermassive black holes.

The far-infrared/sub-millimeter waveband is of particular importance for studying these processes because roughly half of the cosmic energy density produced by galaxies arises from optical/UV starlight that has been absorbed by dust and re-radiated at these wavelengths (see Figure 5.3) .

Existing surveys are already presenting a serious challenge for theorists, revealing many more luminous, massive galaxies at high redshifts than are predicted by simple prescriptions within the hierarchical merging paradigm (e.g. Smail et al. 2002, Patanchon et al. 2009). Sub-millimeter surveys have been extremely limited, however, but already provide tantalizing clues to a strongly evolving population of infrared-luminous galaxies.

HerMES will chart the formation and evolution of infrared galaxies throughout cosmic history. The HerMES has a hierarchal structure containing 7 levels with increasing area but shallower coverage from very deep observations of clusters through levels 1-6 with the shallowest surveys at Level 6 covering around 10 square degrees (see Figure 5.1 and Figure 5.2).

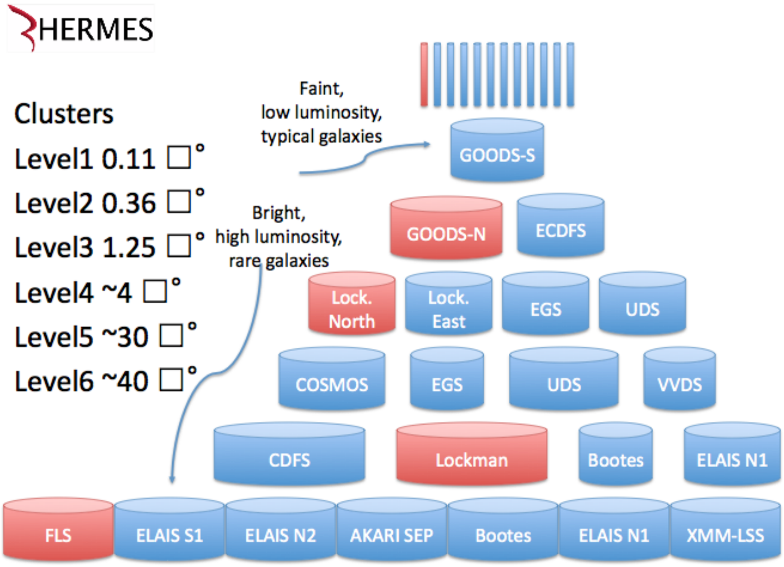

Figure 5.1: The HerMES structure: the area increase with the level but the coverage decreases. In red the field observed in SDP.

Using HerMES data it's possible to measure the bolometric emission of infrared galaxies, study the evolution of the luminosity function, measure their clustering properties, and probe populations of galaxies below the confusion limit through lensing and statistical techniques.

HerMES is closely coordinated with the PACS Evolutionary Probe (PEP) survey. The HerMES program make maximum use of ancillary surveys from radio to X-ray wavelengths to facilitate redshift determination, rapidly identify unusual objects, and understand the relationships between thermal dust emission and other emission mechanisms. HerMES will provide a rich data set legacy for the greater astronomical community to mine for years to come.

HerMES seeks to investigate the following areas of modern astrophysics:

- History of star formation
- Galaxies and quasars

- The role of environment

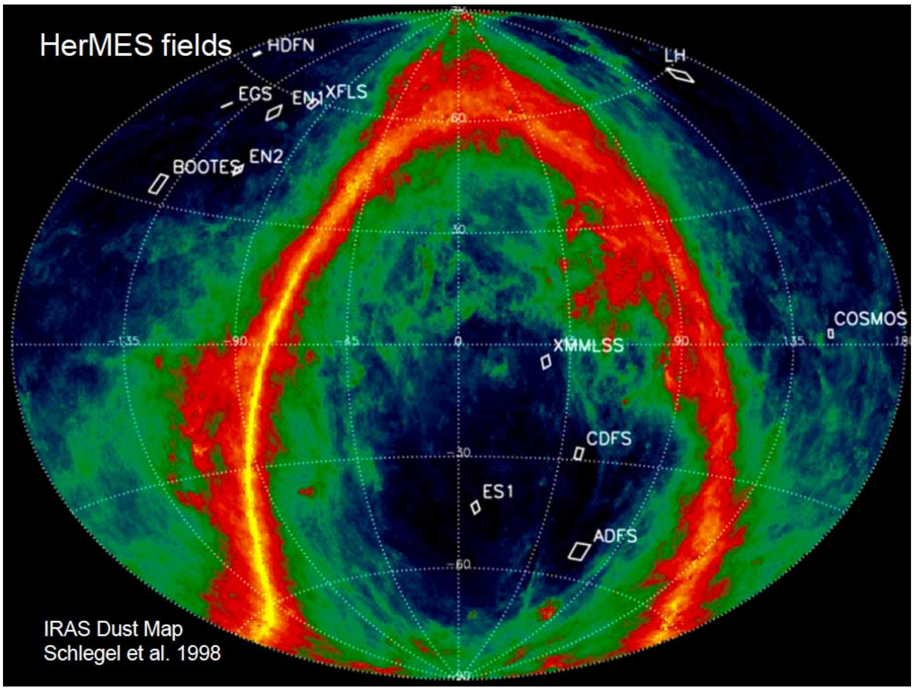

Figure 5.2: The HerMES fields overlapped to the IRAS dust map.

For my work is important to focus on the galaxy evolution: in particular about the fraction of optical-UV radiant energy emitted by young stellar populations which is absorbed by dust in the Inter-Stellar Medium (ISM) and re-emitted at long wavelengths.

In the past a lot of studies take advantage of the space missions (e.g. IRAS, ISO) to explore this aspect. It has been show that the fraction of the energy re-radiated by ISM become very important during the active phases of star formation, galaxy assembly and nuclear activity (e.g. Franceschini et al. 1994, Sanders & Mirabel 1996). All these studies however, are limited to the redshift interval from local to $z \sim 1$, but both theoretical expectations (Franceschini et al. 1994, Franceschini et al. 1997) and preliminary sub-millimetric observations with SCUBA (Holland et al. 1999, Smail et al. 2002) show evidence that major events of star-formation in the universe happened at high redshifts, $z > 1$, and are likely responsible for the origin or assembly of the most massive galaxies today. Only in the last years observations performed with the Spitzer Space Telescope have allowed a better understanding of what happens at redshift grater than 1. In particular the 24 μm observations performed using MIPS instrument have fully confirmed previous expectations of numerous populations of luminous galaxies and active nuclei

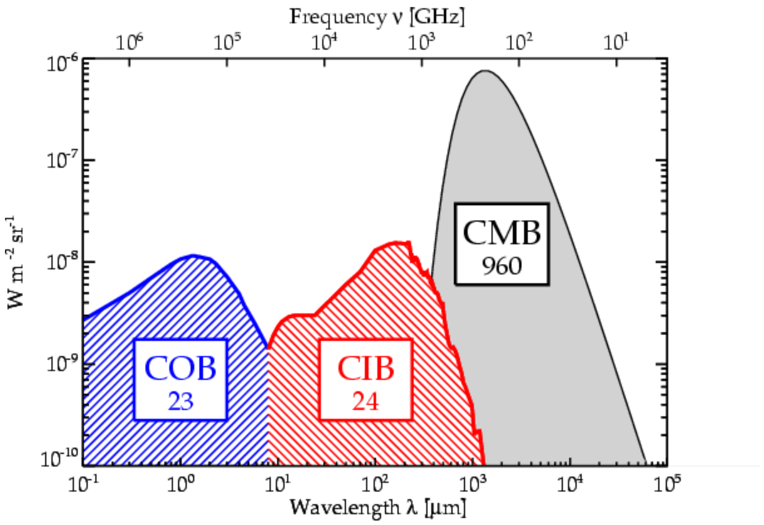

Figure 5.3: Schematic Spectral Energy Distributions of the most important (by intensity) backgrounds in the universe, and their approximate brightness in $nWm^{-2}sr^{-1}$ written in the boxes. From right to left: the Cosmic Microwave Background (CMB), the Cosmic InfraRed Background (CIRB) and the Cosmic Optical Background (COB). From Dole et al. (2006).

at high-redshifts. At longer wavelength the identifications was hardly due to poor Spitzer resolution. For this reason, the HerMES data are important to improve the our knowledge at the long-wavelength, in particular where the CIRB peak.

Some of the early results obtained within HerMES data was published in an Astronomy and Astrophysics special issue (Walmsley et al. 2010a) in July 2010 and in the next Sections I will report some of this results, in particular those obtained in the characterization of confusion noise (Nguyen et al. 2010), in the number counts statistics (Oliver et al. 2010 and Glenn et al. 2010) and in the clustering analysis (Cooray et al. 2010).

5.2 HerMES: The SPIRE confusion limit

One of the great problem in the large survey is the confusion due to poor telescope resolution, particularly for the infrared and sub-millimetric survey. I will describe largely this problem in Chapter 6, but in this subsection I will report the early results obtained in HerMES using the Science Demonstration Phase (SDP) data: indeed with 18.1″, 25.1″and 36.6″ FWHM beams at 250, 350 and 500 μm, respectively, we expect SPIRE maps to be dominated by confused sources.

Because of the confusion problem, it is therefore useful to determine the key

Table 5.1: HerMES field used in Nguyen et al. (2010) to estimate the confusion noise

Field	Area	Scan Mode	Repeats
GOODS-N	$30' \times 30'$	$30''$/s	30
Lockman-North	$35' \times 35'$	$30''$/s	7
Lockman-SWIRE	$218' \times 218'$	$60''$/s	2

characteristics, both of the instrument and the sky, that would allow observers to optimize their observing plans, and/or to make sky surveys that probe as deep and as wide as possible for allocated observing time, in particular:

- the instrument noise, i.e. noise from the detectors, readout electronics and photon noise from the telescope;
- the confusion noise, that is, the variance in the sky map due to the presence of unresolved sources;
- the cosmic variance, arising from underlying large-scale fluctuations in the galaxy number density.

The confusion noise due to sources below a given flux cutoff, x_c, is derived in Condon (1974) to be the second moment of the measured flux distribution:

$$\sigma^2_{conf} = \int_0^{x_c} x^2 dn, \tag{5.1}$$

where x is the measured flux, $x = Sf(\theta, \phi)$, S is the source flux convolved with the normalized beam response, $f(\theta, \phi)$, and dn is the differential source distribution.

In Nguyen et al. (2010) we do a first attempt to estimate the confusion noise in HerMES maps, focusing in particular on three field: GOODS-N, Lockman-SWIRE and Lockman-North. These three fields were observed with different scan modes: GOODS-N and Lockman-North with nominal scan mode (with the spacecraft scanning at $30''$/s), Lockman-SWIRE with fast scan mode (with the spacecraft scanning at $60''$/s)). I summarize the information about these observation in Table 5.1.

Fundamentally, the spatial fluctuations in a map arise due to two sources: instrument noise σ_{inst} and the presence of sources on the sky. The instrument component, will be reduced with integration time, while fluctuations due to the convolution of the sky with the instrument beam, σ_{conf}, will remain. Since the sources of noise are uncorrelated, and if low-frequency correlated noise has been properly accounted for in the low level data reduction, the total variance in the map is simply:

$$\sigma^2_{total} = \sigma^2_{conf} + \sigma^2_{inst}/t \ , \tag{5.2}$$

where t is the integration time. Note that σ_{conf} has unit of surface brightness in mJy/beam, while σ_{inst} in mJy/beam$\sqrt{t}$. A straight line fit of the variance vs. inverse integration time has a slope that determines the instrument variance, σ^2_{inst}, and a non-zero intercept that determines the variance of the sky intensity, σ^2_{conf} (Jarosik et al. 2003). In our analysis we begin by selecting all map pixels with a total integration time between $t - dt < t < t + dt$, where dt is 0.5 times the integration time per sample (i.e. 0.054 s/sample in nominal scan mode). Then we measure the variance, σ^2_{total}, of the pixel values in that subset. Figure 5.4 shows $\sigma(t)^2_{total}$ vs. t^{-1} at 250, 350 and 500 μm in the fields observed in nominal and fast scan mode. GOODS-N pixel sets are shown in black, Lockman-North in green and the shallow Lockman-SWIRE field in red. The black line shows a simultaneous linear fit to all three fields and traces a component proportional to t^{-1} and a non-zero intercept.

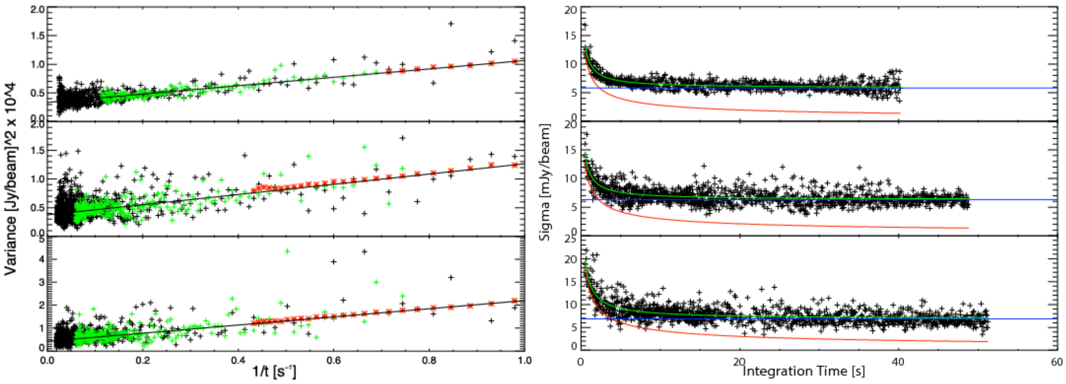

Figure 5.4: **Left:** variance of SPIRE map pixels at 250, 350 and 500 μm (top to bottom) in 6″, 10″and 14″pixels, respectively, in the GOODS-N (black), Lockman-North (green) and Lockman-SWIRE (red) fields. Lockman-SWIRE was only observed once in each scan orientation, and was observed in Fast Scan Mode (60″/s). Despite the shallow field depth and different scan speed, the linear trend with inverse integration time is clearly continuous from short to long integration times. The black line is a linear fit to all pixels in the three fields simultaneously revealing an instrument noise of 8.5 ± 0.4, 9.4 ± 0.5 and 13.3 ± 0.7 mJy/beam$\sqrt{s}$, and a confusion noise of 5.8 ± 0.3, 6.3 ± 0.4 and 6.8 ± 0.4 mJy/beam at 250, 350 and 500 μm. **Right:** pixel noise vs. integration time for all pixels in both fields. Over-plotted are the derived instrument noise (red) and the confusion floor (blue) and the total noise (green). From Nguyen et al. (2010).

The data from the three included fields clearly show that the noise properties of the SPIRE instrument and the SPIRE observed sky are independent of the SPIRE scanning speed and stable from shallow to deep fields. The consistency of the result in deep and shallow fields confirms that this method of noise characterization measures the confusion noise in maps that, themselves, are not confusion limited. In fact, the large area shallow field (red points) in Figure 5.4 show far less scatter about the fit than the fewer pixels in the deep fields since there are many more pixels, providing a larger statistical ensemble. The right side of Figure 5.4 shows the same data in a different graphical representation. The square root of the variance in all three fields (now all in black) is plotted vs. the integration time along with the derived instrument noise (red line) and confusion noise (blue line). If the sky were dark, the noise would integrate down to zero following the red line, while for the real sky the noise can not get below the confusion floor.

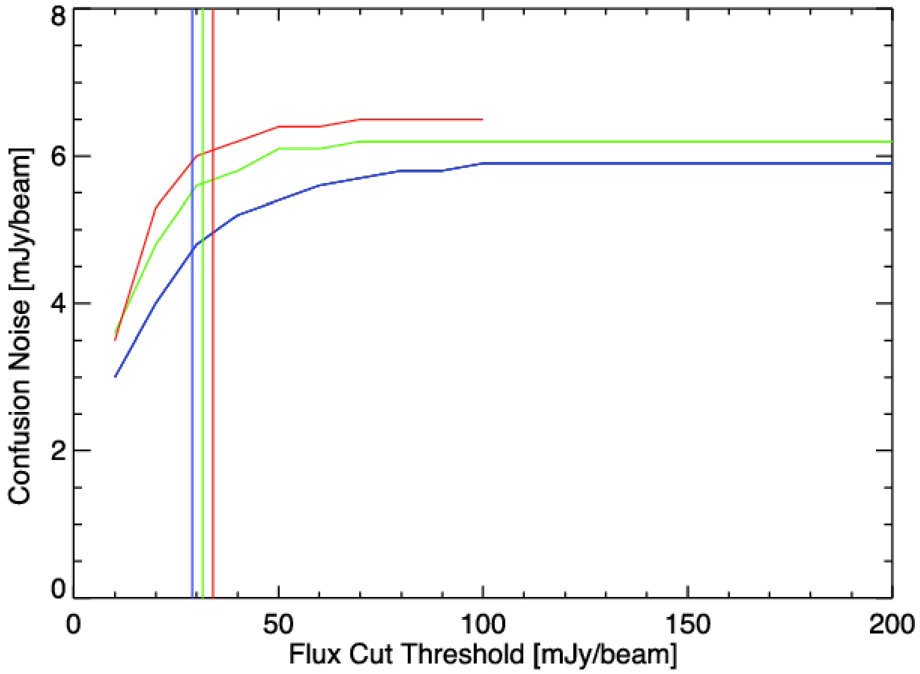

Figure 5.5: Confusion noise as a function of pixel flux cut at 250/350/500 μm in blue/green/red. All pixels within a beam FWHM of a pixel brighter than the indicated flux cut were masked and the confusion noise was re-estimated. Vertical lines indicate $5\sigma_{conf}$ in each band (Nguyen et al. 2010).

The measured noise is reported in Table 5.2. The confusion noise values in Table 5.2 are equivalent to the 1σ point source sensitivities, in mJy, in confusion limited maps. The two rightmost columns are included for observation planning and show the instrument noise scaled from mJy/beam$\sqrt{s}$ repeats for nominal and fast scan mode, respectively.

To confirm the results, we have made also some simulations with known instrument noise and injecting sources drawn from the number counts determined

Table 5.2: Confusion and instrumental noise as estimated by Nguyen et al. (2010)

Band μm	σ_{conf} mJy/beam	σ_{inst} mJy/beam$\sqrt{s}$	σ_{inst} mJy/beam$\sqrt{repeats}$ Nominal^a	 Fast^b
250	5.8 ± 0.3	8.5 ± 0.4	9	12.7
350	6.3 ± 0.4	9.4 ± 0.5	7.5	10.6
500	6.8 ± 0.4	13.3 ± 0.7	10.8	15.3

^{a} 30″/s scan speed
estimated ^{b} 60″/s scan speed

by BLAST (Patanchon et al. 2009). These simulations are used to check for biases due to the non-Gaussian nature of the pixel distribution or correlated noise and to provide better estimated uncertainties in our measurement. The confusion and instrument noise measured in the simulated maps agree with the analytically computed input noise in all three bands, indicating that any bias is insignificant. The consistency of the results in the deep and shallow fields indicates an absence of measurement bias due to non-Gaussianity. The scatter in the instrument and confusion noise determined in these simulations about the known inputs indicates that the statistical uncertainty on the instrument noise is 5% and on the confusion noise 6%, with no significant bias in the recovered values. The agreement among the three fields of varying depth and solid angle also indicate that an additional uncertainty due to cosmic variance is unnecessary.

The noise values reported in Table 5.2 make no significant source cut and, accounting for the possibility that even bright sources are confused, measure the variance in HerMES maps due to all sources up to $10\sigma_{conf}$ or 80 mJy (more than 99% of data). To better understand these results, we try to remove the bright sources and redetermine the confusion noise. The results of this analysis are shown in Figure 5.5. The vertical lines indicate $5\sigma_{conf}$ as measured in the full map. The residual noise estimates are 3.8, 4.6 and 5.2 mJy with a $3\sigma_{conf}$ cut and 4.8, 5.5 and 6.1 mJy with a $5\sigma_{conf}$ cut.

The confusion limit is often quoted in terms of the flux, at which the source density in a map reaches 30 to 50 beams per source. This quantity requires a measurement or a model of the density of sources, and often is derived assuming a power law source distribution with a 3–4 σ_{conf} (Franceschini 1982). BLAST (Devlin et al. 2009) predicts confusion limits corresponding to 40 beams per source for SPIRE of 22, 22 and 18 mJy at 250, 350 and 500 μm, respectively. The best source counts available at the SPIRE wavelengths are probably the HerMES counts themselves, as reported by Oliver et al. (2010) and summarized in the next Section.

The HerMES counts reach 1 source per 40 beams at 19.1 ± 0.6, 17.7 ± 0.6, and 15.1 ± 1.8 mJy at 250, 350 and 500 μm, corresponding to 3.29, 2.81, and 2.60 σ_{conf}, and in rough agreement with BLAST's prediction.

5.3 HerMES: SPIRE galaxy number counts at 250, 350, and 500 μm

The statistical properties of galaxy populations are important probes for understanding the evolution of galaxies. The most basic statistic of galaxy populations is the number counts i.e. the number density of galaxies as a function of flux. The first strong evidence for cosmological evolution came through studying number counts of radio galaxies. A great number of studies was performed in past to well understand the evolution of number counts at far-infrared and sub-millimetric wavelengths, in particular using the data obtained either from space mission (e.g. IRAS, ISO, Spitzer) or from ground-based surveys. These studies found high number counts compared to non-evolving galaxy number count models. This implied that strong evolution of the source populations must have occurred.

At these results we need to add the CIRB that provides unique information on the history of energy injection in the Universe by both star formation and active galactic nuclei as explained in Chapter 1. It is only very recently, using BLAST, that count models have been probed using fluctuation techniques (Patanchon et al. 2009) or directly (Béthermin et al. 2010) at the wavelength where the CIRB peaks (see Figure 5.3).

Since the first IRAS results, many empirical models have been developed to predict and interpret the numbers and luminosities of IR galaxies as a function of redshift. Empirical models are based on a similar philosophy. The spectral energy distributions of different galaxy populations are fixed and the mid-IR, far-IR and sub-millimetric data are used to constrain the luminosity function evolution. Current limits come from the mid-IR, far-IR and sub-millimetric number counts, redshift distributions, luminosity functions, and cosmic IR background. Models all agree on the general trends, with a very strong evolution of the bright- end ($> 10^{11} L\odot$) of the luminosity function and they yield approximately the same comoving number density of infrared luminous galaxies as a function of redshift. The differences between the models are in several details, different assumptions leading sometimes to equally good fits to the current data. In Oliver et al. (2010) we perform a first number count analysis from the HerMES Science Demonstration Phase (SDP) SPIRE data and compare the results with some of these models.

In the analysis we use the catalogues extracted from the maps using the version of SUSSEXractor (Savage & Oliver 2007) implemented in HIPE and taking into account the problem of confusion as described in Section 5.2. The incompleteness in the whole process was estimate by running full simulations processed in the same way as the real data.

The results (showed in Figure 5.7 with Euclidian normalization) show approximately flat counts for S > 100 mJy and then a steep rise. There is flattening to about 20 mJy. The counts show also a good fit with the counts estimated from a *P(D)* fluctuations analysis (see Chapter 6) of BLAST maps (Patanchon et al. 2009).

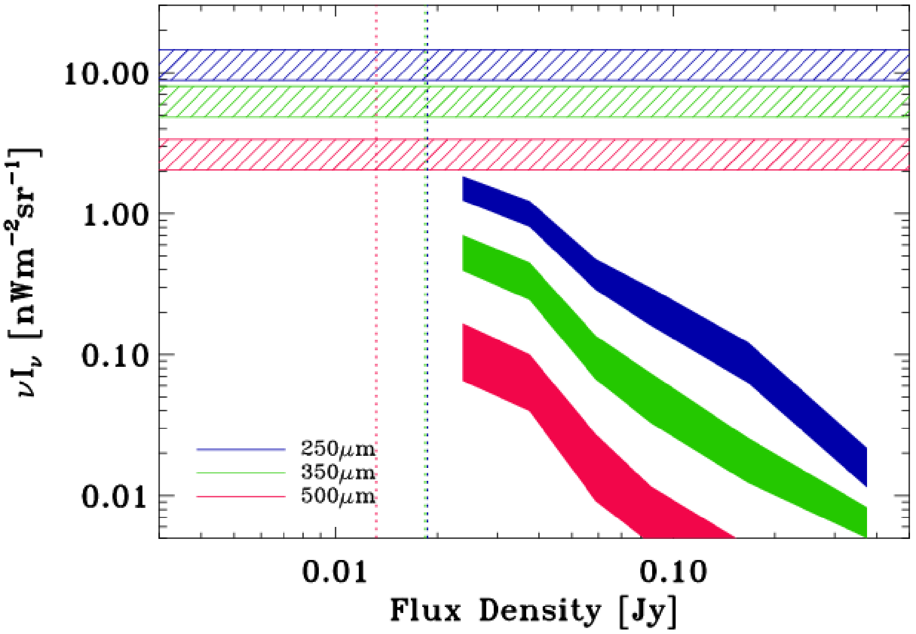

Figure 5.6: The integrated background light at 250, 350, 500 μm from the HerMES counts determined in Figure 5.7. Dotted lines are the flux at which the integrated density is (40 beams)$^{-1}$. The hatched regions are measurements of the COBE background (Lagache et al. 1999). From Oliver et al. (2010)

The flux density at which the integral source counts reach 1 source per 40 beams (with beams defined as 3.87×10^{-5}, 7.28×10^{-5}, 1.48×10^{-4} deg^2) is 18.7 ± 1.2, 18.4 ± 1.1 and 13.2 ± 1.0 mJy at 250, 350 and 500 μm respectively. Likewise the number density at 100 mJy is 12.8 ± 3.5, 3.7 ± 0.4 and 0.8 ± 0.1 deg^{-2}. These last measurements alone will be sufficient to rule out many models. In particular the comparison with SPIRE number counts shows that many models cannot fit the bright end (> 100 mJy). Exceptions are the models of Negrello et al. (2007), Valiante et al. (2009), Franceschini et al. (2010) and Pearson & Khan (2009). Of these only Valiante et al. (2009) can fit the rise from ($20 < S < 100$) mJy. The Valiante et al. (2009) model has "cooler" spectral energy distributions at higher redshift. However, increasing the number of higher redshift galaxies would have a similar effect on the counts so it would be premature to assume the spectral energy distributions need revision.

In Oliver et al. (2010) we also calculated the contribution of the resolved sources to the background intensity as a function of flux (shown in Figure 5.6). At the (40 beams)$^{-1}$depth they resolve 1.73 ± 0.33, 0.63 ± 0.18, 0.15 ± 0.07 nWm^2 or 15, 10, 6% of the nominal measured values at 250, 350 and 500 μm as estimated by Lagache et al. (1999).

Instead, in Glenn et al. (2010) we obtain some constraints for the fainter limits ($<$ 20) mJy performing a *P(D)* analysis of the same maps used by Oliver et al. (2010). For the general theory of *P(D)* analysis refer you to the Chapter 6. In general the best approach for comparing a particular model to data using *P(D)* is to generate pixel histograms as a function of the model parameters and compare directly with the data. However, not all models have smoothly adjustable parameters, and furthermore, if the model is a poor fit to the data this may provide little insight as to at which flux densities the model disagrees with observations. In Glenn et al. (2010) we follow the method applied to BLAST data and described by Patanchon et al. (2009). The Patanchon et al. (2009) method is based upon a simple fit of non physical parametric models to the data. The models are defined by the values of the differential number counts dN/dS at a set of fixed flux densities called knots. A *P(D)* fit requires that the number counts model is continuous. Therefore, we must choose a method of interpolating between the knots, and for a finite number of knots, the interpretation of the results depends on the interpolation method. We consider two methods of interpolation: first, using a power-law extrapolation between each knot (these are multiply-broken power-law fits), and secondly, using a cubic spline in log-log space. For the full method description refer you to the original paper.

The results of this analysis predict a CIRB flux density of 0.54 ± 0.08, 0.39 ± 0.06 and 0.16 ± 0.03 MJy/sr from all sources down to 2 mJy in the three bands (corresponding to the 64 ± 16, 60 ± 20 and 43 ± 12 per cent of the CIRB integrated over the SPIRE bands (Fixsen et al. 1998)). The lower results at 500 μm is due because the size of the SPIRE beam is proportional to wavelength, and hence the 500 μm band is more confused.

The results obtained with this analysis are compared with the previously described results from Oliver et al. (2010) and with the results obtained by Clements et al. (2010). These other two analysis are based upon a “classical” source-extraction technique but our analysis described in Oliver et al. (2010) was performed on the same HerMES fields and for this reason cover the same point-source population. Instead the Clements et al. (2010) analysis is based upon the *Herschel* Astrophysical Terahertz Large Area Survey (H-ATLAS) SDP data but with 250

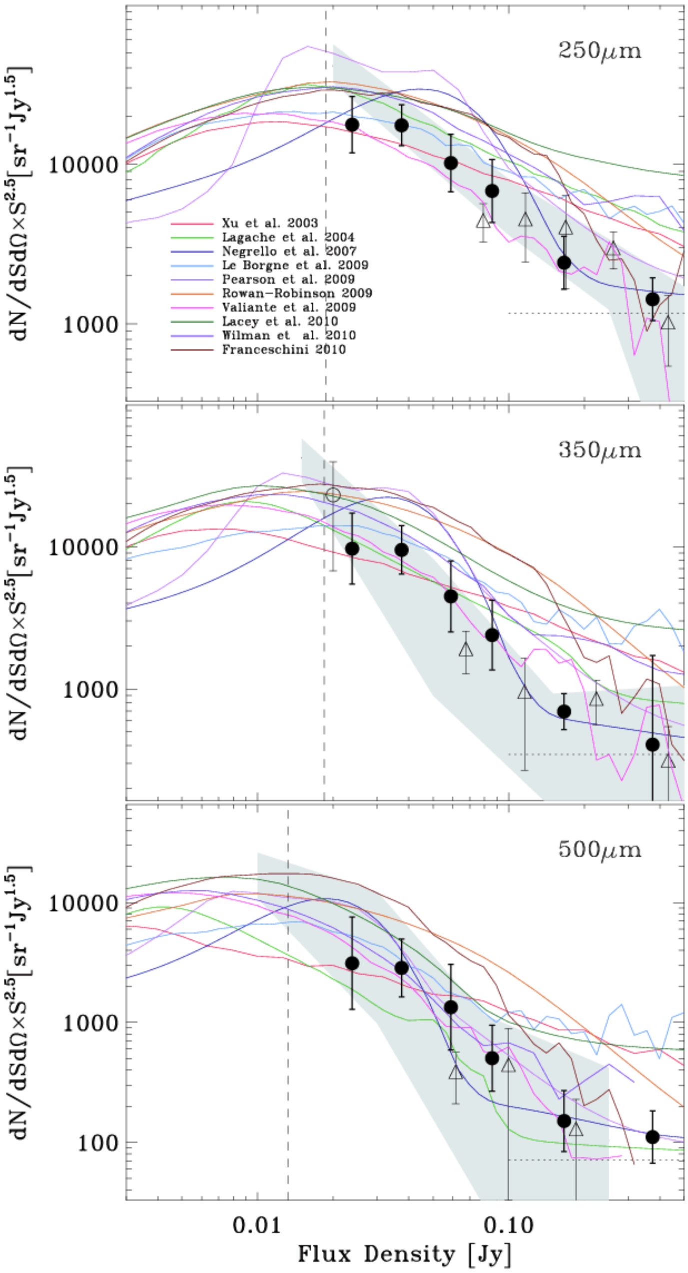

Figure 5.7: Number counts obtained from HerMES source catalogues. Filled circles are the mean number counts averaged over the following fields. GOODS-N & Lockman-North (faintest five bins only) and FLS & Lockman-SWIRE (brightest six bins only) with flux-de-boosting, completeness corrections and field-field error bars. Model fit to fluctuations of BLAST maps (omitting upper-limits, Patanchon et al. 2009) – shaded region; BLAST resolved counts (Béthermin et al. 2010) – open triangles; Khan et al. (2007) data point – open circle; asymptote from modeling of IRAS data (Serjeant & Harrison 2005) – dotted line. Dashed line indicates the flux at which the integrated number density is (40 beams)$^{-1}$. From Oliver et al. (2010)

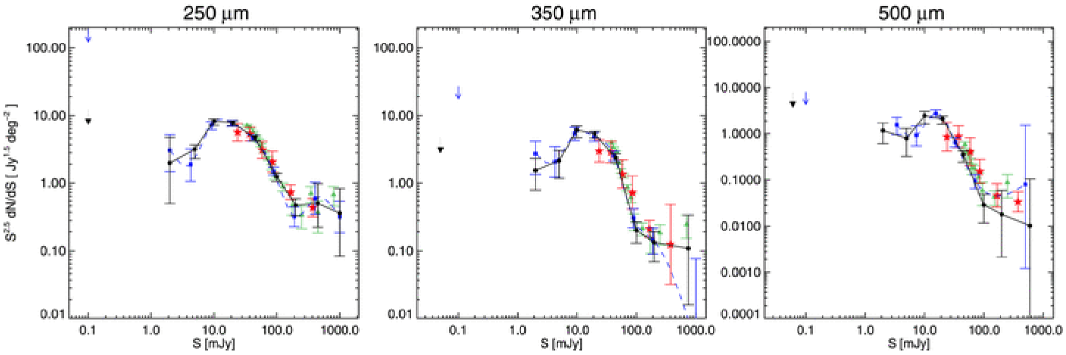

Figure 5.8: Comparison of Euclidean-normalized SPIRE *P(D)* differential number counts (solid lines/circles and dashed lines/squares for the multiply-broken power-law and spline models, respectively) with other SPIRE number counts: first (red stars) the analysis of Oliver et al. (2010) and secondly (green triangles) the H-ATLAS source extraction on an independent field performed by Clements et al. (2010). The errors are the combined statistical and systematic errors (Glenn et al. 2010).

μm source selected at all wavelength, and hence may not entirely probe the same point-source population. The results are shown in Figure 5.8 and show a good agreement with both “classical” source-extraction analysis. The results show also a break in the number counts in all the three bands at 20 mJy. However, the SPIRE data alone do not detect the change in slope in dN/dS necessary to keep the CIRB finite, as the differential counts continue to rise to the lowest limit of our *P(D)* analysis more steeply than S^{-2}.

The results show also bump in the differential counts around 400 mJy at 250 μm but not a 350 and 500 μm (but in these cases the error bars are large). This bump is present also in Clements et al. (2010) analysis and the cause is unclear: lensing is an intriguing possibility, but the signature of lensing to be larger at 500 μm due to stronger negative K-correction effects (Negrello et al. 2007).

The our results reported in Glenn et al. (2010) are compared also with some literature models (see Figure 5.9). No currently available model entirely fit the our results because the theoretical models generically over-predict the number of bright galaxies compared to the number counts from the *P(D)* analysis. In Glenn et al. (2010), we interpret the discrepancy at the bright end likely results from the presence of too many ULIRGs in the theoretical models.

In all three bands at and below 2 mJy, the *P(D)* derived number counts are consistent with the theoretical galaxy number count models also because the upper limits of the lowest flux density knot in each band lie well above the theoretical number count models.

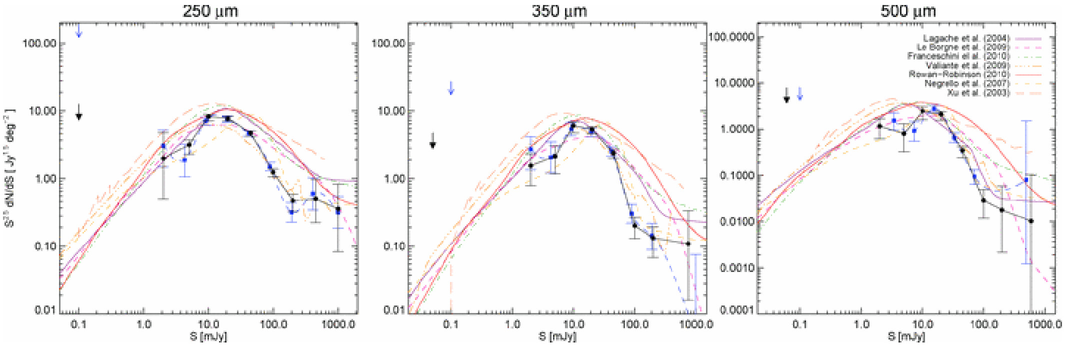

Figure 5.9: Comparison of our Euclidean-normalized differential number counts fits to a selection of models from the literature. The error bars are the combined statistical and systematic errors (Glenn et al. 2010).

The *P(D)* estimated confusion noise (6.5/6.4/6.1±0.2 mJy for the three SPIRE bands respectively) is larger than that measured by Nguyen et al. (2010) and reported previously.

5.4 HerMES: Halo occupation number and bias properties of dusty galaxies from angular clustering measurements

Another important information that we can measure with the HerMES data is the angular correlation function, $w(\theta)$, in particular for the detected sources in Lockman-SWIRE and the Spitzer First Look Survey (FLS) fields, observed as said before, in SDP (Oliver et al. 2010). The results are presented in Cooray et al. (2010). The angular correlation function is of great interest in cosmology as sources are expected to trace the underlying dark matter distribution and the clustering of sources can be related to that of the dark matter halos; $w(\theta)$ is a measure of the probability above Poisson fluctuations of finding two galaxies with a separation θ, $Pd\Omega_1 d\Omega_2 = N[1 + w(\theta)]d\Omega_1 d\Omega_2$, where N is the surface density of galaxies and $d\Omega_i$ are solid angles for each galaxy, corresponding to angle θ.

Previous studies on the spatial correlations of sub-mm galaxies was limited to at most 100 sources, leading either to a limit on the clustering amplitude (Blain et al. 2004) or a marginal detection (Scott et al. 2006). Instead in the Lockman-SWIRE field we have detected 8154, 4899, and 1680 sources with flux densities above 30 mJy at 250, 350, and 500 μm, respectively, in an area of $218' \times 218'$ (Oliver et al. 2010). These counts are supplemented by 3592, 2207, and 1016 sources detected in the FLS field over an area of $155' \times 135'$, again down to the same flux density

Table 5.3: Halo model results using the Lockman-SWIRE $w(\theta)$

Band	Flux density	$N_{\rm gal}$	$\langle z \rangle$	$\log[M_{\rm min}/M_\odot]$	$\log[M_{\rm sat}/M_\odot]$	α_s	$\langle b \rangle_z$	f_s
250μm	$S \gtrsim$ 30mJy	8154	$2.1^{+0.4}_{-0.7}$	$12.6^{+0.3}_{-0.6}$	$13.1^{+0.3}_{-0.5}$	1.3 ± 0.4	2.9 ± 0.4	0.14 ± 0.08
350μm	$S \gtrsim$ 30mJy	4899	$2.3^{+0.4}_{-0.7}$	$12.9^{+0.4}_{-0.6}$	> 13.1	< 1.8	3.2 ± 0.5	< 0.20
500μm	$S \gtrsim$ 30mJy	1680	$2.6^{+0.3}_{-0.7}$	$13.5^{+0.3}_{-1.0}$	> 13.5	< 1.6	3.6 ± 0.8	< 0.24
Combined	$S_{350}/S_{250} \gtrsim 0.85$	3333	2.5 ± 0.4	$13.4^{+0.2}_{-0.3}$	> 13.4	< 1.8	3.4 ± 0.6	< 0.19
Combined	$S_{350}/S_{250} \lesssim 0.85$	3194	$1.7^{+0.5}_{-0.6}$	$12.8^{+0.3}_{-0.5}$	> 12.9	< 1.9	2.6 ± 0.6	< 0.26

$M_{\rm min}$ is the minimum halo mass above which all halos host a central galaxy, $M_{\rm sat}$ is the mass scale at which one satellite galaxy per halo is found, in addition to the central galaxy, α_s is the power-law slope of the satellite occupation number with halo mass, $\langle b \rangle_z$ is the linear bias factor of the sources, and f_s is the satellite fraction. The redshift range is an approximate estimate based on the color-color diagram of the source sample through a comparison to isothermal, modified black-body SEDs with a wide range of dust temperatures and emissivity parameters (see, Figure 5.11 for an example involving $S_{250} > 30$ mJy and for the two color cuts). From Cooray et al. (2010).

in each of the three bands. These numbers allow clustering estimates at the same precision level as the first-generation of clustering studies at shorter IR wavelengths with source samples from Spitzer data (e.g. Magliocchetti et al. 2007). Instead of simple power-law models, the correlation functions of HerMES sources have high enough signal-to-noise ratios that we are also able to constrain parameters of a halo model (Cooray & Sheth 2002).

In Figure 5.10-left, we summarize our first set of results related to $w(\theta)$ measurements for each of the three SPIRE bands and for sources with S $>$ 30 mJy. We show correlation functions measured for sources in both Lockman-SWIRE and FLS fields here. We find no statistical difference in the correlation functions of sources detected in the two fields down to the flux density cut-off of 30 mJy.

In Figure 5.10-right we show the results where we split the 250 μm source sample to two bins in flux density between 20 and 35 mJy and above 35 mJy and where we split the combined sample to two color bins: this is done to test for evolutionary hints in clustering.

To model $w(\theta)$ we need to establish the redshift distribution of the source samples. Given the lack of adequate spectroscopic redshifts, we make use of sub-mm colors to generate a qualitative redshift distribution (e.g., Hughes et al. 2002). While these distributions are generally consistent with certain model predictions (e.g., Valiante et al. 2009) and with sub-mm galaxy data (e.g., Chapman et al. 2005), the redshift distribution we recover is strongly sensitive to the SEDs used and should only be considered as an approximate.

The Table 5.3 summarize the results obtained with the model fitting assuming WMAP 5-year best-fit ΛCDM cosmology (Komatsu et al. 2009). Down to the 30

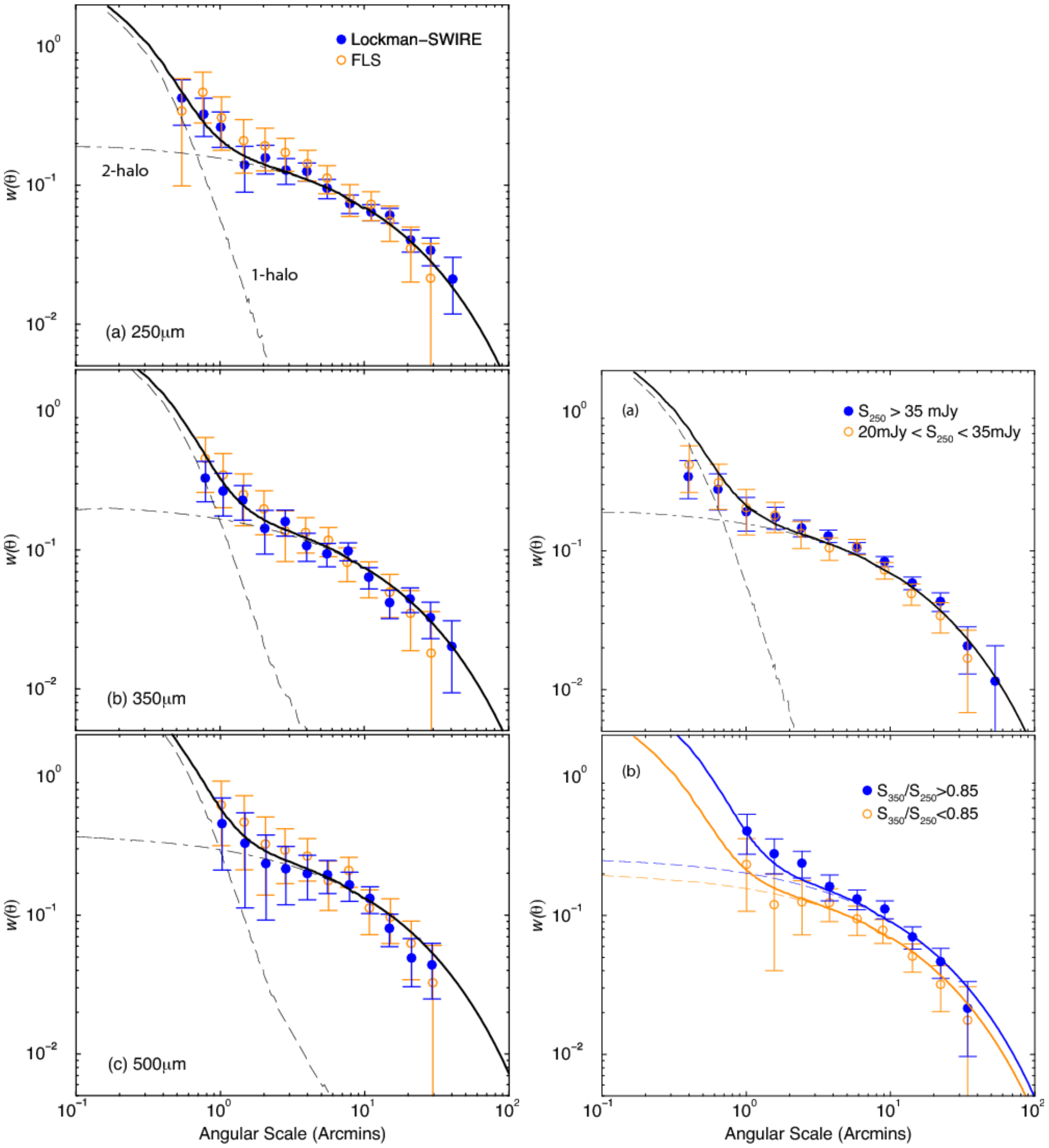

Figure 5.10: **Right** Angular correlation function of SPIRE sources in Lockman-SWIRE and FLS with flux densities above 30 mJy: a) 250 μm; b) 350 μm; and c) 500 μm. The lines are illustrative halo models consistent with best-fit results for the occupation number, with the dot-dashed lines showing the 2-halo term traced by linear clustering and the long-dashed lines showing the 1-halo term coming from multiple sources within the same halo. The solid lines show the total correlation function from our models. **Left** a) Angular clustering of 250 μm sources in Lockman-SWIRE field divided into flux densities between 20 and 35 mJy and above 35 mJy. b) Angular clustering for the combined 250 μm and 350 μm in the Lockman-SWIRE field with $S_{350}/S_{250} < 0.85$ sample again or > 0.85. From Cooray et al. (2010)

mJy flux density cut, we find average bias factors of 2.9 ± 0.4 and 3.6 ± 0.8 for 250 and 500 μm sources, respectively. Fitting a power-law to all data, the correlation lengths, r_0 are 4.5 ± 0.5 Mpc (250 μm) and 6.3 ± 0.7 Mpc (500 μm). While 250 μm sources are more likely to be found in halos with mass $(5 \pm 4) \times 10^{12}$ $M_\odot$, we find that the bright 500 μm sources in our sample occupy halos of $(3.1 \pm 2.8) \times 10^{13}$ $M_\odot$. The difference is because at a given redshift the 500 μm sources are at a higher luminosity. Our modeling allows us to establish that $(14 \pm 8)\%$ of the sources appear as satellites in massive halos than the minimum mass scale. In the case of 350 μm and 500 μm source samples, we have failed to accurately determine the parameters related to satellite occupation number. As a test on the validity of our results to uncertainties in $n(z)$, we also considered two extreme possibilities by placing all sources either at $z \sim 1.5$ or $z \sim 3$ and found parameters within 1σ uncertainties of the estimates quoted in Table 5.3. This is mostly due to the fact that $n(z)$ we use for model fitting, with an example shown in Figure 5.11, is broad with a tail to low redshifts.

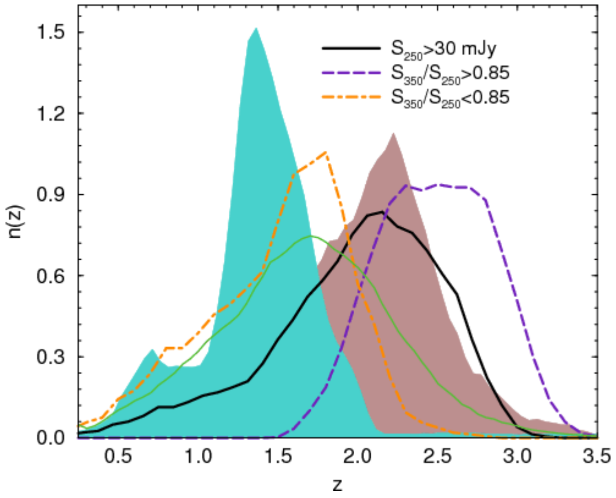

Figure 5.11: Approximate redshift distribution of sources in the Lockman-SWIRE field with $S_{250} > 30$ mJy (thick solid line in black) and for the two cases based involving color cuts with $S_{350}/S_{250} > 0.85$ (magenta dashed line) and $S_{350}/S_{250} < 0.85$ (orange dot-dashed line). The thin solid green line and the two shaded regions in the background show example predictions for the $S_{250} > 30$ mJy sample and the two color cuts, respectively, using models from Le Borgne et al. (2009; thin green line) and Valiante et al. (2009; shaded regions) From Cooray et al. (2010)

Our measurements show some evidence for non-linear clustering at arc-minute angular scales. Compared to 250 μm, an increase in clustering at arc-minute angular scales is less clear at 350 and 500 μm due to the increase in the beam size. In comparison, angular power spectra of BLAST fluctuations did not convincingly reveal a 1-halo term (Viero et al. 2009) and clustering was found to be even below the linear term at smallest angular scales probed. The increase in arc-minute-scale angular clustering we see here demonstrates the crucial role played by superior angular resolution of SPIRE. Beyond this initial study, future work involving understanding the large-scale structure distribution of sub-mm galaxies will pursue additional cross-clustering studies of sub-mm sources with optical and shorter IR wavelengths, and studies of unresolved fluctuations.

5.5 Discussion

To conclude, I want summarize the results obtained in confusion noise characterization and in the number counts and clustering analysis.

In Nguyen et al. (2010) we have made a precision measurement of the confusion and instrument noise in the HerMES SDP SPIRE scan maps. The estimated confusion noise is (5.8 ± 0.3, 6.3 ± 0.4, 6.8 ± 0.4) mJy/beam in the three SPIRE bands, substantially confirmed also using simulations. These results are lower than those that are measured using a *P(D)* analysis (Glenn et al. 2010).

Instead, the number counts analysis was performed in two ways: the first way is the “classical” source-extraction analysis (Oliver et al. 2010), the second way is a *P(D)* analysis performed by Glenn et al. (2010).

Our results are reported in Oliver et al. (2010) and show approximately flat counts for $S > 100$ mJy and the a steep rise (see Figure 5.7). There is flattening to about 20 mJy. Our analysis resolve 15, 10, 6% of the nominal measured values at 250, 350 and 500 μm as estimated by Lagache et al. (1999). The counts show also a good fit with the counts estimated from a *P(D)* fluctuations analysis of BLAST maps (Patanchon et al. 2009). The comparison with some models show some discrepancy in particular at flux greater than 100 mJy. The Franceschini et al. (2010) model is one of the exceptions.

Our *P(D)* analysis, reported in Glenn et al. (2010), show a break in the number counts in all the three bands at 20 mJy and a bump in the differential counts around 400 mJy at 250 μm. The comparison with the model show a discrepancy at high fluxes, probably due to the presence of too many ULIRGs in the theoretical models. At low fluxes (< 2 mJy) all the models are consistent with our *P(D)* analysis. In this case the resolved CIRB integrated in the three bands is the (64 ± 16, 60 ± 20 and 43 ± 12) %.

Our clustering analysis, reported in Cooray et al. (2010), derive an average bias factors of 2.9 ± 0.4 and 3.6 ± 0.8 for 250 and 500 μm sources, respectively and show that the 250 μm sources are more likely to be found in halos with mass $(5 \pm 4) \times 10^{12}\ M_{\odot}$ and the bright 500 μm sources in our sample occupy halos of $(3.1 \pm 2.8) \times 10^{13}\ M_{\odot}$, differences due to the fact that the galaxies founded at 500 μm are more luminous than those detected a shorter wavelength. In general we can derive some evidence for non-linear clustering at arc-minute angular scales.

All these results are very interesting because based upon only first Science Demonstration Phase (SDP) data, when the HerMES program consist in $\sim$ 900 hr of observations.

6

The *P(D)* Analysis

In this chapter I will report my work about the Probability of Deflection (P(D)) analysis. This technique was developed by Scheuer et al. (1957) to study the confusion-limited maps. I applied this technique to better understand the amplitude and slope of counts of unresolved sources. The result of this analysis on Spitzer maps have been used in Franceschini et al. (2010). I will report also the result of this analysis applied to the first SPIRE HerMES Science Demonstration Phase maps.

6.1 Introduction

Studies of the generation and assembly of stellar populations in galaxies largely benefit by far-IR observations, on consideration that the IR flux is a close prior to the rate of star formation (the bulk of which happens in dust-obscured environments). At the same time, major episodes of nuclear AGN accretion are also dust-obscured and visible in the IR. In the last 30 years the NIR-FIR-SUBMM astronomy has experienced a great development. In particular, with the first space missions IRAS and ISO (see Section 1.2), galaxy evolution has been studied in detail and is currently quite precisely know between $0 < z < 1$. IRAS and ISO was insufficient sensitivity at higher redshifts for any significant constraints to be set there but first millimetric and sub-millimetric survey showed that major events of star-formation in the universe happen at $z > 1$ and are likely responsible for the origin or assembly of the most massive galaxies today. A great improvement in our knowledge of the infrared emissivity of source population at great redshift has been recently made possible with the deep sky exploration by the Spitzer and the exciting new data from *Herschel*.

In past, some model (e.g. Franceschini et al. 2001) was rather successful in explaining IRAS and ISO results. But with new data from Spitzer and from *Herschel*

at redshift greater than 1 the models require an update. The new best-fit model by Franceschini et al. (2010) takes advantage from a large variety of new data at high redshift from Spitzer, the data from sub-mm new mission and millimetric ground-based observations. From the model we derive indications about a very rapid increase of galaxy volume emissivity with redshift up to $z \sim 1$, paralleled by an increased incidence in high-z sources of dust extinction and re-radiation, with respect to local galaxies. Besides, the counts from Spitzer 24 μm require a combination of fast evolution for the dominant population and a bumpy spectrum with a substantial PAH emission at redshift 1 to 2.
We have also limitations to study the others MIPS bands ($70-160$ μm) due to source confusion. The confusion is a fundamental problem, particularly for FIR and sub-mm surveys by space telescopes: faint objects crowd together and start to be spatially unresolved from each other and our signal becomes a mixture of objects of various intensities blended together by the Point-Spread Function (PSF) of the instrument. This is due to poor instrument resolution, typically due to diffraction. For this reason we have two problems: we cannot obtain good constraints about faint source counts and we systematically overestimate the sources flux. For solve this problem Scheuer et al. (1957) developed a technique know as *P(D)* - probability of Deflection: this technique is based upon a idea that in addition to the average integrated flux by all sources in a sky area, the background radiation also contains spatial information, the cell-to-cell fluctuations, which can be used to further constrain the source flux distribution and spatial correlation properties. I developed some simple code to derive the *P(D)* distribution from a field map and in this way put some constraints on number counts below the confusion limit.

6.2 Theory of *P(D)* distribution analysis

The *P(D)* technique was first applied to data analysis in radio astronomy (Scheuer et al. 1957 and Wall et al. 1975) and later in X-ray (Scheuer 1974), infrared (Jenkins et al. 1991 & Franceschini et al. 1998) and Lyman-α (Webb et al. 1992). The method derives the probability distribution of measurements in terms of the underlying source count, which may be recovered by a model fitting model: in this way it's possible to obtain information by sources that are much too faint to be detected as individuals.

Two papers by Scheuer (1957, 1974) and one by Condon (1974) give all details about this technique but we want describe some step here derived from Wall & Jenkins (2003) and Franceschini et al. (2010).

The usually most important contribution to the cell-to-cell intensity fluctuations comes from the stochastic nature of the spatial distribution of sources among elementary cells with an effective solid angle ω_{eff} (see below). They can be expressed as

$$(\delta I)^2 = \frac{\omega_{\rm eff}}{4\pi} \int_0^{S_d} S^2 \, \frac{dN}{dS} \, dS. \tag{6.1}$$

What is really measured, however, is not the flux S but the detector's response $x = f(\vartheta, \varphi)$, $f(\vartheta, \varphi)$ being the angular power pattern of the detector. Let

$$R(x) = \int_0^\infty dN\left[x/f(\vartheta, \varphi)\right]/dS \cdot d\omega/f(\vartheta, \varphi) \tag{6.2}$$

be the *mean number of source responses of intensity x in the beam.* For a Poisson distribution of the number of sources producing a response x, its variance equals the mean $R(x)dx$. Adding the variances of all responses up to the cutoff value x_c (brighter sources are considered to be individually detected) gives the contribution of unresolved sources to fluctuations:

$$(\delta I)^2 = \int_0^{x_c} x^2 \, R(x) \, dx. \tag{6.3}$$

The cutoff x_c is chosen to be some factor q times $(\delta I)^2$; usually $q = 3$–5. The RMS background fluctuations (δI) imply a sky noise $\sigma_{conf} = \langle(\delta I)^2\rangle^{1/2}$ for observations with spatial resolution ω_{eff}. Assuming a Gaussian fit with $FWHM = \theta_0$ to the image's PSF:

$$f(\theta) = exp[-4(\theta/\theta_0)^2 ln(2)] \tag{6.4}$$

with $\theta_0 \simeq 1.02\lambda/D$ to represent the Airy function for diffraction-limited observations, we have

$$\sigma^2 = (\delta I)^2 = \pi(\theta/\theta_0)^2 \; \Sigma(x_c), \tag{6.5}$$

$$\Sigma(x_c) = \int_0^{x_c} dx x^2 R(x) = \tag{6.6}$$

$$= \int_0^{x_c} dx x^2 \int_0^\infty d\psi N[x/f(\psi)] exp(4\psi ln(2))$$

with $\psi = \theta/\theta_0$. In practice, it is custom to compute the confusion limit σ_{conf} from the relation

$$\theta_0 = \sigma/\sqrt{\pi\Sigma(x_c)} \tag{6.7}$$

by assuming $\sigma = qx_c$ and $q = 3$ or 5 (e.g. Franceschini et al. 1989). The confusion limit (at 3 or 5 times the RMS confusion noise $\sigma_{conf} = \sigma$) is then easily computed with the zero's of relation 6.7.

The integrated signal D recorded by the detector is the sum of the responses x due to all sources in the angular resolution element. Its probability distribution function *P(D)* is informative on the amplitude and slope of counts of unresolved sources. Scheuer (1957) has shown that, under the assumption of a random sky distribution of sources, its Fourier transform, $p(\omega)$, is a simple function of the FT $r(\omega)$ of $R(x)$: $p(\omega) = \exp[r(\omega) - r(0)]$. It follows:

$$P(D) = \int_{-\infty}^{\infty} p(\omega) \exp(-2\pi i \omega D)\, d\omega = \tag{6.8}$$

$$\int_{-\infty}^{\infty} \exp\left[r(\omega) - r(0) - 2\pi i \omega D\right]\, d\omega = \tag{6.9}$$

$$2\int_{0}^{\infty} \exp\left\{-\int_{0}^{\infty} R(x)\left[1-\cos(2\pi\omega x)\right] dx\right\}\cdot \tag{6.10}$$

$$\cdot\cos\left[\int_{0}^{\infty} R(x)\sin(2\pi\omega x)\, dx - 2\pi\omega D\right] d\omega.$$

This synthetic *P(D)* has to be convolved with the (typically Gaussian) distribution of the instrumental noise to be compared with the observations. Rather than in terms of the total flux per sky beam D, it is more frequent to refer the fluctuation analysis to the flux per unit sky area $D_a = D/\omega_{eff}$, where ω_{eff} is the imager effective area and is defined as

$$\omega_{eff} = \frac{\int_0^{x_c} xR(x)dx}{I(< x_c)} \tag{6.11}$$

with $I(< x_c)$ being the residual background.It turns out that

$$\omega_{eff} \simeq \int f(\vartheta)d\Omega = \pi\int_0^{\infty} d\theta^2 f(\theta) = \pi(\theta_0/2)^2/ln(2) \tag{6.12}$$

for our Gaussian representation of the PSF in eq. (6.4).

Assumed that the number count distribution below the detection limit can be represented as a power-law, $N(> S) = K(S/S_k)^{-\beta}$, then eq. [6.10] can be integrated to get (Condon 1974):

$$\sigma_{conf} = \left[\frac{q^{2-\beta}}{2-\beta}\right]^{1/\beta} (\omega_\sigma \beta K)^{1/\beta} S_k, \tag{6.13}$$

$$\omega_\sigma = \int f(\vartheta, \varphi)^\beta d\Omega \tag{6.14}$$

which allows estimation of the slope of the counts (β) below the detection limit from a given measured value of the cell-to-cell fluctuations σ_{conf}. This constraint on $N(S)$ applies down to a flux limit corresponding to $\sim$ 1 source/beam. Assumed that S_k represents the confusion limit ($S_k = q \times \sigma_{conf}$) of a survey having an areal resolution ω_{eff}, then eq. 6.14 further simplifies to a relation between the number of sources K resolved by the survey (and brighter than S_k) and the parameters q and β:

$$K = \frac{2-\beta}{\beta q^2}\frac{1}{\omega_\sigma} : \tag{6.15}$$

this implies the confusion limit to occur at the flux corresponding to an areal density of $(\beta q^2/[2-\beta])^{-1}$ sources per unit beam area ω_σ. For Euclidean counts and $q = 3$, this corresponds to 1 source/27 beams.

6.3 Method

We can imagine a *P(D)* distribution function as a convolution between the gaussian instrumental noise and a *P(D)* modeled according with the model. An example of this is showed in Figure 6.6. It's so possible, using *P(D)* analysis, test a model and derive information about the instrumental noise. I will describe now the methods used to testing the best-fit model by Franceschini et al. (2010).

To realize an estimate of *P(D)* we need to divide the maps in cells. The problem is to choose the optimal cell area. Studying the problem we derived that the best choose is use a cell area equal to the instrument beam area. The beam area is calculated using:

$$b_a = \frac{\pi}{4\ln 2} \cdot F^2 \tag{6.16}$$

where F is the instrument PSF FWHM. Once divided the map in cells, we need to calculated the total flux contained in these cells and create the histogram for these total fluxes. In any applications of this procedure, to investigate how different spatial sampling influences the *P(D)* analysis, it is important to vary the beam area changing the radius of the beam with step equal to $\pm 0.25 \times p_s$, where p_s is the pixel size of the maps (e.g. for the MIPS 70 μm the p_s is equal to $4''$).

Once we have an estimate of a map's *P(D)* distribution, we can use two ways to testing the model and derive informations about number counts below the confusion limit.

In the first way we can compare a measured *P(D)* with a theoretical *P(D)* distribution derived as reported in Section 6.2 using the Franceschini et al. (2010) model (see Section 6.4). To take into account the instrumental noise, we need to convolve the theoretical *P(D)* distribution with a gaussian distribution representing the instrumental noise (see Figure 6.6).

In the second way we can compare the measured *P(D)* on a real map with the measured *P(D)* on a map simulated in according with a model.

In this case we need to perform some steps:

1. Do a *P(D)* analysis on the real maps;

2. Use the model number counts (both differential and integral) to realize some mock source's catalogs;
3. Convolve these sources with a instrument PSF and put them on a empty map;
4. Add to the simulated map a gaussian instrumental noise and perform a *P(D)* analysis.
5. Compare the "simulated" and "real" *P(D)* results.

To realize the "mocks" catalogues we used the number counts derived from Franceschini et al. (2010) model (see Section 6.4). The mock catalog contains a number of sources equal to those contained in an area of one square degree with flux always derived from Franceschini et al. model. After these steps, we need to scatter these sources on a empty map: the area of this map is equal to one square degree. Before we need to convolve the source's flux with a instrumental PSF (see Figure 6.1 for an example). Once the sources are spread with the PSF, we can associate random position to them and put them on the map.

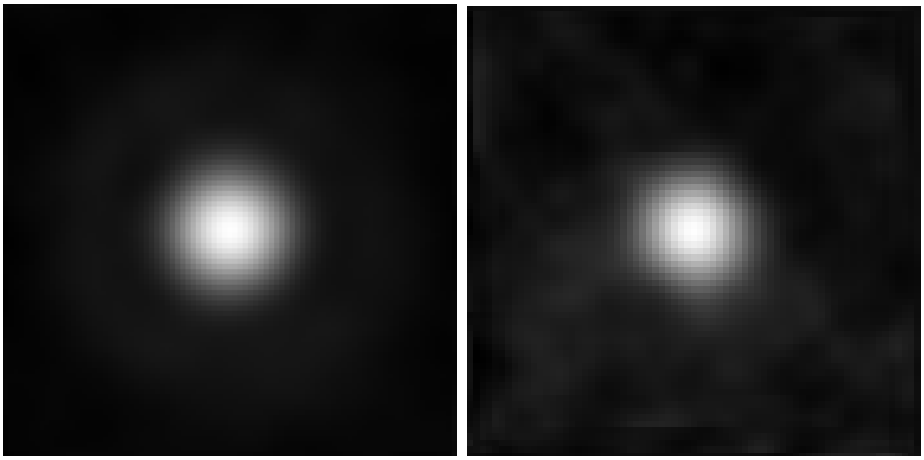

Figure 6.1: **Left:**MIPS 70 μm PSF as released by FIDEL Team. The FWHM is $18''$. **Right:** SPIRE 250 μm PSF based upon SDP data and released by HerMES Team. The FWHM is $18''.1$.

At this point we have a "free-noise" map to which we need to add the instrumental noise. The instrumental noise is a gaussian distribution with RMS σ_i based upon an initial value derived from an estimate. The estimate used is derived in different ways depending on the field considered (Spitzer FIDEL and SPIRE HerMES). I will report in their respective sections the method to obtain this estimate.

Once added the instrumental noise we can perform the *P(D)* analysis and compare the results with the real *P(D)* results: these last two steps are iterated changing the instrumental noise until the "simulated" and "real" results are in good agreement.

6.4 Multi-wavelength modelling of IR galaxy evolution

We applied the *P(D)* analysis to Spitzer data to testing and confirm the Franceschini et al. (2010) model. The Franceschini et al. (2010) adopted multi-wavelength modelling of the IR galaxy evolution follows a similar approach to the one pursued by Franceschini et al. (2001), which was calibrated on a much shallower database essentially restricted to the ISO survey data. The Franceschini et al. (2010) multi-wavelength analysis is not intended to provide us with a detailed and complete justification of the complex physical processes involved in star-formation and galaxy assembly and traced by the IR emission. Instead the model guarantees the best possible adherence to an enormous variety of data on the cosmic source emission from the local to the distant universe and is intended to identify general patterns in galaxy evolution useful for comparison with more physically-based galaxy formation models. Our model population includes contributions by various source categories characterized by different physical and evolutionary properties:

1. the first considered class of sources are non-evolving normal spirals that dominate the multi-wavelength Local Luminosity Functions (LLF) at low luminosities. Such a population was required in the Franceschini et al. (2001) analysis to explain some features in the extragalactic source number counts, particularly those at 15 μm available at that time;

2. a second obvious class of sources to be considered in the model and characterized by high rates of evolution are active galactic nuclei, which are found in substantial numbers in IR selected surveys at all wavelengths;

3. as discussed by Franceschini et al. (2001) and Fadda et al. (2002) among others, AGNs of any kinds are far insufficient to explain the faint IR source statistics, because their high IR luminosities contribute to the counts only at rather bright fluxes ($S_{24} \geqslant 10$ mJy), while they are too rare to explain the large observed numbers at fainter limits. To try explaining the fainter number counts we need to refer to a much more numerous population of fast evolving objects. A third component was then considered, starburst galaxies of moderate luminosities, or LIRGs, which are already present in Franceschini et al. (2001), Elbaz et al. (2002),Eales et al. (1999), among

others. The increasing relevance of this population with redshift has been one of the main outcomes of the ISO mission and has been confirmed by the Spitzer/MIPS observations (Le Floc'h et al. 2005). All these analyses found that the MIPS data require a fast increase in the comoving emissivity up to at least $z \simeq 1$.

4. Current data impose an important modification to the Franceschini et al. (2001) evolutionary scheme: they require the introduction of a fourth evolutionary population component of very luminous starburst galaxies, or ultra-luminous infrared galaxies (ULIRGs), dominating the cosmic IR emissivity above$z \simeq 1.5$. This emerges in particular from the analysis of the galaxy samples selected by the deep Spitzer/MIPS 24 μm surveys, and their improved capability of detecting cosmic far-IR sources at redshifts $z > 1$ and up to $z \simeq 3$ (see Figure 6.2). These observations have revealed the existence of a separate population of ULIRGs at high-redshift, essentially absent or very rare locally, hence characterized by an extremely fast evolution in cosmic time. Millimetric observations with SCUBA since several years, confirmed by other more recent observations, have also found clear evidence of such very luminous objects at high redshifts.

In consideration of the multi-wavelength nature of our used database, the definition of a spectral model is particularly important. Our choice has been to define apriory only the average spectrum of the type-I AGNs, because this has little influence on the model outcomes except for the 24 μm statistics. For the other population components (spirals, LIRGs and ULIRGs, with the exception of the low-luminosity spirals which have cooler spectra), we have basically referred our model spectra to that of the prototype local starburst galaxy, M 82. We have then made adjustments to it so as to achieve a best-fitting to the available data from the mid-IR throughout the millimeter. We anticipate that an interesting outcome of our analysis was that small modifications to the M82 broad-band spectrum are sufficient for obtaining this best-fit.

AGN For the type-I AGN population we assume an SED corresponding to an emission model by a face-on dusty torus and is reported as a green dot-dashed line in Figure 6.2. This average spectrum is taken from the radiative transfer model by Fritz et al. (2006), and was optimized to fit photometric data for AGNs in the SWIRE surveys (see Franceschini et al. 2005; Hatziminaoglou et al. 2008). Note finally that our detailed spectral modelling for AGNs is not critical, because type-I AGNs contribute significantly only to the 24 μm, and to a lower extent to the 70 μm, statistics at the bright fluxes.

Spirals Also in the case of the normal spiral population a precise definition of

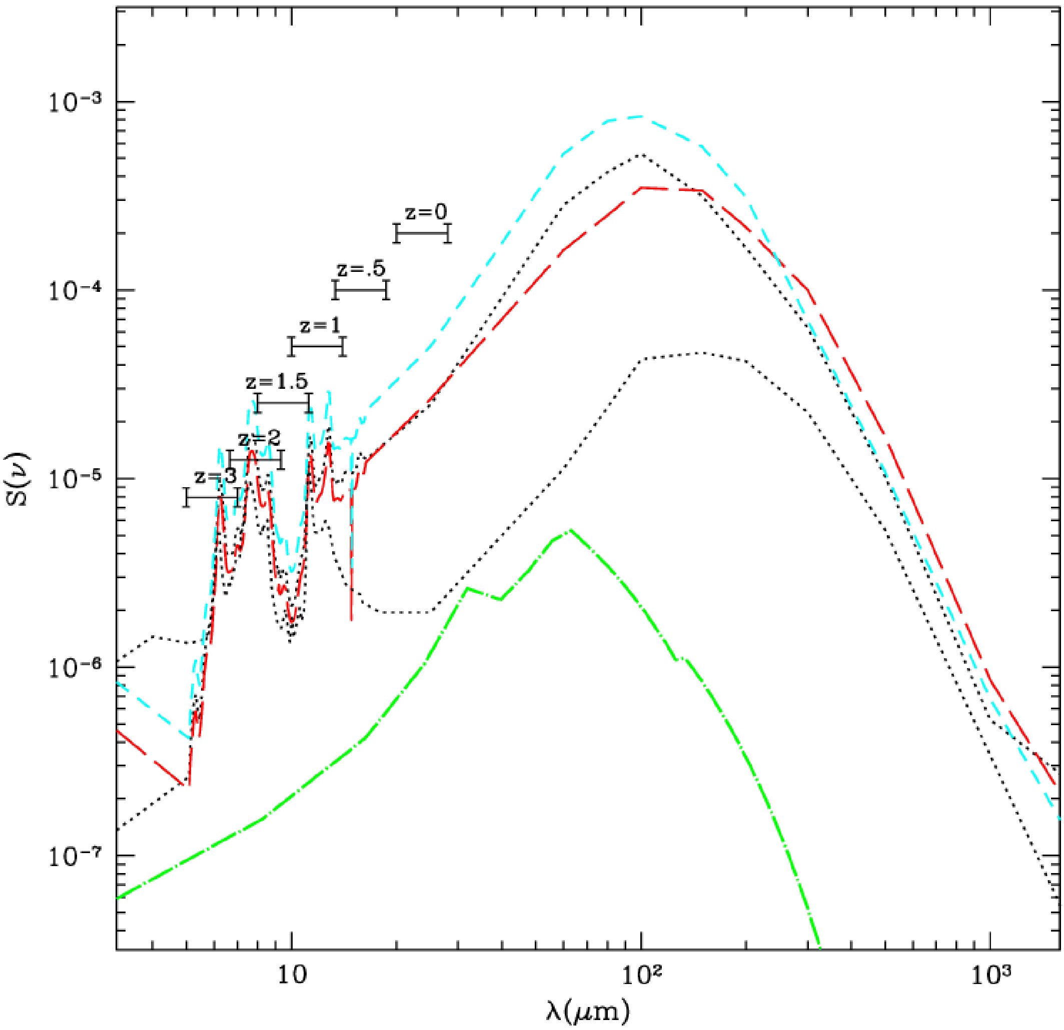

Figure 6.2: The Franceschini et al. (2010) adopted IR spectra of various galaxy populations. The short-dashed cyan line corresponds to our adopted spectrum for the moderate-luminosity LIRG starburst population, while the red long-dashed curve is the spectrum of high-luminosity ULIRG sources. In both cases the spectra are similar to that of the prototype star-forming galaxy M 82 (in the range from 5 to 18 μm it is precisely the ISOCAM spectrum of M 82). The lower dotted line corresponds to a low-luminosity inactive spiral, while the upper dotted line is closer to that of ULIRGs. The lower dot-dash green line is the average type-I AGN spectrum. The boundaries of the MIPS 24 μm filter are also shown in the source rest-frames at various source redshifts: due to the prominent PAH features, we expect relative maxima in the redshift distributions at $z \sim 1$ and ~ 2, in agreement with the observations.

the spectral model is not critical for our attempt to interprete the high-redshift source evolutionary properties. Although spirals dominate the low-luminosity end of the LLFs, their lack of evolution implies that their number density becomes negligible compared to other evolving populations at cosmological redshifts. We have then modelled the redshift-dependent multi-wavelength LLF's of spiral galaxies by assuming SEDs dependent on luminosity, with spectra ranging from those typical of low-luminosity inactive objects with peak emission at 200-300 μm, to those peaking at 60-80 μm characteristic of luminous luminous IR galaxies.

LIRG and ULIRG galaxies Of course, more critical are the assumptions about the spectral fitting of the two luminous galaxy populations considered in the model, the moderate and the high-luminosity objects (i.e. the LIRGs and ULIRGs). To simplify our treatment, we adopted for each one of the two classes a single spectral form, independent of luminosity. For the LIRG and ULIRG objects our best-fit spectra are shown in Figure 6.2. It should be noticed how similar the two spectra are, both of them turning out to be close to the spectrum of the prototype local starburst galaxy M 82.

With our spectral model for the different source populations, we computed Luminosity Functions (LF) at all IR wavelengths by convolving the spectra with the detailed filter response functions of the various photometric channels. Once the redshift-dependent multi-wavelength luminosity functions for our source populations are set, the procedures for comparing them to the variety of data are also straightforward. As illustrated in Figures 6.3 and 6.4, our best-fit model appears to reproduce a wide variety of multi-wavelength IR data, from redshift-dependent luminosity functions to faint number counts, and providing marginally acceptable fits of the background spectral intensity and cell-to-cell fluctuations. There is only a slight tendency of the model fit to remain low in the lowest bin at 24 μm and $0 < z < 0.25$, probably due to the unaccounted effects of the local large-scale structure in the luminosity function data. In any case, the low-z behavior of the model was calibrated on a variety of number count data at bright fluxes (including the IRAS all-sky far-IR counts and those from the Spitzer SWIRE project), which guarantees excellent control of the local IR universal emissivity.

6.5 Multi-wavelength modelling of IR galaxy evolution: the *P(D)* analysis

To obtain good constraints about number counts below the confusion limit we applied the *P(D)* analysis to some Spitzer and SPIRE SDP data. The results are reported in the following sections.

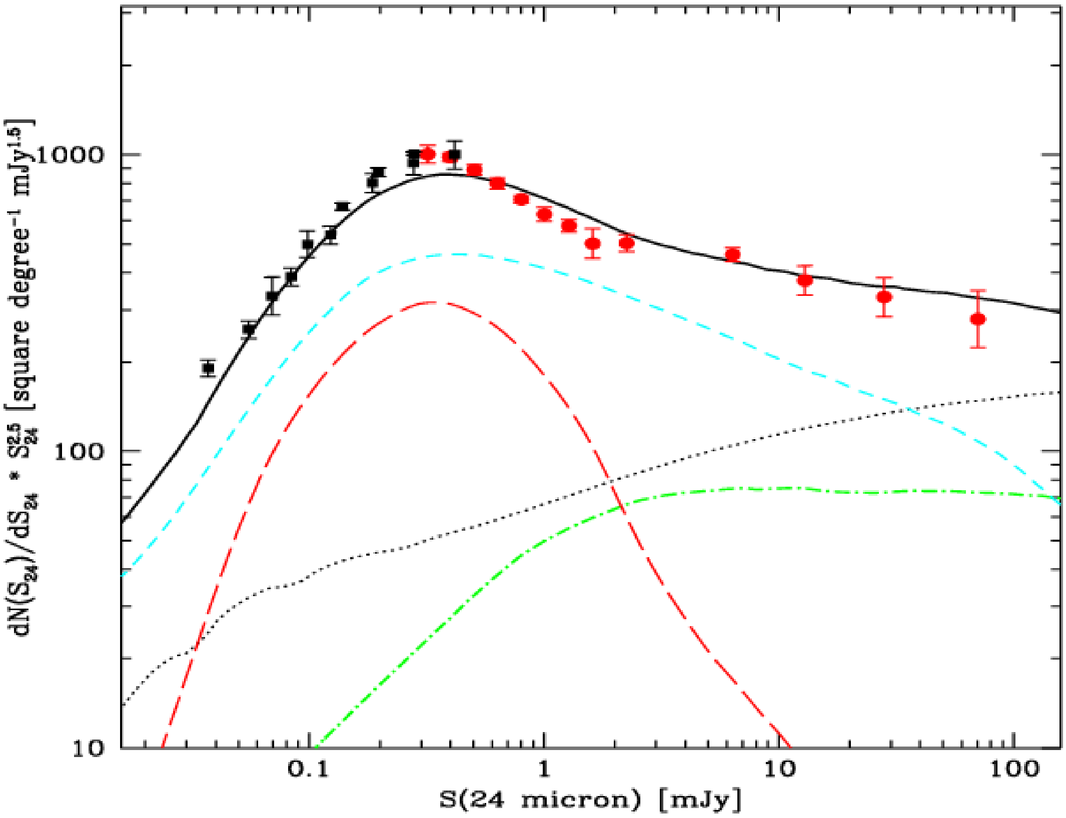

Figure 6.3: Euclidean-normalized differential number counts of extragalactic sources at 24 μm compared with our model fit. The red circles are from the analysis of SWIRE survey data by Shupe et al. (2008), black squares from Papovich et al. (2004). The contribution by type-I AGNs is shown as green dot-dashed line, moderate-luminosity starbursts (the LIRGs) make the cyan short-dash line (type-II AGNs and starbursts are included in the same population on the assumption that in both classes the IR spectrum is dominated by starburst emission). The red long- dashed line corresponds to the population of high-luminosity sources dominating the IR emissivity at high redshifts. The dotted line is the separate contribution of normal spirals, while the continuous line is the total model counts. From Franceschini et al. (2010)

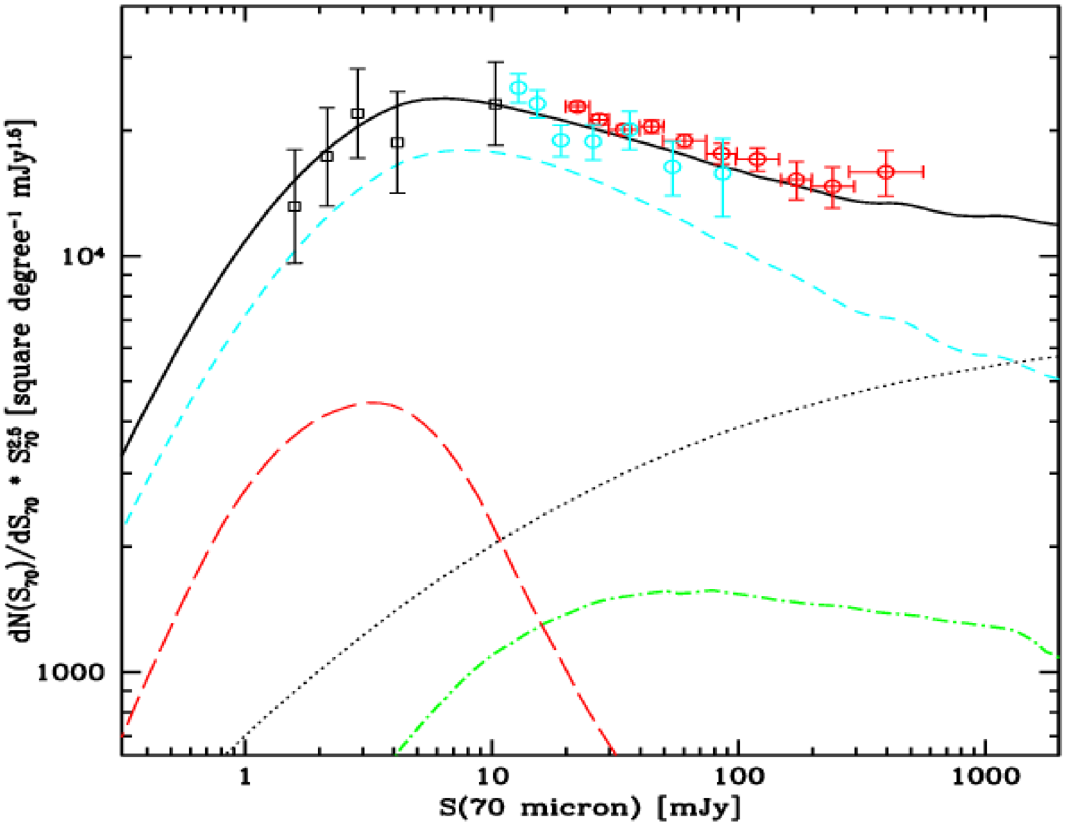

Figure 6.4: Euclidean-normalized differential number counts of extragalactic sources at 70 μm compared with our model fit. Red open circles are from our analysis of the SWIRE survey data, open squares to a very deep survey by Frayer et al. (2006), the cyan circles are the most recent assessment of the counts based on Spitzer/MIPS observations in the COSMOS area by Frayer et al. (2009). The red filled datapoint at bright fluxes is from the IRAS 60 μm survey appropriately scaled to the current effective wavelength (Vaccari et al. 2009). Moderate-luminosity starbursts (including type-II AGNs) make the cyan short-dash line. The red long-dashed line corresponds to the population of high-luminosity sources dominating the IR emissivity at high redshifts. The dotted line is the separate contribution of normal spirals. At bright 70 μm flux densities type-I AGNs, shown as green dot-dashed line, provide an important contribution to the counts. The continuous line is the total model counts. From Franceschini et al. (2010)

6.5.1 Applications to the Spitzer data

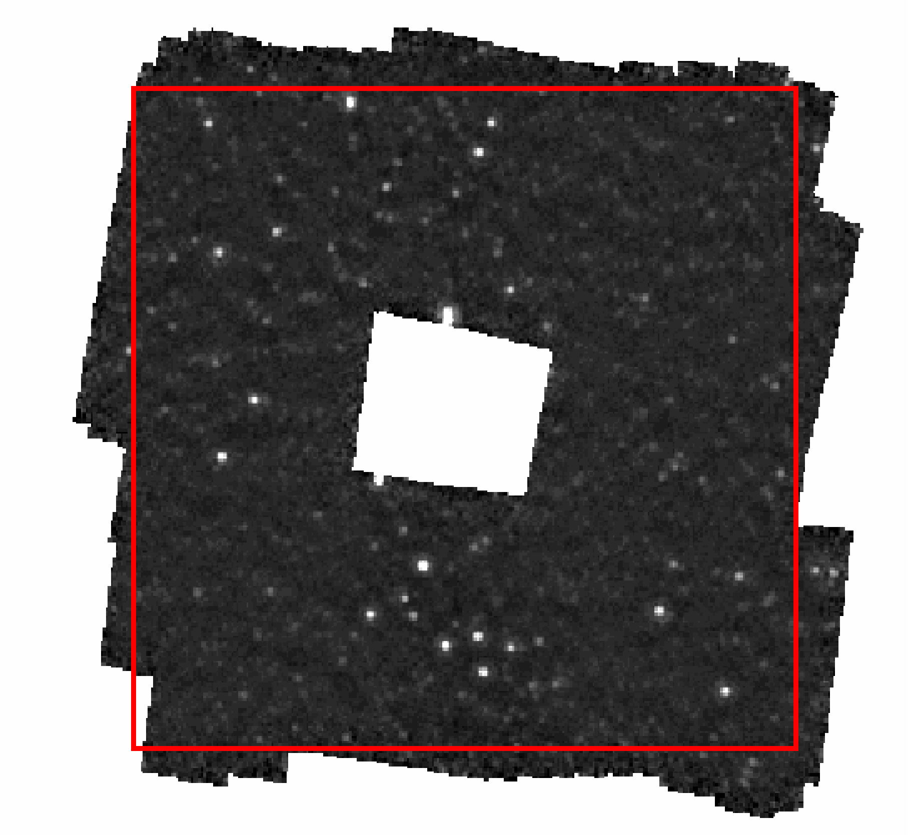

Figure 6.5: ECDFS FIDEL epoch 1+2 MIPS 70 μm observations. The red box has dimensions $30' \times 30'$.

The Far-Infrared Deep Extragalactic Legacy survey (FIDEL) is a Legacy science program being carried out with the Spitzer Space Telescope. The project is making the most sensitive and extensive far-infrared deep field observations with Spitzer to detect warm dust emission from hundreds of relatively ordinary starburst galaxies and active galactic nuclei at redshifts of 1 to 2 (7 to 10 billion years ago), and thousands more nearby. The survey also detects tens of thousands of high redshift objects at mid-infrared wavelengths. The program is obtaining data in three fields on the sky. The bulk of the data is being taken in two fields, the Extended Chandra Deep Field South (ECDFS) and the Extended Groth Strip (EGS). A smaller amount of additional data is being obtained in the GOODS-North area. We used the public maps released with FIDEL Data release 2 (DR2)[1], in particular we have focused on the ECDFS 70 μm maps.

---

[1] `http://irsa.ipac.caltech.edu/data/SPITZER/FIDEL/docs/fidel_dr2.html`

The bulk of the FIDEL ECDFS observations were taken in two epochs separated by approximately six months, in September 2006 and March 2007 (epochs 1 and 2, respectively). The Spitzer telescope orientation rotated by approximately 180 degrees between the two epochs, ensuring reasonably symmetric coverage in the MIPS 24 and 70 μm bandpasses. Data release DR2 presents the combined image from the first and second epoch FIDEL data at 70 μm. All ECDFS epoch 1 and 2 MIPS observations used the photometry-mode Astronomical Observing Templates. In this mode, the field of view is dithered using a combination of telescope and scan mirror offsets around a particular pointing position. Generically, we consider the ECDFS to cover a square region approximately $30' \times 30'$ on the sky, oriented along the J2000 celestial axes. The MIPS observations were optimized to achieve roughly uniform exposure time at 70 microns in the combined epoch 1 + 2 observations.

Figure 6.5 illustrates the layout of the ECDFS epoch 1+2 observations, showing the MIPS images and the relative exposure time maps at 70 μm. In the DR2 ECDFS 70 μm images, the mean exposure time over the majority of the field is approximately 4800s.

We applied the methods described in Section 6.3 to these maps, following the steps before explained.

In particular, before we compared the results obtained from a *P(D)* analysis of the map with the expected theoretical *P(D)* distribution. In the Fig.6.6 we show the results: the plot show the observed histogram (calculated with three beam radius at $16''$, $18''$, $20''$) of deflections per unit sky area for the ECDFS maps that are compared with a gaussian distribution representing the instrumental noise having an RMS of 0.62 mJy/beam and with the probability distribution of deflection modelled according with the best fit model (Franceschini et al. 2010). The black line is the convolution of the two and provides a good fit to the observational distribution.

The *P(D)* analysis confirm the fast convergence of the counts fainter than a few mJy in the 70 μm counts: a shallower convergence of the counts (see Figure 6.4 would imply excess signal in the *P(D)* distribution at flux grater than 0.05 MJy/sr compared to what is observed here. The *P(D)* data reported in the Figure 6.6 impose quite a fast convergence of these counts fainter than 10 mJy.

In this case, the gaussian noise is calculated using a relation derived by Frayer et al. (2006) for the MIPS 70 μm maps. In particular they derive a simple relation between instrumental noise and time exposure maps[2]:

$$\sigma_{instr} \propto t^{-1}(1+\beta t^{0.5}) \tag{6.17}$$

where $\beta = 0.04$.

---

[2] Also the exposure maps are released in DR2

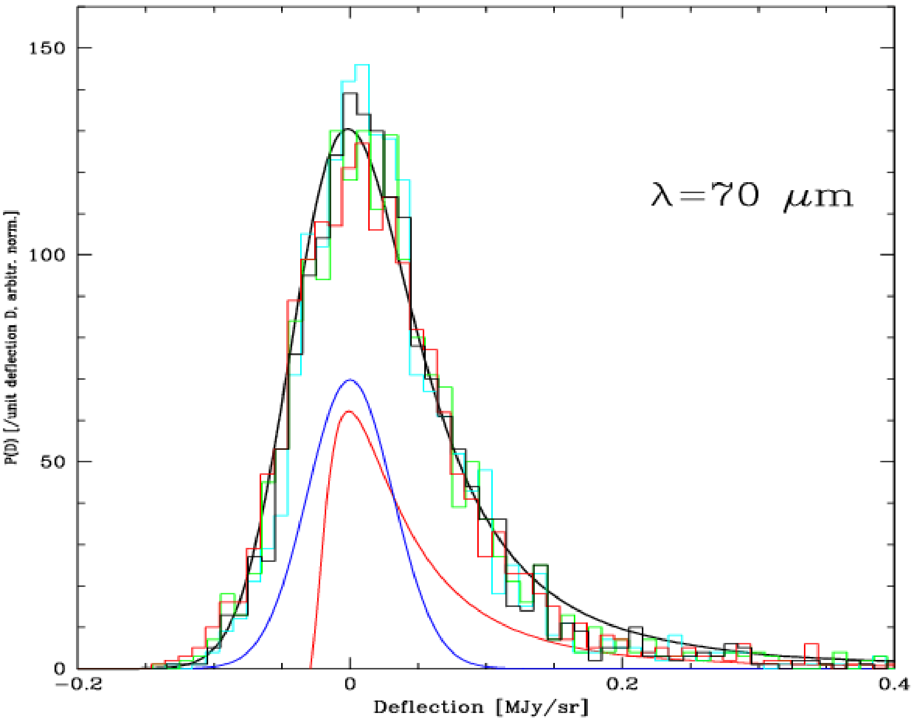

Figure 6.6: Results from ECDFS data at 70 μm. The plot show the observed histogram (calculated with three beam radius at 16″, 18″, 20″) of *P(D)* compared with a gaussian distribution representing the instrumental noise RMS of 0.62 mJy/beam (here in blue) and with the *P(D)* modelled according with the best fit model (Franceschini et al. (2010), here in red). The black line is the convolution of the two and provides a good fit to the observational distribution.

After comparing the real *P(D)* with the theoretical *P(D)* we realized some simulated maps and we compared the *P(D)* results on these maps with the *P(D)* results obtained from real ECDFS maps. In particular, we simulated 31 map in according with before described and we performed, for all this maps, the *P(D)* analysis. Then we calculated the mean of all this *P(D)* distribution. The Figure 6.7 shows the results: we obtained a good fit with a real data using an instrumental noise $\sigma_i = 0.62 mJy/beam$. Also in this case, the good fit confirm substantially the model.

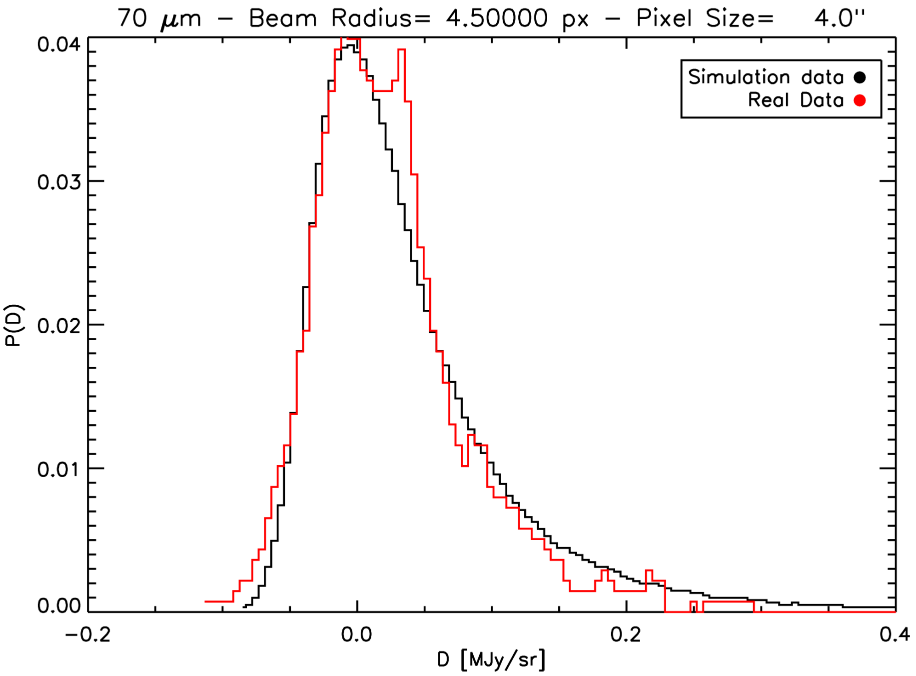

Figure 6.7: Results from *P(D)* analysis applied to 3170 μm simulated maps: the black line show the mean of the *P(D)* distribution, the red line the *P(D)* distribution for the real ECDFS map

6.5.2 HerMES *P(D)* analysis

In this section I report the results of the *P(D)* analysis performed on first HerMES SDP data.

We followed the same procedure used in FIDEL maps:

- *P(D)* analysis on the real maps and comparison with the theoretical *P(D)* distribution;
- maps simulations based upon Franceschini et al. (2010) best-fit model;
- *P(D)* analysis on the simulated maps and comparison with “real maps” *P(D)*

We performed the *P(D)* analysis on different deep fields. In particular we concentrated on a *deep* field (**GOODS-N**) and on a *shallow* field (**LOCK-SWIRE**). This choose was done because using these fields we can compare the results with the confusion study performed by Nguyen et al. (2010) (See Section 5.2. We also used the instrumental noise derived from them as initial value for the simulations, see Table 5.2).

GOODS-N GOODS-N has an area equal to $30' \times 30'$ and was observed by *Herschel* in SDP using the large map mode (see Section 3.2.1) with normal scan speed (30'″/s). The total number of scan was 30. In Figure 6.8 it's possible to see the central area ($16' \times 16'$) of the maps for the three SPIRE bands (Nguyen et al. 2010).

LOCK-SWIRE LOCK-SWIRE is a field larger than GOODS-N (the field area is equal to $218' \times 218'$) and also this field was observed by *Herschel* in SDP using the large map mode, but in this case with scan speed equal to $60''$/s (*fast scan*). This is a shallow field and for this reason the total number of scan was 2.

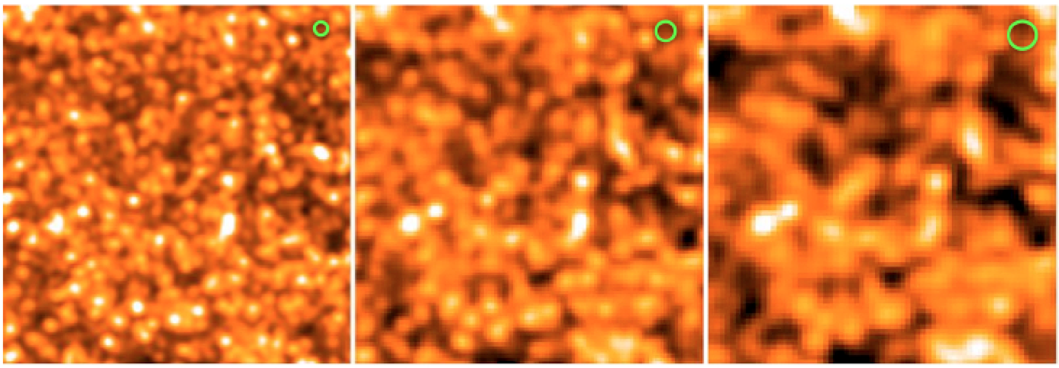

Figure 6.8: The GOODS-N central area ($16' \times 16'$) for the three SPIRE bands (left to right: PSW, PMW, PLW). The green circles indicating the beam FWHM in each band (Nguyen et al. 2010).

SPIRE Beam Size As mentioned before, a fundamental factor for the *P(D)* is the instrument beam size. We used the beam area derived using Equation 6.16. The FWHM, summarized in Table 6.1, was determined by the HerMES team.

Table 6.1: SPIRE pixel size and FWHM

Instrument	λ	FWHM	PXSIZE
PSW	$250\mu m$	$18.1''$	$6''$
PMW	$350\mu m$	$25.1''$	$10''$
PLW	$500\mu m$	$36.3''$	$14''$

Also in this case we changed the beam radius (with step equal to $\pm 0.25 \times p_s$, being p_s the pixel size for the SPIRE bands, reported in Table 6.1) to investigate how different spatial sampling influences the *P(D)* analysis.

The PSF is the term more difficult to obtain: we can use either a theoretical or an experimental PSF, both available in HerMES data. In the simulation we decide to use the experimental PSF for all three SPIRE bands (see a PSW PSF in Figure 6.1).

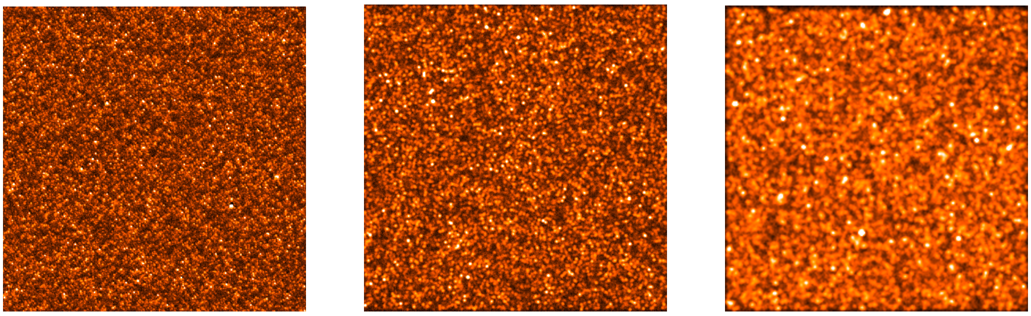
(a) GOODS-N PSW (b) GOODS-N PMW (c) GOODS-N PLW

Figure 6.9: GOODS-N simulated maps: the area represented is equal to $60' \times 60'$.

P(D)* analysis and comparison with theoretical *P(D) We performed a *P(D)* analysis of the maps following the indications reported in Section 6.3. After this step we derived a theoretical *P(D)* from our best-fit model (Franceschini et al. 2010) , we convolved it with a gaussian distribution representing the instrumental noise and we compared the results with the measured *P(D)* distribution. Figure 6.10 shows the results for GOODS-N field and for all the SPIRE bands. The good fit that confirm the model also at SPIRE wavelengths.

***P(D)* analysis on the simulated maps** The *P(D)* analysis was performed in the same way described before for the FIDEL data. We realized 31 simulations for any SPIRE bands and we calculated the mean *P(D)* . The Figure 6.9 reports the results of the simulated maps for the GOODS-N field and for all the three SPIRE bands.

It's possible see in Figure 6.11 the good fitting between “simulated” *P(D)* and “real” *P(D)* at any wavelength and for any field (I report only the results for the optimal beam radius: $18''.1$, $25''.1$, $36''.3$ respectively for PSW, PMW, PLW). This substantially confirm our best-fit model by Franceschini et al. (2010). The results for the instrumental noise is reported in Table 6.2 compared with the Nguyen et al. (2010) and the Glenn et al. (2010) results. We can see that we have a good agreement with Nguyen data for the deep field GOODS-N. For the shallow field LOCK-SWIRE we have a not so good agreement, in particular for the long-wavelength bands (PMW and PLW).

Table 6.2: Instrumental noise $[mJy/beam]$ in GOODS-N (top) and LOCK-SWIRE (bottom). The first column report my result obtained from comparison between measured *P(D)* and theoretical *P(D)* , the second column my result obtained from comparison between measured *P(D)* on real and simulated maps, the third column the results from Nguyen et al. (2010) and the fourth column the results from Glenn et al. (2010)

(a) GOODS-N

Instrument	Theoretical σ_i	Simulated σ_i	Nguyen σ_i	Glenn σ_i
PSW	1.8	1.745	1.645	1.77
PMW	3	1.347	1.370	1.59
PLW	1.7	2.105	1.97	1.89

(b) LOCKSW

Instrument	Theoretical σ_i	Simulated σ_i	Nguyen σ_i	Glenn σ_i
PSW	6	10.467	8.485	9.47
PMW	4	1.684	7.495	8.47
PLW	5.75	17.541	10.819	11.99

6.6 Multi-wavelength modelling of IR galaxy evolution: the results

As just said, in Franceschini et al. (2010) we report on our analysis of a large IR database on high- redshift galaxies at long wavelengths, the bulk of which we obtained from recently completed surveys with the Spitzer Space Telescope, including unpublished results. Spitzer data are complemented by sub-mm surveys from the balloon experiment BLAST, preliminary results of the *Herschel* observatory, millimetric observations with large ground-based telescopes, as well as diffuse extragalactic background measurements, mostly from COBE.

With these data in hand, we have substantially updated the previous Franceschini et al. (2001) modelling of galaxy evolution. Our results agree with Franceschini et al. (2001) at $z < 1$, but much improve their analysis at $z > 1$, where a very luminous source population dominating the IR activity has been established by the new data.
Our main results are summarized in the following:

- The current data completely confirm earlier indications of a very rapid increase in galaxy long-wavelength volume emissivity with redshift up to $z \simeq 1$, paralleled by an increased incidence of dust extinction and thermal dust reprocessing in high-redshift sources, with respect to locally observed galaxies. This is the fastest evolution rate observed for galaxies at any wavelengths ($\rho(z) \propto (1+z)^4$ if averaged over the whole galaxy population). Confusion-limited number counts at longer wavelengths (from 70 to 1100 μm) completely support these findings.

- All the present data require that the fast evolution observed from $z = 0$ to 1 flattens around redshift 1 and keeps approximately flat, at least up to $z \simeq 2.5$. At higher redshifts, the co- moving emissivity may be required to decrease to avoid exceeding the COBE observed intensity of the CIRB, but more data from *Herschel*will be needed for more definite conclusions. In any case, there is a clear tendency in our redshift-dependent bolometric comoving energy density (Figure 6.12) to stay lower than various published results, particularly at higher redshifts than $z \sim 1.5$, based on either large extinction corrections, or large spectral extrapolations.

- Our exploration of the high-redshift ($z > 1$) universe in the far-IR and sub-mm has provided evidence of a population of very luminous galaxies becoming dominant at $z > 1$. The comoving emissivity of the latter is maximal at $z \simeq 2$ and shows a much faster convergence with cosmic time than lower luminosity systems, whose maximal activity is set around $z \simeq 1$. Then an earlier phase of formation for the most luminous/massive galaxies/AGNs is indicated and provides supporting evidence of the peculiar evolutionary pattern named downsizing. At the highest redshifts probed by the present analysis ($1.5 < z < 3$), the luminosity functions (LF) of galaxies appear to be dominated by ultra-luminous sources ($L_{bol} \simeq 10^{12} L_\odot$), while the comoving number density of lower luminosity galaxies is low and their LFs flat (consistent with being not steeper than in the local universe). These flat shapes of the LFs at any redshifts indicated by the present analysis (Figure 6.13) might require significant tuning or modifications of galaxy formation models.

- The IR emissions by cosmic sources analyzed in the Franceschini et al. (2010) include the contributions of both massive-star formation and dust-obscured AGN accretion. Many attempts have been made to disentangle the two, mostly based on deep hard X-ray imaging and Spitzer IRS spectroscopy. All these analyses, however, remain essentially inconclusive in so far that, in high- column-density media, the hard X-ray flux is completely removed by Compton scattering and the mid-IR hot-dust AGN emission may become optically thick. To gain more in-sight, we followed a complementary road of comparing our results on the comoving IR emissivity of sources with recent estimates of the redshift-dependent stellar mass functions of galaxies based on deep (Spitzer/IRAC) near-IR surveys. In our analysis, the comparison of the instantaneous SFR with the integrated mass assembled in stars relies on two model parameters: the AGN fractional contribution to the bolometric IR emission, f_{AGN}, and the slope m of the stellar Initial Mass Function(IMF). Unlike photonic remnants like the background radiation, suffering a $(1+z)^{-1}$ redshift penalty factor, the stellar mass density is an unbiased tracer of the past star formation activity at the high redshifts.

- Using our best-fit evolutionary model, we find that the ob- served redshift-dependent bolometric source emissivity ρ_{IR} can be naturally reconciled with the observed galaxy mass functions by adopting a universal Salpeter IMF ($m = 1.35$) and standard AGN fractions $f_{AGN} \sim 20 - 30\%$ in LIRGs and ULIRGs at all redshifts. Previous analyses referred to higher estimated $\rho_{IR}(z)$ at $z > 1.5$, hence suggested top-heavy IMFs for the more luminous galaxies at higher redshifts or higher AGN fractions.

- We finally caution that with current data we cannot probe deeply into the luminosity functions of high-redshift far-IR sources. Statistical constraints were included in our combined dataset, in particular upper limits on LFs at the faint ends from the use of number counts and the CIRB intensity (including those from cell-to-cell fluctuations). Average spectral shapes for populations of sources were derived based on the multi-wavelength information from the mid-IR to the millimeter.

- We used the *P(D)* analysis to obtain good constraints about faint source counts and in particular to confirm the fast convergence of the counts fainter than a few mJy in the 70 μm counts.

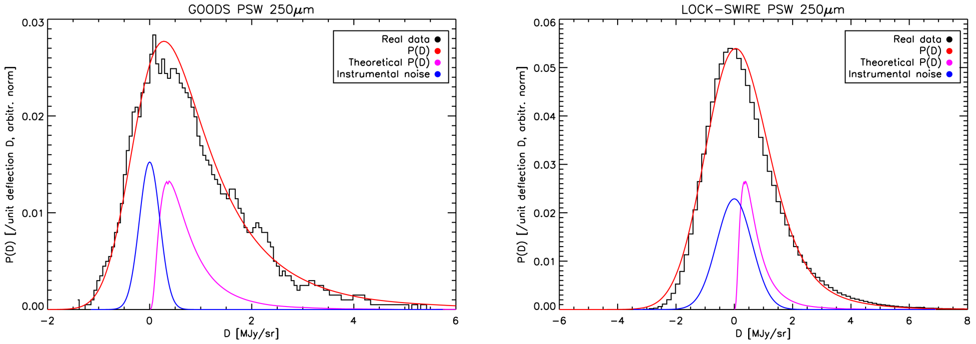

(a) P(D) PSW GOODS-N (b) P(D) PSW LOCKSW

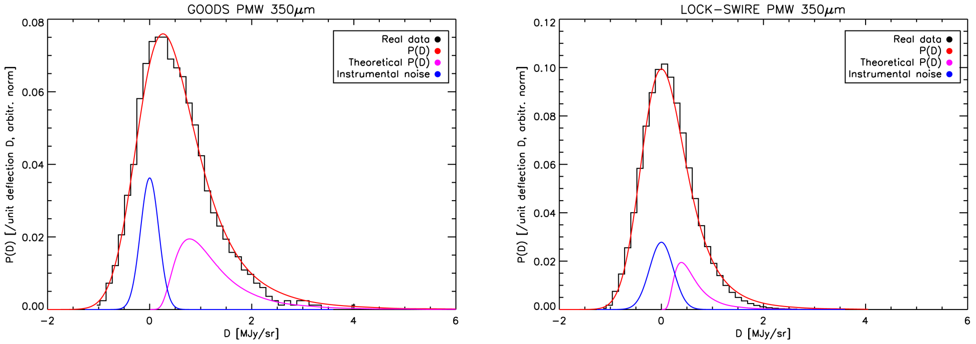

(c) P(D) PMW GOODS-N (d) P(D) PMW LOCKSW

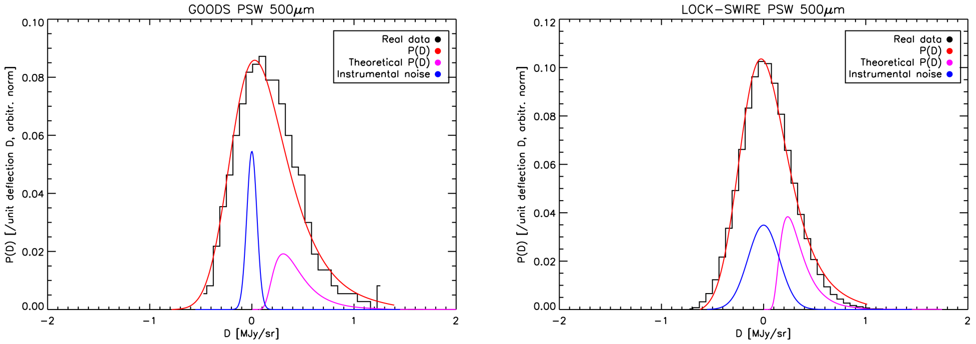

(e) P(D) PLW GOODS-N (f) P(D) PLW LOCKSW

Figure 6.10: *P(D)* results: comparison with the theoretical *P(D)*. From top to bottom PSW, PMW, PLW; the *P(D)* was calculated with beam radius at (18″.1, 25″.1, 36″.3) respectively for the three SPIRE bands. **Left Column.** GOODS-N: the plot show the observed histogram of *P(D)* (here in black) compared with a gaussian distribution (here in blue) representing the instrumental noise RMS of (1.8, 3, 2.1) mJy/beam respectively for the three SPIRE bands and with the P(D) modelled according with the best fit model (Franceschini et al. (2010), here in magenta). The red line is the convolution of the two and provides a good fit to the observational distribution. **Right column.** LOCK-SWIRE: same for the left column, in this case the instrumental noise RMS is (6 , 5.1, 8.75) mJy/beam respectively for the three SPIRE bands

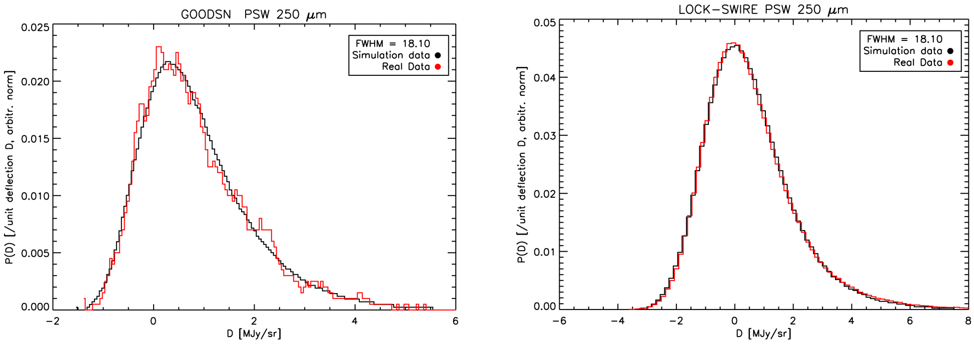

(a) P(D) PSW GOODS-N (b) P(D) PSW LOCKSW

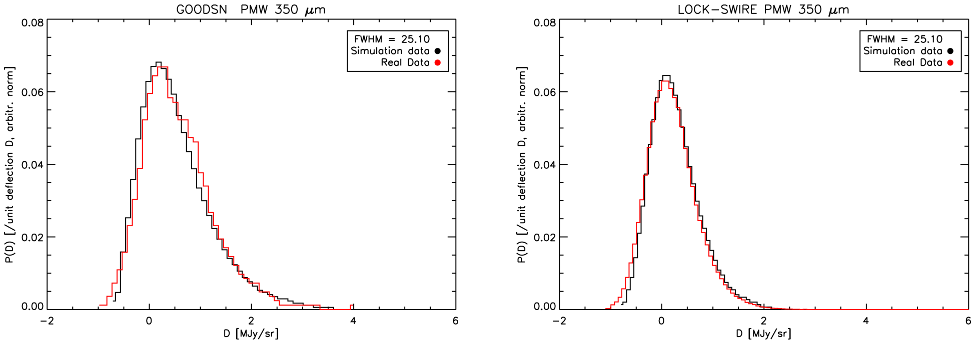

(c) P(D) PMW GOODS-N (d) P(D) PMW LOCKSW

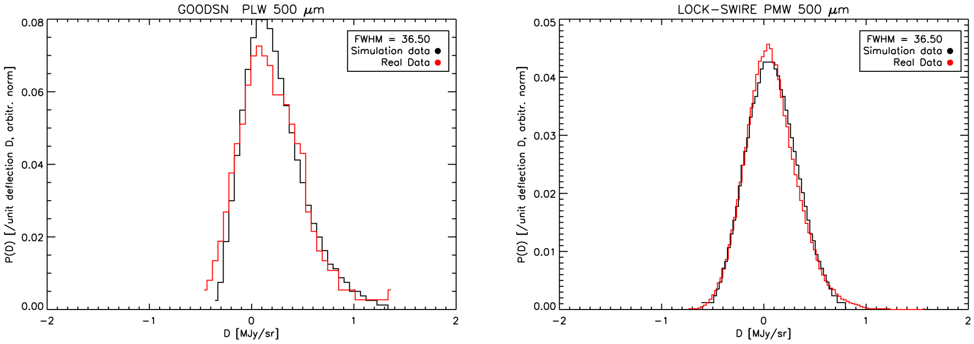

(e) P(D) PLW GOODS-N (f) P(D) PLW LOCKSW

Figure 6.11: *P(D)* results. **Left Column.** GOODS-N: from top to bottom PSW, PMW, PLW comparison between *P(D)* for real data (in red) and and for simulated data (in black). **Right column.** LOCK-SWIRE: from top to bottom PSW, PMW, PLW comparison between *P(D)* for real data (in red) and and for simulated data (in black).

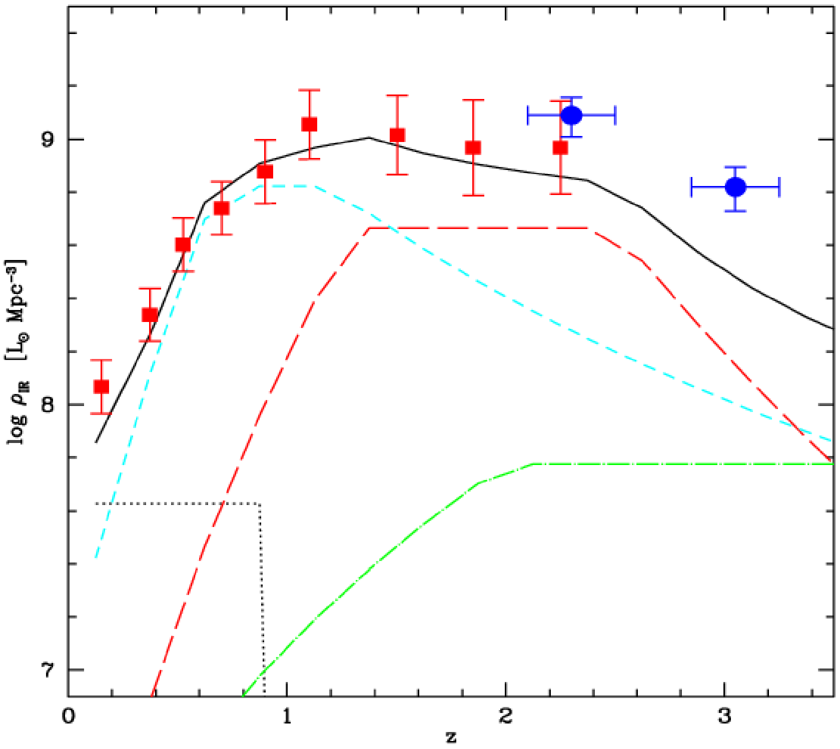

Figure 6.12: Evolution of the comoving bolometric luminosity density from 6 to 1000 μm for the IR-selected galaxy population, based on the Franceschini et al. (2010) model. The luminosity density is expressed here in solar luminosities per cubic Mpc. Green dot-dashed line: type-I AGNs. Cyan short-dashed line: evolving moderate-luminosity starbursts (LIRG). Red long-dashed line: high-luminosity starbursts (ULIRG). Lower dotted black line: quiescent spiral population (note that the spirals are assumed not to evolve in comoving luminosity by our model and then to disappear at $z = 1$). The upper continuous line is the total predicted emissivity. Red filled square data-points are from the analysis of the 24 μm luminosity functions by Rodighiero et al. (2010). Blue data-points are from a large spectroscopic survey at $1.9 < z < 3.4$ by Reddy et al. (2008).

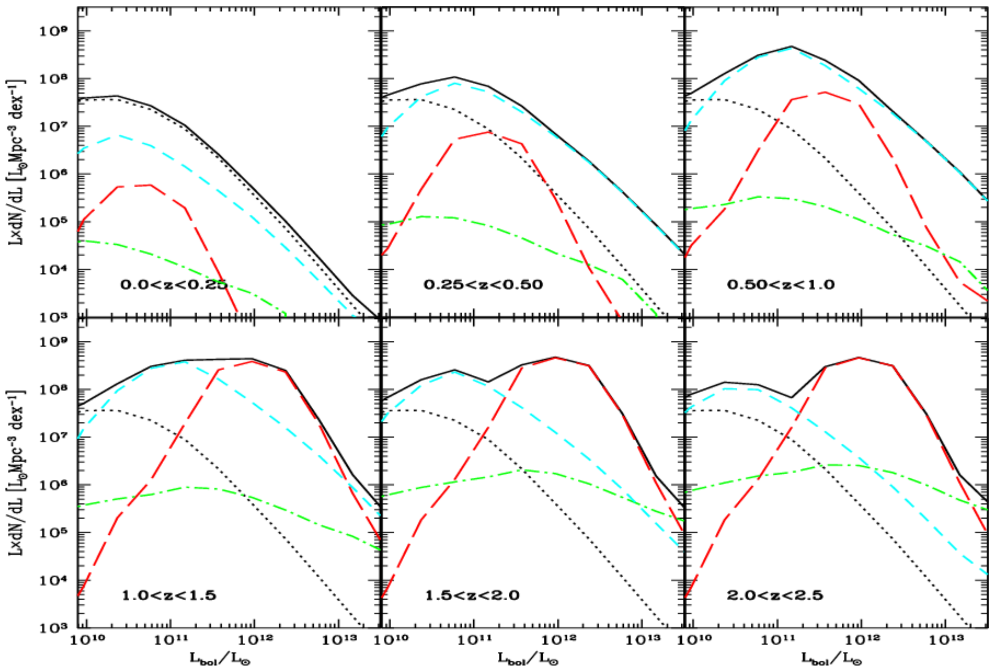

Figure 6.13: The comoving bolometric emissivity from 6 to 1000 μm as a function of luminosity for the IR-selected galaxy population, calculated at various cosmic epochs from$z = 0$ to 2.5. The IR emissivity is expressed here in solar luminosities per cubic Mpc per unit logarithmic interval of L. Line types as in Figure 6.12.

Conclusion

This Thesis deals with problems related to IR/sub-mm astronomy : technical and scientific issues. The main subject of this Thesis is the *Herschel* Space Observatory and in particular, as member of SPIRE ICC, I focused on the problematics of reduction and interactive analysis of data obtained by SPIRE instrument and, as member of *Herschel* SAG 1, I focused on early results obtained by HerMES program in galaxy formation and evolution and observational cosmology.

About the technical work, were the two points touched in this Thesis: the Data Processing Pipeline and the development of tools for interactive data analysis. My contribution to the Data Processing Pipeline consisted in the realization of some tasks used mainly in the processing of SPIRE scan map mode (Large Map and Small Map mode) data (but the tasks are also applicable to all others types of Astronomical Observing Template (AOT)). These tasks are contained in the *spire.ia.pipeline.common.util* package for which I am responsible. But the major work has been done to realize tools to analyze intuitively the “detector timeline” type products. As owner of package *spire.ia.gui* I realized tools to explore/analyze the Photometer Detector Timeline (PDT) and Spectrometer Detector Timeline (SDT) products. These tools are available to the astronomers within Herschel Integrated Processing Environment (HIPE), the official Herschel Common Science System (HCSS) application to retrieve/explore/use/analyze the *Herschel* data.

Regarding the scientific side of the Thesis, the work was mainly concerned about the cosmological surveys: thanks to these large surveys it is possible to try to understand the mechanisms of formation and evolution of galaxies. The largest program of observations done by *Herschel* in this area is that which goes by the name of Herschel Multi-tiered Extragalactic Survey (HerMES). As an introduction to the *Herschel* outcome, first I summarized the main results obtained by others missions in the past, last I reported here the early results (based upon the Science Demonstration Phase (SDP) data) obtained in the characterization of the confusion noise, in the analysis of number counts statistics and in clustering properties by HerMES team.

The characterization of confusion noise is reported by Nguyen et al. (2010): the estimated confusion noise is (5.8 ± 0.3, 6.3 ± 0.4, 6.8 ± 0.4) mJy/beam in the three

SPIRE bands, substantially confirmed also using simulations but lower than that we measured using a *P(D)* analysis (Glenn et al. 2010). The HerMES counts reach 1 source per 40 beams at 19.1 ± 0.6, 17.7 ± 0.6, and 15.1 ± 1.8 mJy at 250, 350 and 500 μm, corresponding to 3.29, 2.81, and 2.60 σ_{conf}.
Using a *P(D)* analysis (Glenn et al. 2010) and using a "classical" source extraction analysis (Oliver et al. 2010) , we produced the first *Herschel* counts numbers statistics. The results show approximately flat counts for $S > 100$ mJy and the a steep rise, a break in the number counts in all the three bands at 20 mJy and a bump in the differential counts around 400 mJy at 250 μm. The resolved Cosmic InfraRed Background (CIRB) integrated in the three bands is (64 ± 16, 60 ± 20 and 43 ± 12) % respectively for Glenn et al. (2010) and (15, 10, 6)% for Oliver et al. (2010).
The clustering analysis (Cooray et al. 2010) show that the 250 μm sources are more likely to be found in halos with mass $(5 \pm 4) \times 10^{12}\ M_{\odot}$ and the bright 500 μm sources occupy halos of $(3.1 \pm 2.8) \times 10^{13}\ M_{\odot}$ and in general we can derive evidence for non-linear clustering at arc-minute angular scales.

The last point of the Thesis is about the use *P(D)* analysis in the multi-wavelength modeling of IR galaxy evolution as presented in Franceschini et al. (2010). Using the *P(D)* technique it's possible to obtain information about the number counts below the confusion limit, in particular to obtain good constraints about faint source counts. Also thanks to this technique was possible update the previous Franceschini et al. (2001) model of galaxy evolution, in particular confirm the fast convergence of the counts fainter than a few mJy in the 70μm counts.

To complete the overview of the problems that we can encounter in IR/sub-mm astronomy, in Appendix I reported also the results about the characterization of the first galaxies selected at 350 μm from ground.

Thanks to the results that *Herschel* is getting and will get in the coming years, we could clarify those aspects which are not clear on the Universe. In particular, with the completion of the observing program of HerMES we probably answer to those cosmological questions about the formation and evolution of galaxies. The *Herschel* mission has at least still two years of life but other missions are planned in the coming years (ALMA, SPICA, etc). The experience gained with *Herschel* will be used for these future missions, both as regards the ground segment and for the scientific side, and the *Herschel* software infrastructure based upon Java, Jython etc. will probably be easily adapted for other missions. The *Herschel* is important also for this reason: *Herschel* opened a new way to develop a mission using open source language, large collaborative teams and reusable software. Fundamentally, we hope that, starting from *Herschel*, in the next years, the IR/sub-mm astronomy can fill that hole mentioned by Sir Frederick William Herschel:

> *Here is truly a hole in Heaven.*

Appendix A

On the nature of the first galaxies selected at 350 μm

In this Appendix I will report the result that we obtained in the identification of first galaxies selected at 350 μm from ground and described in Khan et al. (2009). Submillimeter-selected galaxies (SMGs) were discovered in pioneering lensed and blank-field surveys (e.g., Smail et al. 1997. The majority of SMGs have been selected at long sub-millimeter bands (500–1300 μm). Shorter sub-millimeter wavelengths (200–500 μm) are more demanding for ground-based observers due to high atmospheric absorption (see Chapter 1). In the Khan et al. (2009) we presents a detailed characterization of five 350 μm selected galaxies following the approach of Khan et al. (2005). Multi-wavelength data are presented, and spectral energy distribution (SED) template fitting is used to provide constraints on the photometric redshifts, thermal parameters (IR luminosity and dust temperature), and energy diagnostics.

This work was very important because for the first time we studied the nature of sources selected from ground at 350 μm, study that now are better performed by *Herschel* from the space. The sample, described in the paper that I will report integrally in the following pages, comprises IR-luminous galaxies at $1 < z < 3$ and resolves ∼20% of the 350 μm background at flux densities > 17 mJy. The implied lower limit on the star formation rate density suggests that the bulk of the 350 μm contribution is from galaxies of lower IR luminosity than the ones detected at present flux densities.

My personal contribution to this paper is about identification of source and photometric redshift derivation.

As showed in Figure A.1, finding counterparts for the sources is not straightforward. However the most likely counterparts can be determined following the lines described in the paper.

When all the possible counterparts was identified, we can apply photometric redshift techniques. This technique is an old idea of Baum (1962) but only in the last twenty year the interest was increased. We have two different redshift photometric techniques:

- empirical training set method that consists in derive an empirical relation between magnitudes and redshift using a subsample of objects with measured spectroscopic redshifts;

- fitting of the observed SED's where the observed photometric SEDs are compared to those obtained from a set of reference spectra: the photometric redshift of a given object was derived from the best fit of its photometric SED by set of template spectra.

We applied this second technique, in particular using the HyperZ code (Bolzonella et al. 2000).

To do this technique we needed multi wavelength photometry and we used **B**, **R**, **I**, **Z**, photometry from Subaru telescope, **K** Bands from UKIDDS survey at UKIRT Telescope and IRAC & MIPS photometry. The Figure A.1 (right) show an example of SED fitting for one of the 350 μm source

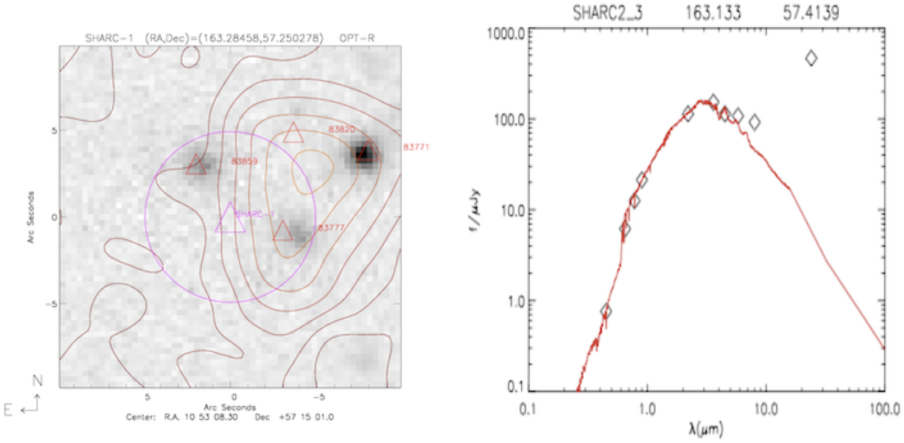

Figure A.1: **Left** Example of counterparts identification for 350 μm source: for this source we have four possible counterparts in **R** band. **Right.** An example of SED fitting using HyperZ code (Bolzonella et al. 2000)

The Astrophysical Journal, 706:319–327, 2009 November 20 doi:10.1088/0004-637X/706/1/319

ON THE NATURE OF THE FIRST GALAXIES SELECTED AT 350 μm

Sophia A. Khan[1,2,3,4,5,15], Pierre F. Chanial[2], S. P. Willner[4], Chris P. Pearson[6,7], M. L. N. Ashby[4], Dominic J. Benford[3], David L. Clements[2], Simon Dye[8], Duncan Farrah[9,10], G. G. Fazio[4], J.-S. Huang[4,5], V. Lebouteiller[10], Emeric Le Floc'h[11,16], Gabriele Mainetti[12], S. Harvey Moseley[3], Mattia Negrello[13], Stephen Serjeant[13], Richard A. Shafer[3], Johannes Staguhn[3,14], Timothy J. Sumner[2], and Mattia Vaccari[12]

[1] Pontificia Universidad Católica, Departamento de Astronomía y Astrofísica, 4860 Vicuña Mackenna, Casilla 306, Santiago 22, Chile
[2] Imperial College London, Blackett Laboratory, Prince Consort Road, London SW7 2AZ, UK
[3] Observational Cosmology Laboratory (Code 665), NASA Goddard Space Flight Center, Greenbelt, MD 20771, USA
[4] Harvard-Smithsonian Center for Astrophysics, 60 Garden Street, Cambridge, MA 02138, USA
[5] Shanghai Key Lab for Astrophysics, Shanghai Normal University, Shanghai 200234, China
[6] Rutherford Appleton Laboratory, Chilton, Didcot, Oxfordshire OX11 0QX, UK
[7] Department of Physics, University of Lethbridge, 4401 University Drive, Lethbridge, Alberta T1J 1B1, Canada
[8] School of Physics and Astronomy, Cardiff University, Queens Buildings, Cardiff, CF24 3AA, UK
[9] Astronomy Centre, University of Sussex, Falmer, Brighton, UK
[10] Department of Astronomy, Cornell University, 610 Space Sciences Building, Ithaca, NY 14853, USA
[11] Institute for Astronomy, University of Hawaii, 2680 Woodlawn Drive, Honolulu, HI 96815, USA
[12] Department of Astronomy, University of Padova, Vicolo Osservatorio 3, I-35122, Padova, Italy
[13] Department of Physics and Astronomy, Open University, Walton Hall, Milton Keynes MK7 6AA, UK
[14] Department of Astronomy, University of Maryland, College Park, MD 20742, USA

Received 2009 July 15; accepted 2009 October 2; published 2009 October 29

ABSTRACT

We present constraints on the nature of the first galaxies selected at 350 μm. The sample includes galaxies discovered in the deepest blank-field survey at 350 μm (in the Boötes Deep Field) and also later serendipitous detections in the Lockman Hole. In determining multiwavelength identifications, the 350 μm position and map resolution of the second generation Submillimeter High Angular Resolution Camera are critical, especially in the cases where multiple radio sources exist and the 24 μm counterparts are unresolved. Spectral energy distribution templates are fitted to identified counterparts, and the sample is found to comprise IR-luminous galaxies at $1 < z < 3$ predominantly powered by star formation. The first spectrum of a 350 μm selected galaxy provides an additional confirmation, showing prominent dust grain features typically associated with star-forming galaxies. Compared to submillimeter galaxies selected at 850 and 1100 μm, galaxies selected at 350 μm have a similar range of far-infrared color temperatures. However, no 350 μm selected sources are reliably detected at 850 or 1100 μm. Galaxies in our sample with redshifts $1 < z < 2$ show a tight correlation between the far- and mid-infrared flux densities, but galaxies at higher redshifts show a large dispersion in their mid- to far-infrared colors. This implies a limit to which the mid-IR emission traces the far-IR emission in star-forming galaxies. The 350 μm flux densities ($15 < S_{350} < 40$ mJy) place these objects near the *Herschel*/SPIRE 350 μm confusion threshold, with the lower limit on the star formation rate density suggesting the bulk of the 350 μm contribution will come from less luminous infrared sources and normal galaxies. Therefore, the nature of the dominant source of the 350 μm background—star-forming galaxies in the epoch of peak star formation in the universe—could be more effectively probed using ground-based instruments with their angular resolution and sensitivity offering significant advantages over space-based imaging.

Key words: galaxies: high-redshift – galaxies: starburst – infrared: galaxies – submillimeter

Online-only material: color figures

1. INTRODUCTION

Submillimeter-selected galaxies (SMGs) were discovered in pioneering lensed and blank-field surveys (e.g., Smail et al. 1997; Barger et al. 1998; Eales et al. 1999) with the 850 μm optimized Submillimeter Common User Bolometer Array (SCUBA; Holland et al. 1999) and later in similar surveys with millimeter detectors (e.g., MAMBO, BOLOCAM, etc.; Bertoldi et al. 2000; Laurent et al. 2005). SMGs mainly comprise massive, star-forming galaxies (see, e.g., Fox et al. 2002) around $z \sim 2$ (Chapman et al. 2005) with the bulk of the emission generated at rest-frame far-IR wavelengths. SMGs are thus part of the IR-luminous galaxy population, which includes galaxies found in the local universe by the *Infrared Astronomical Satellite* (*IRAS*) All Sky Survey (Soifer et al. 1984; Joseph & Wright 1985; Soifer et al. 1987) and other galaxies detected in mid- and far-IR bands, most notably (in terms of number selected) with the *Infrared Space Observatory* (Kessler et al. 1996), the *Spitzer Space Telescope* (Werner et al. 2004), and the *Akari Infrared Satellite* (Murakami et al. 2007) out to $z \sim 2$ (see, e.g., Rowan-Robinson et al. 1997; Puget et al. 1999; Aussel et al. 1999; Elbaz et al. 2002; Chary et al. 2004; Lonsdale et al. 2004; Le Floc'h et al. 2004, 2005; Yan et al. 2004; Matsuhara et al. 2006).

The majority of SMGs have been selected at long submillimeter–millimeter bands (500–1300 μm). Shorter submillimeter wavelengths (200–500 μm) are more demanding for ground-based observers. For example, on a good night at Mauna Kea, atmospheric transmission is about ∼30% at 350 μm but $\gtrsim$80% at 850 μm (Serabyn et al. 1998). Despite this, the first galaxy selected *purely* by 350 μm emission—SMM J143206.65+341613.4 (=SSG 1, Short Submillimeter Galaxy 1)

---

[15] ALMA Fellow.

[16] *Spitzer* Fellow.

Table 1
The First Five 350 μm-Selected Galaxies

IAU Name	Nickname	Other name	VLA Position (J2000)		350 μm Position (J2000)	
			R.A.	Decl.	R.A.	Decl.
SMM J143206.65+341613.4	SSG 1	···	14 32 06.58	+34 16 11.9	14 32 06.65	+34 16 13.4
SMM J143206.11+341648.4	SSG 2	···	14 32 06.04	+34 16 46.7	14 32 06.11	+34 16 48.4
SMM J105308.3+571501	LH 350.1	SHARC II Source 3	10 53 07.89	+57 15 00.3	10 53 08.3	+57 15 01
SMM J105232.3+572448	LH 350.2	SHARC II Source 4	10 53 32.26	+57 24 47.4	10 52 32.3	+57 24 48
SMM J105243.2+572309	LH 350.3	LOCK 350.1	10 52 43.17	+57 23 09.7	10 52 43.2	+57 23 09

Notes. VLA positions are for VLA counterparts as identified in this paper. IAU names are based on 350 μm positions.

—was discovered (Khan et al. 2005) in a deep, blank survey of the Boötes Deep Field with the second generation Submillimeter High Angular Resolution Camera (SHARC II; Dowell et al. 2003; Moseley et al. 2004) along with a second detection, SMM J143206.11+341648.4 (=SSG 2; Khan 2006; Khan et al. 2007). This survey, reaching 13 mJy and currently the deepest at 350 μm, obtained the first constraints on the 350 μm source counts. Three additional 350 μm selected galaxies have been found in serendipitous SHARC II follow-up observations of 850 μm and 1100 μm SMGs in the Lockman Hole (Laurent et al. 2006; Coppin et al. 2008).

Short-wavelength submillimeter surveys are expected to principally select star-forming galaxies at $1 < z < 3$ (see, e.g., Pearson & Khan 2009; Khan et al. 2007; Khan 2006), the epoch of peak star formation in the universe (e.g., Hopkins & Beacom 2006). Source count models that reproduce the observed 350 μm counts include a predominantly IR-luminous galaxy population evolving with redshift (e.g., Pearson & Khan 2009; Franceschini et al. 2009), but more observations are needed to verify these predictions.

This paper presents a detailed characterization of each of the five 350 μm selected galaxies following the approach of Khan et al. (2005). Multiwavelength data are presented, and spectral energy distribution (SED) template fitting is used to provide constraints on the photometric redshifts, thermal parameters (IR luminosity and dust temperature), and energy diagnostics. Additionally, the first mid-IR spectrum of a 350 μm selected galaxy, obtained using *Spitzer*'s Infrared Spectrograph (Houck et al. 2004), is given. The properties of the sample are compared with 850 and 1100 μm selected SMGs. Table 1 identifies the five sources and includes short nicknames used for convenience. The *WMAP* first year cosmological parameters ($H_0 = 71\,\mathrm{km\,s^{-1}\,Mpc^{-1}}$, $\Omega_m = 0.27$, $\Omega_\Lambda = 0.73$; Bennett et al. 2003) are used throughout this work.

2. OBSERVATIONS, DATA REDUCTION, AND COUNTERPART IDENTIFICATION

2.1. Observations

The SHARC II observations, data reduction, and source extraction procedure for the Boötes Deep Field survey are discussed in detail by Khan et al. (2007). Further details of source extraction are given by Khan (2006). Monte Carlo simulations for determining the survey completeness also provide a measure of the flux boosting. Approximately, 4000 artificial sources of random intensity and position were inserted into the raw data map, then extracted using the same procedure as for the real sources (Khan et al. 2007). For recovered $\geqslant 3\sigma$ sources with input flux densities >15 mJy, the ratio of the measured flux density to the input flux density indicates that the average flux boosting is 1.07 ± 0.23. Given the multiwavelength confirmation on SSG 1 and SSG 2, low outliers can be ruled out. Therefore, we proceed without applying a correction factor to these sources and assume that this also holds for the sources in the Lockman Hole. For the Lockman Hole, published 350 μm flux densities were combined with public B, R, I, and z photometry from the Subaru Lockman Hole survey (Dye et al. 2008), K band imaging from UKIDSS (Lawrence et al. 2007), archival *Spitzer* IRAC (Fazio et al. 2004) and MIPS (Rieke et al. 2004) imaging, and 1.4 GHz data from Biggs & Ivison (2006). These compiled photometric data are presented in Table 2.

Additional 1.2 mm photometry of SSG 1 was obtained using MAMBO in 2005 January for ∼3 hr in photometry mode. The horn antenna design produces incomplete sampling of the field, and because there was no jiggling, SSG 2 was not observed. The data were reduced using the standard package (MOPSIC).

New VLA observations of the Boötes Deep Field were obtained on 2006 April 11. The VLA was in A configuration, giving a synthesized beam size of 1″.36 × 1″.50 at 1.5 GHz. Wide field imaging mode was used in order to avoid bandwidth smearing: two 25 MHz IFs of two polarizations each with seven channels per IF. The phase center was located 10″ north of SSG 1 to avoid any possible phase center artifacts. Standard wide field imaging techniques were employed, including self-calibration and three-dimensional corrections. The final image was generated with AIPS parameter ROBUST = 1, giving an rms noise ≈10 μJy beam^{-1}. Automatic source search and flux density measurements were done with AIPS task SAD. Both SSG 1 and 2 were detected, but neither was spatially resolved.

Initial *Spitzer*/IRAC and MIPS data were obtained during surveys of the NOAO Deep Wide Field in Boötes (Eisenhardt et al. 2004). Significantly deeper observations were later obtained in 2006 February as part of the IRAC GTO program (Program ID 520). The IRAC observations consisted of six dithered 100 s frames in each IRAC field of view, covering the SHARC II survey area in all four IRAC bands. Multiplexer bleed and other detector artifacts were removed by applying the Spitzer Science Center's (SSC) artifact mitigation code to the S14 version of the automated IRAC pipeline Basic Calibrated Data products. These cosmetically enhanced frames were then mosaiced using IRACProc v4.0beta (Schuster et al. 2006) to ensure correct treatment of the noise for both point and extended sources. The MIPS observations consisted of eight 30 s cycles at 24 μm only and covered the entire 350 μm map area. The data were reduced following standard procedures (Gordon et al. 2005), and source flux densities were measured with point spread function fitting. The 99% confidence region of SSG 1 contains two visible-wavelength sources. The new 24 μm imaging shows that the source chosen as the most likely submillimeter counterpart by Khan et al. (2005) is responsible for ∼75% of the 24 μm emission.

Table 2

Photometry for Counterparts of 350 μm Selected Galaxies

λ_{obs}	SSG 1	SSG 2	LH 350.1	LH 350.2	LH 350.3
B (μJy)	<0.3	0.1 ± 0.02	2.1 ± 0.020	0.07 ± 0.007	0.24 ± 0.009
R	0.8 ± 0.1	0.3 ± 0.1	3.6 ± 0.033	0.27 ± 0.013	0.52 ± 0.014
I	2.2 ± 0.1	< 0.9	5.5 ± 0.051	0.47 ± 0.017	0.65 ± 0.018
z	···	···	9.2 ± 0.085	1.09 ± 0.040	0.78 ± 0.036
J	10.5 ± 1.1	< 7.9	11.7 ± 0.65	2.7 ± 0.45	1.3 ± 0.41
K	42.0 ± 1.4	< 11.5	32.2 ± 0.89	7.6 ± 0.56	<1.5
3.6 μm	73.8 ± 0.3	5.6 ± 0.3	75.5 ± 7.0	21.1 ± 2.0	10.5 ± 1.1
4.5 μm	58.5 ± 0.5	7.4 ± 0.5	74.8 ± 6.9	23.0 ± 2.2	13.2 ± 1.5
5.8 μm	37.7 ± 2.1	8.1 ± 2.1	54.2 ± 7.0	13.0 ± 4.5	16.2 ± 5.2
8.0 μm	45.8 ± 2.2	3.0 ± 2.2	80.7 ± 8.6	40.1 ± 6.0	18.9 ± 5.6
24 μm	523.8 ± 58.7	187.2 ± 29.4	576 ± 13[a]	204 ± 24[a]	<80.2[b]
70 μm (mJy)	< 40	< 40	···	···	···
160 μm	< 100	< 100	···	···	···
350 μm	23.2 ± 7.9	17.1 ± 6.4	28.4 ± 9.2	37.0 ± 13.4	32.8 ± 8.9
850 μm	···	···	<6	<6	<6
1100 μm	···	···	1.1 ± 1.4	−0.2 ± 1.4	2.4 ± 1.4
1200 μm	0.142 ± 0.4	···	···	···	···
20 cm (μJy)	49.8 ± 11.4	53.1 ± 11.4	52.5 ± 5.2	32.0 ± 4.6	15.8 ± 4.8

Notes. For non-detections, the flux density at the radio position is used. Upper limits are 3σ. These data are used in the STARDUST2 SED template fitting.

[a] Flux density is deblended using [3.6] μm positions.

[b] Flux density cannot be deblended, used as a limit instead.

The *Spitzer*/IRS observation of SSG 1 was designed according to the recommended SSC setup. For each slit, there were six pointings along the slit at 24″ spacing, all centered on the slit in its narrow dimension. This is equivalent to the normal point source method except that the target is observed in six different slit positions instead of the usual two, lessening the effects of flat-fielding errors and bad pixels. In 3.1 hr (the total for the AOR, including peakups and overheads), there were five cycles of LL1 (19.5–38.0 μm) and seven of LL2 (14.0–21.3 μm) with 120 s ramps at each of the six slit positions. The data were reduced using the pipeline S15, cleaned using IRSCLEAN, and extracted with SMART (Higdon et al. 2004). Two extraction techniques were compared: the first method involved extracting the spectra from the individual images and taking the median spectrum; the second method was to align the images, and then extract the spectrum. There was little difference in the final spectrum using either technique, and the spectrum is shown in Figure 1. The most prominent features in the SSG 1 spectrum are due to polycyclic aromatic hydrocarbons (PAHs). For quantitative analysis, PAHs can be measured from integrating the flux above a baseline, but this method tends to underestimate the flux density as compared to a profile decomposition method such as the one used by PAHFIT (Smith et al. 2007; see also Galliano et al. 2008 for more detailed consideration of the two approaches). While both methods give similar PAH ratios and similar spatial variations of PAH strengths, absolute flux densities will differ due to assumptions about the PAH profiles.

2.2. Counterpart Identification

The additional deep 24 μm and 1.4 GHz imaging of the Boötes field yielded counterparts in these bands for SSG 1 and 2 with low probabilities of chance association (Khan et al. 2007). The more precise positions were then used to identify optical and mid-IR counterparts. Finding counterparts for the three sources in the Lockman Hole is not straightforward: Figure 2 shows thumbnail images of the fields at various wavelengths. As can be seen, there exist multiple radio detections for two of the 350 μm objects. However the *most likely* counterparts can be determined with the following rationale.

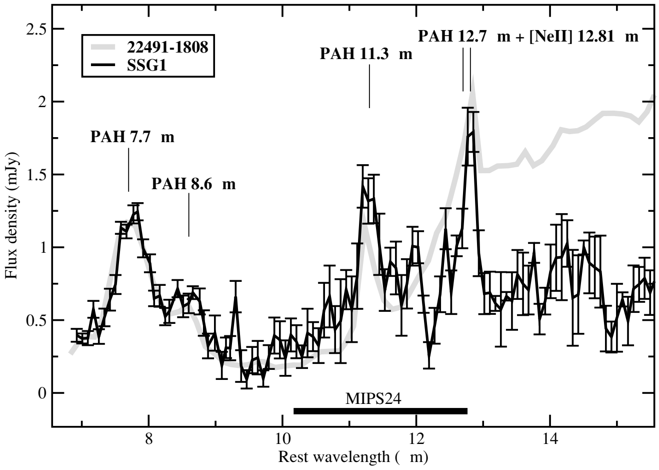

Figure 1. Mid-IR spectrum of SSG 1 as observed by *Spitzer* IRS, indicated by black line. 1σ error bars are shown. Wavelengths are in the rest frame based on the derived redshift $z = 1.05$. The spectrum of IRAS 22491−1808, used as a template to derive the redshift, is shown in gray. Prominent dust grain emission features are also indicated. The MIPS 24 μm passband is shown by the heavy black line below the spectrum.

1. *LH 350.1.* The 1.4 GHz image shows two potential counterparts, but only the southern one is within the 9″ SHARC II beam. In the visible images this appears to be a blend of two sources. The photometric redshift for this southerly source was obtained using HYPER-Z (Bolzonella et al. 2000) in conjunction with the *BRIzJK* [3.6][4.5] photometry, similar to the approach of Dye et al. (2008). The best-fitting solution is a starburst template at $z = 1.19^{+0.33}_{-0.14}$. The northern 1.4 GHz object is not associated with any visible-light detection, although it is prominent in the IRAC and MIPS images. Those images also show two more sources: an easterly object whose SED suggests it is a star or a low-redshift

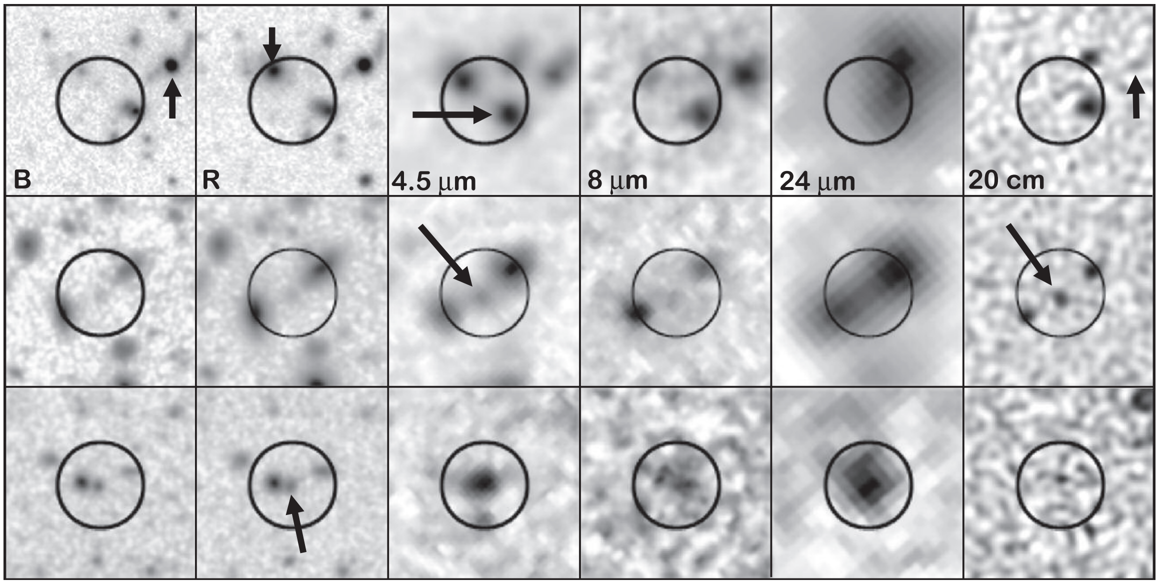

Figure 2. Visible, mid-IR, and radio imaging of LH 350.1 (top), LH 350.2 (middle), and LH 350.3 (bottom). Each image is 20″ on a side with a 9″ diameter circle centered on the SHARC II 350 μm position. North is up and east to the left. Arrows in the LH 350.1 panels indicate the unrelated QSO RDS 054A (*B* and 20 cm panels), a star or low-redshift E galaxy (*R* panel), and the proposed SMG counterpart (4.5 μm panel). Arrows in the LH 350.2 and 350.3 panels indicate the proposed SMG counterparts.

Table 3
Best-fitting Parameters from STARDUST2 Template Fitting

Nick Name	$\log(L_{\rm IR}({\rm SD2})/L_\odot)$ [$L_{\rm IR}$(CE)][a]	$T_{\rm dust}$(SD2)	$z_{\rm phot}$(SD2)	S_{850}(SD2)[b] (mJy)
SSG 1	$11.9^{+0.1}_{-0.1}$ [12.0]	$33.2^{+2.3}_{-2.3}$	$1.03^{+0.16\ {\rm c}}_{-0.14}$	2.4 ± 0.8
SSG 2	$12.4^{+0.1}_{-0.1}$ [12.6]	$43.9^{+2.4}_{-9.2}$	$1.97^{+0.8}_{-0.3}$	2.7 ± 0.7
LH 350.1	$12.3^{+0.10}_{-0.13}$ [12.5]	$30.3^{+1.5}_{-1.2}$	$1.27^{+0.16}_{-0.09}$	6.7 ± 2.7
LH 350.2	$11.9^{+0.13}_{-0.24}$ [11.9]	$31.9^{+3.4}_{-2.8}$	$1.26^{+0.14}_{-0.12}$	2.4 ± 0.6
LH 350.3	$12.6^{+0.13}_{-0.24}$ [<13.0]	$34.1^{+2.4}_{-1.8}$	$2.71^{+0.03}_{-0.14}$	7.6 ± 2.0

Notes.

[a] The luminosity from the Chary–Elbaz template fit, $L_{\rm IR}$(CE), is obtained from the 24 μm flux density and the STARDUST2 photometric redshift $z_{\rm phot}$(SD2) (or spectroscopic redshift for SSG 1).

[b] Predicted 850 μm flux densities from the STARDUST2 fit.

[c] Spectroscopic redshift for SSG 1 is 1.05 ± 0.01.

elliptical galaxy, and well to the west, the QSO RDS 054A at $z = 2.416$ (Schmidt et al. 1998), which is not expected to make a strong contribution to the 350 μm emission.

2. *LH 350.2.* The 1.4 GHz image shows three sources within the beam. However, the two outermost objects are well resolved in the visible imaging, suggesting that they are likely to be relatively nearby. Photo-*z* fitting puts both at $z \sim 0.4$, and SED template fitting puts a contribution to the 350 μm emission of <20% (assuming a dust temperature, $T_d > 30$ K). Therefore, the very red middle object is likely to be the predominant source of the 350 μm emission with a best-fitting photo-*z* of $1.21^{+0.13}_{-0.20}$.
3. *LH 350.3.* There is a strong 24 μm and weak 1.4 GHz source within 6″ of the 350 μm position. The *B* through 4.5 μm images suggest that the mid-IR flux is a combination of two sources with the radio position lining up on the redder, western object. Best-fitting photometric redshifts are $z = 2.47^{+0.51}_{-0.97}$ and $z = 0.56^{+0.28}_{-0.39}$ for the western and eastern objects, respectively. There remains the possibility of a merging system because the secondary solution for the eastern source is $z = 2.60^{+0.32}_{-0.33}$. Based on the radio identification, the western object is taken as the main source of the submillimeter emission.

3. CONSTRAINTS ON THE PHOTOMETRIC REDSHIFT AND THERMAL EMISSION

The multiwavelength photometry in Table 2 was used to derive photometric redshifts and thermal emission parameters. Following the same approach as Khan et al. (2005), the STARDUST2 template fit was used (P. F. Chanial 2009, in preparation) to simultaneously obtain the photometric redshift $z_{\rm phot}$, dust temperature T_d, and the 8–1000 μm IR luminosity $L_{\rm IR}$. Templates were based on local starbursts, and χ^2 was minimized through a Levenberg–Marquardt technique. For SSG 1, the redshift obtained for the IRS spectrum in Figure 1 was used in the fit, but $z_{\rm spec} = 1.05$ agrees well with the $z_{\rm phot} = 1.03$ from the template fitting. The best-fit parameters are given in Table 3, and the best-fitting templates are shown in Figure 3.

For SSG 1, SSG 2, and LH 350.3, the 350 μm flux density is well fitted by the template, but in the cases of LH 350.2 and 3, the quality of the fit at 350 μm is clearly affected by the longer submillimeter data, which constrain the slope on the Rayleigh–Jeans side of the spectrum. Additionally, the 24 μm flux density is useful in determining which side of the peak the 350 μm data point lies. Usually, the mid-IR is not used to constrain the rest-frame far-IR continuum emission because specific dust grains

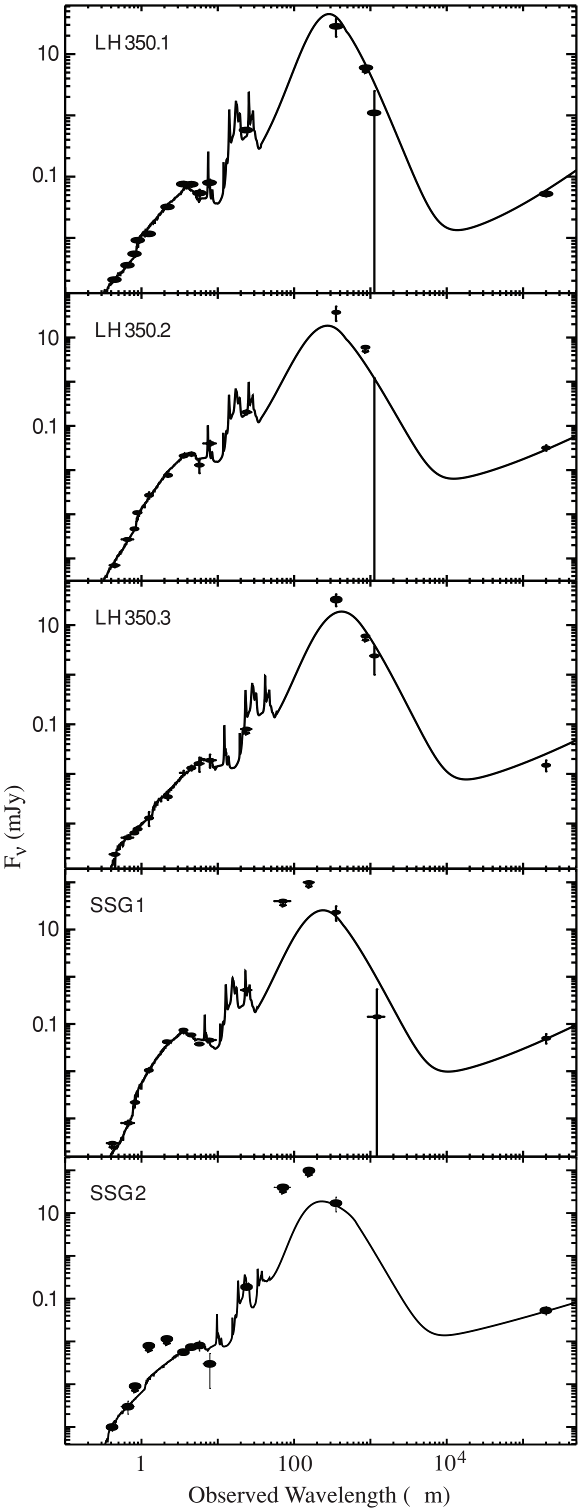

Figure 3. Best-fitting SED templates from STARDUST2. Wavelengths are in the observed frame.

and active galactic nuclei (AGNs) can have a major effect on mid-IR flux densities. Usage of the MIPS band was checked for a sample of SMGs (from Coppin et al. 2008) by comparing template fits using measurements at 350 μm, 850 μm, and radio with measurements at 24 μm, 350 μm, and radio plus long-submillimeter limits. The two approaches agree within the STARDUST2 uncertainties. This indicates our thermal parameters are not noticeably biased by the inclusion of the mid-IR data (see P. F. Chanial 2009, in preparation, for more details).

For LH 350.3, the lack of a defining 1.6 μm rest-frame stellar continuum feature makes a significant AGN contribution plausible, although the relatively low radio flux density would argue against this. Because of the absence of AGN templates in STARDUST2, the LH 350.3 data were also fitted using another routine with a mixture of AGNs and starburst templates (Negrello et al. 2009). In this template fit, the favored solution is a starburst at $z_{\rm phot} = 3.8$ (but without including the radio flux density). Therefore, we consider LH 350.3 to be, like the rest of this sample, predominantly star forming. Given the photometric redshift estimates from hyper-z, STARDUST2, and Negrello et al. (2009), it is possible that LH 350.3 is the most distant galaxy so far discovered at short-submillimeter wavelengths.

3.1. Energy Source Diagnostics

As can be seen in Figure 3, all five sources are well fitted in the mid-IR by templates that include features associated with star formation, i.e., a rest-frame 1.6 μm stellar continuum bump and apparent PAH emission. For SSG 1, the presence of PAH is confirmed by the mid-IR spectrum, as shown in Figure 1. An emission line from [Ne II] is likely present though blended with possible PAH emission at 12.7 μm. The dust continuum is relatively flat until (rest wavelength) ~15.5 μm. Although the 9.7 μm silicate absorption is relatively weak, it is within the range seen in local IR-luminous galaxies. Table 4 gives the emission feature fluxes, and a standard template (IRAS 22491−1808, an IR-luminous galaxy with moderately strong PAH emission) was used to obtain an overall best-fitting redshift from the spectral features of 1.05 ± 0.01.

The values of $L_{\rm PAH}$ for the 7.7 and 11.3 μm rest-frame emission (6.8 and 2.0×10^9 $L_\odot$) are consistent with the $L_{\rm PAH}$ versus $L_{\rm IR}$ distribution of Pope et al. (2008) for a sample of 850 μm selected SMGs. (This comparison used the integrated line flux densities with the $L_{\rm IR}$ given in Table 3.) The 7.7 μm PAH luminosity also provides an estimate of the star formation rate (SFR) of 340 $M_\odot$ yr^{-1} following the relation given by Weedman & Houck (2008). Given the strong star-forming features in the mid-IR spectrum, this compares favorably with the SFR derived from $L_{\rm IR}$ of 136 $M_\odot$ yr^{-1} following the relation given by Kennicutt (1998).

4. DISCUSSION

The different survey depths make it complicated to produce fair statistics for number counts. The Lockman Hole surveys (Laurent et al. 2006; Coppin et al. 2008) were targeted at known sources, and sensitivity for serendipitous sources varied with distance from the target source. Even the blank field survey in Boötes had sensitivity varying with location (see Figure 3 of Khan et al. 2007). However, simply considering the flux densities of the five detections and the total survey area (15.1 arcmin^2),[17] we estimate resolving ~20% of the 350 μm contribution to the cosmic infrared background (CIB; Fixsen et al. 1998) at $S > 17$ mJy. This fraction is reasonable given that the bulk of the background will be generated by galaxies near the break in the differential counts. It is also consistent with the 30% estimate at $S > 13$ mJy from the source counts of Khan et al. (2007).

A lower limit on the star formation rate density (SFRD) can be found using the thermal parameters in Table 3 and the

---

[17] 5.8 arcmin^2 for the Boötes observations; for LH 350.1 and 2 (Laurent et al. 2006) the map area is assumed to be that of the arguably similar SHADES observation of LH 350.3 of 3.1 arcmin^2 (Coppin et al. 2008).

Table 4
Features in the SSG 1 Spectrum

Feature	Rest Wavelength (μm)	Line Center (μm)	Line Flux (10^{-22} W cm^{-2})
PAH	7.7	15.9	14.5 ± 4.4
PAH	8.6	17.4	12.4 ± 1.8
[S IV]	10.5	21.7	1.2 ± 1.8
PAH	11.3	23.1	46.1 ± 5.3
PAH	12.7	26.0	3.0 ± 0.6
[Ne II][a]	12.8	26.9	3.3 ± 0.4
[Ne V]	14.3	29.7	0.5 ± 0.3

Note. [a] The [Ne II] emission line could be blended with the 12.7 μm PAH feature.

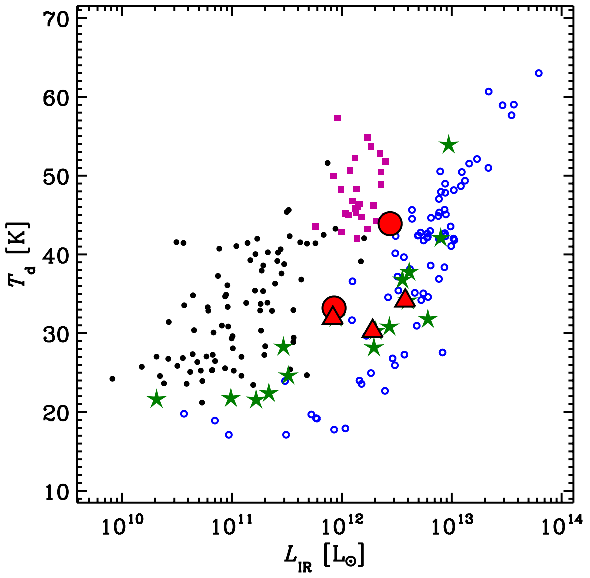

Figure 4. IR luminosity-dust temperature distribution for various IR-luminous galaxy samples. For the 350 μm selected galaxies, the red circles show SSG 1 and SSG 2, and triangles show LH 350.1, 350.2, and 350.3. Green stars represent the 850 and 1100 μm selected SMGs for which there is 350 μm follow-up photometry. This is compared with 850 μm selected SMGs from Chapman et al. (2005; open blue circles) and *IRAS* galaxies from Dunne et al. (2000; filled black squares) and D. L. Clements et al. (2009, in preparation) (purple squares).

(A color version of this figure is available in the online journal.)

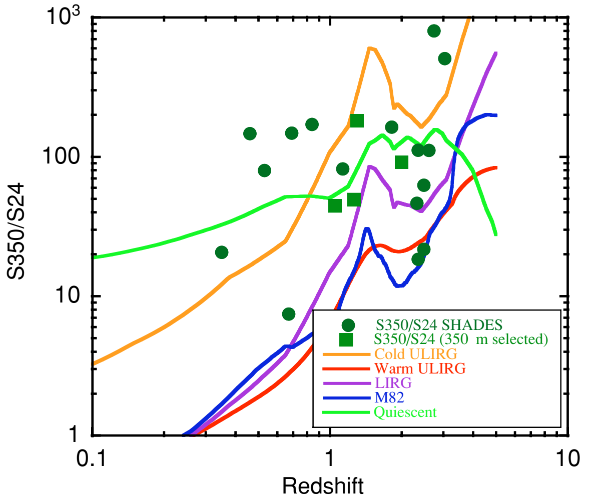

Figure 5. 350 μm: 24 μm flux density ratio as a function of redshift for various SMG samples as indicated in the legend. Lines show the same ratio for local SED templates from Efstathiou et al. (2000).

(A color version of this figure is available in the online journal.)

comoving volume in $1 < z < 3$. The conversion from far-IR luminosity to SFR is given by Kennicutt (1998). The result for this epoch is 0.017 $M_\odot$ yr^{-1} Mpc^{-3}, much lower than the values presented by Hopkins & Beacom (2006). This implies that the bulk of the 350 μm contribution to the SFRD is from less luminous infrared galaxies and normal galaxies, consistent with observations of IR-luminous galaxies in different bands (e.g., Le Floc'h et al. 2005) and the predictions from source count models (e.g., Pearson & Khan 2009).

Our 350 μm selected galaxies can be compared with sources selected at longer submillimeter wavelengths. Suitable samples that include 350 and 24 μm photometry come from Coppin et al. (2008), Laurent et al. (2006), and Kovács et al. (2006). The photometric redshifts and thermal parameters for these SMGs were again found using STARDUST2. Where there is no spectroscopic redshift, the photo-z was obtained from optical and mid-IR magnitudes given by Dye et al. (2008) and Clements et al. (2008). Following the $L_{\rm IR}$–T_d distribution by Blain et al. (2004), there appear to be two trends separating the predominantly local *IRAS* galaxies from the higher redshift SMGs (see Figure 4). Compared with those selected at 850 and 1100 μm, the 350 μm selected sources have similar dust temperatures and give no indication of temperature bias according to selection wavelength. Deeper 800–1000 μm imaging (e.g., with ALMA—Wootten & Thompson 2009) of the 350 μm selected population would provide a more direct comparison of any selection biases.

Mid-IR surveys to probe the $1 < z < 3$ galaxy population have the advantage of better angular resolution, aiding counterpart identification (and hence more reliable redshift estimation), but a significant disadvantage is that without further far-IR observations, constraints on the rest-frame far-IR thermal emission must be indirectly inferred. The 350:24 flux density–redshift distribution for the SHARC II 350 μm selected SMGs compared with the 850 and 1100 μm selected SMGs is shown in Figure 5 alongside colors from various templates from Efstathiou et al. (2000). The overall distribution suggests that all samples are drawn from the same IR-luminous galaxy population, and the good agreement with the templates suggests these are predominantly luminous and ultraluminous infrared galaxies.[18]

Studies of infrared galaxies are often limited by unavailability of data at wavelengths longer than 24 μm. In such cases, the IR luminosity can be estimated using only the 24 μm flux density and various SED templates (Chary & Elbaz 2001) combined with an estimated redshift. For the SMG samples, the thermal emission estimates found this way compare surprisingly well with those from STARDUST2 for $z \lesssim 1$ as shown in Figure 6.

---

[18] $10^{11}\,L_\odot < L_{\rm IR} < 10^{12}\,L_\odot$ and $L_{\rm IR} > 10^{12}\,L_\odot$, respectively.

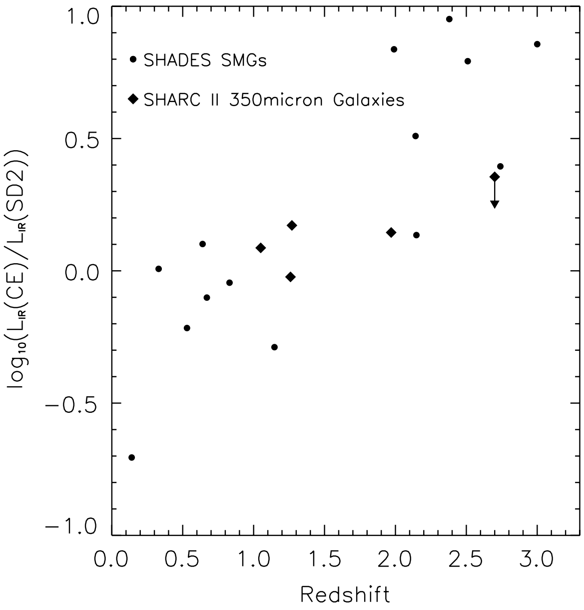

Figure 6. Ratio of best-fitting IR (8–1000 μm) luminosities obtained from the CE and STARDUST2 fitting, as a function of redshift. The diamonds denote the 350 μm selected galaxies, and filled circles denote the 850 and 1100 μm selected galaxies. The diamond with arrow denotes an upper limit. Sources with redshifts beyond the usable range for the CE model (∼3) are excluded from consideration.

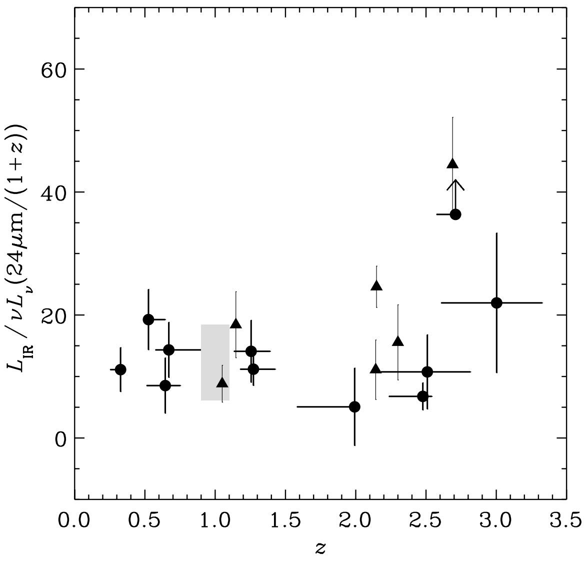

Figure 7. Ratio of far-IR luminosity to monochromatic luminosity at observed wavelength of 24 μm as a function of redshift. Data are shown for the 350, 850, and 1100 μm selected SMGs. Numerator of the ratio is the rest-frame far-IR (8–1000 μm) luminosity derived from the STARDUST2 template fitting. The denominator is the rest-frame luminosity for the 24 μm observation, i.e., monochromatic luminosity, νL_ν, at rest-frame wavelength 24 μm/$(1 + z)$. At $z \approx 1$, observed 24 μm corresponds to rest 12 μm, which as Spinoglio et al. (1995) suggested gives a good measure of total luminosity. The shaded region on the plot shows the Spinoglio et al. data for local luminous infrared galaxies as they would appear at $z = 1$. Filled triangles denote sources with spectroscopic redshift, while filled circles denote sources with photometric redshifts from the STARDUST2 template fit.

For these galaxies, the dominant errors on both luminosity predictors will arise from the photo-z fitting; these errors are highly non-Gaussian and non-trivial to determine. To some extent, the agreement in Figure 6 can be attributed to small number statistics and selection. The overall variation in the ratio over a wider redshift range could also imply a heterogenous SMG population. This would be consistent with the color in Figure 5 but with a varying degree of AGN contribution. Another condition on this sample is the requirement of bright optical, mid-IR, and most importantly radio identifications; at high redshift, an AGN will boost the radio flux density and the emission in other bands (notably in the mid-IR), allowing this type of analysis to be performed. However, none of the sources in the sample appear to be strongly affected by an AGN. At higher redshifts multiwavelength analysis becomes much more difficult. Some of the higher-z 850/1100 μm galaxies could simply have incorrectly identified 24 μm counterparts (see, e.g., Younger et al. 2007).

The rest-frame 12 μm flux density has been suggested to be a "pivot point" for SEDs (Spinoglio et al. 1995; see also Elbaz et al. 2002), giving a fixed $L_{12}/L_{\rm FIR}$ for both starbursts and AGNs. This correlation was determined from local *IRAS* sources, but at $z \sim 1$, the rest frame 12 μm is shifted into the 24 μm band, and thus the relation at this redshift can be examined directly by our sample. We expect this relation to hold if the populations are similar. An observed difference in the populations is that distant mid-IR sources show stronger dust grain emission features around 12 μm compared to the local IR-luminous galaxy population. This difference could be due to differing AGN fractions (Wu et al. 2009).

Figure 7 shows the ratio of far-IR luminosity to observed *Spitzer*/MIPS 24 μm monochromatic luminosity as a function of redshift. The ratio flattens out at $z \sim 1$ as the rest-frame 12 μm emission is shifted into the MIPS 24 μm band, but the dispersion increases at higher redshift. This suggests that the local empirical far-IR/12 μm relation could apply to earlier epochs where the galaxy is undergoing rapid evolution, making rest-frame 12 μm flux densities a better tracer of IR luminosity (Spinoglio et al. 1995) than other mid-IR emission features, e.g., 7.7 μm PAH selected at $z \sim 2$. At $z \sim 1.4$, the silicate absorption feature is redshifted into the MIPS 24 μm band and affects the flux density measurement. This effect is emphasized in Figure 5, where an excess in the 350/24 μm colors is evident in the model SEDs, and galaxies in the redshift range where the silicate feature would cause a deficit in the 24 μm flux ($1.3 < z < 1.6$) are notably absent from Figure 7.

Various studies have suggested that the far-IR luminosity can be deduced solely from mid-IR observations of galaxies. Bavouzet et al. (2008) have shown that the far-IR luminosity of dusty galaxies observed with *Spitzer* correlate closely with the corresponding 8 and 24 μm mid-IR luminosities. These studies were limited to redshifts $z \lesssim 1$ by the necessity to use *Spitzer* bands at 70 and 160 μm to calculate the far-IR luminosity. The mid-IR to far-IR luminosity relation was tentatively extended to higher redshifts ($z \sim 2$) by stacking the far-infrared fluxes in the long-wavelength *Spitzer* bands, and these stacked results were used by Caputi et al. (2007) to calculate the bolometric luminosity function at $z \approx 2$. In contrast, our submillimeter observations directly access the high-redshift universe without the need for stacking images to obtain far-infrared fluxes. From Figure 7, we observe a tight correlation between the far- and mid-IR flux densities in our sample between $1 < z < 2$, but there is a large dispersion in the infrared colors at $z > 2$. For $z > 2$, the 24 μm band is sampling rest wavelengths shorter than 8 μm, and the far-IR luminosity cannot be accurately predicted from such observations. In order to confirm the mid-IR/far-IR relation for $1 < z < 2$ and to test the relation to higher redshifts, large samples of SMGs will be required. Such samples will be available following the large surveys planned with Herschel SPIRE (at 250, 350, and 500 μm; Griffin et al. 2008).

5. CONCLUSION

The discovery of the first 350 μm selected galaxies using SHARC II offers a different insight into IR-luminous galaxies than those selected in either the mid-IR or in longer submillimeter bands. The present sample comprises IR-luminous galaxies at $1 < z < 3$ and resolves ~20% of the 350 μm background at $S > 17$ mJy. The implied lower limit on the SFRD suggests that the bulk of the 350 μm contribution is from galaxies of lower IR luminosity than the ones detected at present flux densities.

The combination of 350 μm and mid-IR flux densities allows us to examine the relation of the mid- and far-IR emission in dusty galaxies at high redshift. There is surprisingly good agreement at $z < 2$, with the flattening of the IR:24 $\mu\text{m}/(1+z)$ luminosity ratio at $z \sim 1$ evidence for the local empirical relation of rest-frame 12 μm IR luminosity tracing IR luminosity applying to distant IR-luminous galaxies. The wider dispersion at $z > 2$ suggests a limit to which the mid-IR can be used as a proxy for far-IR emission. We also find, by comparing our 350 μm selected sample to samples chosen at 850 μm and millimeter wavelengths, no evidence for a cold color temperature bias in SMGs. These results will be further tested through surveys with *Herschel*-SPIRE, which will detect SMGs in unprecedented numbers.

The present 350 μm selected sample, with $15 < S_{350} < 40$ mJy, is near the SPIRE 350 μm blank-field detection limit (e.g., Pearson & Khan 2009; Franceschini et al. 2009) and also the detection limits of current longer-wavelength submillimeter instruments. Counterpart identification is difficult even with the available angular resolution and will be far more difficult for space-based surveys with smaller telescopes. The achievable sensitivity and resolution of ground-based detectors will therefore provide a necessary complement to the space-based surveys, especially in characterizing the nature of the faint SMG population. Whether the first 350 μm selected galaxies are typical of the population will be probed through the combination of surveys with SPIRE and future surveys from the ground (e.g., SCUBA 2–450 μm; Holland et al. 2006).

We thank Tom Phillips and the CSO for observing time and assistance during our runs, and Darren Dowell, Colin Borys, Attila Kovacs, Rick Arendt, Dave Chuss, and Bob Silverberg for providing observing and data reduction support. We thank Glenn Laurent and Kristen Coppin for advice on their 350 μm Lockman Hole follow-up surveys, Mark Brodwin and Yen-Ting Lin for assistance in compiling the Boötes optical and near-IR photometry, and Rob Ivison for providing the radio maps for the Lockman Hole sources.

The Caltech Submillimeter Observatory is supported by NSF contract AST-0229008. This work is based in part on observations made with the *Spitzer Space Telescope*, which is operated by the Jet Propulsion Laboratory, California Institute of Technology under a contract with NASA. This work is based in part on data collected at *Subaru* Telescope, which is operated by the National Astronomical Observatory of Japan. The *Subaru* data are those used by Dye et al. (2008). This research has made use of the NASA/IPAC Extragalactic Database (NED), which is operated by the Jet Propulsion Laboratory, California Institute of Technology, under contract with the National Aeronautics and Space Administration. This research has made use of the SIMBAD database, operated at CDS, Strasbourg, France. This research draws upon data provided by Buell Jannuzi & Arjun Dey and by Richard Elston & Anthony Gonzalez (Elston et al. 2006) as distributed by the NOAO Science Archive. NOAO is operated by the Association of Universities for Research in Astronomy (AURA), Inc., under a cooperative agreement with the National Science Foundation. The UKIDSS project is defined by Lawrence et al. (2007). UKIDSS uses the UKIRT Wide Field Camera (WFCAM; Casali et al. 2007). We used data from the fourth data release (DR4).

S.A.K. is partially supported through FONDECYT Proyecto 1070992 and ALMA-Conicyt. Support for E.L.F.'s work was provided by NASA through the Spitzer Space Telescope Fellowship Program.

Facilities: CSO, *Spitzer*, UKIRT, *Subaru*, VLA, IRAM/MAMBO

REFERENCES

Aussel, H., Elbaz, D., & Cesarsky, C. J. 1999, Ap&SS, 266, 307
Barger, A. J., et al. 1998, Nature, 394, 248
Bavouzet, N., Dole, H., Le Floc'h, E., Caputi, K. I., Lagache, G., & Kochanek, C. S. 2008, A&A, 479, 83
Bennett, C. L., et al. 2003, ApJS, 148, 1
Bertoldi, F., et al. 2000, A&A, 360, 92
Biggs, A. D., & Ivison, R. J. 2006, MNRAS, 371, 963
Blain, A. W., Chapman, S. C., Smail, I., & Ivison, R. 2004, ApJ, 611, 52
Bolzonella, M., Miralles, J.-M., & Pell'o, R. 2000, A&A, 363, 476
Caputi, K. I., et al. 2007, ApJ, 660, 116
Casali, M., et al. 2007, A&A, 467, 777
Chapman, S. C., Blain, A. W., Smail, I., & Ivison, R. J. 2005, ApJ, 622, 772
Chary, R., & Elbaz, D. 2001, ApJ, 556, 562
Chary, R., et al. 2004, ApJS, 154, 80
Clements, D. L., et al. 2008, MNRAS, 387, 247
Coppin, K., et al. 2008, MNRAS, 384, 1597
Dowell, C. D., et al. 2003, Proc. SPIE, 4855, 73
Dunne, L., et al. 2000, MNRAS, 315, 115
Dye, S., et al. 2008, MNRAS, 386, 1107
Eales, S., et al. 1999, ApJ, 515, 518
Efstathiou, A., Rowan-Robinson, M., & Siebenmorgen, R. 2000, MNRAS, 313, 734
Eisenhardt, P. R., et al. 2004, ApJS, 154, 48
Elbaz, D., Cesarsky, C. J., Chanial, P., Aussel, H., Franceschini, A., Fadda, D., & Chary, R. R. 2002, A&A, 384, 848
Elston, R. J., et al. 2006, ApJ, 639, 816
Fazio, G. G., et al. 2004, ApJS, 154, 10
Fixsen, D. J., et al. 1998, ApJ, 508, 123
Fox, M., et al. 2002, MNRAS, 331, 839
Franceschini, A., Rodighiero, G., Vaccari, M., Marchetti, L., & Mainetti, G. 2009, A&A, submitted (arXiv:0906.4264)
Galliano, F., et al. 2008, ApJ, 679, 310
Gordon, K. D., et al. 2005, PASP, 117, 503
Griffin, M., et al. 2008, Proc. SPIE, 7010, 4
Higdon, S. J. U., et al. 2004, PASP, 116, 975
Holland, W. S., et al. 1999, MNRAS, 303, 659
Holland, W. S., et al. 2006, Proc. SPIE, 6275, 45
Hopkins, A. M., & Beacom, J. F. 2006, ApJ, 651, 142
Houck, J. R., et al. 2004, ApJS, 154, 18
Joseph, R. D., & Wright, G. S. 1985, MNRAS, 214, 87
Kennicutt, R. C., Jr. 1998, ApJ, 498, 541
Kessler, M. F., et al. 1996, A&A, 315, 27
Khan, S. A. 2006, PhD thesis, Univ. London
Khan, S. A., et al. 2005, ApJ, 631, L9
Khan, S. A., et al. 2007, ApJ, 665, 973
Kovács, A., et al. 2006, ApJ, 650, 592
Laurent, G. T., et al. 2005, ApJ, 623, 742
Laurent, G. T., et al. 2006, ApJ, 643, 38
Lawrence, A., et al. 2007, MNRAS, 379, 1599
Le Floc'h, E., et al. 2004, ApJS, 154, 170
Le Floc'h, E., et al. 2005, ApJ, 632, 169
Lonsdale, C., et al. 2004, ApJS, 154, 54
Matsuhara, H., et al. 2006, PASJ, 58, 673

Moseley, S. H., et al. 2004, NIMPA, 520, 417
Murakami, H., et al. 2007, PASJ, 59, 369
Negrello, M., et al. 2009, MNRAS, 394, 375
Pearson, C. P., & Khan, S. A. 2009, MNRAS, 399, L11
Pope, A., et al. 2008, ApJ, 675, 1171
Puget, J. L., et al. 1999, A&A, 345, 29
Rieke, G. H., et al. 2004, ApJS, 154, 25
Rowan-Robinson, M., et al. 1997, MNRAS, 289, 490
Schmidt, M., et al. 1998, A&A, 329, 495
Schuster, M. T., Marengo, M., & Patten, B. M. 2006, Proc. SPIE, 6270, 627020
Serabyn, E., Weisstein, E. W., Lis, D. C., & Pardo, J. R. 1998, Appl. Opt., 37, 2185
Smail, I., Ivison, R. J., & Blain, A. W. 1997, ApJ, 490, L5
Smith, J. D. T., et al. 2007, ApJ, 656, 770
Soifer, B. T., Neugebauer, G., & Houck, J. R. 1987, ARA&A, 25, 187
Soifer, B. T., et al. 1984, ApJ, 278, L71
Spinoglio, L., et al. 1995, ApJ, 453, 616
Weedman, D. W., & Houck, J. R. 2008, ApJ, 686, 127
Werner, M. W., et al. 2004, ApJS, 154, 1
Wootten, A., & Thompson, A. R. 2009, Proc. IEEE, 97, 1463
Wu, Y., Charmandaris, V., Huang, J., Spinoglio, L., & Tommasin, S. 2009, ApJ, 701, 658
Yan, L., et al. 2004, ApJS, 154, 60
Younger, J. D., et al. 2007, ApJ, 671, 1531

Appendix B

SPIRE Mask definition

In the context of the SPIRE data processing pipelines, masks are defined as indicators of a condition as it relates to the data. The SPIRE data processing pipelines are divided into a series of levels. Within each of these levels, there are certain data products that have been defined. The structure of the SPIRE data products at each level of the processing pipelines has an implication on the manner in which mask information is represented.

Level-0 – Level-0.5 Processing The Level-0 data products do not contain placeholder in which mask information may be stored. As such, for the Level-0 to Level-0.5 stage of the SPIRE data processing pipelines, mask information must reside outside of the data products themselves. In the **Level-0 to Level-0.5 stage** of the SPIRE data processing pipelines, mask information is maintained in a set of calibration products: the Channel Mask product and the Instrument Mode Mask product. Mask information in these calibration products applies to all samples for a given detector channel.

Level-0.5 – Level-2 Processing The SPIRE detector data products used in the Level-0.5 to Level-2 stages for the SPIRE data processing pipelines all contain placeholders that may be used to store mask information. In each of these products, a 32-bit integer is reserved for each sample for each detector, referred to as a Sample Mask. Mask information is represented by bits in a Sample Mask, with different bits representing different mask conditions.

The conditions that are represented by Sample Masks are divided into three categories: Unusable, Informational, and Correctable (see Section 3.3.1). The following sections provide definitions for these categories and discuss how the SPIRE pipeline modules should process data samples that fall into these categories.

A list of the sample masks that are currently defined in SPIRE data processing pipeline is given in the following table.

BIT NUMBER	(BIT VALUE)	**Mask Name**	*Description*

0 (1) = **MASTER**: *If the value is set, then the data should not be used*
1 (2) = **INVALID_TIME**: *indicates that the sample has an invalid time*
2 (4) = **ADC_LATCH**: *indicates that there was a possible ADC latchup error*
3 (8) = **TRUNCATED**: *indicates that the ADC conversion resulted in data being truncated*
4 (16) = **TRUNCATED_UNCORR**: *indicates that the ADC truncation is not corrected*
5 (32) = **GLITCH**: *a glitch was detected in the sample*
6 (64) = **GLITCH_UNCORR**: *a glitch was detected and has not been removed from the sample*
7 (128) = **ISDEAD**: *indicates that the channel is dead*
8 (256) = **ISNOISY**: *indicates that the channel is noisy*
9 (512) = **ISNOCHOPSKY**: *indicates that the channel is not chopped to sky*
10 (1024) = **VOLTAGE_OOL**: *voltage value that lies outside the range of the fitted portion of the bolometer responsivity curve*
11 (2048) = **GLITCH_FIRST_LEVEL**: *a glitch was detected in the sample during first level deglitching*
12 (4096) = **GLITCH_FIRST_LEVEL_UNCORR**: *a glitch was detected during first level deglitching and has not been removed from the sample*
13 (8192) = **GLITCH_SECOND_LEVEL**: *a glitch was detected in the sample during second level deglitching*
14 (16384) = **GLITCH_SECOND_LEVEL_UNCORR**: *a glitch was detected during first level deglitching and has not been removed from the sample*
15 (32768) = **ISSLOW**: *indicates that the sample has been recorded on a channel that has been deemed as slow*
16 (65536) = **VOLTAGE_BELOW_K3**: *indicates that Flux Converstion (Photometer) or Non-linearity Correction (Spectrometer) module encountered a Voltage sample whose value was less than the K3 calibration factor*
17 (131072) = **NO_RESP_DATA**: *indicates that V0_flag and/or the K_flag was set to true for a given channel thereby signifying that no flux conversion (Photometer) or linearization (Spectrometer) is possible*
18 (262144) = **TSIGNAL_HDV**: *indicates that thermistor/DP signal deviations larger than expected from temperature drift alone*
19 (524288) = **BSM_CHOP_OOL**: *indicates that the recorded sample falls outside the BSM chop soft limits*
20 (1048576) = **BSM_JIGG_OOL**: *indicates that the recorded sample falls outside the BSM jiggle soft limits*
21 (2097152) = **JUMP_THERMISTORS_DARKS_SIGNAL**: *Indicates sudden signal jumps in the timelines of thermistors and dark channels*
22 (4194304) = **NO_THERMISTOR_AVAILABLE**: *Indicates that all of the available thermistors in a given array*
23 (8388608) = **SCAN_POSITIONING_SLEW**: *Indicates that portions of the timeline that are not part of the nominal science scans of a scan map, i,e, it should be set for all data between nominal scan legs. This includes parts where the scan speed is not nominal, and slews of the spacecraft for purposes of gyro calibration*
24 (16777216)= **NO_DARKCHANNEL_AVAILABLE**: *Indicates that all of the available DP detectors (i.e. dark channels) in a given array are affected by either saturation or signal jump.*

Appendix C

Add turnaround for Photometer Detector Timelines - Module Design

C.1 Module Information

C.1.1 Module Owner

Gabriele Mainetti (gabriele.mainetti@unipd.it)

C.1.2 Others Contributing

Pasquale Panuzzo

C.1.3 Applicable Documents

- Herschel Products Definition Document, Part I (HERSCHEL-HSC-DOC-0959).
- Herschel Products Definition Document, Part II (HERSCHEL-HSC-DOC-0959).
- E. Polehampton SPIRE Data Products Specification (SPIRE-RAL-DOC-002005).
- C. Pearson, SPIRE Pipeline Description (SPIRE-RAL-DOC-002437, Draft 1.5, 25 July 2008).

C.1.4 Module Description

This module join scan line detector timelines with the detector timelines of the leading and trailing turnaround building block in scan maps.

C.2 Input Data Products

C.2.1 Input Observational Data Products

The module take as input three Photometer Detector Timeline Product(PDT). For the product definition see:
`http://130.246.35.182/icc/product_definitions/Data_products/html_files/PDT.html`

C.2.2 Output Data Products

The final output of this module is a Photometer Detector Timeline Product (PDT). For the product definition see:
`http://130.246.35.182/icc/product_definitions/Data_products/html_files/PDT.html`

C.3 Module Design

This module is developed as a Herschel task, inheriting from the Task superclass.

C.3.1 Module Method

The purpose of this module is to join scan line detector timelines with the detector timelines of the leading and trailing turnaround building block in scan map. The module use three input PDT:

1. pdt: detector timeline of the scan line;
2. leading: detector timeline of the leading turnaround building block;
3. trailing: detector timeline of the trailing turnaround building block.

The only mandatory parameter is the scan line PDT: if the leading and trailing input are not set, the output of the module is equal to the input.

The module reads the scan line PDT and propagates the meta data to the output. Finally, the module combines in the output the dataset of the three input

PDT.
The module catch the exception (BadDataException) when not corrected data are passed as input (e.g. missing dataset in the leading or trailing PDT).

C.3.2 Open Issues

C.3.3 Improvements

C.3.4 Problems

Appendix D

Add turnaround for Photometer Detector Timelines - Test Plan

D.1 Module Information

D.1.1 Module Owner

Gabriele Mainetti (gabriele.mainetti@unipd.it)

D.1.2 Others Contributing

Pasquale Panuzzo

D.1.3 Applicable Documents

- Herschel Products Definition Document, Part I (HERSCHEL-HSC-DOC-0959).

- Herschel Products Definition Document, Part II (HERSCHEL-HSC-DOC-0959).

- E. Polehampton SPIRE Data Products Specification (SPIRE-RAL-DOC-002005)

- C. Pearson, SPIRE Pipeline Description (SPIRE-RAL-DOC-002437, Draft 1.5, 25 July 2008).

D.1.4 Module Description

This module join scan line detector timelines with the detector timelines of the leading and trailing turnaround building block in scan maps.

D.2 Input Data Products

D.2.1 Input Observational Data Products

The module take as input three Photometer Detector Timeline Product(PDT). For the product definition see:
`http://130.246.35.182/icc/product_definitions/Data_products/html_files/PDT.html`

D.2.2 Output Data Products

The final output of this module is a Photometer Detector Timeline Product (PDT). For the product definition see:
`http://130.246.35.182/icc/product_definitions/Data_products/html_files/PDT.html`

D.3 Module Test Plan

The testing procedures are detailled in the following.

1. Testing the module with three (scan line, leading and trailing) well-formed input. The test verifies that the output is not null, that the all datasets contained in the input are passed to the output, that for any channel (e.g. PSWE8) the three inputs are joined properly in the output, that the output metadata contains the right version of the task in the "CREATOR" field.
2. Testing the module with null leading and following input PDT.
3. Testing the module exception when datasets contained in the leading input are not the same datasets contained in the scan line and trailing input (e.g removing the "signal" dataset from trailing input).
4. Testing the module exception when datasets contained in the trailing input are not the same datasets contained in the scan line and leading input (e.g removing the "signal" dataset from trailing input).

Appendix E

Add turnaround for Nominal House Keeping Timelines - Module Design

E.1 Module Information

E.1.1 Module Owner

Gabriele Mainetti (gabriele.mainetti@unipd.it)

E.1.2 Others Contributing

Pasquale Panuzzo

E.1.3 Applicable Documents

- Herschel Products Definition Document, Part I (HERSCHEL-HSC-DOC-0959).
- Herschel Products Definition Document, Part II (HERSCHEL-HSC-DOC-0959).
- E. Polehampton SPIRE Data Products Specification (SPIRE-RAL-DOC-002005)
- C. Pearson, SPIRE Pipeline Description (SPIRE-RAL-DOC-002437, Draft 1.5, 25 July 2008).

E.1.4 Module Description

This module join scan line Nominal House Keeping timelines (NHKT) with the NHKT of the leading and trailing turnaround building block in scan maps.

E.2 Input Data Products

E.2.1 1.2.1 Input Observational Data Products

The module will take as input three Nominal House Keeping Timeline Product. For the product definition see:
`http://130.246.35.182/icc/product_definitions/Data_products/html_files/NHKT.html`

E.2.2 Output Data Products

The final output of this module is a Nominal House Keeping Timeline Product. For the product definition see:
`http://130.246.35.182/icc/product_definitions/Data_products/html_files/NHKT.html`

E.3 Module Design

This module is developed as a Herschel task, inheriting from the Task superclass.

E.3.1 Module Method

The purpose of this module is to join scan line detector timelines with the detector timelines of the leading and trailing turnaround building block in scan map. The module use three input NHK Timelines:

1. nhkt: NHK Timeline of the scan line;
2. leading: NHK Timeline of the leading turnaround building block;
3. trailing: NHK Timeline of the trailing turnaround building block.

The only mandatory parameter is the scan line NHKT: if the leading and trailing input are not set, the output of the module is equal to the input.

Below is a list of all the steps performed by the module:

1. The module reads the detector timeline of the scan line;
2. The module propagates the meta data to the output;
3. The module combines in the output the dataset of the three input NHK Timeline
4. Finally, the module performs a control about the entries in the timeline: if the entries are not unique or sorted, the module removes the duplicate and sorts the value.

E.3.2 Open Issues

E.3.3 Improvements

E.3.4 Problems

Appendix F

Add turnaround for Nominal House Keeping Timelines - Test Plan

F.1 Module Information

F.1.1 Module Owner

Gabriele Mainetti (gabriele.mainetti@unipd.it)

F.1.2 Others Contributing

Pasquale Panuzzo

F.1.3 Applicable Documents

- Herschel Products Definition Document, Part I (HERSCHEL-HSC-DOC-0959).
- Herschel Products Definition Document, Part II (HERSCHEL-HSC-DOC-0959).
- E. Polehampton SPIRE Data Products Specification (SPIRE-RAL-DOC-002005)
- C. Pearson, SPIRE Pipeline Description (SPIRE-RAL-DOC-002437, Draft 1.5, 25 July 2008).

F.1.4 Module Description

This module join scan line Nominal House Keeping timelines (NHKT) with the NHKT of the leading and trailing turnaround building block in scan maps.

F.2 Input Data Products

F.2.1 Input Observational Data Products

The module will take as input three Nominal House Keeping Timeline Product. For the product definition see:
`http://130.246.35.182/icc/product_definitions/Data_products/html_files/NHKT.html`

F.2.2 Output Data Products

The final output of this module is a Nominal House Keeping Timeline Product. For the product definition see:
`http://130.246.35.182/icc/product_definitions/Data_products/html_files/NHKT.html`

F.3 Module Test Plan

The testing procedures are detailled in the following.

1. Testing the module with only the scan line NHKT input. The test verifies that the output is sorted.
2. Testing the module with leading and scan line NHKT input. The test verifies that the output contains the right datasets and is sorted.
3. Testing the module with leading, scan line and trailing NHKT input. The test verifies that the output contains the right datasets and that the output is sorted.
4. Testing the module exception when datasets contained in the leading or trailing input are not the same datasets contained in the others input (e.g removing the "signal" dataset from trailing input).
5. Testing the module if the data in the output are not unique and/or not sorted.

Appendix G

Cut turnaround from Timelines - Module Design

G.1 Module Information

G.1.1 Module Owner

Gabriele Mainetti (gabriele.mainetti@unipd.it)

G.1.2 Others Contributing

Pasquale Panuzzo

G.1.3 Applicable Documents

- Herschel Products Definition Document, Part I (HERSCHEL-HSC-DOC-0959).
- Herschel Products Definition Document, Part II (HERSCHEL-HSC-DOC-0959).
- E. Polehampton SPIRE Data Products Specification (SPIRE-RAL-DOC-002005)
- C. Pearson, SPIRE Pipeline Description (SPIRE-RAL-DOC-002437, Draft 1.5, 25 July 2008).

G.1.4 Module Description

This module cut a Photometer Scan Product (PSP) timelines that were previously joined with the detector timelines of the leading and trailing turnaround building block in scan maps.

G.2 Input Data Products

G.2.1 1.2.1 Input Observational Data Products

The module will take as input an Photometer Scan Product (PSP). For the product definition see:
`http://130.246.35.182/icc/product_definitions/Data_products/html_files/PSP.html`

G.2.2 Input Control Parameters

extend: Parameter to keep half of turnaround data.

G.2.3 Output Data Products

The final output of this module is a Photometer Scan Product (PSP). For the product definition see:
`http://130.246.35.182/icc/product_definitions/Data_products/html_files/PSP.html`

G.3 Module Design

This module is developed as a Herschel task, inheriting from the Task superclass.

G.3.1 Module Method

The purpose of this module is to cut the PSP timelines that were previously joined with the detector timelines of the leading and trailing turnaround building block in scan maps. Below is a list of all the steps performed by the module:

1. Creates a empty PSP;
2. Read the metadata from the input PSP;

3. Propagates the metadata to the output;
4. Read the start date (startDate) and the end date (endDate) of the input PSP: this value are linked at the scan line previously joined with the detector timelines of the leading and trailing turnaround building block;
5. Set the "startNominalScanLine" and the "endNominalScanLine" output metadata parameters to startDate and endDate values;
6. If the extended parameter is selected, the module define a new startDate and endDate so that keep half of the turnaround data. To do this the module:
    (a) Read the input sample time (sampleTime);
    (b) Get the first entries (firstEntries) in sampleTime and set the startDate to the startDate=startDate+(firstEntries/2)
    (c) Get the last entries (lastEntries) in sampleTime and set the endDate to the endDate=endDate+(lastEntries/2)
7. If the extended parameter is selected, the module update the "startDate" and the "endDate" output metadata parameter to the new value of startdate and endDate;
8. Finally, for any dataset contained in the PSP input, the module selects the values between starDate and endDate and put them in the PSP output.

G.3.2 Open Issues

G.3.3 Improvements

G.3.4 Problems

Appendix H

Cut turnaround from Timelines - Test Plan

H.1 Module Information

H.1.1 Module Owner

Gabriele Mainetti (gabriele.mainetti@unipd.it)

H.1.2 Others Contributing

Pasquale Panuzzo

H.1.3 Applicable Documents

- Herschel Products Definition Document, Part I (HERSCHEL-HSC-DOC-0959).
- Herschel Products Definition Document, Part II (HERSCHEL-HSC-DOC-0959).
- E. Polehampton SPIRE Data Products Specification (SPIRE-RAL-DOC-002005)
- C. Pearson, SPIRE Pipeline Description (SPIRE-RAL-DOC-002437, Draft 1.5, 25 July 2008).

H.1.4 Module Description

This module cut a Photometer Scan Product (PSP) timelines that were previously joined with the detector timelines of the leading and trailing turnaround building block in scan maps.

H.2 Input Data Products

H.2.1 Input Observational Data Products

The module will take as input an Photometer Scan Product (PSP). For the product definition see:
`http://130.246.35.182/icc/product_definitions/Data_products/html_files/PSP.html`

H.2.2 Input Control Parameters

extend: Parameter to keep half of turnaround data.

H.2.3 Output Data Products

The final output of this module is a Photometer Scan Product (PSP). For the product definition see:
`http://130.246.35.182/icc/product_definitions/Data_products/html_files/PSP.html`

H.3 Module Test Plan

The testing procedures are detailled in the following.

1. Testing with corrected input and "extend" parameter not set. The test verifies that the output contains the right datasets, that the output metadata contains the right version of the task in the "Creator" field, that the channels were cut correctly.

2. Testing with corrected input and "extend" parameter set. The test verifies that the output contains the right datasets, that the output metadata contains the right version of the task in the "Creator" field, that the channels were cut correctly, that the extended time was selected correctly.

References

Ade, P. A. R., Pisano, G., Tucker, C., & Weaver, S. 2006in (SPIE), 62750U

Baum, W. A. 1962, in IAU Symposium, Vol. 15, Problems of Extra-Galactic Research, ed. G. C. McVittie, 390–+

Béthermin, M., Dole, H., Cousin, M., & Bavouzet, N. 2010, A&A, 516, 43

Blain, A. W., Chapman, S. C., Smail, I., & Ivison, R. 2004, ApJ, 611, 52

Bolzonella, M., Miralles, J., & Pelló, R. 2000, A&A, 363, 476

Chapman, S. C., Blain, A. W., Smail, I., & Ivison, R. J. 2005, ApJ, 622, 772

Chattopadhyay, G., Glenn, J., Bock, J. J., et al. 2003, IEEE Transactions on Microwave Theory Techniques, 51, 2139

Clements, D. L., Rigby, E., Maddox, S., et al. 2010, A&A, 518, L8+

Condon, J. J. 1974, ApJ, 188, 279

Cooray, A., Amblard, A., Wang, L., et al. 2010, A&A, 518, L22+

Cooray, A. & Sheth, R. 2002, Phys. Rep., 372, 1

de Graauw, T., Helmich, F. P., Phillips, T. G., et al. 2010, A&A, 518, L6+

Devlin, M. J., Ade, P. A. R., Aretxaga, I., et al. 2009, Nature, 458, 737

Dohlen, K., Origne, A., Pouliquen, D., & Swinyard, B. M. 2000, in Society of Photo-Optical Instrumentation Engineers (SPIE) Conference Series, Vol. 4013, Society of Photo-Optical Instrumentation Engineers (SPIE) Conference Series, ed. J. B. Breckinridge & P. Jakobsen, 119–128

Dole, H., Lagache, G., Puget, J., et al. 2006, A&A, 451, 417

Doyle, D., Pilbratt, G., & Tauber, J. 2009, Proceedings of the IEEE, 97, 1403

Duband, L., Clerc, L., Ercolani, E., Guillemet, L., & Vallcorba, R. 2008, Cryogenics, 48, 95

Eales, S., Lilly, S., Gear, W., et al. 1999, ApJ, 515, 518

Elbaz, D., Cesarsky, C. J., Chanial, P., et al. 2002, A&A, 384, 848

Fadda, D., Flores, H., Hasinger, G., et al. 2002, A&A, 383, 838

Fischer, J., Klaassen, T., Hovenier, N., et al. 2004, Appl. Opt., 43, 3765

Fixsen, D. J., Dwek, E., Mather, J. C., Bennett, C. L., & Shafer, R. A. 1998, ApJ, 508, 123

Franceschini, A. 1982, Ap&SS, 86, 3

Franceschini, A., Andreani, P., & Danese, L. 1998, MNRAS, 296, 709

Franceschini, A., Aussel, H., Bressan, A., et al. 1997, in ESA Special Publication, Vol. 401, The Far Infrared and Submillimetre Universe., ed. A. Wilson, 159–+

Franceschini, A., Aussel, H., Cesarsky, C. J., Elbaz, D., & Fadda, D. 2001, A&A, 378, 1

Franceschini, A., Manners, J., Polletta, M. d. C., et al. 2005, AJ, 129, 2074

Franceschini, A., Mazzei, P., de Zotti, G., & Danese, L. 1994, ApJ, 427, 140

Franceschini, A., Rodighiero, G., Vaccari, M., et al. 2010, A&A, 517, 74

Frayer, D. T., Huynh, M. T., Chary, R., et al. 2006, ApJ, 647, L9

Frayer, D. T., Sanders, D. B., Surace, J. A., et al. 2009, AJ, 138, 1261

Fritz, J., Franceschini, A., & Hatziminaoglou, E. 2006, MNRAS, 366, 767

Fulton, T. R., Baluteau, J., Bendo, G., et al. 2010, in Presented at the Society of Photo-Optical Instrumentation Engineers (SPIE) Conference, Vol. 7731, Society of Photo-Optical Instrumentation Engineers (SPIE) Conference Series

Genzel, R. & Cesarsky, C. J. 2000, ARA&A, 38, 761

Glenn, J., Conley, A., Béthermin, M., et al. 2010, MNRAS, 409, 109

Griffin, M., Dowell, C. D., Lim, T., et al. 2008, in Presented at the Society of Photo-Optical Instrumentation Engineers (SPIE) Conference, Vol. 7010, Society of Photo-Optical Instrumentation Engineers (SPIE) Conference Series

Griffin, M. J., Abergel, A., Abreu, A., et al. 2010, A&A, 518, L3+

Griffin, M. J., Bock, J. J., & Gear, W. K. 2002, Appl. Opt., 41, 6543

Guiderdoni, B., Bouchet, F. R., Puget, J., Lagache, G., & Hivon, E. 1997, Nature, 390, 257

Hargrave, P., Bock, J., Brockley-Blatt, C., et al. 2006in (SPIE), 627513

Hatziminaoglou, E., Fritz, J., Franceschini, A., et al. 2008, MNRAS, 386, 1252

Hauser, M. G., Arendt, R. G., Kelsall, T., et al. 1998, ApJ, 508, 25

Holland, W. S., Robson, E. I., Gear, W. K., et al. 1999, MNRAS, 303, 659

Hughes, D. H., Aretxaga, I., Chapin, E. L., et al. 2002, MNRAS, 335, 871

Hughes, D. H., Serjeant, S., Dunlop, J., et al. 1998, Nature, 394, 241

Jarosik, N., Barnes, C., Bennett, C. L., et al. 2003, ApJS, 148, 29

Jenkins, C. R. & Reid, I. N. 1991, AJ, 101, 1595

Kessler, M. F., Steinz, J. A., Anderegg, M. E., et al. 1996, A&A, 315, L27

Khan, S. A., Chanial, P. F., Willner, S. P., et al. 2009, ApJ, 706, 319

Khan, S. A., Shafer, R. A., Benford, D. J., et al. 2005, ApJ, 631, L9

Khan, S. A., Shafer, R. A., Serjeant, S., et al. 2007, ApJ, 665, 973

Komatsu, E., Dunkley, J., Nolta, M. R., et al. 2009, ApJS, 180, 330

Lagache, G., Abergel, A., Boulanger, F., Désert, F. X., & Puget, J. 1999, A&A, 344, 322

Le Borgne, D., Elbaz, D., Ocvirk, P., & Pichon, C. 2009, A&A, 504, 727

Le Floc'h, E., Papovich, C., Dole, H., et al. 2005, ApJ, 632, 169

Levenson, L., Marsden, G., Zemcov, M., et al. 2010, MNRAS, 409, 83

Low, F. J., Rieke, G. H., & Gehrz, R. D. 2007, ARA&A, 45, 43

Magliocchetti, M., Silva, L., Lapi, A., et al. 2007, MNRAS, 375, 1121

Moreno, R. 2010, *Neptune and Uranus planetary brightness temperature tabulation* available from ESA *Herschel* Science Centre, 2010

Naylor, D. A. & Tahic, M. K. 2007, J. Opt. Soc. Am. A, 24, 3644

Negrello, M., Perrotta, F., González-Nuevo, J., et al. 2007, MNRAS, 377, 1557

Neugebauer, G. & Leighton, R. B. 1969, NASA Special Publication, 3047

Nguyen, H. T., Schulz, B., Levenson, L., et al. 2010, A&A, 518, L5

Oliver, S. J., Wang, L., Smith, A. J., et al. 2010, A&A, 518, L21

PACS. 2010, PACS observers' manual, `http://herschel.esac.esa.int/Docs/PACS/pdf/pacs_om.pdf`

Papovich, C., Dole, H., Egami, E., et al. 2004, ApJS, 154, 70

Patanchon, G., Ade, P. A. R., Bock, J. J., et al. 2009, ApJ, 707, 1750

Pearson, C. & Khan, S. A. 2009, MNRAS, 399, L11

Pilbratt, G. L., Riedinger, J. R., Passvogel, T., et al. 2010, A&A, 518, L1+

Pisano, G., Hargrave, P., Griffin, M., et al. 2005, Appl. Opt., 44, 3208

Poglitsch, A., Waelkens, C., Geis, N., et al. 2010, A&A, 518, L2+

Puget, J., Abergel, A., Bernard, J., et al. 1996, A&A, 308, L5+

Reddy, N. A., Steidel, C. C., Pettini, M., et al. 2008, ApJS, 175, 48

Rodighiero, G., Vaccari, M., Franceschini, A., et al. 2010, A&A, 515, A8+

Sanders, D. B. & Mirabel, I. F. 1996, ARA&A, 34, 749

Savage, R. S. & Oliver, S. 2007, ApJ, 661, 1339

Scheuer, P. A. G. 1957, Mathematical Proceedings of the Cambridge Philosophical Society, 53, 764

Scheuer, P. A. G. 1974, MNRAS, 166, 329

Schulz, B., Bock, J. J., Lu, N., et al. 2008, in Presented at the Society of Photo-Optical Instrumentation Engineers (SPIE) Conference, Vol. 7020, Society of Photo-Optical Instrumentation Engineers (SPIE) Conference Series

Scott, S. E., Dunlop, J. S., & Serjeant, S. 2006, MNRAS, 370, 1057

Serjeant, S. & Harrison, D. 2005, MNRAS, 356, 192

Shupe, D. L., Rowan-Robinson, M., Lonsdale, C. J., et al. 2008, AJ, 135, 1050

Smail, I., Ivison, R. J., & Blain, A. W. 1997, ApJ, 490, L5+

Smail, I., Ivison, R. J., Blain, A. W., & Kneib, J. 2002, MNRAS, 331, 495

Soifer, B. T., Helou, G., & Werner, M. 2008, ARA&A, 46, 201

SPIRE. 2010, SPIRE observers' manual - HERSCHEL-HSC-DOC-0789, ESA Herschel Science Centre

Swinyard, B. M., Dohlen, K., Ferand, D., et al. 2003, in Society of Photo-Optical Instrumentation Engineers (SPIE) Conference Series, Vol. 4850, Society of Photo-Optical Instrumentation Engineers (SPIE) Conference Series, ed. J. C. Mather, 698–709

Turner, A. D., Bock, J. J., Beeman, J. W., et al. 2001, Appl. Opt., 40, 4921

Vaccari, M. 2004, PhD thesis, Università degli Studi di Padova

Vaccari, M., Marchetti, L., Franceschini, A., & Perez-Fournon, I. 2009, in Multiwavelength Astronomy and Virtual Observatory, ed. D. Baines & P. Osuna, 45–+

Valiante, E., Lutz, D., Sturm, E., Genzel, R., & Chapin, E. L. 2009, ApJ, 701, 1814

Viero, M. P., Ade, P. A. R., Bock, J. J., et al. 2009, ApJ, 707, 1766

Wall, J. V. & Cooke, D. J. 1975, MNRAS, 171, 9

Wall, J. V. & Jenkins, C. R. 2003, Practical statistics for astronomer (Cambridge University Press)

Walmsley, C. M., Bertout, C., Combes, F., et al. 2010a, A&A, 518

Walmsley, C. M., Bertout, C., Combes, F., et al. 2010b, A&A, 521

Waskett, T. J., Sibthorpe, B., Griffin, M. J., & Chanial, P. F. 2007, MNRAS, 381, 1583

Webb, J. K., Barcons, X., Carswell, R. F., & Parnell, H. C. 1992, MNRAS, 255, 319

Werner, M. W., Roellig, T. L., Low, F. J., et al. 2004, ApJS, 154, 1